



**PHOTOCATALYTIC PERFORMANCE OF NITROGEN-PLATINUM GROUP
METAL CO-DOPED TiO₂ SUPPORTED ON CARBON NANOTUBES FOR
VISIBLE-LIGHT DEGRADATION OF ORGANIC POLLUTANTS IN WATER**

By

Alex Tawanda Kuvarega

Student Number: 200946017

Thesis in fulfilment of the requirement for the degree



PHILOSOPHIAE DOCTOR

in

CHEMISTRY

in the

FACULTY OF SCIENCE

of the

UNIVERSITY OF JOHANNESBURG

Supervisor : PROF RWM KRAUSE

Co-supervisor : PROF BB MAMBA

October 2012

DECLARATION



AFFIDAVIT: MASTER AND DOCTORAL STUDENTS TO WHOM IT MAY CONCERN

This serves to confirm that I _____
Full Name(s) and Surname

ID Number/
Passport _____

Student number _____ enrolled for the Qualification

in the Faculty of Science

Herewith declare that my academic work is in line with the Plagiarism Policy of the University of Johannesburg with which I am familiar.

I further declare that the work presented in the _____ (minor dissertation/dissertation/thesis) is authentic and original unless clearly indicated otherwise and in such instances full reference to the source is acknowledged and I do not pretend to receive any credit for such acknowledged quotations, and that there is no copyright infringement in my work. I declare that no unethical research practices were used or material gained through dishonesty. I understand that plagiarism is a serious offence and that should I contravene the Plagiarism Policy notwithstanding signing this affidavit, I may be found guilty of a serious criminal offence (perjury) that would amongst other consequences compel the University of Johannesburg to inform all other tertiary institutions of the offence and to issue a corresponding certificate of reprehensible academic conduct to whomever requests such a certificate from the institution.

Signed at Johannesburg _____ on this _____ of _____ 2013

Signature _____ Print name _____

STAMP: COMMISSIONER OF OATHS

Affidavit certified by a Commissioner of Oaths

This affidavit conforms with the requirements of the JUSTICES OF THE PEACE AND COMMISSIONERS OF OATHS ACT 16 OF 1963 and the applicable Regulations published in the GG NNR 1258 of 21 July 1972; GN 903 of 10 July 1998; GN 109 of 2 February 2001 as amended.

DEDICATION

This thesis is dedicated to my late mother, Lorraine, who was a source of encouragement and inspiration throughout my life. My father – you nurtured me to be the man I am today. My wife, Rachel, for the myriad of ways in which, throughout our life together, you have actively supported me in my determination to find and realise my potential and to make this contribution to our world.



CONFERENCE PRESENTATIONS

The work contained in this thesis has been presented at national and international conferences.

- ❖ Kuvarega A.T., Krause R.W.M. and Mamba B.B. *Multiwalled Carbon Nanotubes Decorated with Nitrogen, Palladium Co-Doped TiO₂ (MWCNT/N, Pd Co-Doped TiO₂) for Visible Light Photocatalytic Degradation of Eosin Yellow in Water. **Poster presentation.** Department of Science and Technology/Centre of Excellence in Strong Materials (DST/CoE-SM), Student Presentation Workshop 2012. University of the Witwatersrand, South Africa, 30 May 2012.*
- ❖ Kuvarega A.T., Nkambule T.I., Krause R.W.M., Mamba B.B. and Haarhoff J. *Synthesis and Characterisation of Pd Modified N Doped TiO₂ for Photocatalytic Degradation of Natural Organic Matter (NOM) Fractions. **Oral presentation.** Water Institute of South Africa (WISA) 2012. Cape Town ICC, South Africa, 6 – 9 May 2012.*
- ❖ Kuvarega A.T., Krause R.W.M. and Mamba B.B. *Multiwalled Carbon Nanotubes Decorated with Nitrogen, Palladium Co-Doped TiO₂ (MWCNT/N, Pd Co-Doped TiO₂) for Visible Light Photocatalytic Degradation of Eosin Yellow in Water. **Oral presentation.** South African Chemical Institute Young Chemist's/Nanotechnology Young Researcher's Symposium. Vaal University of Technology, 14 October 2011.*
- ❖ Kuvarega A.T., Krause R.W.M. and Mamba B.B. *Multiwalled Carbon Nanotubes Decorated with Nitrogen, Palladium Co-Doped TiO₂ (MWCNT/N, Pd Co-Doped TiO₂) for Visible Light Photocatalytic Degradation of Eosin Yellow in Water. **Oral presentation.** Department of Science and Technology/National Research Foundation (DST/NRF) Centre of Excellence in Strong Materials (DST/CoE-SM). Carbon Nanotube and*

Composites Research Showcase Day 2011. University of the Witwatersrand, 4 October 2011.

- ❖ Kuvarega A.T., Krause R.W.M. and Mamba B.B. *Nitrogen, Palladium - Codoped TiO₂ for Efficient Visible Light Photocatalytic Dye Degradation.* **Poster presentation.** 10th International Conference on Materials Chemistry 10 (MC10). University of Manchester, UK, 4 – 7 July 2011.
- ❖ Kuvarega A.T., Krause R.W.M. and Mamba B.B. *Nitrogen, Palladium - Codoped TiO₂ for Efficient Visible Light Photocatalytic Dye Degradation.* **Oral presentation.** SACI, Young Scientist Symposium. University of Johannesburg, Doornfontein Campus, 19 November 2010.
- ❖ Kuvarega A.T., Krause R.W.M. and Mamba B.B. *Effect of Palladium Dopant Amount in Nitrogen, Palladium - Codoped TiO₂ on Photocatalytic Dye Degradation.* **Oral presentation.** DST/NIC Symposium. University of the Western Cape, South Africa, 23-25 November 2010.
- ❖ Kuvarega A.T., Krause R.W.M. and Mamba B.B. *Effect of Palladium Dopant Amount in Nitrogen, Palladium Co-Doped TiO₂ on Photocatalytic Dye Degradation.* **Oral presentation.** DST/NIC Water Technology Workshop. Mintek, South Africa, 29 - 30 July 2010.
- ❖ Kuvarega A.T., Krause R.W.M. and Mamba B.B. *Synthesis and Fabrication of Polymer/CNT Composites for Application in Water Purification.* **Poster presentation.** Department of Science and Technology/National Research Foundation (DST/NRF) Centre of Excellence in Strong Materials (DST/CoE-SM). Annual Meeting. University of the Witwatersrand, 3 May 2010.

PEER REVIEWED PUBLICATIONS

Results emanating from this study have either been published or submitted to peer-reviewed journals for publication.

- ❖ Kuvarega A.T., Krause R.W.M. and Mamba B.B. (2012). Multiwalled carbon nanotubes decorated with nitrogen, palladium co-doped TiO₂ (MWCNT/N, Pd co-doped TiO₂) for visible light photocatalytic degradation of eosin yellow in water. *J. Nanopart. Res.* 14, 776. DOI: 10.1007/s11051-012-0776-x.
- ❖ Nkambule T.I, Kuvarega A.T., Krause R.W, Mamba B.B and Haarhoff J. (2012). Synthesis and characterization of Pd-Modified N-doped TiO₂ for photocatalytic degradation of natural organic matter. *Environ. Sci. Pollut. Res.* 19, 4120 – 4132.
- ❖ Kuvarega A.T., Krause R.W.M. and Mamba B.B. (2011). Nitrogen/palladium co-doped TiO₂ for efficient visible light photocatalytic dye degradation. *J. Phys. Chem. C* 115, 22110 – 22120.
- ❖ Kuvarega A.T., Krause R.W.M. and Mamba B.B. Pearl-bead-necklace structured double walled carbon nanotube/nitrogen, palladium co-doped TiO₂ (DWCNT/N,Pd TiO₂) nanocomposites for dye degradation under visible light irradiation. *Mater. Chem. Phys.* (Under review)
- ❖ Kuvarega A.T., Krause R.W.M. and Mamba B.B. Photocatalytic performance of nitrogen, osmium co-doped TiO₂ for removal of Eosin Yellow in water under visible-light irradiation. *J.Nanosci Nanotechnol.* (Accepted)

-
- ❖ Ndlovu T., Kuvarega A. T., Arotiba A.O., Sampath S., Krause R.W.M. and Mamba B.B. Exfoliated graphite/titanium dioxide nanocomposites for the photodegradation of eosin yellow. *Ind. Eng. Chem. Res.* (under Review)



ACKNOWLEDGEMENTS

I would like to express my sincere gratitude to the following people and institutions for all their support, dedication and assistance:

- Prof. R.W.M. Krause and Prof. B.B. Mamba for offering me the opportunity to enrol as a Ph.D. student in their group. I appreciate their advice, supervision and guidance throughout this research. I truly enjoyed working in the laboratory, which is so well equipped, not only with instruments, but also with chemicals. I also appreciate the freedom they offered me in my research. Many thanks also for all the support, discussions, corrections of the papers, posters, presentations and the thesis. Additionally, many thanks for affording me the opportunity to attend many interesting conferences and workshops.
- The University of Johannesburg, Department of Applied Chemistry under the Faculty of Science and the NRF/DST Centre of Excellence in Strong Materials, South Africa for funding and financial support.
- The Nano-Research Group for the discussions, ideas and of course for the informal nano meetings.
- I have had the chance to collaborate with some colleagues in our group. Special mention goes to Dr. T.I. Nkambule. Thank you for your expertise, guidance and contribution to the work on NOM fractionation and photodegradation.

-
- Professor Alexander Ziegler, your assistance with TEM and SEM analyses is greatly appreciated; Zikhona Tetana – thank you for the extra time you spared for assistance with EDS analyses; Dr Sharon Moeno, thank you for the comments, suggestions and recommendations.

 - Mr Pholoso Matjele, Mrs Leah Moshe and the entire staff of the Department of Applied Chemistry for their help in many ways.

 - My wife Rachel, my sisters Junior, Norah, Mary and Easter, and my brother Felix for their support, love and for always believing in my capabilities.

 - My friends and colleagues for their friendship and help in many different ways.



ABSTRACT

Elimination of toxic organic compounds from wastewater is currently one of the most important subjects in water-pollution control. Among the many organic pollutants are dyes and emerging pollutants such as natural organic matter (NOM). Dyes such as Eosin Yellow (EY), an anionic xanthene fluorescent dye, can originate from many sources such as textile industrial processes, paper pulp industries and agricultural processes. Most dyes are problematic because they are resistant to conventional chemical or biological water-treatment methods and therefore persist in the environment. NOM consists of a highly variable mixture of products found in water and soils. NOM is formed as a result of the decomposition of plant and animal material and is a precursor to the formation of disinfection by-products (DBP) during water disinfection. These organic compounds cause undesirable colour, taste and odour in water. NOM affects the capacity of other treatment processes to effectively remove organic micro-pollutants or inorganic species that may be present in the water. Its removal also uses up chemicals and energy and so it is expensive to treat.

Titanium dioxide (TiO_2) has emerged as one of the most fascinating materials in the modern era due to its semiconducting and catalytic properties. TiO_2 is a large band-gap semiconductor that exists mainly in the anatase (band gap 3.2 eV) and rutile (band gap 3.0 eV) phases. Its response to UV light has led to increased interest in its application in the photocatalysis research field. It has been investigated extensively for its super hydrophilicity and use in environmental remediation and solar fuel production. In spite of extensive efforts to apply TiO_2 for environmental remediation, photocatalytic activity in the visible region has remained quite low hence the ultimate goal of this research was to fabricate highly photoactive catalysts composed of non-metal, platinum-group metal (PGM) co-doped TiO_2 and carbon nanotubes (CNTs) and to apply them for water purification using solar radiation.

Nitrogen, PGM co-doped TiO₂ (PGM = Pd or Os) photocatalysts were prepared using a modified sol-gel method involving calcination of the hydrolysis products of titanium isopropoxide, Ti(OC₃H₇)₄, dissolved in 2-propanol, with aqueous ammonia. Anatase-phase TiO₂ particles in the size range of 10 nm to 20 nm were synthesised and confirmed by XRD, Raman, TEM and SEM analysis. Co-doping imparted a red shift in the absorption edges of the materials. Nitrogen and PGM co-doped TiO₂ were synthesised in high yield and applied to the photocatalytic degradation of EY and NOM. The photocatalytic performance was dependent on the amount of Pd dopant.

The N, Pd co-doped TiO₂ (0.6%) was also evaluated for the removal of NOM from water under visible-light irradiation. The highest photodegradation for the NOM fractions was achieved for the hydrophobic fraction (71% to 96%) while the transphilic fraction (14% to 15% degradation) was least affected. These results are far better than those achieved by most NOM-removal methods such as coagulation where highest NOM-removal efficiencies of about 75% are achieved.

For the N, Os co-doped TiO₂, calcination temperature had a significant effect on the photocatalytic activity of the material and this was attributed to the possible formation, at high temperature, of OsO₂ supported on the TiO₂. DRUV-Vis analysis revealed a red shift in absorption with increasing calcination temperature, confirmed by a decrease in the band gap of the material. The rutile phase was found to be more effective in degrading the EY dye ($k_a = 1.84 \times 10^{-2} \text{ min}^{-1}$) compared to the anatase phase ($k_a = 9.90 \times 10^{-3} \text{ min}^{-1}$) regardless of the increase in particle size. A mechanism for the enhanced photoactivity of the N, PGM co-doped TiO₂ was proposed based on the electron-trapping capability of the PGM as well as the effect of N in reducing the TiO₂ band gap.

Nanocomposite assemblies composed of different proportions of MWCNTs, DWCNTs or EG and anatase co-doped TiO₂ were also synthesised by the modified sol-gel method. Higher CNT levels led to their aggregation and consequently poor coverage by N, Pd co-doped TiO₂. High degradation rate constants of $3.42 \times 10^{-2} \text{ min}^{-1}$ and $5.18 \times 10^{-3} \text{ min}^{-1}$ were realised for the 0.5%

MWCNT/N, Pd co-doped TiO₂ composite, using simulated solar light and visible light, respectively. The 2.0% DWCNT/N, Pd TiO₂ composite showed the highest photoactivity (99.87% EY removal after 3 h, $k_a = 3.220 \times 10^{-2} \text{ min}^{-1}$), whilst the 40.0% DWCNT/N, Pd TiO₂ composite (89.72% EY removal after 3 h, $k_a = 9.990 \times 10^{-3} \text{ min}^{-1}$) was the least efficient. EG-TiO₂ was found to be a very good adsorbent of the dye, though photoactivity was lower compared to the CNT/TiO₂ nanocomposites.

The photocatalytic enhancement at low CNT percentages was attributed to the synergistic effects of the supporting and electron-transfer channelling role of the CNTs as well as the electron-trapping effects of the Pd metal. These phenomena favour the separation of the photogenerated electron-hole pairs, reducing their recombination rate, leading to significantly enhanced photocatalytic activity. The results obtained in the photodegradation studies suggest a potential application of nanotechnology, in the latter stages of the water-treatment train, for the removal of EY and NOM from water.



TABLE OF CONTENTS

<u>Section</u>	<u>Page</u>
Declaration	ii
Dedication	iii
Conference presentations	iv
Peer reviewed publications.....	vi
Acknowledgements	viii
Abstract	x
Table of Contents	xiii
List of Figures.....	xxi
List of Tables	xxviii
List of Abbreviations	xxx
CHAPTER 1: INTRODUCTION	1
1.1 BACKGROUND	1
1.2 PROBLEM STATEMENT	2
1.3 JUSTIFICATION	3
1.4 AIM AND OBJECTIVES.....	8
1.4.1 Aim.....	8
1.4.2 Objectives	8
1.5 THESIS OUTLINE	10
1.6 REFERENCES	11
CHAPTER 2: LITERATURE REVIEW	15
2.1 INTRODUCTION	15

2.1.1	Water availability.....	15
2.1.2	Water pollution.....	16
2.2	NANOTECHNOLOGY AND THE ENVIRONMENT.....	17
2.3	TiO ₂ AS A SEMICONDUCTOR.....	18
2.4	FUNDAMENTAL ASPECTS OF TiO ₂ PHOTOCATALYSIS.....	21
2.5	LIMITATIONS OF TiO ₂ AS A PHOTOCATALYST.....	23
2.6	STRATEGIES FOR IMPROVING TIO ₂ PERFORMANCE.....	24
2.6.1	Non-metal doping.....	25
2.6.1.1	Nitrogen doping.....	26
2.6.1.2	Carbon doping.....	27
2.6.2	Metal doping.....	28
2.6.2.1	Alkaline earth-metal doping.....	29
2.6.2.2	Transition metal doping.....	29
2.6.2.3	Lanthanide doping.....	34
2.6.3	Co-doping.....	36
2.7	CARBON NANOTUBES.....	38
2.7.1	Functionalisation of carbon nanotubes.....	40
2.7.2	Carbon nanotube-TiO ₂ nanocomposites.....	41
2.8	NANOPARTICLE RECOVERY.....	45
2.9	APPLICATIONS OF TiO ₂ -BASED PHOTOCATALYTS.....	45
2.9.1	Photo-induced hydrophilic coatings and self-cleaning devices ...	45
2.9.2	Wastewater treatment.....	46
2.9.3	Water splitting.....	46
2.9.4	Dye-sensitised solar cells.....	46
2.9.5	Bactericides.....	47
2.10	TOXICITY OF NANOPARTICLES.....	47
2.11	CONCLUDING REMARKS.....	47
2.12	REFERENCES.....	49
CHAPTER 3: EXPERIMENTAL METHODOLOGY.....		63
3.1	INTRODUCTION.....	63
3.2	REAGENTS AND SOLVENTS.....	63

3.3	FABRICATION OF NANOPARTICLES.....	63
3.3.1	Sol-gel method for TiO ₂ nanostructures	64
3.3.2	Modified sol-gel method for N, PGM co-doped TiO ₂	65
3.4	CCVD SYNTHESIS OF DOUBLE WALLED CARBON NANOTUBES (DWCNTs)	65
3.4.1	Catalyst preparation	65
3.4.2	Synthesis of DWCNTs	66
3.4.3	Purification of DWCNTs	66
3.4.4	Functionalisation of DWCNTs	66
3.5	SYNTHESIS OF MULTI WALLED CARBON NANOTUBES (MWCNTs)...	67
3.5.1	Purification of MWCNTs	67
3.5.2	Functionalisation of MWCNTs.....	67
3.5.3	Modified sol-gel method for synthesis of carbon nanotube/nitrogen, platinum group metal (CNT/N, PGM) co-doped TiO ₂ nanocomposites	68
3.6	CHARACTERISATION OF MATERIALS	68
3.6.1	Fourier transform infrared (FT-IR) spectroscopy	69
3.6.2	Raman spectroscopy	70
3.6.3	Ultraviolet-visible (UV-Vis) spectroscopy	71
3.6.3.1	Diffuse reflectance measurements	71
3.6.3.2	Determination of material band gaps from absorption coefficient.....	73
3.6.4	X-ray Diffraction (XRD)	74
3.6.4.1	Crystallite phases and sizes	75
3.6.5	Thermogravimetric analysis(TGA)	76
3.6.6	Scanning electron microscopy (SEM)	77
3.6.6.1	Energy dispersive X-ray spectroscopy (EDS)	77
3.6.7	Transmission electron microscopy (TEM)	78
3.6.8	X-ray photoelectron spectroscopy (XPS)	79
3.7	PHOTODEGRADATION EXPERIMENTS	80
3.8	PHOTODEGRADATION KINETICS	83
3.8.1	Kinetic model	83
3.8.2	Global effective quantum yield model, ϕgE_{eff}	88

3.9	REFERENCES	90
-----	------------------	----

CHAPTER 4: NITROGEN, PALLADIUM CO-DOPED TiO₂ FOR EFFICIENT

VISIBLE-LIGHT PHOTOCATALYTIC DYE DEGRADATION..... 93

4.1	INTRODUCTION	93
4.2	EXPERIMENTAL DETAILS	94
4.2.1	Preparation of materials	94
4.2.2	Material characterisation	95
4.2.3	Evaluation of photocatalytic activity	95
4.3	RESULTS AND DISCUSSION	95
4.3.1	FT-IR studies	95
4.3.2	Raman analysis	96
4.3.3	XRD analysis	98
4.3.4	Optical properties.....	100
4.3.5	SEM, TEM and EDS analyses	105
4.3.6	Thermal analysis.....	106
4.3.7	XPS studies	107
4.4	DYE PHOTODEGRADATION STUDIES	111
4.5	CONCLUSION.....	116
4.6	REFERENCES	117

CHAPTER 5: SYNTHESIS AND CHARACTERISATION OF Pd MODIFIED N-

DOPED TiO₂ FOR PHOTOCATALYTIC DEGRADATION OF NATURAL

ORGANIC MATTER (NOM) FRACTIONS..... 121

5.1	INTRODUCTION	121
5.2	METHODOLOGY	124
5.2.1	Preparation of material.....	124
5.2.2	Characterisation of materials	124
5.3	WATER SAMPLING AND CHARACTERISATION	124
5.3.1	Sample collection.....	124

5.3.2	Bulk water characterisation	124
5.3.3	Organic carbon analysis.....	124
5.3.4	Ultraviolet-visible (UV-Vis) spectrophotometric analysis	125
5.3.5	NOM fractions	125
5.3.5.1	Fractionation of NOM.....	126
5.3.5.2	Polarity rapid assessment method (PRAM)	126
5.3.5.3	The modified PRAM.....	128
5.4	PHOTOCATALYTIC DEGRADATION EXPERIMENTS.....	129
5.5	RESULTS AND DISCUSSION	129
5.5.1	FT-IR characterisation.....	129
5.5.2	Raman characterisation	130
5.5.3	XRD characterisation	131
5.5.4	Optical properties.....	132
5.5.5	Morphological properties.....	134
5.5.6	Thermal properties	135
5.5.7	Bulk water characterisation of samples.....	136
5.5.8	Ultraviolet-visible (UV-Vis) spectrophotometric analysis	137
5.6	NOM PHOTODEGRADATION STUDIES	138
5.6.1	Bulk NOM.....	138
5.6.2	NOM fractions	140
5.6.3	Photodegradation mechanism	144
5.7	CONCLUSION	147
5.8	REFERENCES	148

**CHAPTER 6: PHOTOCATALYTIC PERFORMANCE OF NITROGEN, OSMIUM
CO-DOPED TiO₂ FOR REMOVAL OF EOSIN YELLOW IN WATER UNDER**

VISIBLE-LIGHT IRRADIATION	153	
6.1	INTRODUCTION	153
6.2	MATERIALS AND METHODS	154
6.2.1	Preparation of materials	154
6.2.2	Material characterisation	155

6.2.3	Evaluation of photocatalytic activity	155
6.3	RESULTS AND DISCUSSION	155
6.3.1	FT-IR analysis	155
6.3.2	Raman analysis	156
6.3.3	XRD analysis	158
6.3.4	Optical properties	160
6.3.5	SEM and EDS analyses	165
6.3.6	TEM analysis	166
6.3.7	Thermal properties	168
6.4	DYE PHOTODEGRADATION STUDIES	169
6.5	CONCLUSION	175
6.6	REFERENCES	176

**CHAPTER 7: MULTIWALLED CARBON NANOTUBES DECORATED WITH
NITROGEN, PALLADIUM CO-DOPED TiO₂ (MWCNT/N, Pd CO-DOPED TiO₂)
FOR VISIBLE-LIGHT PHOTOCATALYTIC DEGRADATION OF EOSIN YELLOW
IN WATER..... 182**

7.1	INTRODUCTION	182
7.2	EXPERIMENTAL DETAILS	184
7.2.1	Preparation of MWCNTs	184
7.2.2	Preparation of the nanocomposites	184
7.2.3	Material characterisation	185
7.2.4	Evaluation of photocatalytic activity	185
7.3	RESULTS AND DISCUSSION	186
7.3.1	FT-IR studies	186
7.3.2	Raman studies	187
7.3.3	XRD analysis	189
7.3.4	SEM and EDS analyses	190
7.3.5	TEM analysis	192
7.3.6	TGA studies	194
7.3.7	Optical properties	195

7.4	PHOTODEGRADATION STUDIES	199
7.5	CONCLUSION	205
7.6	REFERENCES	206

CHAPTER 8: PEARL-BEAD-NECKLACE-STRUCTURED DOUBLE-WALLED CARBON NANOTUBE/NITROGEN, PALLADIUM CO-DOPED TiO₂ (DWCNT/N, Pd TiO₂) NANOCOMPOSITES FOR DYE DEGRADATION UNDER VISIBLE-LIGHT IRRADIATION 210

8.1	INTRODUCTION	210
8.2	MATERIALS AND METHODS	212
8.2.1	Synthesis of DWCNTs	212
8.2.2	Preparation of the nanocomposites	212
8.2.3	Material characterisation	213
8.2.4	Evaluation of photocatalytic activity	213
8.3	RESULTS AND DISCUSSION	213
8.3.1	FT-IR studies	213
8.3.2	Raman analysis	215
8.3.3	XRD studies	218
8.3.4	Optical properties	220
8.3.5	SEM and EDS analyses	225
8.3.6	TEM and EDS analyses	226
8.3.7	Thermal properties	231
8.4	PHOTOCATALYTIC DEGRADATION STUDIES.....	232
8.5	CONCLUSION	241
8.6	REFERENCES	242

CHAPTER 9: EXFOLIATED GRAPHITE/TiO₂ (EG-TiO₂) NANOCOMPOSITES FOR THE PHOTOCATALYTIC DEGRADATION OF EOSIN YELLOW..... 247

9.1	INTRODUCTION	247
-----	--------------------	-----

9.2	EXPERIMENTAL DETAILS	249
9.2.1	Preparation of Exfoliated Graphite	249
9.2.2	Preparation of Exfoliated Graphite/ TiO ₂ nanocomposite	249
9.2.3	Material characterisation	250
9.2.4	Evaluation of Photocatalytic Activity	250
9.3	RESULTS AND DISCUSSION	250
9.3.1	Characterisation of EG and EG-TiO ₂	250
9.3.2	Photodegradation studies	254
9.4	CONCLUSION	259
9.5	REFERENCES	260
 CHAPTER 10: CONCLUSIONS AND FUTURE PERSPECTIVES		264
10.1	CONCLUSIONS	264
10.2	FUTURE PERSPECTIVES	267



LIST OF FIGURES

<u>Figure</u>	<u>Description</u>	<u>Page</u>
Figure 2.1	Band positions of several semiconductors in contact with an aqueous electrolyte at pH 1	19
Figure 2.2	Unit cells of the rutile, anatase and brookite phases of TiO ₂ [grey and purple spheres represent O and Ti, respectively].....	20
Figure 2.3	Anatase and rutile band gaps and activation wavelength	21
Figure 2.4	Scheme of the TiO ₂ photocatalysis mechanism	23
Figure 2.5	Mechanism of non-metal doped TiO ₂ photocatalysis	27
Figure 2.6	Formation of electron traps through Schottky barrier formation (NM – noble metal)	30
Figure 2.7	Some „pros and cons“ of mono-doping methodologies	35
Figure 2.8	Band-gap reduction and electron trapping in nitrogen, metal co-doped TiO ₂ [M – metal]	36
Figure 2.9	Some applications of CNTs.....	39
Figure 2.10	TEM images of (a) bare functionalised MWCNTs; and (b) MWCNT coated with N, Pd co-doped TiO ₂	42
Figure 2.11	CNT/TiO ₂ composite showing free channelling of electrons through CNTs for enhanced photoactivity	43
Figure 3.1	The modified sol-gel method for synthesis of N, PGM co-doped TiO ₂	65
Figure 3.2	Elemental analysis techniques showing detection range, sensitivity and lateral resolution.....	69
Figure 3.3	A 0° incident light integrating sphere attachment	72
Figure 3.4	Tauc plots for Commercial TiO ₂ (P25) and N,Pd co-doped TiO ₂ (n = 2)	74

Figure 3.5	Experimental setup for photodegradation experiments using a 150 W Eurolux lamp.....	81
Figure 3.6	Experimental setup for photodegradation experiments using a solar simulator.....	82
Figure 3.7	Output of the solar simulator with an AM 1.5 Global Filter	82
Figure 3.8	Normal incident solar spectra at sea level on a clear day	83
Figure 4.1	Chemical structure of Eosin Yellow.....	94
Figure 4.2	FT-IR spectra of N, Pd co-doped TiO ₂ with different palladium concentrations.....	96
Figure 4.3	Raman spectra of N, Pd co-doped TiO ₂ with different palladium concentrations.....	97
Figure 4.4	XRD patterns of N, Pd co-doped TiO ₂ with different palladium concentrations (A – anatase)	99
Figure 4.5	Diffuse reflectance UV-Vis spectra of N, Pd co-doped TiO ₂ with different palladium concentrations	101
Figure 4.6	Kubelka-Munk plots of N, Pd co-doped TiO ₂ with different palladium concentrations	102
Figure 4.7	UV-Vis absorption spectra of N, Pd co-doped TiO ₂ with different palladium concentrations	103
Figure 4.8	Tauc plots of N, Pd co-doped TiO ₂ with different palladium concentrations.....	104
Figure 4.9	(a) SEM image; (b) and (c) TEM images; and (d) EDX spectrum of N, Pd co-doped TiO ₂ (0.6% Pd)	106
Figure 4.10	TGA curves of N, Pd co-doped TiO ₂ with different palladium concentrations.....	107
Figure 4.11	XPS survey scan of (a) N, Pd co-doped TiO ₂ (0.6% Pd); and (b) N-doped TiO ₂	108
Figure 4.12	High resolution XPS scan over (a) Pd 3d; (b) Ti 2p; (c) O 1s in N, Pd TiO ₂ ; and (d) N 1s in N TiO ₂	110

Figure 4.13	Eosin Yellow degradation profile using N, Pd TiO ₂ (0.6% Pd) ..	111
Figure 4.14	Eosin Yellow degradation by various photocatalysts	113
Figure 4.15	Proposed visible-light-induced photocatalytic mechanism of N, Pd co-doped TiO ₂ photocatalyst.....	114
Figure 4.16	Kinetics of EY degradation in the first 60 min of visible-light irradiation	116
Figure 5.1	Experimental setup for PRAM.....	127
Figure 5.2	Experimental setup for the modified PRAM	129
Figure 5.3	FT-IR spectrum of N, Pd co-doped TiO ₂ (0.6% Pd)	130
Figure 5.4	Raman spectrum of commercial and N, Pd co-doped TiO ₂	131
Figure 5.5	XRD pattern of commercial TiO ₂ and N, Pd co-doped TiO ₂ (A - anatase; R - rutile)	132
Figure 5.6	(a) Diffuse reflectance spectra; (b) absorption spectra; (c) Kubelka-Munk plots; and (d) Tauc plots of N, Pd co-doped TiO ₂ and commercial TiO ₂ (Degussa P25).....	133
Figure 5.7	(a) SEM image; (b) TEM images; and (c) EDX spectrum of N, Pd co-doped TiO ₂ (0.6% Pd).....	135
Figure 5.8	TGA curve of N, Pd co-doped TiO ₂	136
Figure 5.9	UV scan of samples	137
Figure 5.10	UV scan over time for the P1 sample using (a) P25; and (b) N, Pd co-doped TiO ₂	138
Figure 5.11	UV scan over time for the P2 sample using (a) P25; and (b) N, Pd co-doped TiO ₂	139
Figure 5.12	UV scan over time for the P3 sample using (a) P25; and (b) N, Pd co-doped TiO ₂	139
Figure 5.13	UV scans over time of hydrophobic (HPO) NOM fraction	142
Figure 5.14	UV scans over time for the hydrophilic (HPI) NOM fraction	142
Figure 5.15	UV scans over time for the transphilic (TPI) NOM fraction.....	143

Figure 5.16	Proposed photocatalytic degradation mechanism of NOM by N, Pd co-doped TiO ₂	145
Figure 6.1	FT-IR spectra of N, Os co-doped TiO ₂ calcined at different temperatures.....	156
Figure 6.2	Raman spectra of N, Os co-doped TiO ₂ calcined at different temperatures.....	157
Figure 6.3	XRD spectra of N, Os co-doped TiO ₂ calcined at different temperatures (A = anatase; R = rutile).....	159
Figure 6.4	UV-Vis absorption spectra of N, Os co-doped TiO ₂ calcined at different temperatures.....	161
Figure 6.5	Diffuse reflectance UV-Vis spectra of N, Os co-doped TiO ₂ calcined at different temperatures.....	162
Figure 6.6	Kubelka-Munk spectra of N, Os co-doped TiO ₂ calcined at different temperatures.....	163
Figure 6.7	Diffuse reflectance UV-Vis spectra of N, Os co-doped TiO ₂ calcined at different temperatures.....	164
Figure 6.8	(a) and (b) SEM images; and (c) EDS spectrum of N, Os co-doped TiO ₂ calcined at 500°C.....	166
Figure 6.9	TEM images of N, Os co-doped TiO ₂ calcined at (a) 350°C; (b) 500°C; (c) 650°C; and (d) 800°C.....	167
Figure 6.10	TGA curves of N, Os co-doped TiO ₂	169
Figure 6.11	EY photodegradation by N, Os co-doped TiO ₂ calcined at different temperatures.....	170
Figure 6.12	EY photodegradation kinetics by N, Os co-doped TiO ₂ calcined at different temperatures.....	172
Figure 6.13	Normalised rate constants of N, Os co-doped TiO ₂ calcined at different temperatures.....	174
Figure 6.14	Proposed mechanism for EY photodegradation under visible-light irradiation.....	175

Figure 7.1	Illustration of the synthesis of N, Pd co-doped TiO ₂ decorated MWCNTs	185
Figure 7.2	FT-IR spectra of MWCNT/N, Pd co-doped TiO ₂ with different MWCNT ratios	186
Figure 7.3	Raman spectra of MWCNT/N, Pd co-doped TiO ₂ with different MWCNT ratios	187
Figure 7.4	Raman spectra of MWCNT/N, Pd co-doped TiO ₂ showing the D and G bands	188
Figure 7.5	XRD patterns of MWCNT/N, Pd co-doped TiO ₂ with different MWCNT ratios (A = anatase phase)	189
Figure 7.6	SEM images of (a) 0.5% MWCNT/N, Pd TiO ₂ ; (b) N, Pd TiO ₂ decorated MWCNT showing a small uncovered gap; (c) 5% MWCNT/N, Pd TiO ₂ ; and (d) aggregation in 10% MWCNT/N, Pd TiO ₂	191
Figure 7.7	Full-scale EDS scan of 2% MWCNT/N, Pd co-doped TiO ₂	192
Figure 7.8	TEM images of (a) N, Pd co-doped TiO ₂ (0.5% Pd); (b) and (c) 0.5% MWCNT/ N, co-doped Pd TiO ₂ showing MWCNTs completely covered with N, Pd co-doped TiO ₂ ; (d) MWCNT with N, Pd co-doped TiO ₂ particle as well as aggregates; (e) MWCNT covered with N, Pd co-doped TiO ₂ and N, Pd co-doped TiO ₂ aggregates; and (f) unevenly covered MWCNTs (5.0% MWCNT/N, Pd co-doped TiO ₂) showing some Pd particles	193
Figure 7.9	TGA curves of MWCNT/N, Pd co-doped TiO ₂ with different MWCNT ratios	195
Figure 7.10	UV-Vis diffuse reflectance spectra of different MWCNT/N, Pd co-doped TiO ₂ nanocomposites.....	196
Figure 7.11	Kubelka-Munk plots of different MWCNT/N, Pd co-doped TiO ₂ nanocomposites	197
Figure 7.12	Tauc plots of MWCNT/N, Pd co-doped TiO ₂ nanocomposites..	198

Figure 7.13	Photodegradation of EY on N, Pd TiO ₂ and MWCNT/N, Pd co-doped TiO ₂ nanocomposites under (a) simulated solar light irradiation; and (b) visible-light irradiation ($\lambda > 450$ nm)	200
Figure 7.14	Kinetics of EY degradation under (a) simulated solar radiation; and (b) visible light	202
Figure 7.15	Proposed exciton processes for the MWCNT/N, Pd co-doped TiO ₂ catalysts under visible-light irradiation.....	205
Figure 8.1	FT-IR spectra of pristine and oxidised DWCNTs	214
Figure 8.2	FT-IR spectra of DWCNT/N, Pd TiO ₂ nanocomposites	215
Figure 8.3	Raman spectra of pristine and oxidised DWCNT showing the D and G bands as well as the RBMs	217
Figure 8.4	Raman spectra of DWCNT/N, Pd co-doped TiO ₂ with different DWCNTs ratios	218
Figure 8.5	XRD patterns of DWCNT/N, Pd co-doped TiO ₂ with different DWCNT ratios (A = anatase phase, R = rutile phase).....	219
Figure 8.6	DRUV-Vis spectra of the DWCNT/N, Pd TiO ₂ nanocomposites	221
Figure 8.7	UV-Vis absorption spectra of the DWCNT/N, Pd TiO ₂ nanocomposites	222
Figure 8.8	Kubelka-Munk spectra of the DWCNT/N, Pd TiO ₂ nanocomposites	223
Figure 8.9	Tauc plots of the DWCNT/N, Pd TiO ₂ nanocomposites	224
Figure 8.10	SEM images of (a) pristine; and (b) oxidised DWCNTs; and EDS spectra of (c) pristine; and (d) oxidised DWCNTs	226
Figure 8.11	TEM images of (a) pristine DWCNTs; and (b) oxidised DWCNTs	227
Figure 8.12	SEM images of (a) 10.0% DWCNT/N, Pd TiO ₂ ; and (b) 20.0% DWCNT/N, Pd TiO ₂	228

Figure 8.13	TEM images of pearl-bead-necklace-structured 20.0% DWCNT/N, Pd TiO ₂ nanocomposite (a) lower magnification; and (b) higher magnification.....	229
Figure 8.14	EDS of 20.0% DWCNT/N, Pd TiO ₂ nanocomposite.....	230
Figure 8.15	Reaction scheme for the formation of DWCNT/N, Pd TiO ₂ nanocomposites.....	231
Figure 8.16	Thermograms of pristine and oxidised DWCNTs and their derivatives (inset).....	232
Figure 8.17	Eosin Yellow photodegradation under simulated solar irradiation.....	234
Figure 8.18	Eosin Yellow photodegradation profiles using 20.0% DWCNT/N, Pd TiO ₂	235
Figure 8.19	Eosin Yellow photodegradation kinetics.....	238
Figure 8.20	Proposed mechanisms for the photocatalytic enhancement.....	241
Figure 9.1	SEM image of EG-TiO ₂	251
Figure 9.2	TEM images of EG-TiO ₂ at different magnifications.....	251
Figure 9.3	(a) XRD and (b) Raman spectra of EG-TiO ₂	253
Figure 9.4	(a) Percentage dye adsorption (b) normalised photodegradation trend.....	255
Figure 9.5	Kinetics of EY degradation.....	257
Figure 9.6	Illustration of the photocatalytic activity of the EG-TiO ₂ nanocomposite for the degradation of eosin yellow under visible light irradiation.....	259
Figure 10.1	Comparison of the dye degradation efficiency of the highest performing photocatalysts.....	266

LIST OF TABLES

<u>Table</u>	<u>Description</u>	<u>Page</u>
Table 2.1	Work functions (ϕ) of selected noble metals	30
Table 4.1	Effect of Pd dopant level on average crystallite size and phase composition.....	100
Table 4.2	Effect of Pd dopant level on band gap	105
Table 4.3	Core-level XPS elemental analysis results for the N-doped TiO ₂ and N, Pd co-doped TiO ₂	111
Table 4.4	Percentage degradation after exposure to visible radiation	113
Table 5.1	The different SPE cartridges and various types of sorbents used	127
Table 5.2	Bulk characteristics of the NOM samples from plant P	136
Table 5.3	Percentage UV ₂₅₄ reduction of the three NOM samples using commercial TiO ₂	141
Table 5.4	UV absorbance over time for the different NOM fraction samples	144
Table 5.5	Percentage UV ₂₅₄ reduction of the three NOM samples by photocatalytic degradation	147
Table 6.1	Crystallite size and phase composition of N, Os co-doped TiO ₂ calcined at different temperatures [A = Anatase, R = Rutile].....	160
Table 6.2	Direct band-gap values for N, Os co-doped TiO ₂ calcined at different temperatures	165
Table 6.3	EY adsorption and degradation by different N, Os co-doped TiO ₂ samples.....	171
Table 6.4	Apparent first-order rate constants of N, Os co-doped TiO ₂ nanoparticles calcined at different temperatures.....	173
Table 7.1	Effect of MWCNTs on average particle size.....	190

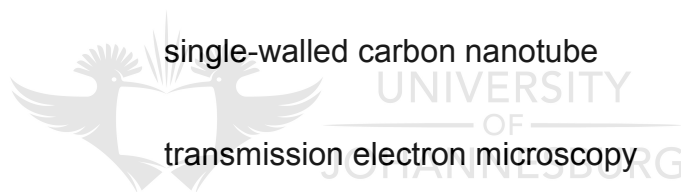
Table 7.2	Effect of MWCNTs on band gap in MWCNT/N, Pd co-doped TiO ₂ nanocomposites.....	199
Table 7.3	Dye adsorption and EY photodegradation under simulated solar radiation	201
Table 7.4	Dye adsorption and EY photodegradation under visible radiation ($\lambda > 450$ nm).....	202
Table 7.5	EY photodegradation rate constants under simulated solar radiation and visible radiation.....	204
Table 8.1	Effect of MWCNTs on average particle size.....	220
Table 8.2	Band-gap energies of the DWCNT/N, Pd TiO ₂ nanocomposites.....	225
Table 8.3	Dye adsorption, degradation and rate constants.....	239
Table 9.1	BET surface area, Pore volume and Pore size	253
Table 9.2	Dye adsorption, dye degradation and rate constants for EG-TiO ₂ and Degussa P25	258



LIST OF ABBREVIATIONS

ATR	attenuated total reflectance
CCVD	catalytic chemical vapour deposition
CNT	carbon nanotube
DOC	dissolved organic carbon
DOM	dissolved oxygen matter
DWCNT	double-walled carbon nanotube
EBSD	electron back-scattered diffraction detector
EG	exfoliated graphite
EY	eosin yellow
FT-IR	Fourier transform infrared
HPI	hydrophilic
HPO	hydrophobic
LVRPA	local volumetric rate of photon absorption
MB	methylene blue
MS	mass spectrometry
MWCNT	multiwalled carbon nanotube

NHE	normal hydrogen electrode
NOM	natural organic matter
OVRPA	overall volumetric rate of photon absorption
PGM	platinum-group metal
PRAM	polarity rapid assessment method
SEM	scanning electron microscopy
SPE	solid phase extraction
SUVA	specific ultraviolet absorbance
SWCNT	single-walled carbon nanotube
TEM	transmission electron microscopy
TGA	thermogravimetric analysis
THM	trihalomethane
TOC	total organic carbon
TPI	transphilic
TWCNTs	triple-walled carbon nanotubes
UV	ultraviolet
UV-Vis	ultraviolet visible
VRPA	volumetric rate of photon absorption



WDS	wavelength dispersive X-ray spectroscopy
XPS	X-ray photoelectron spectroscopy
XRD	X-ray diffraction



CHAPTER 1

INTRODUCTION

1.1 BACKGROUND

The shortage of clean water resources and an increase in water demand due to rapid industrialisation, population growth and long-term droughts have become an issue worldwide. About 1.2 billion people lack access to safe drinking water globally, 2.6 billion have little or no sanitation, and millions (mostly children) die annually from diseases transmitted through unsafe water.^{1,2} These figures are expected to increase in the future due to increasing discharge of micro-pollutants and contaminants into the natural water bodies driven by a quest for better human life, further stressing the available traditional sources. A growing number of contaminants ranging from heavy metals and distillates to emerging micro-pollutants such as endocrine-disrupting compounds and nitrosamines are finding their way into water-supply systems.² This presents a big challenge for the current and future generations, posing a significant threat to the well-being of humans, especially in developing nations.³

Water also strongly affects energy and food production, industrial output and the quality of the environment, affecting economies of both developing and industrialised nations. In the coming decades, water scarcity may become a watchword that prompts action ranging from human population migration to war, unless new ways to supply safe clean water are found.² Among the innumerable pollutants discharged into water bodies are synthetic dyes from textile industries. Dyes are vital chemicals used in several industries such as those involved in producing fabric, food, furniture and paint. The dumping or accidental discharge of dye wastewater into waterways has a major impact on the quality and aesthetics of water resources. The World Bank estimates that 17% to 20% of industrial water pollution comes from textile dyeing and treatment.⁴ This percentage represents an

appalling environmental challenge that has prompted researchers globally to look into developing universal methods for effective wastewater treatment.⁴

1.2 PROBLEM STATEMENT

Conventional water-decontamination methods can address many of the water-treatment challenges with improvements in quality and supply. However, the treatment methods are often chemically, energetically, operationally and financially intensive. They are focused on large systems requiring substantial engineering expertise and infrastructure, which precludes their use globally. Furthermore, intensive chemical treatments such as the use of ammonia, chlorine compounds, hydrochloric acid, sodium hydroxide, ozone, permanganate, alum and ferric salts, coagulation and filtration aids, anti-scalants, corrosion control chemicals, ion-exchange resins and regenerants can add to the problems of contamination and salinisation of freshwater sources.² Chlorination, for example, has been the most commonly and widely used disinfection process. However, the disinfection by-products generated from chlorination are mutagenic and carcinogenic to human health.¹ Some dyes are reduced to by-products that contain potentially hazardous aromatic amines.⁴ Residuals resulting from the treatment (sludge, brines and toxic wastes) need proper disposal lest they cause further water pollution.² There is a need for the development of robust and innovative new technologies and materials to address challenges associated with the provision of safe and clean drinking water. A recent flurry of activity in research on water treatment offers some hope in mitigating the impact of water pollution around the world.^{2,5}

Environmental nanotechnology is considered a key area in addressing the current water-pollution challenges. Examining materials at the nanoscale has stimulated the development and use of novel and cost-effective technologies for environmental remediation, including pollutant detection and degradation. There is hope that nanotechnology applications and products will lead to a cleaner and healthier environment. There is great anticipation that nanotechnology will play a significant role in providing solutions for cheap access to clean water for communities in developing countries.³

1.3 JUSTIFICATION

The past few years have seen tremendous research and development in the area of photocatalysis. Photocatalysis using semiconductor particles has found increasing interest in solving global pollution problems. Organic pollutant degradation in water is one of the major applications of this technology. Titania, (TiO_2) has so far been shown to be one of the most promising semiconductor materials used for both fundamental research and practical applications compared to other semiconductor photocatalysts, because it is highly photoreactive, cheap, non-toxic, chemically and biologically inert and photostable. Despite the positive attributes of TiO_2 , there are a few drawbacks associated with its use: (i) charge carrier recombination occurs within nanoseconds; and (ii) the band-edge absorption threshold does not allow utilisation of visible light because its band gap is rather large, (3.0 eV to 3.2 eV), and thus only a small percentage of the solar spectrum ($\lambda < 380$ nm, corresponding to the UV region) is absorbed. To circumvent these particular limitations, a number of strategies have been proposed to improve the light-absorption features and increase the carrier life-time characteristics of TiO_2 . It has been shown that the photocatalytic activity of a catalyst can be influenced by its crystal structure, surface area, size distribution, porosity, band gap and surface hydroxyl group density. The limitations of a particular semiconductor as a photocatalyst for a particular use can be surmounted by modifying these surface properties. At the moment, convenient alternatives for substituting TiO_2 in photocatalytic detoxification systems are still limited. This underlines the need for continued research in TiO_2 -based photocatalysis.⁶

The energy of the photons required for the detoxification of polluted water is the most important source of costs during the operation of photocatalytic water-treatment plants. This suggests that solar energy could be used as an economically and ecologically sensible light source for photocatalysis.⁷ A number of investigations aimed at activating TiO_2 photocatalysts using visible light have been carried out. These include preparation of TiO_2 as nanosized particles, doping and coating with metals or modification with other semiconductors. These methods

suffer from thermal or photo-induced instability, poor reproducibility of photo activity and an increase in the density of carrier recombination centres which significantly lower the photocatalytic activity. This imposes a limit on the practical applicability of these methods for industrial use. TiO_2 works under mild conditions with mild oxidants at atmospheric temperature and pressure. However, as the concentration and number of contaminants increase, problems such as catalyst deactivation, slow kinetics, low photo efficiencies and unpredictable mechanisms start to emerge. It is clear that TiO_2 needs some modification to undertake practical applications of industrial and environmental interest.⁸

Nitrogen-doped TiO_2 is continuously attracting increasing attention because of its potential as a material for visible-light-induced environmental photocatalysis. In nitrogen-doped TiO_2 , substitution of oxygen by nitrogen is predicted to lower the band-gap energy as the N p states of the dopants mix with the oxygen 2p states, contributing to a net band-gap narrowing.^{9,10} Nitrogen doping has also been shown to extend the light-absorption onset of TiO_2 from 380 nm (UV) to above 450 nm (visible), offering possible photocatalytic activity under visible-light irradiation. It is also believed that TiO_2 oxygen sites substituted by nitrogen atoms form isolated impurity energy levels above the valence band, further narrowing the band gap.⁹ Irradiation with UV radiation excites electrons in both the valence band and the impurity energy levels, but illumination with visible light only excites electrons in the impurity energy levels. Another line of thinking is that oxygen-deficient sites formed in the grain boundaries evoke visible-light activity and the nitrogen occupying the oxygen-deficient sites are important for blocking reoxidation.¹¹ However, due to strongly localised N 2p states just above the valence band, the photocatalytic efficiency of N-doped TiO_2 is lower because isolated empty states tend to trap photogenerated electrons, reducing the photogenerated current. In general, non-metal doping intrinsically brings the serious problem of massive charge carrier recombination, which largely limits the visible-light photocatalytic activity of non-metal doped TiO_2 . From the viewpoint of practical application, higher photocatalytic reaction efficiency is required and should be pursued further since the photocatalytic efficiency of non-metal-doped TiO_2 under visible light is still low.¹²

Loading co-catalysts onto the surface of semiconductor photocatalysts is one of the well-known methods for enhancing their activity. Noble metals, such as Ag, Pt, Au, Rh and Pd have been studied and shown to be very effective in enhancing TiO₂ photocatalysis. Heterojunctions are formed at the metal semiconductor interface facilitating transfer of photo-excited electrons from the conduction band to the metal particles deposited on the surface of TiO₂ because the Fermi levels of these noble metals are lower than that of TiO₂. The high electronegativity of the noble metal nanoparticles means the Fermi level can be shifted to negative potentials, consequently increasing the accumulation of electrons. The equilibration of the Fermi-level between the metal itself and the semiconductor thus favours electron accumulation on the composite metal/TiO₂ system. The loading of noble metals on TiO₂ is believed to improve the photocatalytic activity due to enhancement of pollutant adsorption and separation of photogenerated electron-hole pairs. After excitation, the electron moves to the metal where it becomes trapped and electron-hole recombination is suppressed, promoting the lifetime of holes for pollutant degradation. The metal is also important because of its own catalytic activity and modification of the semiconductor by changing the distribution of electrons. This leads to an increase in hydroxyl groups around the semiconductor which in turn affects the photocatalytic process on the semiconductor surface.¹³ The beneficial effect of noble metal doping depends to a large extent on the percentage loading. Different loading levels have different effects on the TiO₂ in terms of the photocatalytic activity.¹⁴ Higher metal loadings lead to reduced photoefficiency as the metal particles become electron-hole recombination centres. Surface plasmon resonance (SPR) effects are also thought to play a role. Pt and Au are rare and very expensive metals. More research is needed to find low-cost noble metal dopants which can offer an acceptable improvement in TiO₂ photocatalytic activity for practical applications. In addition, the use of metals should take into account possible metal toxicity issues and leaching from the catalyst.¹¹

South Africa is a major producer of platinum-group metals (PGMs). It supplies more than 80% of the world's PGM needs. The primary demand driver is the booming automobile market, with the manufacture of autocatalysts consuming

over 60% of both platinum and palladium production as well as 85% of the rhodium mined. Many of the unique physical and chemical characteristics of PGMs make them indispensable to modern technology and industry. Their catalytic properties make them ideally suited to many applications aimed at countering the effects of environmental pollution.¹⁵ PGMs are mined together; however, Pt and Rh are much more expensive due to their established industrial applications while Pd, Os, Ir and Ru have not found wide applications.

The use of PGMs as catalysts in decontaminating water could add to the many applications of these metals for environmental remediation. However, introduction of metals into the TiO₂ lattice also suffers from the existence of carrier recombination centres and the formation of strongly localised d states in the band gap, which significantly reduces carrier mobility.¹⁶ Although non-metal and metal doping can effectively enhance visible-light photocatalytic activity of TiO₂, many experimental studies have demonstrated that mono-doping reduces the photogenerated current because the partially occupied impurity bands can act as recombination centres on the TiO₂, which reduces the charge carriers' mobility to the surface for photocatalysis.

Co-doping, which is the introduction of two different dopants on TiO₂, is a recent attempt at improving the photocatalytic properties of TiO₂, taking advantage of the positive synergistic effects of the dopants on the properties of the TiO₂. Non-metal/non-metal, metal/metal and non-metal/metal co-doping has been shown to reduce the recombination centres because co-doping can passivate the defect bands produced by mono-doping, preventing them from acting as recombination centres.¹⁷

Non-metal/metal co-doped TiO₂ is a new class of attractive and promising second-generation photocatalysts with superior charge recombination suppression and reduced energy gap. To design a visible-light photocatalyst using the co-doping method, one needs to identify suitable impurity combinations that will reduce the energy gap and enhance optical absorption in the visible region as well as trap electrons to reduce charge carrier recombination. Exhibiting high 4d and 5d atomic

orbital energies, PGMs are more likely to trap photogenerated electrons from the host TiO_2 conduction band. Non-metals like nitrogen on the other hand have higher atomic p orbital energies than oxygen, so they form impurity levels above the host valence band. This reduces the photo-excitation energy, shifting the absorption to the visible region. Therefore, PGMs are predicted to be the best choices as electron traps and N as the preferred band-gap tuning dopant.¹⁸ Such material engineering strategies may overcome the difficulties of some previous schemes whilst providing some guidance for improving the photocatalytic activity of TiO_2 for organic pollutant photodegradation in water.

Recent research and development in the improvement of photocatalytic activity of TiO_2 has been focusing on hybrid materials of TiO_2 and CNTs, due to the large specific surface area and unique electrical properties of CNTs. The unique one-dimensional geometric structure, large surface area, high electrical conductivity, elevated mechanical strength and strong chemical inertness of CNTs provide new features for their application as supports for semiconductor photocatalysts. Principally, the support has three main functions: (i) to increase the surface area of photocatalytic material; (ii) to reduce particle agglomeration and to improve the optical, chemical and electrical properties of the photocatalytic material; and (iii) to govern the useful lifetime of the photocatalyst. Supports may also improve the activity of the photocatalyst by acting as co-catalysts.¹⁹ CNTs not only provide large surface areas for the dispersion of active semiconductors, but also improve the adsorption properties of the photocatalysts, enhance their photocatalytic activities and extend the light-response region to the visible end. The synergistic effects of CNTs and semiconductors endow the nanocomposites with superb properties and excellent performance. The coupling of TiO_2 with CNTs has been shown to provide a synergistic effect which can enhance the overall efficiency of the photocatalytic process.^{20,21} CNT/ TiO_2 nanocomposites have attracted increased attention in the literature in relation to the treatment of contaminated water and air. Due to their high electrical conductivity, photogenerated electrons in TiO_2 may move freely towards the CNT surface, leaving an excess of valence band holes in the TiO_2 to migrate to the surface and react with adsorbed pollutants.²² The separation of the photo-generated electron-hole pairs is

facilitated by formation of heterojunctions at the CNT/TiO₂ interface. Thermal conductance may also play a role in photocatalytic enhancement.

The search for cheaper, cleaner and more sustainable solar light harvesters provides a strong impetus to develop more affordable, active, selective and stable new catalysts to convert solar radiation into useful chemical energy for driving oxidative pollutant degradation reactions in aqueous medium. Currently, there is very little research activity on supporting co-doped TiO₂ on SWCNTs, DWCNTs and MWCNTs for water-treatment application.²³ The loading of non-metal/PGM co-doped TiO₂ onto different types of CNTs may result in materials with the appropriate light-harvesting and catalytic properties for the desired water-treatment applications. To date, only limited kinetic studies have been conducted to establish the charge carrier transfer processes in CNT/TiO₂ nanocomposites. A better understanding of interfacial charge transfer kinetics is important in designing more efficient photocatalysts for organic pollutant photodegradation in water.

1.4 AIM AND OBJECTIVES



UNIVERSITY
OF
JOHANNESBURG

1.4.1 Aim

The main goal of the present work is to show the intrinsic correlation between the physicochemical properties of the N, PGM co-doped TiO₂ and CNT/N, PGM co-doped TiO₂ nanomaterials and their functionalities in solving the ever-increasing environmental problems associated with water pollution with a special focus on organic pollutants.

1.4.2 Objectives

While it is difficult to find photocatalysts that possess an optimum combination of morphological, optical, electronic and chemical properties for solar-driven applications, this research is guided by efforts to tailor modified TiO₂-based materials with a favourable combination of these properties. Therefore the objectives of this research thesis were to:

- Synthesise nitrogen/PGM co-doped TiO_2 (PGM = Pd or Os) photocatalysts using a modified sol-gel method followed by characterisation of the synthesised materials both by macroscopic (XRD and thermal analysis methods) and microscopic (SEM, EDS, TEM, Raman, FT-IR, UV-Vis) techniques.
- Determine the effect of dopant concentration and calcination temperature on the optical, morphological, thermal, chemical and electronic properties of the nitrogen/PGM co-doped TiO_2 and their reactivity for the photodegradation of Eosin Yellow under visible-light irradiation.
- Synthesise MWCNTs by nebulised spray pyrolysis and DWCNTs by CCVD methods followed by characterisation of the nanotubes by macroscopic and microscopic techniques.
- Synthesise MWCNT/N, Pd co-doped TiO_2 nanocomposites through the use of a modified sol-gel method followed by their characterisation by employing various physicochemical characterisation techniques.
- Design and synthesise DWCNT/N, Pd co-doped TiO_2 nanocomposites by a modified sol-gel method followed by their characterisation by various physicochemical characterisation techniques.
- Determine the effect of incorporating CNTs in CNT/N, Pd co-doped TiO_2 on the optical, morphological, thermal, chemical and electronic properties of the nanocomposites and their reactivity in the oxidation of eosin yellow under simulated solar irradiation.
- Synthesise and characterise EG- TiO_2 nanocomposites for application in dye photocatalytic degradation.
- Determine the photocatalytic efficiencies of the prepared photocatalysts for degradation and removal of eosin yellow and/or NOM in water under visible-light irradiation using laboratory-scale experiments.

1.5 THESIS OUTLINE

The following outline gives a brief summary of the contents of the chapters presented in this thesis.

Chapter 2 gives a literature review of the study undertaken. The chapter begins with a discussion on water pollution and the integration of nanotechnology in solving the ever-increasing environmental challenges. The principles of TiO₂ photocatalysis are discussed. Approaches to preparing visible-light-active TiO₂ are presented and the relevant literature in this field is discussed. The use of CNTs as adsorbents, strong supports and photosensitisers in TiO₂-based photocatalysis is discussed. Applications of TiO₂-based photocatalysts and possible toxicity issues conclude the chapter.

Chapter 3 provides a discussion of experimental methodology and analytical procedures that were used in this research project. The sol-gel method is discussed as one of the principal nanoparticle synthesis techniques. Different physicochemical characterisation techniques are also discussed. In addition, details on the experimental setup are highlighted.

Chapter 4 highlights the characterisation of N, Pd co-doped TiO₂ nanoparticles and evaluation of the materials for the degradation of Eosin Yellow, a model synthetic dye. The effect of dopant concentration and radiation source on the photoactivity of the materials is discussed. Interpretation of the results based on the synergistic effects of co-doping is also presented.

Chapter 5 introduces an actual water pollutant in the form of natural organic matter (NOM) and outlines how N, Pd co-doped TiO₂ may be useful in addressing its presence in water systems. Results based on the UV-Vis measurement of NOM at UV₂₅₄ are interpreted and discussed.

Chapter 6 explores the use of osmium as a co-dopant in N, Os co-doped TiO₂ and its effect in enhancing the photoactivity of TiO₂ towards the degradation of Eosin Yellow in water. The effect of calcination temperature on the morphology and

optical properties of the resulting materials is discussed. Photocatalytic enhancement is discussed in terms of possible formation of OsO_2 on the rutile TiO_2 nanoparticles.

Chapter 7 describes the use of MWCNTs as supports for N, Pd co-doped TiO_2 for photocatalytic dye degradation. The properties of the materials are discussed and related to their photocatalytic activity. Synergistic effects of the supporting and sensitisation roles of MWCNTs are explored and discussed.

Chapter 8 introduces the synthesis of DWCNTs and their use as supports for N, Pd co-doped TiO_2 . The unique pearl-bead-necklace structures are evaluated for their activity towards the photodegradation of an aqueous solution of Eosin Yellow. Synergistic effects are discussed in terms of the superior electron-channelling effects of the DWCNT as well as the formation of Schottky barriers at the Pd- TiO_2 interfaces.

Chapter 9 describes the synthesis of EG- TiO_2 for application in photocatalytic dye degradation. The puffed structure and the high surface area of exfoliated graphite are some of the desirable properties for their incorporation in the EG- TiO_2 nanocomposites. Possible mechanisms for the photodegradation are highlighted.

Chapter 10 summarises the major findings of this work in the form of conclusions. Recommendations and future perspectives are also presented in this chapter.

References: Literature sources cited in this study are found at the end of each chapter.

1.6 REFERENCES

1. Chong M.N., Jin B., Chow C.W.K and Saint C. (2010). Recent developments in photocatalytic water treatment technology: A review. *Water Res.* 44, 2997 – 3027.

2. Shannon M.A., Bohn P.W., Elimelech M., Georgiadis J.G., Marinas B.J. and Mayes A.N. (2008). Science and technology for water purification in the coming decades. *Nature* 452, 301 – 310.
3. Dosch H. and Van de Voorde M.H. (eds.). (2009). *GENNESYS White Paper. A New European Partnership between Nanomaterials Science and Nanotechnology and Synchrotron Radiation and Neutron Facilities*. Max-Planck-Gesellschaft, Stuttgart. pp 219 - 221. ISBN 978-3-00-027338-4.
4. Chan S.H.S., Wu T.Y., Juan J.C. and Teh C.Y. (2011). Recent developments of metal oxide semiconductors as photocatalysts in advanced oxidation processes (AOPs) for treatment of dye waste-water. *J. Chem. Technol. Biotechnol.* 86, 1130 – 1158.
5. Theron J., Walker J.A. and Cloete T.E. (2008). Nanotechnology and water treatment: Applications and emerging opportunities. *Crit. Rev. Microbiol.* 34, 43 – 69.
6. Sakthivel S., Shankar M.V., Palanichamy M., Arabindoo B., Bahnemann D.W. and Murugesan V. (2004). Enhancement of photocatalytic activity by metal deposition: characterisation and photonic efficiency of Pt, Au and Pd deposited on TiO₂ catalyst. *Water Res.* 38, 3001 – 3008.
7. Phuntsho S. and Okour Y. (2008). Visible light responsive titanium dioxide (TiO₂). *J. Korean Ind. Eng. Chem.* 19, (1), 1 – 16.
8. Morikawa T., Asahi R., Ohwaki T., Aoki K., Suzuki K. and Taga Y. (2005). Visible–light photocatalyst – Nitrogen Doped Titanium Dioxide. *R&D Rev. of Toyota CRDL* 40, (3), 45 – 50.
9. Emeline A.V., Kuznetsov V.N., Rybchuk V.K. and Serpone N. (2008). Visible light active titania nanocatalysts: The case of N-doped TiO₂s – Properties and some fundamental issues. *Int. J. Photoenergy*, DOI 10.1155/2008/258394

10. Wang J., Tafen D.N., Lewis J.P., Hong Z., Manivannan A., Zhi M., Li M., and Wu N. (2009). Origin of photocatalytic activity of nitrogen-doped TiO₂ nanobelts. *J. Am. Chem. Soc.* 131, (34), 12290 – 12297.
11. Malato S., Fernandezibanez P., Maldonado M.I., Blanco J. and Gernjak W. (2009). Decontamination and disinfection of water by solar photocatalysis: Recent overview and trends. *Catal. Today* 147, 1 – 59.
12. Wu Z., Dong F., Liu Y. and Wang H. (2009). Enhancement of the visible light photocatalytic performance of C-doped TiO₂ by loading with V₂O₅. *Catal. Commun.* 11, 82 – 86.
13. Chen X. (2005). Synthesis and Investigation of Novel Nanomaterials for Improved Photocatalysis. Ph.D. Thesis. Department of Chemistry, Case Western Reserve University, Cleveland, Ohio, USA.
14. Haick H. and Paz Y. (2003). Long-range effects of noble metals on the photocatalytic properties of titanium dioxide. *J. Phys. Chem. B* 107, 2319 – 2326.
15. IMPLATS (Distinctly Platinum), (2005). Annual Report. www.implats.co.za
16. Run L. and Niall E.J. (2009). Band gap engineering of (N, Ta) co-doped TiO₂: a first principles calculation. *Chem. Phys. Lett.* 478, (4-6), 175 – 179.
17. Zhang J., Xi J. and Ji Z. (2012). Mo + N codoped TiO₂ sheets with dominant {001} facets for enhancing visible-light photocatalytic activity. *J. Mater. Chem.* DOI: 10.1039/c2jm32391e.
18. Ma X., Wu Y., Lu Y., Xu J., Wang Y. and Zhu Y. (2011). Effect of compensated co-doping on the photoelectrochemical properties of anatase TiO₂ photocatalyst. *J. Phys. Chem. C* 115, 16963 – 16969.
19. Pirkanniemi K. and Sillanp M. (2002). Heterogeneous water phase catalysis as an environmental application: A review. *Chemosphere* 48, 1047 – 1060.

20. Xin X. and Weide Z. (2011). Photocatalysis of carbon nanotubes - semiconductor composites. *Prog. Chem.* 23, (4), 657 – 668.
21. Chen L., Pang X., Yu G. and Zhang J. (2010). *In-situ* coating of MWNTs with sol-gel TiO₂ nanoparticles. *Adv. Mat. Lett.* 1, (1), 75 – 78.
22. Gao B., Chen G.Z. and Puma G.L. (2009). Carbon nanotubes/titanium dioxide (CNTs/TiO₂) nanocomposites prepared by conventional and novel surfactant wrapping sol-gel methods exhibiting enhanced photocatalytic activity. *Appl. Catal. B: Environ.* 89, 503 – 509.
23. Kuvarega A.T., Krause R.W.M. and Mamba B.B. (2012). Multiwalled carbon nanotubes decorated with nitrogen, palladium co-doped TiO₂ (MWCNT/N, Pd co-doped TiO₂) for visible light photocatalytic degradation of Eosin Yellow in water. *J. Nanoparticle Res.* 14, 776. DOI: 10.1007/s11051-012-0776



CHAPTER 2

LITERATURE REVIEW

2.1 INTRODUCTION

The main focus of this review is on water pollution and the role of nanotechnology in the removal of pollutants in water. The chapter begins with a brief overview of nanotechnology and future prospects towards the development of functional materials to solve the ever-increasing environmental problems of water pollution. This will be followed by an explanation of basic mechanisms of TiO₂-driven photocatalysis. A review of the literature describing the synthesis and modification methods of TiO₂-based photocatalysts and possible synergistic effects from the inclusion of nitrogen and platinum group metals follows. An overview of various approaches to improve TiO₂ photo reactivity and photo response in the visible region follows, including the incorporation of carbon nanotubes. Finally, the application of TiO₂ and CNT/TiO₂-based photocatalysts in water decontamination will be discussed.

2.1.1 Water availability

Water covers more than 70% of the Earth's surface area, while less than 3% of it is potable. Safe, abundant clean water is vital for sustainable development. Without safe, clean water, there is continual decline in the well-being of humans, increasing poverty and hunger, as well as increasing levels of conflict. The effects of climate change make the challenges of conserving water resources even more difficult. Developing nations are worst affected.¹ In 2009, Africa's population exceeded 1 billion and it continues to increase at a rate of 2.4% annually. Of this population, 341 million people lack access to clean drinking water and a further 589 million have no access to adequate sanitation. In both cases, availability of this precious resource is not keeping pace with population growth, which means it

will be highly unlikely that the 2015 Millennium Development Goals (MDGs) will be met.²⁻⁴

2.1.2 Water pollution

While non-availability is an issue, water contamination is another major concern which threatens the survival of many organisms and mankind. Intensive farming, rapid industrialisation and increasingly sophisticated lifestyles have added artificial chemicals into the water bodies. The world is facing formidable challenges in meeting rising demands for clean water as the available supplies of freshwater are stressed due to: (i) extended droughts; (ii) population growth; (iii) untreated wastewater entering the environment from industry and domestic sources; (iv) more stringent health-based regulations; and (v) competing demands from a variety of users and increasing water re-use meaning the pollutants not removed are recycled.⁵

Industrial and mining effluents continue to increase in volume and in complexity due to the presence of new and diverse types of contaminants. In addition, the load of diffuse pollution on water sources is increasing due to poor sanitation in many informal settlements as well as runoff from agricultural, mining and industrial activities. The quality of most inland raw water sources continues to deteriorate as a result of the discharge of effluents into these sources. Discharge of treated effluents into water sources has negative quality effects related to the presence of other contaminants in the treated effluents. These include contaminants such as heavy metals, organics, biological and other inorganic contaminants. Some of these contaminants are suspected to or known have negative health effects even at very low concentrations.⁵ Advanced treatment processes are therefore required to remove these potentially harmful contaminants or reduce their concentration to very low levels. The fact that most water-treatment works only employ conventional processes underpins the vulnerability of water-supply systems to produce water of the required quality. It is evident that conventional approaches and treatment technologies are not adequate to solve these mounting water-supply and water-quality problems. Therefore, new and improved technologies

need to be developed to effectively address these challenges. Water security or safeguarding water-treatment systems against potential chemical and biological terrorist acts is also becoming a critical issue in water-resource planning.

2.2 NANOTECHNOLOGY AND THE ENVIRONMENT

Nanotechnology has been defined in simple terms as research and development at the atomic, molecular or macromolecular scales. Nanoparticles make up the building blocks for nanotechnology, and are referred to as particles with at least one dimension less than 100 nm.⁶ Nanotechnology is a rapidly developing modern area of science and technology covering many areas of physics, chemistry, engineering, medicine, materials science and biology. The unique properties of materials at the nanometre scale and the outstanding performance of the nanoscale devices are the main reasons for the immense growth of this field. Controlled assembly of nanoparticles has been proposed as one of the most promising ways to achieve the targets of nanotechnology.⁷ It is therefore necessary to develop novel processes for the fabrication of nanomaterials that can serve as the basis for the development of highly functional novel technologies for tackling environmental pollution problems.

Nanocatalysis is one of the subfields of nanotechnology. Nanocatalysts exhibit unique properties that originate from the highly reduced dimensions of the active catalytic aggregates. Consequently, the main aim of nanocatalysis is the promotion, enhancement, steering and control of chemical reactions by changing the size, dimension, chemical composition and morphology or charge state of the catalyst or the reaction centre. It may also entail changing the kinetics through nanopatterning of the catalytic material. For these systems, the chemical and physical properties are often controlled by size effects which in turn control the non-scalable chemical activity, specificity and selectivity.⁸

Studies aimed at gaining deep insights into the development of novel nanomaterials and understanding their properties are major themes of current interdisciplinary basic and applied research endeavours. Characterisation and

elucidation of the physical and chemical properties of these materials are among the outstanding challenges of modern materials science. Such materials may provide answers to the growing world environmental remediation challenges. Researchers need to come up with solutions on a global scale to these environmental pollution problems which are compounded by lack of sufficient clean and natural energy sources. Attention and concern should be focused on the vital need for ecologically clean chemical technologies, materials and processes.

2.3 TiO₂ AS A SEMICONDUCTOR

The mushrooming field of nanotechnology is finding applicability in the field of environmental protection.⁶ Nanotechnology is emerging and occupying special status in semiconductor materials and catalysts. Various n-type semiconductor metal oxides and sulphides such as TiO₂, ZnO, CdS, SnO₂ and WO₃, are suitable materials for photocatalytic elimination of organic pollutants in water based on their band positions relative to the normal hydrogen electrode (NHE) (**Figure 2.1**). However, most of them have limitations such as: (a) large band gap, often requiring near UV light ($\lambda < 400$ nm) to induce electron photo-excitation; (b) instability in aqueous medium, leading to photocatalyst decomposition; and (c) high electron-hole recombination rates. TiO₂ is regarded as the most suitable photocatalytic semiconducting material due to its high stability toward photo-corrosion, superb aqueous stability and relatively favourable band-gap energy.⁹

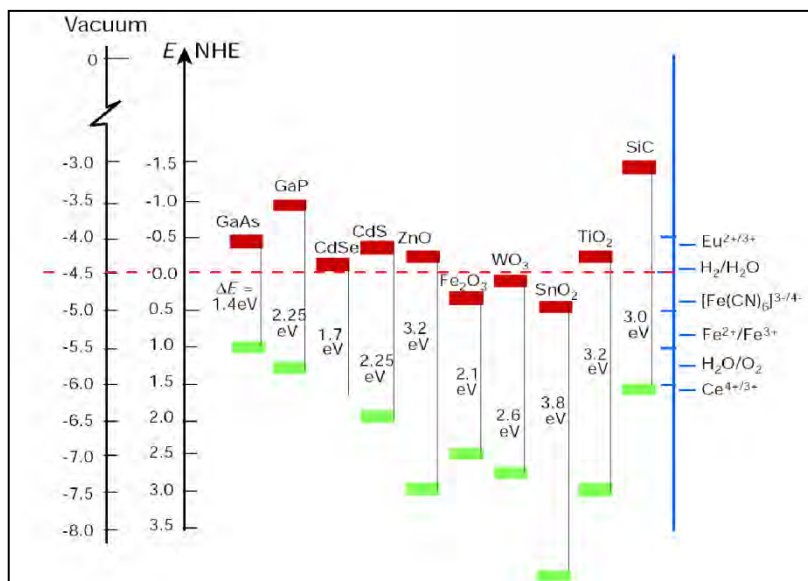


Figure 2.1 Band positions of several semiconductors in contact with an aqueous electrolyte at pH 1⁹

Semiconductor photocatalysis using TiO_2 has attracted tremendous attention from researchers worldwide in addressing the reduction and elimination of environmental pollutants in water and air, taking advantage of the conversion of light energy into useful chemical energy. The publication in 1971 of work on heterogeneous photocatalysis by Formenti *et al.* followed a year later by another on electrochemical photolysis of water at a semiconductor electrode by Fujishima and Honda, prompted a true revolution based on the extensive use of TiO_2 as a photocatalyst. Interest in this semiconductor has grown exponentially ever since.^{10,11} Success stories of a number of processes such as hydrogen production, effluent detoxification and disinfection as well as organic syntheses have since been reported.¹²⁻¹⁶

TiO_2 exists in four identified crystalline polymorphs: anatase (tetragonal), rutile (tetragonal), brookite (orthorhombic) and TiO_2 (B) (monoclinic). All TiO_2 forms can be described as an arrangement of slightly elongated TiO_6 octahedra connected in different ways by vertices and edges (**Figure 2.2**).¹⁷

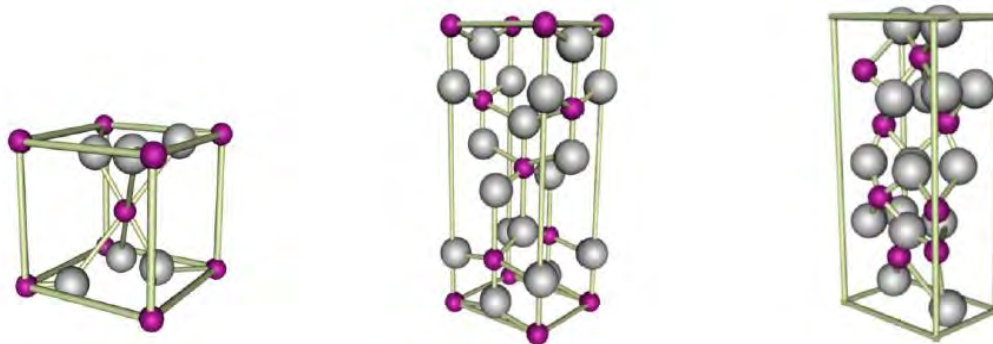


Figure 2.2 Unit cells of the rutile, anatase and brookite phases of TiO_2 ¹⁸
[grey and purple spheres represent O and Ti, respectively]

The anatase and rutile forms are the most common and have been applied in photocatalysis. Although the rutile is generally considered the most stable polymorph, differences in the Gibbs free energy of formation between rutile and anatase are small (lower than $15 \text{ kJ}\cdot\text{mol}^{-1}$).¹⁷ The anatase structure is preferred over other polymorphs for water-decontamination applications because of its higher electron mobility, low dielectric constant and lower density. The increased photoreactivity is due to the slightly higher Fermi level, lower capacity to adsorb oxygen and higher degree of hydroxylation in the anatase phase. The rutile phase is stable at most temperatures and pressures. It is formed by the transformation of the anatase or brookite structures through calcination which leads to particle-size increases.¹⁹ The anatase polymorph can be easily obtained by synthesis at low temperature treatments (below 400°C), whilst the rutile form frequently starts to appear at moderate temperatures (400°C - 600°C) becoming the predominant phase after annealing at temperatures of above 600°C . The anatase and rutile forms have band gaps of 3.2 eV and 3.0 eV, respectively (**Figure 2.3**).^{20,21}

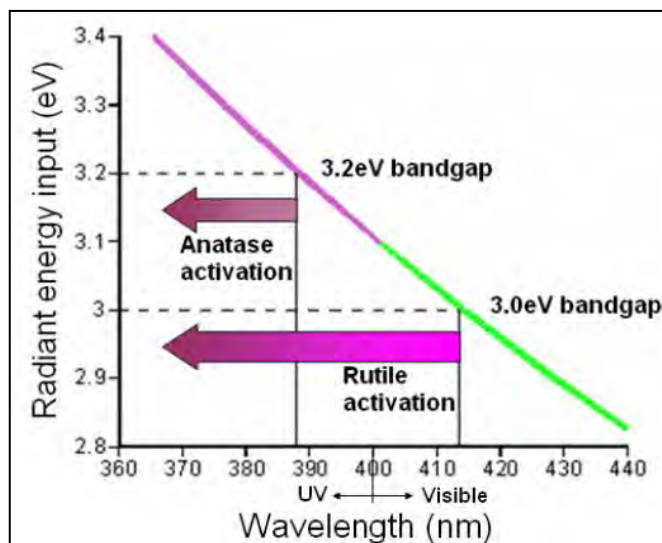
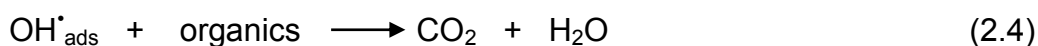
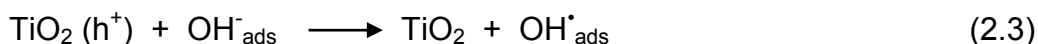
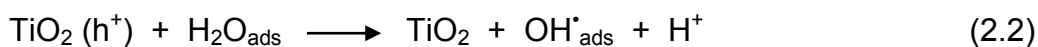
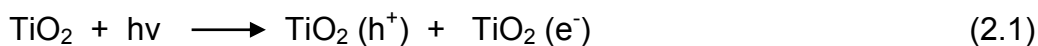


Figure 2.3 Anatase and rutile band gaps and activation wavelength ²²

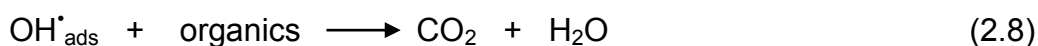
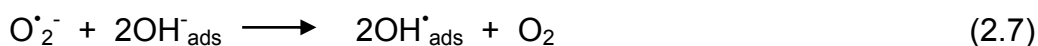
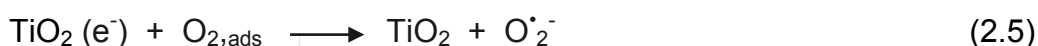
The activity of the rutile phase as a photocatalyst is generally very poor and the reasons for this are still poorly understood. However, some researchers have concluded that the rutile phase can be active or inactive, depending on the preparation conditions.²³

2.4 FUNDAMENTAL ASPECTS OF TiO₂ PHOTOCATALYSIS

The basic theory of TiO₂ photocatalysis is initiated by the absorption of sufficiently energetic photons to match the band-gap energy of the photoactive material. This induces electron (e⁻) promotion from the valence band (VB) to the conduction band (CB), leaving an electron-deficient positive hole (h⁺) in the valence band (**Figure 2.4**). The valence band is mainly formed by the overlapping of the oxygen 2p orbitals, whereas the conduction band is mainly constituted by the 3d orbitals, with t_{2g} symmetry of the Ti⁴⁺ cations. Most of these photogenerated electron-hole pairs recombine, releasing the absorbed energy as light or more frequently, as heat. However, a small percentage of these carriers migrate to the surface where they are trapped. The trapped electrons and holes can reduce or oxidise species adsorbed (ads) onto the surface of the material. Alternatively, the positive holes can react with surface-bound water or hydroxyl ions to generate highly oxidising hydroxyl radicals (OH[•]).



The electrons, on the other hand, react with the available O_2 producing the superoxide radical anion ($\text{O}_2^{\cdot-}$). These radicals can scavenge adsorbed water or hydroxyl ions to generate more hydroxyl radicals (OH^*).



Most organic photodegradation reactions can be attributed to the high oxidising power of these hydroxyl radicals.^{17,24-26}

The overall photocatalysis reaction as portrayed in **Figure 2.4** can be divided into five independent steps:²⁷

- (i) Mass transfer of the organic pollutants in the liquid phase to the TiO_2 surface.

- (ii) Adsorption of the organic contaminants onto the photon-activated TiO_2 surface (i.e. surface activation by photon energy occurs simultaneously in this step).
- (iii) Photodegradation of the adsorbed organics on the TiO_2 surface.
- (iv) Desorption of the intermediates from the TiO_2 surface.
- (v) Transfer of the intermediates from the interface region to the bulk fluid.

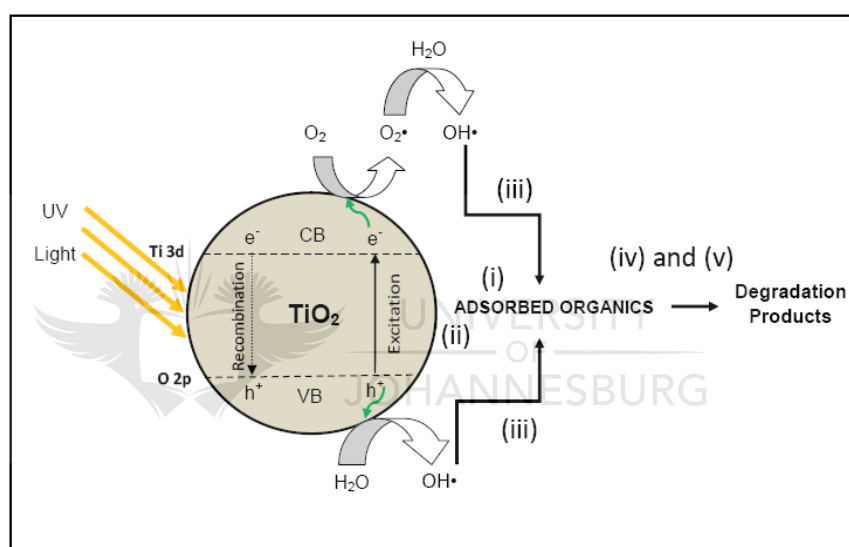


Figure 2.4 Scheme of the TiO_2 photocatalysis mechanism

2.5 LIMITATIONS OF TiO_2 AS A PHOTOCATALYST

Despite the achievements and remarkable advantages in its applications towards environmental cleanup, TiO_2 photocatalysis has significant limitations. The major drawback of TiO_2 photocatalysis arises from the mismatch between the TiO_2 band gap energy and the sunlight spectra, which overlap only in the UVA (400 nm to 320 nm) and UVB (320 nm to 290 nm) ranges. Only high-energy UV irradiation sources can activate TiO_2 . As a consequence, this technology can only take advantage of less than 5% of the solar energy impinging on the Earth's surface, limiting its potential as an environmentally sustainable technology.²⁸⁻³¹

Another serious limitation of TiO₂ photocatalysis is its low effectiveness due to the low rate of charge transfer to the surface and the high recombination rate of electron-hole pairs, which lowers the rate of photo-oxidation of organic compounds on the surface of the catalyst.³² In general, TiO₂ photocatalytic reaction rates are moderate and thus this technology is not appropriate for high throughput processes such as decontamination of heavily polluted industrial effluents.^{12,33} Increment of photon flux increases the reaction rate, but saturation is usually achieved at relatively low irradiance. This consequently reduces the energy efficiency of the process.^{30,34} While high photocatalytic activity has been reported using TiO₂ in suspension due to enhanced mass transport, the nanosized TiO₂ particles are difficult to handle and remove after their application in water decontamination. Further steps are required to remove the TiO₂ nanoparticles from the treated water, pushing up the water-treatment costs.³⁵ A detrimental consequence of increasing the quantity of TiO₂ in the reaction vessel is the increased turbidity created by the high TiO₂ concentration. This decreases the light penetration depth, drastically lowering the rate of photocatalytic reactions.³⁶ This has profoundly influenced research in photocatalysis with attempts at modifying TiO₂ to achieve efficient photoactivity in the visible spectrum topping current semiconductor photocatalysis research.^{17,28,29,31,37}

2.6 STRATEGIES FOR IMPROVING TIO₂ PERFORMANCE

A number of approaches have been suggested to improve the photocatalytic activity of TiO₂. One of the promising routes is the modification of the TiO₂ surface to enhance its sensitivity to visible light. The introduction of a small percentage of foreign atoms into the regular intrinsic crystal lattice of a semiconductor produces dramatic changes in the electronic properties of the semiconductor. This process of tuning the electronic properties of the semiconductor by introducing foreign atoms is called doping. An ideal dopant must increase the valence-band edge of the semiconductor, thus reducing the band gap, without lowering the conduction band. It must either improve or at least minimise electron-hole recombination in order to reduce any loss in quantum yield. It should not impart any instability to the semiconductor, be it thermal or chemical, and should be inexpensive to apply.

2.6.1 Non-metal doping

In recent times, a considerable amount of research has focused on the enhancement of TiO₂-based photocatalysis by modification of the TiO₂ with non-metals with the main aim of narrowing its band gap.³⁸ The pioneering work by Asahi *et al.* has stimulated an explosion of interest in TiO₂ doping with non-metals.³⁹ However, not all these studies are as innovative and original as one would like to see, sometimes contributing to the confusion more than to the understanding of the problem. There is also an open debate on how doping achieves enhanced TiO₂ photoactivity, as well as disagreements in many of the conclusions drawn from the results. One of the reasons for this may be attributed to the different strategies used to incorporate the non-metal dopants into the titanium dioxide. The different doping procedures probably lead, at least in some cases, to materials with somewhat different properties.⁴⁰ Questions concerning the chemical nature, the location in the solid and the involvement in photoactivity of the non-metal species still need to be addressed. It is essential to know whether the dopant species are primarily interstitial or substitutional, as this will affect the material properties accordingly. It is also important to determine whether the species tend to segregate at the surface of the material or are preferentially incorporated into the sub-surface or bulk sites because this can strongly influence the surface reactivity and photocatalytic properties. Another crucial question concerns the interaction between the non-metal impurities and oxygen vacancies or the titanium metal and how it affects the stability of the resulting material.⁴⁰ These gaps in knowledge need to be filled to gain a better understanding of the underlying principles governing TiO₂ band-gap tuning using non-metals.

Recent studies have shown that the desired band-gap narrowing of TiO₂ can be achieved by employing non-metal elements such as N, C, B, S, P, F, I, Cl and Br. Modified TiO₂ generally shows stronger absorption in the visible region owing to band-gap narrowing and enhanced photodegradation of organic pollutants under visible-light irradiation.^{39,41-46}

2.6.1.1 Nitrogen doping

Among the many non-metal dopants studied, nitrogen has been widely accepted as an effective dopant for band gap reduction as well as photocatalytic enhancement under visible-light irradiation. The band gap of TiO_2 is narrowed as a few crystal lattice oxygen atoms are substituted by nitrogen, enabling the TiO_2 to have photocatalytic activity under visible light without reducing its activity under UV light.

Currently, there are three different opinions on band-gap narrowing and photocatalytic enhancement in N-doped TiO_2 . Band-gap narrowing was explained by the formation of hybrids between N 2p orbitals with O 2p states in anatase TiO_2 doped with nitrogen because their energies are very close. This enhances the ability of TiO_2 to absorb visible light. In an experiment, films and powders of $\text{TiO}_{2-x}\text{N}_x$ showed enhanced photocatalytic activity compared to TiO_2 under visible light ($\lambda \geq 500$ nm) in photodegradation of methylene blue and gaseous acetaldehyde. The materials also exhibited a red shift in the absorption edge attributed to N doping.³⁹

Another line of thinking attributes the improved properties of N-doped TiO_2 to the formation of intra-band-gap impurity energy levels above the valence band of TiO_2 (**Figure 2.5**). In a study by Irie *et al.*, $\text{TiO}_{2-x}\text{N}_x$ powders were prepared by annealing anatase TiO_2 powder under NH_3 flow. They found that regardless of the value of x, the quantum yield values by irradiating with visible light were lower than those with UV light. This was attributed to the TiO_2 oxygen lattice sites being substituted by nitrogen atoms to form isolated impurity energy levels above the valence band (VB). Irradiation with UV light would excite electrons in both the VB and the impurity energy levels, but irradiation with visible light only excites electrons in the impurity energy levels. If substituting nitrogen for the oxygen sites in TiO_2 narrows the band gap, then the quantum yield values would be the same whether irradiating with visible light or UV light.⁴⁷

This idea was also supported by Zhao and Liu, who concluded that TiO_2 doped with substitutional nitrogen has shallow acceptor states above the valence band. In contrast, TiO_2 doped with interstitial nitrogen has isolated impurity states in the middle of the band gap due to hybridised N 2p and O 2p states.⁴⁸

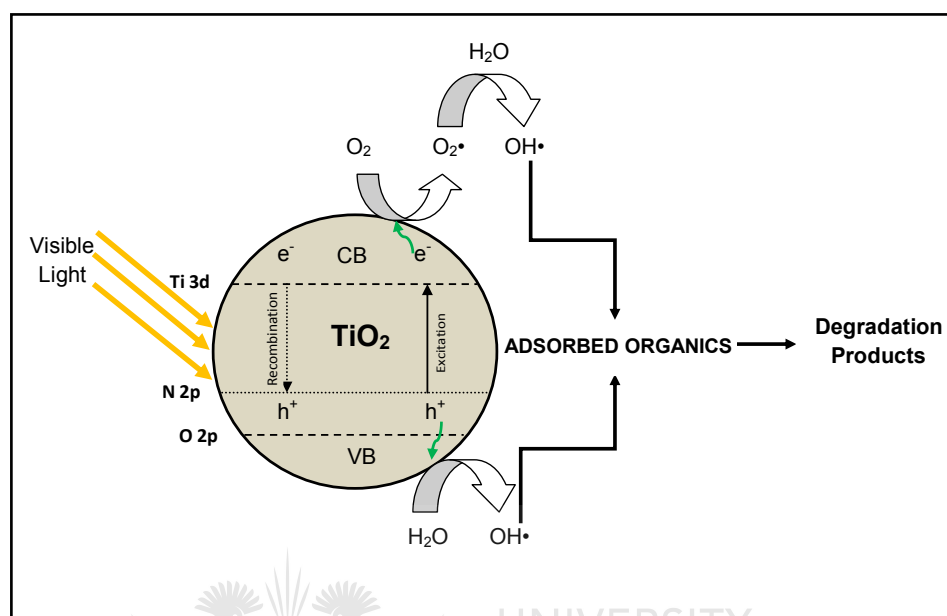


Figure 2.5 Mechanism of non-metal doped TiO_2 photocatalysis

Ihara *et al.* proposed the idea of oxygen vacancies created at the grain boundaries on polycrystalline particles. They concluded that oxygen-deficient sites formed on grain boundaries are important for inducing visible-light activity, whilst nitrogen doping on the part of oxygen-vacancy sites becomes an important re-oxidation suppressor.⁴⁹ Lack of understanding of the microstructure, electronic structure and impurity-existent form led to these controversies. Only with better understanding of these phenomena can an efficient N-doped TiO_2 photocatalyst which meets the practical requirements be prepared.⁴⁸

2.6.1.2 Carbon doping

Carbon doping has also been reported to result in intra-band-gap states just above the valence band of TiO_2 from which visible-light excitation becomes feasible. Due to these intra-band-gap states, the C-doped TiO_2 exhibits weak sub-band-gap light absorption starting at about 735 nm. A sample of C-doped TiO_2 was found to

contain between 0.4% and 4.0% carbon in the form of carbonate and elemental carbon as indicated by X-ray photoelectron spectra (XPS).^{28,31} Carbon-doped TiO₂ was reported to be efficient for the degradation of phenol with an initial concentration of 30 ppm under visible-light ($\lambda > 420\text{nm}$) irradiation due to the shifting of the absorption edge to a lower energy level.⁵⁰ In another study, carbon-modified TiO₂ was tested for its photocatalytic activity on the degradation of 4-chlorophenol (0.15 mM) under visible light ($\lambda \geq 400\text{ nm}$). First-order rate constants of 6.1×10^{-3} and $1.0 \times 10^{-3}\text{ min}^{-1}$ for the C-modified TiO₂ and P25, respectively, were reported.⁵¹ Carbon could improve the photoactivity of TiO₂ by stabilising the anatase structure and increasing adsorption of organic molecules onto the photocatalyst surface. Incorporation of carbonaceous species has also been reported to play the role of sensitisation to induce the visible-light absorption and response.⁵² Carbon-doped TiO₂ was prepared by the sol-gel method and calcined at 350°C for 2 h in air. The material was successful in degrading phenol (0.21 mM) in an aqueous suspension, under visible light of wavelength greater than 400 nm.⁵³ Understanding the origin of the shifted absorption and its relationship to the photocatalytic chemistry is essential in these C-doped materials.

2.6.2 Metal doping

Despite success reports pertaining to band gap narrowing and enhanced photocatalytic activity of non-metal doped TiO₂ under visible-light irradiation, more effort is still needed to improve the photo efficiency of TiO₂. Focus has shifted to doping TiO₂ with metals or metal ions to trap the charge carriers in order to hinder recombination and to shift the band gap into the region of visible light. However, the photoactivity of the metal-doped TiO₂ photocatalyst significantly depends on the nature of the dopant ion and its content, its concentration, preparation method, nature of the target pollutant, type of TiO₂ used and the operating conditions. Both positive and negative results have been reported from doping with metal ions.⁵⁴ Doping with metals is believed to result in an overlap of the Ti 3d orbitals with the d levels of the metals causing a batho-chromic shift in the absorption band edge of TiO₂. This band-gap reduction favours the use of visible light to activate the TiO₂ depending on the type of the metal dopant and its concentration. Different types of

metals have been used as dopants to improve the photo efficiency of TiO_2 in pollutant degradation. These include alkaline earth metals, transition metals including noble metals, as well as platinum-group metals and lanthanides or rare-earth metals.⁵⁵

2.6.2.1 Alkaline earth-metal doping

The challenge to tailor a good photocatalyst that can efficiently harness the energy from natural sunlight, which consists of no more than 5% UV light and 45% visible light has prompted researchers to consider introducing dopants such as alkaline earth metals into the TiO_2 lattice. Li *et al.* prepared alkaline earth-metal-ion-doped TiO_2 by the impregnation and co-precipitation methods and evaluated their performance for photocatalytic hydrogen production.⁵⁶ Be^{2+} -doped TiO_2 was shown to exhibit the highest photocatalytic activity as the Be^{2+} can occupy an interstitial site on the TiO_2 , increasing the electron density of the doped TiO_2 , which increases the photocatalytic activity. Mg^{2+} or Ca^{2+} ions on the other hand occupy a substitutional site on the TiO_2 . This results in a decrease in electron density of the doped TiO_2 , changing the TiO_2 into a p type semiconductor, which reduces the photocatalytic activity compared to Be^{2+} -doped TiO_2 . The radii of Sr^{2+} and Ba^{2+} were reported to be too large for the ions to enter the TiO_2 lattice. Therefore, Sr^{2+} and Ba^{2+} would be located mainly on the surface of TiO_2 , which might favour separation of the charge carriers to some extent, and eventually cause a slight enhancement of the photoactivity compared to the non-doped TiO_2 . The alkaline earth-metal ions were found to enhance the photocatalytic activities of the doped TiO_2 in the order: $\text{Be}^{2+} \gg \text{Ca}^{2+} > \text{Mg}^{2+} > \text{Sr}^{2+} = \text{Ba}^{2+}$.⁵⁶

2.6.2.2 Transition metal doping

The presence of transition metal-ion dopants in the TiO_2 crystalline matrix significantly influences photoreactivity, charge carrier recombination rates and interfacial electron-transfer rates. These properties are crucial for the degradation of pollutants in an aqueous medium. A plethora of articles featuring transition-metal-doped TiO_2 for various applications has emerged in recent years.⁵⁷⁻⁶⁵

Among the many transition metals used as dopants to modify the TiO₂ structure are noble metals (Au, Pt, Ag, Rh, Ru, Ir, Os and Pd). A common approach is to modify the surface of TiO₂ with these electron-accepting metals that form a Schottky barrier at the metal/TiO₂ interface, preventing electrons transferred to the metal phase from recombining with the holes (Figure 2.6).

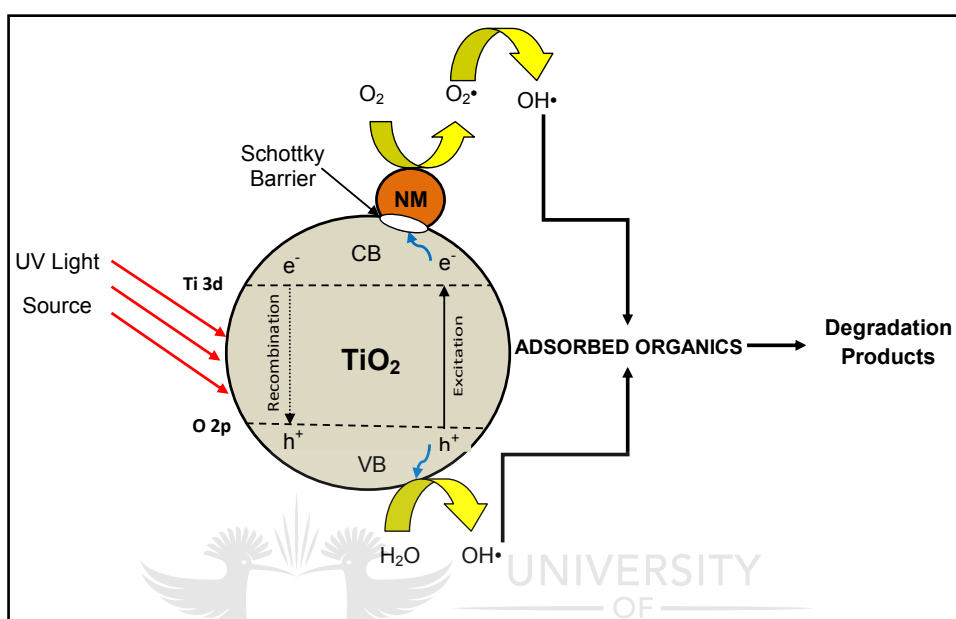


Figure 2.6 Formation of electron traps through Schottky barrier formation (NM – noble metal)

Considering the electron affinity of TiO₂ ($\chi = 3.9$ eV) and the work functions of the noble metals (Table 2.1) barrier heights between 0.4 eV and 1.8 eV are achievable.^{66,67}

Table 2.1 Work functions (ϕ) of selected noble metals

Noble metal	Work function (ϕ)
Pt	5.7
Pd	5.1
Ir	5.3
Au	5.1
Rh	5.0
Os	4.8
Ru	4.7
Ag	4.3

Noble metal deposits are also relatively stable even under photo-irradiation in an aerated atmosphere.⁶⁹ However, the use of expensive noble metals like Au, Pt and Pd raises the material cost. Alternative low-cost noble metals are highly desired for the development of practical water-decontamination photocatalysts.

Cao *et al.* prepared Ag-doped TiO₂ nanoparticles by a sol-gel method and applied them in the photodegradation of acetamiprid, a widely used insecticide in China.⁷⁰ The presence of Ag in crystalline TiO₂ was found to increase the photocatalytic activity of TiO₂, with the photocatalytic degradation velocity constant (*k*) increasing rapidly with an increase in Ag content from 0.02 to 0.06. Optimum levels of Ag were found to be between 4% and 8%.⁹⁵ In another study, titania hybrid photocatalysts containing 0.5 wt%, 1.0 wt%, 2.0 wt% and 5.0 wt% of rhodium (III) were prepared by chemisorption of RhCl₃ · 3H₂O onto anatase hydrate powder. Upon visible-light irradiation this photocatalyst induced a quicker mineralisation of 4-chlorophenol whereas cyanuric acid, which is known to be mineralised in the presence of the analogous Pt(IV) modified TiO₂, was not degraded.⁷¹ Chen *et al.* tested the effect of Pt dosage on the photocatalytic activity of TiO₂ for the decomposition of 9 mg/l *o*-cresols under visible light. The band-gap energies were observed to be 3.11 eV for pure TiO₂ and 2.95 eV for 1.5 wt% Pt/TiO₂. More than 90% *o*-cresols were shown to be decomposed by 0.5wt % Pt/TiO₂. The degradation rate constants of *o*-cresol for the 0.5wt% Pt/TiO₂ were 4.8 times than those obtained with pure TiO₂. The presence of Ti³⁺ prevents the recombination of electrons and holes due to the formation of the Schottky Barrier between platinum and TiO₂.⁷² In a study on gold-doped TiO₂, 2 wt% of gold was photo-deposited onto the surfaces of commercial TiO₂ powders. Au deposition activated all tested photocatalysts to react under visible-light irradiation. Visible-light-induced oxidation of 2-propanol by aerated gold-modified TiO₂ suspensions was initiated by excitation of gold surface plasmon. Light exposure experiments revealed that the photocatalytic reaction rate depends strongly on properties of TiO₂, such as particle size, surface area and crystalline form as well as the properties of gold deposits, such as size and shape.⁷³

Nanoparticles of TiO_2 were synthesised by the sol-gel method followed by photo-deposition of about 1% noble metal to give M/TiO_2 ($\text{M} = \text{Ag}, \text{Au}, \text{and Pt}$). The M/TiO_2 catalysts showed remarkable photocatalytic activity towards the degradation of oxalic acid and formic acid as well as the decolourisation of textile dye tartrazine under visible irradiation. The photocatalytic efficiency of all the catalysts followed a similar trend in the degradation studies and the order of the photocatalytic activity of the different catalysts was: $\text{Au/TiO}_2 > \text{Ag/TiO}_2 \sim \text{Pt/TiO}_2 > \text{synthesised TiO}_2 > \text{TiO}_2$ (P25 Degussa).^{74,75}

Palladium-doped nanocrystalline anatase TiO_2 was prepared by solution combustion method and evaluated for the photocatalytic degradation of various dyes such as alizarin red S, methylene blue, orange G and Rhodamine B as well phenol and 4-chlorophenol under UV exposure. Pd-ion substituted TiO_2 showed significantly higher photocatalytic activity compared to un-substituted TiO_2 for nitric oxide (NO) reduction and NO decomposition. However, the initial rate of degradation for all the dyes, phenol and 4-chlorophenol was lower in Pd-substituted and impregnated TiO_2 compared to that of un-substituted TiO_2 . This lower reaction rate was attributed to a decrease in the surface area of the materials.⁷⁶ Although noble-metal doping could be efficient in prolonging the surface charge separation, their availability and cost-effectiveness for an industrial application need to be considered. In most studies, however, the optimum amount seems to be less than 2%. For this reason attention is now being focused on the more economical, readily available transition metals as TiO_2 dopants.

Recently, transition metals (Cr, Mn, Fe, Co, Ni, Cu and Zn) have been used to replace noble metals as TiO_2 dopants, to reduce the overall catalyst production costs. Fe-doped TiO_2 was reported to show high dye-degradation efficiency of 90% and 75% total organic carbon (TOC) removal efficiency of Acid Blue 92 upon UV light irradiation. The incorporation of transition-metal ions into the TiO_2 lattice was found to alter or lower the band-gap energy and shift the catalyst absorbance edge closer to the visible-light region.⁵⁵ The photo-reactivities of 21 metal ion-doped colloids were quantified in terms of both the conduction band electron reduction of an electron acceptor (CCl_4 dechlorination) and the valence band hole

oxidation of an electron donor (CHCl_3 degradation). Doping with Fe^{3+} , Ru^{3+} , V^{4+} , Mo^{5+} , Os^{3+} , Re^{5+} , and Rh^{3+} ions substantially increased photoactivity for the degradation of CHCl_3 under UV irradiation, whereas doping with Co^{3+} and Al^{3+} decreased the photoactivity. All dopants with a closed-shell electronic configuration (Li^+ , Mg^{2+} , Al^{3+} , Zn^{2+} , Ga^{3+} , Zr^{4+} , Nb^{5+} , Sn^{4+} , Sb^{5+} , and Ta^{5+}) showed little effect on the observed photoreactivity. No enhanced photoreactivity with Mn^{3+} was observed since it can trap both electrons and holes.⁷⁷

Hydrothermally synthesised nano- TiO_2 was doped with transition metal ions (V, Cr and Fe) and the samples were tested for their photocatalytic activity in the mineralisation of xylene (vapour phase), methylene blue and active dye PR (liquid phase). In comparison to non-doped TiO_2 , V-, Cr- and Fe-doped TiO_2 samples exhibited much higher photocatalytic activity using visible light.⁷⁸

Devi *et al.* examined the effects of V^{5+} , Mo^{6+} and Th^{4+} doping into the TiO_2 matrix for the degradation of chlorpyrifos under UV/solar irradiation.⁵⁸ The undoped TiO_2 showed the highest degradation efficiency compared to all the doped TiO_2 samples under UV light. This may be due to the fact that mid-band gaps created by the dopants may serve as sites for recombination. The optimum dopant concentration in these studies was found to be 0.06%. Th^{4+} doped TiO_2 showed enhanced photocatalytic activity compared to all other catalysts under solar light due to (i) the large surface area; (ii) large shift in the band gap; (iii) higher concentration of surface adsorbed water and hydroxyl groups; and (iv) effective separation of electrons and holes. The larger shift in the absorption band to the visible region increases the efficiency of the photocatalysts to absorb more photons under solar light.⁷⁹ Other metal ions such as W(VI), inhibit the anatase to rutile transformation leading to stability of the anatase phase at high temperature. Although stronger visible-light absorbance may be achieved through metal doping, the relationship between visible-light absorbance and photocatalytic efficiency is not simple. A careful optimisation of the metal-ion additive concentration is needed to achieve high photocatalytic efficiency in these metal-ion modified TiO_2 photocatalysts. One disadvantage of base-metal doping is the easy of leaching into the water.

2.6.2.3 Lanthanide doping

It is desired that the deposition of metal ions on TiO_2 can modify the photoconductive properties by increasing the charge-separation efficiency between electrons and holes, and also by acting as traps for electrons, inhibiting volume and surface recombination of electrons and holes that reduce the photo-efficiency of TiO_2 .⁸⁰

Interest in using rare earth (RE) metals (La, Nd, Sm, Eu, Gd, Yb and Pr) as TiO_2 dopants is due to their unique chemical, physical and electronic properties, i.e. (i) possession of an f-orbital increases the adsorption of certain organic pollutants onto TiO_2 by forming complexes with Lewis bases; (ii) being a good electron trapper; and (iii) having a unique electronic structure that enhances the optical properties of the catalyst. It was established in a recent study that the photocatalytic activity of TiO_2 could be enhanced by doping RE metal ions on commercial Degussa P25. Among the studies, Ce doping at 1.0% was found to exhibit the best decolourisation activity of methylene blue, in which 1.0 wt% Ce-doped TiO_2 could bleach the targeted dye completely in just 400 min under UV irradiation at 18 W.⁵⁵

Bakardjieva and Murafa studied the effects of RE (La, Ce, Pr, Nd, Sm, Eu, Dy, Gd) on the physical and chemical properties of TiO_2 prepared by a sol-gel method. The photocatalytic activity of the prepared samples was probed by the photocatalytic decomposition of Orange II dye in aqueous slurry under irradiation at 254, 365 and 400 nm wavelength. The best photocatalytic properties in the visible region were shown by TiO_2 doped with Nd^{3+} ions ($k = 0.0272 \text{ min}^{-1}$ for UV and 0.0143 min^{-1} for visible light).⁸¹ RE metals were incorporated into TiO_2 by a sol-gel method using rare earth (RE = La^{3+} , Ce^{3+} , Er^{3+} , Pr^{3+} , Gd^{3+} , Nd^{3+} , Sm^{3+}) metal salts and tetra-*n*-butyl titanate as precursors. Their photocatalytic activities were evaluated using nitrite as a target pollutant. There was an increase in photoactivity probably due to the higher adsorption, red shifts to longer wavelengths and the increase in the interfacial electron transfer rate. Nitrite was almost completely degraded over RE/ TiO_2 catalysts after longer irradiation times.⁸² El-Bahy *et al.* found Gd^{3+} -doped

TiO₂ to be more effective than La³⁺, Nd³⁺, Sm³⁺, Eu³⁺, and Yb³⁺ because Gd³⁺/TiO₂ had the lowest band gap and particle size, as well as the highest surface area and pore volume. Lanthanide ions (La³⁺, Nd³⁺, Sm³⁺, Eu³⁺, Gd³⁺ and Yb³⁺)/doped TiO₂ nanoparticles were successfully synthesised by a sol-gel method and their photocatalytic activities were evaluated using Direct Blue dye (DB 53) as a decomposition target. Gd³⁺/TiO₂ was the most effective photocatalyst with a dye-removal efficiency of 100%.⁸³ Among all the RE elements, Eu and Er ions are considered the best choice as TiO₂ dopants because of their excellent physical and chemical properties. The RE ions can form complexes with TiO₂ to form RE–O–Ti bonds on the inner sphere surface. The formation of this bond inhibits the anatase to rutile transformation and the formed complex enhances the ability of the material to adsorb foreign ions. In addition, the absorption of the resulting RE-doped TiO₂ is shifted to the visible region due to the many variable energy levels formed from the RE.^{82,83}

Recent reports concluded that metal doping leads to unstable materials that undergo corrosion and long-term leaching of the metal dopant causing a gradual decay in the photocatalytic performance of the material. On the other hand, doping with non-metallic elements requires harsh preparation conditions. This is compounded by the difficulty in determining the degree of doping using chemical analyses. Mono-doping is also characterised by considerable difficulty in reproducing the photocatalytic activity that is frequently dependent on the exact preparation procedure and the doping level⁸⁴ (**Figure 2.7**)

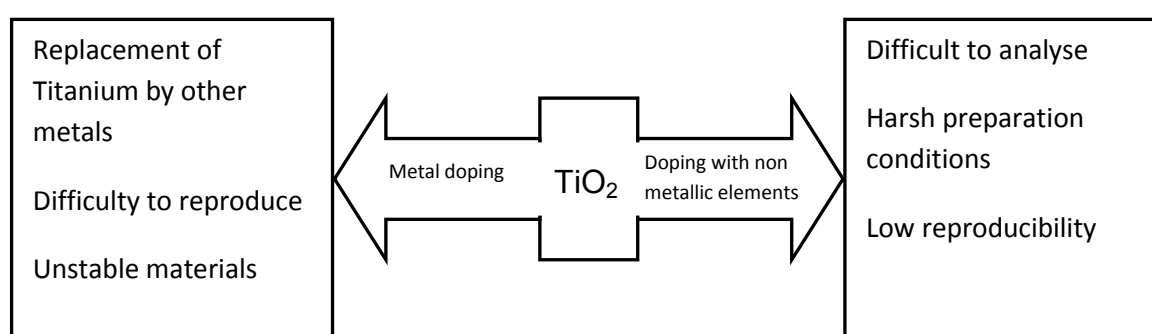


Figure 2.7 Some 'pros and cons' of mono-doping methodologies⁸⁴

It is against this background that researchers need to explore further the underlying theory behind enhanced photoactivity in this field.^{85,86}

2.6.3 Co-doping

Motivated by the positive photocatalytic response realised through non-metal and metal doping of TiO₂, strategies aimed at further enhancing the quantum efficiency of the TiO₂-based materials saw the sprouting of a material engineering technique known as co-doping. This TiO₂ modification technique has gained wide attention in recent years. Taking advantage of the possible synergistic effects on the photocatalytic activity of the material, various forms of double metal dopants, double non-metal dopants, double metal, non-metal dopants and even tri-dopants have been introduced on TiO₂.⁸⁷⁻⁹⁰ The objective in many of these studies is to advance the material engineering of TiO₂ by altering the optical properties through specially designing trap sites for both electrons and holes as well as reducing the band gap (**Figure 2.8**).⁹¹ Besides shifting the absorption edge of TiO₂ successfully from the ultraviolet region to the visible-light region, co-doping also improves the physical properties of TiO₂ such as specific surface area and crystallite size whilst prohibiting the phase transformation of anatase to rutile phase.⁹²

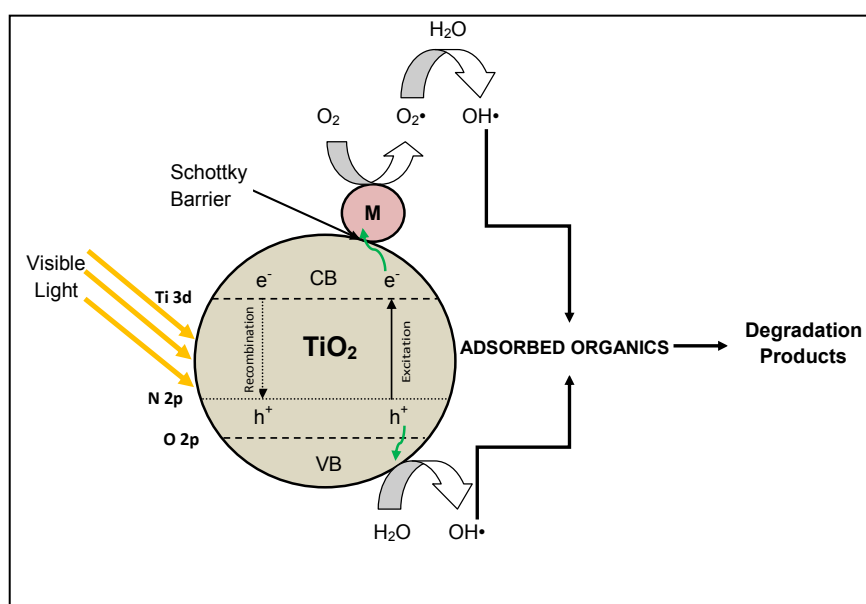


Figure 2.8 Band-gap reduction and electron trapping in nitrogen, metal co-doped TiO₂ [M – metal]

Improved performance of TiO₂ under visible light is achieved up to an optimal doping level, after which performance deteriorates when the dopants become recombination centres for photogenerated electron-hole pairs.⁹³ In a study by Yang *et al.*, C-doped and C- and V-doped TiO₂ photocatalysts for acetaldehyde photodegradation were prepared using a sol-gel process. Both catalysts showed enhanced activity for the degradation of acetaldehyde under visible-light irradiation (>420 nm). The 1.0% V-containing co-doped TiO₂ had the highest activity under visible-light irradiation. The increase in the activity was attributed to a change in the surface of the catalyst resulting from vanadium substitution. In addition to functioning as a photosensitiser that shifts the optical response of TiO₂ from the ultraviolet to the visible-light region, the doped elemental carbon increased the surface area and improved the dispersion of vanadium.⁹⁴

Praseodymium doping in Pr/N co-doped TiO₂ was found to inhibit the growth of crystalline size and the transformation from anatase to rutile. Pr/N-TiO₂ samples exhibited enhanced visible-light photocatalytic activity compared to N-TiO₂, undoped TiO₂ and commercial P25. The nitrogen atoms were incorporated into the crystal lattice of TiO₂ and resulted in band-gap narrowing. Pr doping could reduce the radiative recombination of photogenerated electrons and holes in TiO₂. The improvement in photocatalytic activity was ascribed to the synergistic effects of nitrogen and Pr co-doping.⁹⁵ TiO₂ nanoparticles co-doped with nitrogen and silver (Ag₂O/TiO_xN_{1-x}) were found to be effective visible-light driven photocatalysts. The catalyst showed strong bactericidal activity against *Escherichia coli* (*E. coli*) under visible-light irradiation ($\lambda > 400$ nm). It was postulated that the Ag₂O species trapped the photogenerated electrons in the process of Ag₂O/TiON photocatalytic reaction, thus inhibiting the recombination of electrons and holes in agreement with the stronger photocatalytic bactericidal activity of Ag₂O/TiON. The presence of nitrogen and silver resulted in a clear shift in the absorption band of the Ag₂/TiO₂ into the visible-light range (>400 nm).⁹⁶

Results on C, N co-doped TiO₂ demonstrated that the optical response of TiO₂ can be shifted from UV to the visible-light region with the introduction of carbon and nitrogen. Nitrogen atoms substituted some of the lattice oxygen atoms on TiO₂ and

most of the carbon was in the form of elemental carbon. The surface area of the co-doped catalyst was increased and its photocatalytic efficiency enhanced. The photocatalytic tests indicated that the co-doped catalyst had higher activity for the degradation of methylene blue (MB) compared to pure TiO_2 both under visible light and UV irradiation, which was attributed to the synergetic effects of carbon and nitrogen dopants.⁹⁷

Overall, co-doping is an effective method for improving the performance of TiO_2 . The simultaneous introduction of different dopants generates synergistic effects which enhance the properties of the final TiO_2 product. Benefits of co-doping include: (1) a high percentage of the anatase phase is obtained; (2) phase transformation of the anatase phase to the rutile phase is inhibited; (3) small crystallite size with high specific surface area is obtained; (4) band-gap narrowing by shifting the optical absorption wavelength of TiO_2 from UV light to visible light is achieved; (5) recombination of photogenerated electrons and holes is reduced; and (6) dopants can act as active sites for pollutant adsorption to facilitate the photodegradation reactions.⁹⁸

2.7 CARBON NANOTUBES

Carbon nanotubes (CNTs), considered as a new form of pure carbon, can be visualised as hexagonal carbon networks or graphene sheets rolled up into a seamless cylinder. The unique morphology and structure of carbon nanotubes (CNTs) keep attracting a great number of researchers to explore the novel properties of these materials.⁹⁹ CNTs are mainly divided into four classes: (1) single-walled carbon nanotubes (SWCNTs) which consist of a single layer graphene wall; (2) double-walled carbon nanotubes (DWCNTs) which consist of two-layer graphene walls, that combine the structural and physical properties of SWCNTs and MWCNTs; (3) triple-walled carbon nanotubes (TWCNTs) which consist of three-layer graphene walls; and (4) multi-walled carbon nanotubes (MWCNTs) which consist of more than three-layer graphene walls. The amazing mechanical and electronic properties of the nanotubes stem from their quasi one-dimensional structures and the graphite-like arrangement of the carbon atoms in

the shells. Thus, CNTs have high Young's modulus and tensile strength, which make them preferable for composite materials with improved mechanical properties. The electronic properties significantly vary depending on the chirality and the number of graphene walls. In general, SWCNTs are a mixture of metallic and semiconducting material, depending sensitively on their geometrical features, while MWCNTs are regarded as metallic conductors. Especially for SWCNTs, the electronic properties vary from metallic to semiconducting depending on their structures. Basic studies and engineering applications of SWCNTs and MWCNTs have provided great results, but research and applications of DWCNTs have been relatively scarce.⁹⁹⁻¹⁰¹

The remarkable mechanical, electrical, biological, optical and thermal properties of CNTs make them attractive and promising candidates in technological areas such as energy, information, aerospace, medicine and chemical industries, where they can be used as gas adsorbents, templates, actuators, composite reinforcements, catalyst supports, filters or chemical sensors, among other things (**Figure 2.9**). For the same reasons, they are promising building blocks for hybrid materials.¹⁰²

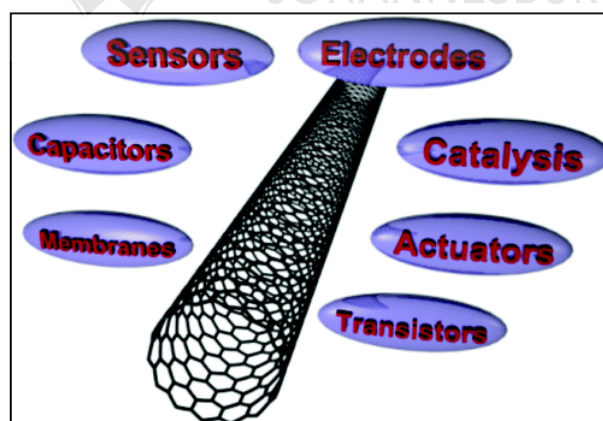


Figure 2.9 Some applications of CNTs¹⁰³


Additionally, as a result of the one-dimensional nature of CNTs, electrons can be conducted in nanotubes without being scattered. The absence of scattering of the electrons during conduction is known as ballistic transport and allows the nanotube to conduct without dissipating energy as heat.⁹⁹ This property is quite

enticing in the fabrication of CNT-inorganic hybrids in which electron channelling through the CNT is desirable.

2.7.1 Functionalisation of carbon nanotubes

Early research work on CNTs focused mainly on determining and exploiting the properties of the pristine materials. More recently, further insight into the chemistry of CNTs, particularly their functionalisation, has begun to dominate the field with attempts to produce composite materials with novel properties complementary to those of the pristine nanotubes.¹⁰⁴ Chemical functionalisation of CNTs was initially an attempt to address their poor solubility. Pristine CNTs align parallel with one another forming ropes or bundles, thus increasing Van der Waals interactions and decreasing their free energy. This prevents their dissolution in aqueous media, necessary for much of the chemistry envisaged for these materials.¹⁰⁵

The main approaches for the functionalisation of CNTs can be grouped into two main categories:

- 
- (a) The covalent anchoring of chemical groups, through reactions on the CNT skeleton.
 - (b) The non-covalent supramolecular adsorption or wrapping of various functional molecules onto the tubes.

With covalent functionalisation, functional groups are attached to the CNT ends or sidewalls. Covalent functionalisation is performed by oxidative treatments of CNTs. This results in the opening of the highly reactive semi fullerene-like caps. CNT oxidation thus yields opened tubes with oxygen-containing functional groups (predominantly carboxyl, carbonyl and hydroxyl groups) at both the sidewalls and the tube endings. These groups can then be used as chemical anchors for further derivatisation. In non-covalent functionalisation, the tube surface can be modified via Van der Waals forces and π - π interactions, by adsorption or wrapping of polynuclear aromatic compounds, surfactants, polymers or biomolecules. The main advantage of the non-covalent functionalisation of CNTs, compared to the

covalent one, is that with the former, chemical functionalities can be introduced onto the CNTs without affecting the structure and electronic network of the tubes.⁹⁹

Intensive functionalisation may result in drastically altered CNT properties and is therefore not a viable option for many electronic applications. For this reason many researchers are interested in MWCNTs with outer wall functionalities and intact inner walls. The development of novel methods that facilitate the processing of CNTs while having little impact on their properties or providing the option to restore them in a subsequent step would therefore be desirable.¹⁰³ Functional groups attached to CNTs may result in their improved dispersion in aqueous solvents besides acting as anchor sites for attachment of functional materials such as TiO₂. This has enabled the use of solution processing techniques such as the sol-gel method which facilitates the fabrication of CNT/TiO₂-based devices, opening a field for new applications.¹⁰³

2.7.2 Carbon nanotube-TiO₂ nanocomposites

CNT/TiO₂ nanocomposites have been the subject of extensive investigation in recent times due to their ability to increase reactive charge carrier lifetimes and extend the optical absorption into the visible spectrum. However, the interfacial charge-transfer interactions between TiO₂ and the CNTs are not completely understood.^{106,107} Nanocomposites containing CNTs have also attracted great attention because of the unique electrical and structural characteristics of CNTs. The unique electronic properties including the possibility to behave as either metallic or semiconducting depending on their geometry, the excellent electron conductance, high surface area and strong adsorption capacities have led researchers to give them consideration as potential supports for TiO₂-based photocatalytic materials. TiO₂ can be coated on CNTs to reduce agglomeration and increase the surface area for pollutant adsorption¹⁰⁸ (**Figure 2.10**).

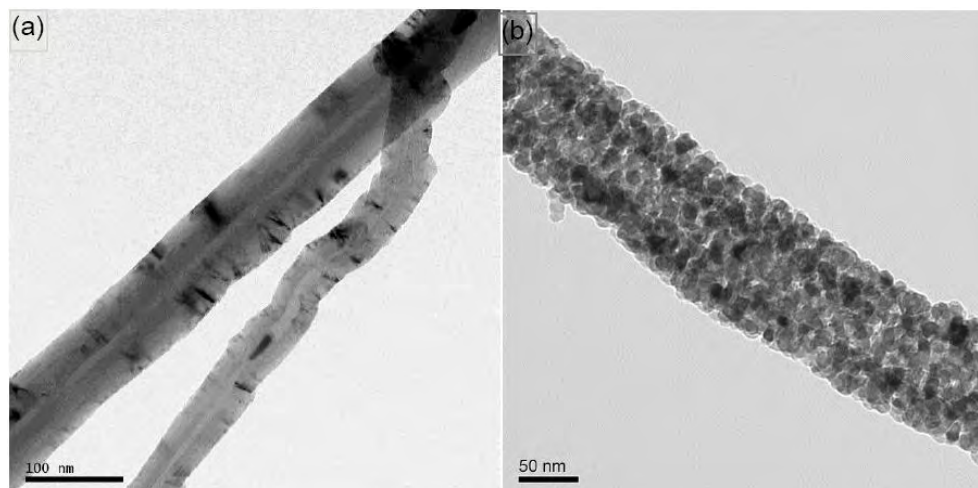


Figure 2.10 TEM images of (a) bare functionalised MWCNTs; and (b) MWCNT coated with N, Pd co-doped TiO₂

CNT/TiO₂ composites are believed to provide many applications and exhibit cooperative or synergetic effects between the metal oxide and CNTs, consequently boosting the photocatalytic activity of the material for the target reactions. For efficient photodegradation, the target compounds need to be in contact or directly attached to the material surface because the generated radicals have a short lifetime. One way to improve adsorption is to combine TiO₂ with good adsorbents such as CNTs. This could improve the photo-efficiency and address the problem of poor adsorption of many target compounds on the TiO₂.¹⁰⁹⁻¹¹¹

Some authors have attributed the CNT/TiO₂ photocatalytic enhancement to the conductive structure of the CNTs scaffolds which is believed to favour the separation of the photo-generated electron-hole pairs by the formation of heterojunctions at the CNT/TiO₂ interface. TiO₂ is an n-type semiconductor; however, in the presence of CNTs, photogenerated electrons may move freely towards the CNT surface, as CNTs may have a lower Fermi level. This leaves an excess of valence-band holes on the TiO₂ that migrate to the surface and participate in photocatalytic degradation of organic pollutants. The TiO₂ therefore effectively behaves as a p-type semiconductor (**Figure 2.11**). In addition, application of anodic potentials on irradiated CNT/TiO₂ composites is anticipated to lead to further photoactivity enhancement.¹¹²

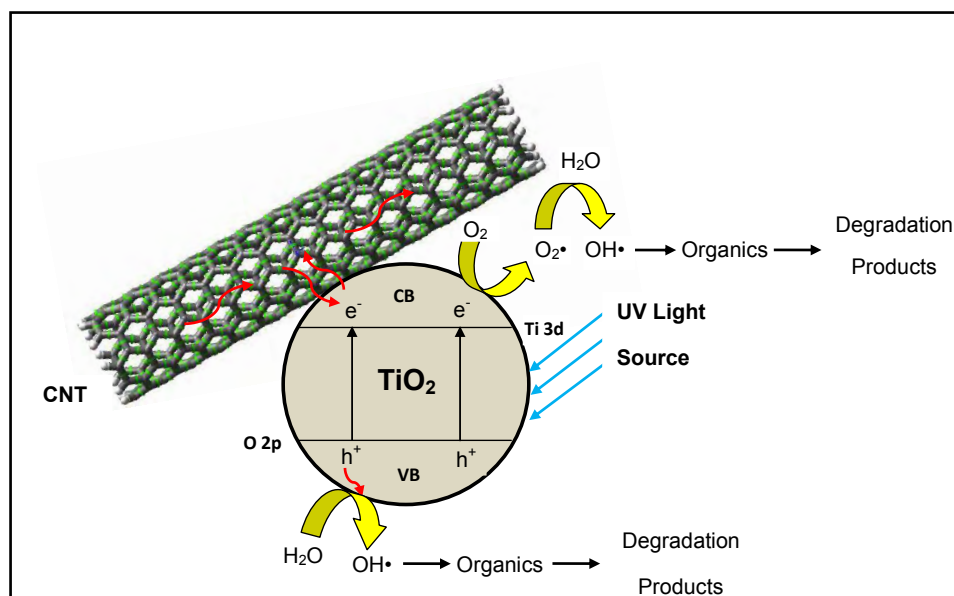


Figure 2.11 CNT/TiO₂ composite showing free channelling of electrons through CNTs for enhanced photoactivity

CNT/TiO₂ composites have found applications in areas such as solar energy utilisation, microelectronics, optoelectronics and heterogeneous photocatalysis.¹¹³ Environmental applications of CNT/TiO₂ nanocomposites include the treatment of contaminated water and air by heterogeneous photocatalysis, hydrogen evolution, CO₂ photo reduction, dye sensitised solar cells and sensor devices.¹¹² High active, visible-light-driven photocatalysts were prepared via a sol-gel method by forming N-doped TiO₂ supported on multi-walled carbon nanotubes (MWCNTs). Their photocatalytic activities were evaluated by photodegradation of methanol under visible-light irradiation and a maximum conversion rate of 94% was reported for the MWCNT/N-doped TiO₂ composite compared to 20% for the Degussa P25. MWCNTs acted as supports for the N-doped TiO₂ system. Incorporation of nitrogen resulted in a red shift in the absorption edge of the material through band-gap reduction whilst enhancement in photoactivity was attributed to retardation of electron-hole recombination through electron trapping by the MWCNTs.¹¹⁴ Zhang and Oh deposited Fe and TiO₂ on MWCNTs via a sol-gel method and applied the material in the degradation of an organic dye methylene blue under visible-light irradiation. Higher degradation efficiency was observed under visible-light irradiation for the Fe/TiO₂-MWCNT compared to the Fe/TiO₂ and un-doped TiO₂. The presence of Fe and MWCNTs was reported to synergistically enhance the

photoactivity by trapping the photogenerated electrons and increasing the lifetime of holes for oxidative degradation.¹¹⁵

In another study, the effect of carbon nanotubes (CNTs) on the adsorption and the photocatalytic properties of TiO₂ (P25) for the treatment of azo dyes was investigated. The results showed that the presence of CNTs improves the adsorption of the dyes onto P25 due to the strong interaction between P25 and CNTs. The mechanism for the enhancement of the photocatalytic activity of P25 by CNTs was proposed based on the excitation of electrons from the valence band to the conduction band of TiO₂. Once in the conduction band of TiO₂, electrons may migrate onto CNTs, which have a special structure for facilitating electron transport. This reduces the possibility of the recombination of electron-hole pairs. Meanwhile, O₂ adsorbed on the surface of CNTs may accept electrons and form O₂^{•-} radicals, which scavenge water molecules to result in the formation of OH[•] radicals in the system. This results in more radicals in the system, resulting in the faster degradation of the dyes.¹¹⁶

Despite the achievements realised in the synthesis and application of CNT/TiO₂ nanocomposites in pollutant removal from water, the phenomena behind the enhancement in photocatalytic activity through the interaction of CNTs and TiO₂ is still not fully understood. Previous research offers speculation rather than proof that these phenomena occur. The degree of coverage of CNTs with the TiO₂ is an issue that still needs to be addressed. While much of the work in this area has focused on SWCNT/TiO₂ and MWCNT/TiO₂, other types of CNTs like DWCNTs need to be explored in terms of their performance in nanocomposites. There is still a myriad of opportunities with regard to the use of different types of CNT/TiO₂ nanocomposites for environmental decontamination. This, coupled with innumerable CNT/TiO₂ nanocomposite fabrication techniques and a better understanding of their physical and chemical properties, is bound to result in further improvements in the quantum yields of these materials. The growing body of data requires new analyses of the challenges and opportunities facing photocatalysis in order to assess which of the materials are best suited for a

particular application, with emphasis on one of the niche areas for this technology, namely water decontamination.

2.8 NANOPARTICLE RECOVERY

There is growing concern over the recovery of TiO_2 or CNT/ TiO_2 nanocomposites from the reactor in the event that the photocatalytic process is scaled up for industrial application. The post-treatment process to separate the catalyst from the treated water is difficult and may result in overbearing treatment costs. This contributes significantly to the total cost for the operation of the system. In addition, the catalyst particles dispersed in the aqueous solution tend to coagulate and agglomerate in a prolonged photocatalytic degradation process, causing reduction in both the surface area and treatment efficiency. In most bench-scale studies, catalysts are often separated by simple centrifugation or filtration. However, this is not feasible for separating the catalyst at an industrial scale, mainly due to the energy and time consumed by the separation processes. Consequently, research on the immobilisation or synthesis of TiO_2 particles with magnetic behaviour is gaining momentum.⁵⁵

2.9 APPLICATIONS OF TiO_2 -BASED PHOTOCATALYTS

There are a number of examples of applications of TiO_2 environmental photocatalysis that are already at or near the stage of implementation or commercialisation.

2.9.1 Photo-induced hydrophilic coatings and self-cleaning devices

The deposition of dirt, soot, vehicle exhaust fumes and other particulates on walls results in the necessity of cleaning the surfaces of buildings. The growth of organisms, such as bacteria, algae and fungi disfigures the facades of buildings and results in mechanical weakening and eventual destruction. To prevent this, buildings can be coated with a layer of TiO_2 photocatalyst. On irradiation with light of sufficient energy, photocatalysis occurs, chemically breaking down the organic

particles adsorbed on the surface of the photocatalyst. Also, the contact angle of water is reduced, making the surface super-hydrophilic which would allow dirt to be removed easily. This process promotes self-cleaning and antifogging of mainly glass surfaces.^{19,91}

2.9.2 Wastewater treatment

Studies have shown photocatalysis with TiO₂ nanoparticles to be useful for the degradation of wastewater pollutants. This process has several advantages including mineralisation of organic pollutants like aliphatics, aromatics, polymers, dyes, surfactants, pesticides and herbicides to CO₂, water and mineral acids. No disposable waste solids are generated and mild temperatures and pressure conditions are used. Photocatalysis with TiO₂ nanoparticles uses two kinds of reaction systems, namely suspension and immobilised systems.¹⁹ The used catalyst finally becomes a solid waste that should be appropriately disposed.

2.9.3 Water splitting

Water splitting is often termed „the holy grail“ of heterogeneous photocatalysis and much has already been reported about the use of TiO₂ in promoting photocatalytic processes associated with either the oxidative or reductive aspects of this reaction. Hydrogen has great potential as a source of energy from the aspects of environmental preservation and energy security for a sustainable society in the future. For this purpose, production of H₂ from renewable resources and natural energy sources is an attractive alternative. TiO₂ photocatalysis using solar energy has been widely studied as a possible avenue to produce hydrogen from water taking advantage of the decomposition of water into oxygen and hydrogen without the application of an external voltage.^{19,91}

2.9.4 Dye-sensitised solar cells

Dye-sensitised solar cells (DSSCs) convert visible-light energy to electrical energy through charge separation in sensitizer dyes adsorbed on a wide band-gap semiconductor, such as TiO₂. Numerous sensitizers have been prepared, and their

performance tested. However, the conversion efficiency of DSSCs is still lower than that of the silicon-based photovoltaic cells. To obtain a high conversion efficiency, optimisation of the short-circuit photocurrent (I_{sc}) and open circuit potential (V_{oc}) of the cell is essential.¹¹⁷

2.9.5 Bactericides

The ability of TiO_2 or its modified forms produce hydroxyl radicals that kill bacteria, destroy viruses and perform chemical transformations on a wide range of biomolecules under UV or visible irradiation is an intriguing and commercially important attribute of this material's photocatalytic properties. Numerous studies have explored these phenomena with high surface area and thin-film TiO_2 samples.⁹¹

2.10 TOXICITY OF NANOPARTICLES

The interaction between nanoparticles and the human body is currently poorly understood. System biologists are beginning to understand better what takes place during the interaction of cell membranes and cell organelles with nanoparticles using scientific concepts such as genomics, proteomics and metabolomics. The convergence of these biological sciences with nanotechnology offers opportunities to fine-tune the toxicological risk. The toxicology of nanoparticles is often linked to the production of free radicals. There is a need to couple such toxicity tests with studies on the aggregation of nanoparticles. Thus, studies aimed at correlating the nanostructure with its toxicological properties, including the interpretation of properties in terms of structure and interactions of nanoparticles in various biological mixed systems, make a strong case for further studies related to the toxicity assessment of these particles.¹¹⁸ Most studies on TiO_2 have not shown any negative impacts on human health.¹¹⁹

2.11 CONCLUDING REMARKS

There is greater potential for environmental nanotechnologies to contribute to economic growth and innovation while at the same time allowing sustainable

development and protection of the environment. Various approaches for environmental remediation have been successfully demonstrated at laboratory scale but, in the majority of cases, still require verification of their efficacy and safety in the field. Solar photocatalysis is an active method which harnesses energy from the sun to degrade many different pollutants. Titanium dioxide nanoparticles have shown significant efficacy in this respect and have already been incorporated in commercial products such as cosmetics, paints, self-cleaning glasses and cement for construction products.

Doping TiO_2 with nitrogen has been shown to increase light absorption but does not necessarily increase catalytic activity. Experiments confirmed, however, that doped titania is indeed catalytically active under visible light. Catalytic coatings based on these doped titania nanoparticles are currently under development for environmental and public health applications. Doping with noble metals can increase the efficiency of TiO_2 by harnessing energy from the low-energy incident photons. However, there is a need for careful selection of the dopants as well as the dopant levels. Cheap, readily available noble metals are more preferable as dopants. Composites of TiO_2 with CNTs have led to enhanced photoactivity only at specific and appropriate CNT/ TiO_2 ratios. The development of instruments that can probe directly at the nanometre scale has sparked a technological revolution that makes it possible to analyse materials at such scale. More fundamental research to better understand naturally occurring processes at the nanoscale and their relation to macro-scale phenomena is still needed. There is a need for developing systems that are capable of harnessing the power of natural systems to drive the important chemical processes on the material surfaces. Possibilities of translating these technologies into industrial-level processes still need to be established.

Although photocatalysis at both laboratory and pilot scale has been shown to be an effective method for water decontamination, further research is needed to control the treatment in order to eliminate toxic products. There is a need for investigation into the potential risks associated with the use of nanoparticles for water purification. Additionally, issues such as the long-term fate of the nanoparticles in the environment, the detection of nanoparticles in various

environmental media, safe disposal, the life-cycle analysis and many others still need to be addressed.

2.12 REFERENCES

1. *Africa's Water Quality – A Chemical Science Perspective*. A report by the Pan Africa Chemistry Network (PACN) supported by the Royal Society of Chemistry (RSC) and Syngenta, UK. . March 2010.
2. United Nations Population Fund (2009). *State of World Population 2009. Facing a Changing World: Women, Population and Climate*.
3. WHO/UNICEF (2008). *A Snapshot of Drinking Water and Sanitation in Africa*. WHO/UNICEF Joint Monitoring Programme for Water Supply and Sanitation.
4. WHO/UNICEF (2008). *A Snapshot of Sanitation in Africa*. WHO/UNICEF Joint Monitoring Programme for Water Supply and Sanitation.
5. Dharmendra K.T., Behari J. and Prasenjit S. (2008). Application of nanoparticles in waste water treatment. *World Appl. Sci. J.* **3** (3), 417 – 433.
6. Biswas P. and Wu C.Y. (2005). Nanoparticles and the environment. *J. Air Waste Manage. Assoc.* **55**, 708 – 746.
7. Kaneko M. and Okura I. (2002). *Photocatalysis: Science and Technology*. Springer-Verlag, Berlin, Heidelberg, New York. pp 1 – 2.
8. Zein U. and Landman U. (2008). *Nanocatalysis: Nanoscience and Technology*. Springer-Verlag, Berlin, Heidelberg, New York pp 245 – 265.
9. Gratzel M. (2001). Photoelectrochemical cells. *Nature* **414**, 338 – 344.
10. Fujishima A. and Honda K. (1972). Electrochemical photolysis of water at a semiconductor electrode. *Nature*, **238**, 37 – 38.

11. Formenti M., Juillet F., Meriaudeau P. and Teichner S.J. (1971). Heterogeneous photocatalysis for partial oxidation of paraffins. *Chem. Technol.* 1, 680 – 686.
12. Herrmann J.M. (1999). Heterogeneous photocatalysis: Fundamentals and applications to the removal of various types of aqueous pollutants. *Catal. Today* 53, (1), 115 – 129.
13. Hoffmann M.R., Martin S.T., Choi W. and Bahnemann D.W. (1995). Environmental applications of semiconductor photocatalysis. *Chem. Rev.* 95, (1), 69 – 96.
14. Linsebigler A. L., Lu G. and Yates J.T. (1995). Photocatalysis on TiO₂ surfaces: Principles, mechanisms, and selected results. *Chem. Rev.* 95, (3), 735 – 758.
15. Mills A. and Le Hunte S. (1997). An overview of semiconductor photocatalysis. *J. Photochem. Photobiol. A* 108, 1 – 35.
16. Fujishima A., Rao T.N. and Tryk D.A. (2000). Titanium dioxide photocatalysis. *J. Photochem. Photobiol. C* 1, (1), 1 – 21.
17. Alonso M.D.H., Fresno F., Suarez S. and Coronado J.M. (2009). Development of alternative photocatalysts to TiO₂: Challenges and opportunities. *Energy Environ. Sci.* 2, 1231 – 1257.
18. Khataee A.R., Kasiri M.B. and Alidokht L. (2011). Application of response surface methodology in the optimisation of photocatalytic removal of environmental pollutants using nanocatalysts. *Environ. Technol.* 32, 1669 – 1684.
19. Gupta S.M. and Tripathi M. (2011). A review of TiO₂ nanoparticles. *Chin. Sci. Bull.* 56, (16) 1639 – 1657.

20. Chen X. and Mao S.S. (2007). Titanium dioxide nanomaterials: Synthesis, properties, modifications, and applications. *Chem. Rev.* 107, 2891 – 2959.
21. Sun Q. and Xu Y. (2010). Evaluating intrinsic photocatalytic activities of anatase and rutile TiO₂ for organic degradation in water. *J. Phys. Chem. C* 114, 18911 – 18918
22. Yao Y. (2009). Titanium Dioxide/Carbon Nanotube Composite for Photoreactive Membrane Filtration. Ph.D. Thesis. Northwestern University, Chicago, Illinois, USA. p 42.
23. Sclafani A., Palmisano L. and Schiavello M. (1990). Influence of the preparation methods of titanium dioxide on the photocatalytic degradation of phenol in aqueous dispersion. *J. Phys. Chem.* 94, 829 – 832.
24. Shon H., Phuntsho S., Okour Y., Cho D.L., Kim K.S., Li H.J., Na S., Kim J.B. and Kim J.H. (2008). Visible light responsive titanium dioxide (TiO₂). *J. Korean Ind. Eng. Chem.* 19, (1), 1 – 16.
25. Kazuhito H., Hiroshi I. and Akira F. (2005). TiO₂ photocatalysis: A historical overview and future prospects. *Japanese J. Appl. Phys.* 44, (12) 8269 – 8285.
26. Turchi C.S. and Ollis D.F. (1990). Photocatalytic degradation of organic water contaminants: Mechanisms involving hydroxyl radical attack. *J. Catal.* 122, (1), 178 – 192.
27. Chong M.N., Jin B., Chow C.W.K. and Saint C. (2010). Recent developments in photocatalytic water treatment technology: A review. *Water Res.* 44, 2997 – 3027.
28. Dong F., Guo S., Wang H., Li X. and Wu Z. (2011). Enhancement of the visible light photocatalytic activity of C-doped TiO₂ nanomaterials prepared by a green synthetic approach. *J. Phys. Chem. C* 115, (27), 13285 – 13292.

29. Tian G., Chen Y., Pan K., Wang D., Zhou W., Ren Z. and Fu H. (2010). Efficient visible light-induced degradation of phenol on N-doped anatase TiO₂ with large surface area and high crystallinity. *Appl. Surface Sci.* 256, 3740 – 3745.
30. Romero M., Blanco J., Sanchez B., Vidal A., Malato S., Cardona A.I. and Garcia E. (1999). Solar photocatalytic degradation of water and air pollutants: challenges and perspectives. *Solar Energy* 66, (2), 169 – 182.
31. Sakthivel S. and Kisch H. (2003). Day light photocatalysis by carbon-modified titanium dioxide. *Angew. Chem. Int. Ed.* 42, 4908 – 4911.
32. Hajkova P., Spatenka P., Krumeich J., Exnar P., Kolouch A. and Matousek J. (2009). The influence of surface treatment on photocatalytic activity of PE CVD TiO₂ thin films. *Plasma Process. Polym.* 6, S735 - S740.
33. Augugliaro V., Litter M., Palmisano L. and Soria J. (2006). The combination of heterogeneous photocatalysis with chemical and physical operations: A tool for improving the photo-process performance. *J. Photochem. Photobiol. C: Photochem. Rev.* 7, 127 – 144.
34. Malato S., Blanco J., Vidal A., Alarcon D., Maldonado M.I., Caceres J. and Gernjak W. (2003). Applied studies in solar photocatalytic detoxification: An overview. *Solar Energy*, 75, (4), 329 – 336.
35. Parent Y., Blake D., Magrini B.K., Lyons C., Turchi C., Watt A., Wolfrum E. and Praire M. (1996). Solar photocatalytic process for the purification of water: State of development and barriers to commercialisation. *Solar Energy* 56, 429 – 437.
36. Ghorai T.K. (2011). Photocatalytic degradation of 4-Chlorophenol by CuMoO₄-Doped TiO₂ nanoparticles synthesized by chemical route. *Open J. Phys. Chem.* 1, 28 – 36.

37. Gandhe A.R. and Fernandes J.B. (2005). A simple method to synthesize visible light active N-doped anatase (TiO_2) photocatalyst. *Bull. Catal. Soc. India* 4, 131 – 134.
38. Jang J.S., Kim H.G., Ji S.M., Bae S.W., Jung J.H., Shon B.H. and Lee J.S. (2006). Formation of crystalline $\text{TiO}_{2-x}\text{N}_x$ and its photocatalytic activity. *J. Solid State Chem.* 179, 1067–1075.
39. Asahi R., Morikawa T., Ohwaki T., Aoki K. and Taga Y. (2001). Visible-light photocatalysis in nitrogen-doped titanium oxides. *Sci.* 293, 269 – 271.
40. Di Valentin C., Finazzi E., Pacchioni G., Selloni A., Livraghi S., Paganini M.C. and Giamello E. (2007). N-doped TiO_2 : Theory and experiment. *Chem. Phys.* 339, 44 – 56
41. Morikawa T., Asahi R., Ohwaki T., Aoki K., Suzuki K. and Taga Y. (2005). Visible light photocatalyst-Nitrogen doped titanium dioxide. *R & D Rev. Toyota CRDL* 40, (3), 45 – 50.
42. Spadavecchia F., Cappelletti G., Ardizzone S., Bianchi C.L., Cappelli S., Oliva C., Scardi P., Leoni M. and Fermo P. (2010). Solar photoactivity of nano-N- TiO_2 from tertiary amine: role of defects and paramagnetic species. *Appl. Catal. B Environ.* 96, (3-4), 314 – 322.
43. Yu H., Zheng X., Yin Z., Tao F., Fang B. and Hou K. (2007). Preparation of Nitrogen-doped TiO_2 nanoparticle catalyst and its catalytic activity under visible light. *Chin. J. Chem. Eng.* 15, (6), 802 – 807.
44. Qin H.L., Gu G.B. and Liu S. (2008). Preparation of nitrogen-doped titania with visible-light activity and its application. *C. R. Chimie* 11 95 – 100.
45. Todorova N., Giannakopoulou T., Romanos G., Vaimakis T., Yu J. and Trapalis C. (2008). Preparation of fluorine doped TiO_2 photocatalysts with controlled crystalline structure. *Int. J. Photoenergy*, DOI: 10.1155/2008/534038.

46. Xie Y., Zhao Q., Zhao X.J. and Li Y. (2007). Low temperature preparation and characterisation of N-doped and N-S-codoped TiO₂ by sol-gel route. *Catal. Lett.* 118, 231–237.
47. Irie H., Watanabe Y. and Hashimoto K. (2003). Nitrogen-concentration dependence on photocatalytic activity of TiO_{2-x}N_x powders. *J. Phys. Chem. B* 107, 5483 - 5486.
48. Zhao Z. and Liu Q. (2008). Mechanism of higher photocatalytic activity of anatase TiO₂ doped with nitrogen under visible-light irradiation from density functional theory calculation. *J. Phys. D. Appl. Phys.* 41, 1 – 10.
49. Ihara T., Miyoshi M., Triyama Y., Marsumato O. and Sugihara S. (2003). Visible-light-active titanium oxide photocatalyst realized by an oxygen-deficient structure and by nitrogen doping. *Appl. Catal. B* 42, 403 – 409.
50. Lee S., Yun C.Y., Hahn M.S., Lee, J. and Yi J. (2008). Synthesis and characterisation of carbon-doped titania as a visible-light-sensitive photocatalyst. *Korean J. Chem. Eng.* 25, (4), 892 – 896.
51. Cheng Y., Sun H., Jin W. and Xu N. (2007). Photocatalytic degradation of 4-chlorophenol with combustion synthesized TiO₂ under visible light irradiation. *Chem. Eng. J.* 128, 127–133
52. Lettmann C., Hildebrand K., Kisch H., Macyk W. and Maier W.F. (2001). Visible light photodegradation of 4-chlorophenol with a coke-containing titanium dioxide photocatalyst. *Appl. Catal. B* 32, 215 – 227.
53. Gorska P., Zaleska A., Suska A. and Hupka J. (2009). Photocatalytic activity and surface properties of carbon-doped titanium dioxide. *Physicochem. Probl. Miner. Process.* 43, 21 – 30.
54. Dvoranova D., Brezova V., Mazur M. and Malati M.A. (2002). Investigations of metal-doped titanium dioxide titanium dioxide photocatalysts. *Appl. Catal. B: Environ.* 37, 91 – 105.

55. Chan S.H.S., Wu T.Y., Juan J.C. and Teh C.Y. (2011). Recent developments of metal oxide semiconductors as photocatalysts in advanced oxidation processes (AOPs) for treatment of dye waste-water. *J. Chem. Technol. Biotechnol.* 86, 1130 – 1158.
56. Li Y., Peng S., Jiang F., Lu G. and Shuben Li S. (2007). Effect of doping TiO₂ with alkaline-earth metal ions on its photocatalytic activity. *J. Serb. Chem. Soc.* 72, (4), 393 – 402.
57. Liu W., Zhao X., Cao L., Zou B., Zhang G., Lu L. and Cui H. (2009). A facile method for fabrication of highly ordered hollow Ag/TiO₂ nanostructure and its photocatalytic activity. *Mater. Lett.* 63, 2456 – 2458.
58. Devi L.G. and Murthy B.N. (2008). Characterisation of Mo doped TiO₂ and its enhanced photo catalytic activity under visible light. *Catal. Lett.* 125, 320 – 330.
59. Maicu M., Hidalgo M.C., Colon G. and Navio J.A. (2011). Comparative study of the photodeposition of Pt, Au and Pd on pre-sulphated TiO₂ for the photocatalytic decomposition of phenol. *J. Photochem. Photobiol. A: Chem.* 217, 275 – 283.
60. Panagiotopoulou P. and Kondarides D.I. (2004). Effect of morphological characteristics of TiO₂-supported noble metal catalysts on their activity for the water–gas shift reaction. *J. Catal.* 225, 327 – 336.
61. Choi J., Park H. and Michael R. Hoffmann M.R. (2010). Effects of single metal-ion doping on the visible-light photoreactivity of TiO₂. *J. Phys. Chem. C* 114, 783 – 792.
62. Kim S.B., Lee J.Y., Jang H.T., Cha W.S. and Hong S.C. (2003). Enhanced photocatalytic activity of TiO₂ by metal doping for degradation of VOCs in air. *J. Ind. Eng. Chem.* 9, (4), 440 – 446.

63. Riyas S., Krishnan G. and Das P.N.M. (2008). Liquid phase photooxidation of toluene in the presence of transition metal oxide doped titania. *J. Braz. Chem. Soc.* 19, (5), 1023 – 1032.
64. Park Y., Kang S.H. and Cho W. (2011). Exfoliated and reorganized graphite oxide on titania nanoparticles as an auxiliary co-catalyst for photocatalytic solar conversion. *Phys. Chem. Chem. Phys.* 13, 9425 – 9431.
65. Linsebigler A.L., Lu G., and Yates J.T., Jr. (1995). Photocatalysis on TiO₂ surfaces: Principles, mechanisms, and selected results. *Chem. Rev.* 95, 735 – 758.
66. Wu M.C., Sapi A., Avila A., Szabo M., Hiltunen J., Huuhtanen M., Toth G., Kukovecz A., Konya Z., Keiski R., Su W.F., Jantunen H. and Kordas K. (2011). Enhanced photocatalytic activity of TiO₂ nanofibers and their flexible composite films: Decomposition of organic dyes and efficient H₂ generation from ethanol–water mixtures. *Nano Res.* 4, (4), 360 – 369.
67. Drummond T.J. (1999). Work functions of the transition metals and metal silicides. *J. Appl. Phys.* 1 – 34.
68. Lee S.K. and Mills A. (2003). Platinum and palladium in semiconductor photocatalytic systems; Factors affecting the purification of water and air. *Platinum Metals Rev.* 47, (2), 61 – 72.
69. Kowalska E., Mahaney O.O.P., Abe R. and Ohtani B. (2010). Visible-light-induced photocatalysis through surface plasmon excitation of gold on titania surfaces. *Phys. Chem. Chem. Phys.* 12, 2344 – 2355.
70. Cao Y., Tan H., Shi T., Tang T. and Li J. (2008). Preparation of Ag-doped TiO₂ nanoparticles for photocatalytic degradation of acetamiprid in water. *J. Chem. Technol. Biotechnol.* 83, 546 – 552.
71. Dai Z.M., Burgeth G., Parrino F. and Kisch H. (2009). Visible light photocatalysis by a titania–rhodium(III) complex. *J. Organomet. Chem.* 694, 1049 – 1054.

72. Chen H.W., Ku Y. and Kuo Y.L. (2007). Effect of Pt/TiO₂ characteristics on temporal behaviour of o-cresol decomposition by visible light-induced photocatalysis. *Water Res.* 41, 2069 – 2078
73. Kowalska E., Abe R. and Ohtani B. (2009). Visible light-induced photocatalytic reaction of gold-modified titanium(IV) oxide particles: action spectrum analysis. *Chem. Commun.* (2), 241 – 243.
74. Rupa A.V., Divakar D. and Sivakumar T. (2009). Titania and noble metals deposited titania catalysts in the photodegradation of tartrazine. *Catal. Lett.* 132, 259 – 267.
75. Mogyrosi K., Kmetyko A., Czirbus N., Vereb G., Sipos P. and Dombi A. (2009). Comparison of the substrate dependent performance of Pt-, Au- and Ag-doped TiO₂ photocatalysts in H₂ production and in decomposition of various organics. *React. Kinet. Catal. Lett.* 98, (2), 215 – 225.
76. Vinu R. and Madras G. (2008). Synthesis and photoactivity of Pd substituted nano-TiO₂. *J. Mol. Catal. A: Chem.* 291, 5 – 11.
77. Choi W., Termin A. and Hoffmann M.R. (1994). The role of metal ion dopants in quantum-sized TiO₂: Correlation between photoreactivity and charge carrier recombination dynamics. *J. Phys. Chem.* 98, 13669 – 13679.
78. Vu A.T., Nguyen Q.T., Bui T.H.L., Tran M.C., Dang T.P. and Tran T.K.H. (2010). Synthesis and characterisation of TiO₂ photocatalyst doped by transition metal ions (Fe³⁺, Cr³⁺ and V⁵⁺). *Adv. Nat. Sci.: Nanosci. Nanotechnol.* DOI:10.1088/2043-6254/1/1/015009.
79. Devi L.G., Murthy B.N. and Kumar S.G. (2009). Photocatalytic activity of V⁵⁺, Mo⁶⁺ and Th⁴⁺ doped polycrystalline TiO₂ for the degradation of chlorpyrifos under UV/solar light. *J. Mol. Catal. A: Chem.* 308, 174 – 181.

80. Sanchez E. and Lopez T. (1995). Effect of the preparation method on the bandgap of titania and platinum-titania sol-gel materials. *Mater. Lett.* 25, (5-6), 271 – 275.
81. Bakardjieva S.S. and Murafa N. (2009). Preparation and photocatalytic activity of rare earth doped TiO₂ nanoparticles. *Mater. Chem. Phys.* 114, (1), 217 – 226.
82. Xu A.W., Gao Y. and Liu H.Q. (2002). The preparation, characterisation, and their photocatalytic activities of rare-earth-doped TiO₂ nanoparticles. *J. Catal.* 207, (2), 151 – 157.
83. El-Bahy Z.M., Ismail A.A. and Mohamed R.M. (2009). Enhancement of titania by doping rare earth for photodegradation of organic dye (Direct Blue). *J. Hazard. Mater.* 166, (1), 138 – 143.
84. Primo A., Corma A. and Garcia H. (2011). Titania supported gold nanoparticles as photocatalyst. *Phys. Chem. Chem. Phys.* 13, 886 – 910.
85. Liu H., Yu L., Chen W. and Yingyi Li Y. (2012). The progress of TiO₂ nanocrystals doped with rare earth ions. *J. Nanomater.* DOI:10.1155/2012/235879.
86. Hwang D.W., Lee, J.S. Li W. and Oh S.H. (2003). Electronic band structure and photocatalytic activity of Ln₂Ti₂O₇ (Ln = La, Pr, Nd). *J. Phys. Chem. B* 107, (21), 4963 – 4970.
87. Li Y., Ma G., Peng S., Lu G. and Li S. (2008). Boron and nitrogen co-doped titania with enhanced visible-light photocatalytic activity for hydrogen evolution. *Appl. Surface Sci.* 254, 6831 – 6836.
88. Xing M., Wu Y., Zhang J. and Chen F. (2010). Effect of synergy on the visible light activity of B, N and Fe co-doped TiO₂ for the degradation of MO. *Nanoscale* 2, 1233 – 1239.

89. Li Q., Rongcai R., Mintz E.A. and Shang J.K. (2007). Enhanced visible-light photocatalytic degradation of humic acid by palladium-modified nitrogen-doped titanium oxide. *J. Am. Ceram. Soc.* 90, (12), 3863 – 3868.
90. Li D., Chen Z., Chen Y., Li W., Huang H., He Y. and Fu X. (2008). A new route for degradation of volatile organic compounds under visible light: Using the bifunctional photocatalyst Pt/TiO_{2-x}N_x in H₂-O₂ atmosphere. *Environ. Sci. Technol.* 42, 2130–2135.
91. Henderson M.A. (2011). A surface science perspective on TiO₂ photocatalysis. *Surface Sci. Rep.* 66, (6-7), 185 – 297.
92. Wen C., Zhu Y.J., Kanbara T., Zhu H.Z. and Xiao C.F. (2009). Effects of I and F codoped TiO₂ on the photocatalytic degradation of methylene blue. *Desalination* 249, (2), 621 – 625.
93. Niishiro R., Konta R., Kato H., Chun W. J., Asakura K. and Kudo A. (2007). Photocatalytic O₂ evolution of rhodium and antimony-codoped rutile-type TiO₂ under visible light irradiation. *J. Phys. Chem. C* 111, (46), 17420 – 17426.
94. Yang X., Cao C., Hohn K., Erickson L, Maghirang R., Hamal D. and Klabunde K. (2007). Highly visible-light active C- and V-doped TiO₂ for degradation of acetaldehyde. *J. Catal.* 252, 296 – 302.
95. Yang J., Dai J. and Li J. (2011). Synthesis, characterisation and degradation of Bisphenol A using Pr, N co-doped TiO₂ with highly visible light activity. *Appl. Surface Sci.* 257, 8965 – 8973.
96. Wu P., Xie R., Imlay K. and Shang J. (2010). Visible-light-induced bactericidal activity of titanium dioxide codoped with nitrogen and silver. *Environ. Sci. Technol.* 44, 6992 – 6997.
97. Yang X., Cao C., Erickson L., Hohn K., Maghirang R. and Klabunde K. (2008). Synthesis of visible-light-active TiO₂-based photocatalysts by carbon and nitrogen doping. *J. Catal.* 260, (1), 128 – 133.

98. Tan Y.N., Wong C.L. and Mohamed A.R. (2011). An overview on the photocatalytic activity of nano-doped-TiO₂ in the degradation of organic pollutants. *ISRN Mater. Sci.* DOI:10.5402/2011/261219.
99. Karousis N., Tagmatarchis N. and Tasis D. (2010). Current progress on the chemical modification of carbon nanotubes. *Chem. Rev.* 110, 5366 – 5397.
100. Feng J.M., Wang R., Li Y.L., Zhong X.H., Cui L., Guo Q.J. and Hou F. (2010). One-step fabrication of high quality double-walled carbon nanotube thin films by a chemical vapour deposition process. *Carbon* 48, (13), 3817 – 3824.
101. Yang K., Han H., Pan X., Chen N. and Gu M. (2008). The effect of chemical treatment on the crystallinity of multi-walled carbon nanotubes. *Journal of Phys. Chem. Solids* 69, (1), 222 – 229.
102. Eder D. (2010). Carbon nanotube-inorganic hybrids. *Chem. Rev.* 110, 1348 – 1385.
103. Schnorr J.M. and Swager T.M. (2011). Emerging applications of carbon nanotubes. *Chem. Mater.* 23, (3), 646 – 657.
104. Lynam C., Minett A.I., Habas S.E., Gambhir S. and Officer D.L. (2008). Functionalising carbon nanotubes. *Int. J. Nanotechnol.* 5, (2-3), 331 – 351.
105. Thess A., Lee R., Nikolaev P., Dai H., Petit P., Robert J., Xu C., Lee Y.H., Kim S.G., Rinzler A.G., Colbert D.T., Scuseria G.E., Tomanek D., Fischer J.E. and Smalley R.E. (1996). Crystalline ropes of metallic carbon nanotubes. *Sci.* 273, (5274) 483 – 487.
106. Liang Y.T., Vijayan B.K., Lyandres O., Gray K.A. and Hersam M.C. (2012). Effect of dimensionality on the photocatalytic behaviour of carbon-titania nanosheet composites: Charge transfer at nanomaterial interfaces. *J. Phys. Chem. Lett.* 3, (13), 1760 – 1765.

107. Xu Y.J., Zhuang Y. and Fu X. (2010). New insight for enhanced photocatalytic activity of TiO₂ by doping carbon nanotubes: A case study on degradation of benzene and methyl orange. *J. Phys. Chem. C* 114, 2669 – 2676.
108. Akhavan O., Azimirad R., Safad S. and Larijani M.M. (2010). Visible light photo-induced antibacterial activity of CNT-doped TiO₂ thin films with various CNT contents. *J. Mater. Chem.* 20, 7386 – 7392.
109. Wang W., Serp P., Kalck P. and Faria J.L. (2005). Visible light photodegradation of phenol on MWNT-TiO₂ composite catalysts prepared by a modified sol-gel method. *J. Mol. Catal. A: Chem.* 235, 194 – 199.
110. Frank O., Kalbac M., Kavan L., Zuckalova M., Prochazka J., Klementova M. and Dunsch L. (2007). Structural properties and electrochemical behaviour of CNT-TiO₂ nanocrystal heterostructures. *Phys. Stat. Sol. (b)* 244, (11), 4040 – 4045. DOI 10.1002/pssb.200776158.
111. Ziegmann M. and Fritz H. Frimmel F.H. (2010). Photocatalytic degradation of clofibric acid, carbamazepine and iomeprol using conglomerated TiO₂ and activated carbon in aqueous suspension. *Water Sci. Technol.* 61, (1) 273 – 281.
112. Gao B., Chen G.Z. and Puma G. L. (2009). Carbon nanotubes/titanium dioxide (CNTs/TiO₂) nanocomposites prepared by conventional and novel surfactant wrapping sol-gel methods exhibiting enhanced photocatalytic activity. *Appl. Catal. B: Environ.* 89, 503 – 509.
113. Dong H. and Lu K. (2009). Attaching titania nanoparticles onto shortened carbon nanotubes by electrostatic attraction. *Int. J. Appl. Ceram. Technol.* 6, (2), 216 – 222.
114. Huang B.S., Chang F.Y. and Wey M.Y. (2010). An efficient composite growing N-doped TiO₂ on multi-walled carbon nanotubes through sol-gel process. *J. Nanopart. Res.* 12, (7), 2503 – 2510.

115. Zhang K. and Oh W.C. (2010). Kinetic study of the visible light-induced sonophotocatalytic degradation of MB solution in the presence of Fe/TiO₂-MWCNT Catalyst. *Bull. Korean Chem. Soc.* 31, (6) 1589 – 1595.
116. Yu Y., Yu J.C., Chan C.Y., Che Y.K., Zhao J.C., Ding L., Ge W.K. and Wong P.K. (2005). Enhancement of adsorption and photocatalytic activity of TiO₂ by using carbon nanotubes for the treatment of azo dye. *Appl. Catal. B: Environ.* 61, 1 – 11.
117. Chen C.Y., Wu S.J., Wu C.G., Chen J.G. and Ho K.C. (2006). A ruthenium complex with super high light-harvesting capacity for dye-sensitized solar cells. *Angew. Chem. Int. Ed.* 45, 5822 – 5825.
118. Dosch H. and Van de Voorde M.H. (2009). *GENNESYS White Paper. A New European Partnership between Nanomaterials Science and Nanotechnology and Synchrotron Radiation and Neutron Facilities.* Max-Planck-Gesellschaft, Stuttgart, Germany. pp 219 – 221. ISBN 978-3-00-027338-4.
119. Argyle V. and Robinson B. (2006). Are Nanoparticles Safe? Chemistry in New Zealand, 12-15.

CHAPTER 3

EXPERIMENTAL METHODOLOGY

3.1 INTRODUCTION

This chapter gives a detailed account of the experimental procedures and characterisation techniques followed in achieving the objectives of this study.

3.2 REAGENTS AND SOLVENTS

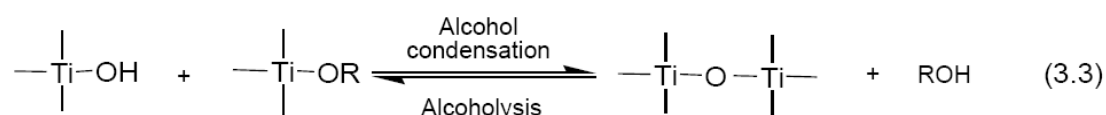
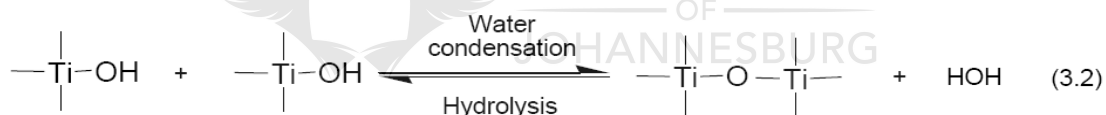
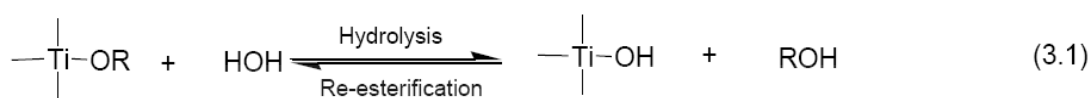
Unless otherwise specified, all chemicals and reagents were purchased from credible suppliers and used without further purification. The purity of such chemicals was ascertained to be acceptable for the intended reactions. Deionised water was used for all calibration solution preparations.

3.3 FABRICATION OF NANOPARTICLES

Self-assembly is one of the common techniques for fabricating nanoparticles. In this process molecular sub-units spatially organise into well-defined supra-molecular structures, creating advanced materials out of nanoparticle building blocks. However, controlling particle size and shape during synthesis is still a major challenge. Nevertheless, some physical and solid state chemical methods have been developed for synthesising these nanoparticles.¹ These include the sol-gel method, solvo-thermal process, reverse micellar, hydrothermal method, sputtering and implantation techniques and electrochemical methods.² Of these methods, the sol-gel process is regarded as a promising alternative due to its low sintering temperature, versatility of processing and homogeneity at molecular level. Sol-gel processing is a wet chemical synthesis approach that can be used to generate nanoparticles by gelation, precipitation and hydrothermal treatment.

3.3.1 Sol-gel method for TiO₂ nanostructures

Titania (TiO₂) nanoparticles can be synthesised by the sol-gel method from hydrolysis of titanium precursors. This process normally proceeds via an acid or base catalysed hydrolysis step of titanium(IV) alkoxide followed by condensation. The development of Ti-O-Ti chains is favoured under conditions of low water content, low hydrolysis rates and excess titanium alkoxide in the reaction mixture (Equations (3.1) to (3.3)). Three-dimensional polymeric skeletons with close packing result from the development of Ti-O-Ti chains. Formation of Ti(OH)₄ is favoured by high hydrolysis rates under medium amount of water. Presence of a large quantity of Ti-OH and insufficient development of three-dimensional polymeric skeletons lead to loosely packed first-order particles.³



Synthesis is followed by drying of the gels or precipitates to remove the water or alcohol to yield the powdered material. This amorphous powder is then calcined in air to form crystallites of TiO₂. The structure and size of TiO₂ crystallites significantly depends on the calcination temperature. Thermal treatment of TiO₂ gels at higher temperature promotes phase transformation from thermodynamically metastable anatase to the more stable and condensed rutile phase. As dehydration occurs during heat treatment, crystallites grow to dimensions larger than those of the original particles.³

3.3.2 Modified sol-gel method for N, PGM co-doped TiO₂

A modified sol-gel method was used to synthesise N, PGM co-doped TiO₂ and CNT/N, PGM co-doped TiO₂. In general, the titanium precursor, titanium isopropoxide was added to a solvent, 2-propanol. The mixture was stirred to form the titanium alcoholate solution. A solution of ammonium hydroxide, the N source, containing the appropriate amount of the PGM dopant was then slowly added to the titanium alcoholate solution with stirring to form the hydrolysed sample. This sample was further stirred until a homogenous sol-gel was formed. The sol-gel was then dried at 80°C to form the amorphous powder which was then calcined to give the crystalline co-doped material (**Figure 3.1**).

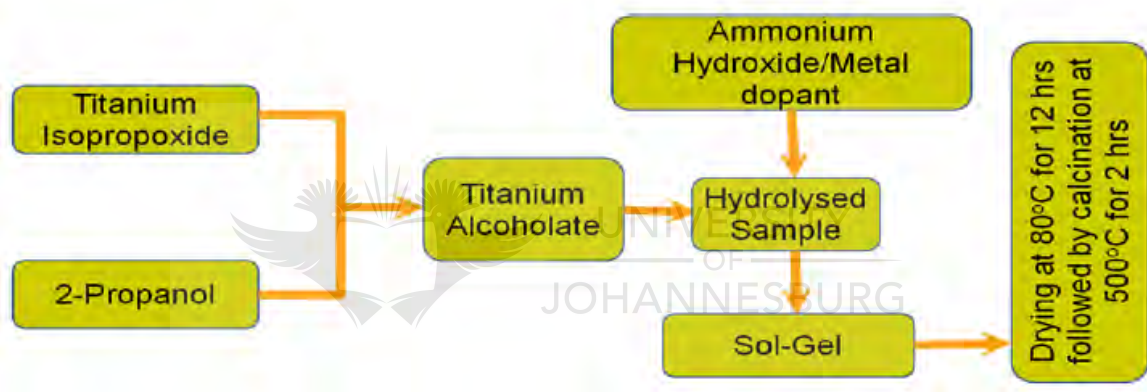


Figure 3.1 The modified sol-gel method for synthesis of N, PGM co-doped TiO₂

3.4 CCVD SYNTHESIS OF DOUBLE WALLED CARBON NANOTUBES (DWCNTs)

3.4.1 Catalyst preparation

The catalyst with the elemental composition Mg_{0.94}Co_{0.05}Mo_{0.01}O was prepared by combustion of metal nitrates of Mg and Co and hexaammonium heptamolybdate tetrahydrate in the presence of citric acid.⁴ In a typical experiment Mg(NO₃)₂·6H₂O (70.53g), Co(NO₃)₂·6H₂O (4.29g), (NH₄)₆Mo₇O₂₄·4H₂O (3.72g) and citric acid (170.16g) were dissolved in deionised water and the solution was heated at 150°C with stirring to concentrate it by evaporating the water. The heating and stirring

were continued until the gel turned purplish in colour. The solution was then placed in a crucible and heated at 550°C overnight resulting in a light and fluffy khaki brown oxide. This oxide was finely ground and used as a catalyst in the synthesis of DWCNTs. Citric acid was used as fuel in the combustion process.

3.4.2 Synthesis of DWCNTs

Methane gas, used as the carbon source, was decomposed on the metal catalyst surface in the presence of hydrogen, a process gas. In a typical experiment, the catalyst (0.5 g) was loaded into a ceramic boat which was then placed in a tubular quartz tube connected to the gases and heated in an electric furnace at 1 000°C for 2 h. Hydrogen gas (H₂) and methane gas (CH₄) were passed through the catalyst at constant flow rates of 50 ml/min and 200 ml/min, respectively. After 2 h the furnace and methane gas were switched off and hydrogen flow maintained until the furnace cooled down to about 400°C. The hydrogen gas supply was then turned off and the ceramic boat containing the DWCNTs was removed from the furnace. The as-prepared or pristine DWCNTs were obtained.

3.4.3 Purification of DWCNTs

The pristine DWCNTs contain impurities such as graphite nanoparticles, amorphous carbon, smaller fullerenes and metal catalyst particles. These impurities have to be removed from the carbon nanotubes before they can be used for applications as composite material. They were sonicated in concentrated HCl (150 ml) for 3h. Sonication frees the nanotubes from the unreacted metal particles making it easier for the acid to remove the impurities. The purified DWCNTs were washed several times with deionised water and filtered until the filtrate was neutral and then dried in an oven at 90°C overnight.

3.4.4 Functionalisation of DWCNTs

Purified DWCNTs (2 g) were sonicated in a mixture of concentrated H₂SO₄ and HNO₃ (1:3 by volume) at room temperature (22°C) for 3 h. The harsh oxidation conditions were meant to introduce carboxyl, hydroxyl or carbonyl groups on the

DWCNTs. These groups provide anchoring points for the covalent attachment of TiO_2 during the sol-gel process. The oxidised DWCNTs were then washed several times with deionised water and filtered until the filtrate pH was close to pH 7. The residual DWCNTs were dried at 90°C overnight.

3.5 SYNTHESIS OF MULTI WALLED CARBON NANOTUBES (MWCNTs)

MWCNTs were synthesised using the nebulised-spray-pyrolysis method followed by acid functionalisation. Ferrocene (2.00 g) was added to toluene (50 mL) and placed in an atomisation chamber. This solution was nebulised using a high-frequency ultrasonic beam with a frequency of 1.54 MHz. A geyser resulted at the surface that generated a spray which was carried into the quartz tube placed in the furnace. The temperature of the furnace was maintained at 900°C . Ultra-pure argon was used as a carrier gas and the gas flow rate was maintained at 500 mL/min using a gas flow controller. The pyrolysis was carried out for 45 min. After the reaction, the flow rate of argon was reduced to 80 mL/min. A black film of MWCNTs was formed on the inner surface of the tubing which was removed with a brush after the tube had cooled down.

3.5.1 Purification of MWCNTs

The MWCNTs were purified by heating in air at 500°C for 1 h to remove amorphous carbon and multi-shell carbon nanocapsules. The black product was allowed to cool and then immersed in concentrated hydrochloric acid (100 mL) to remove most of the iron particles. The product was then washed with distilled water and thereafter dried in an oven at 150°C for 12 h.

3.5.2 Functionalisation of MWCNTs

Purified MWCNTs were functionalised by heating under reflux in concentrated nitric acid (50 mL) for 6 h. This procedure removed the remaining iron particles and introduced some functional groups onto the surface of the MWCNTs. The functional groups included the hydroxyl and carboxyl groups. After the acid treatment, MWCNTs were washed with distilled water until the pH of the filtrate

approached pH 7. The resulting MWCNTs were then filtered and dried at 60°C overnight in air and further used for the preparation of the nanocomposites.

3.5.3 Modified sol-gel method for synthesis of carbon nanotube/nitrogen, platinum group metal (CNT/N, PGM) co-doped TiO₂ nanocomposites

An appropriate amount of CNTs was sonicated in 2-propanol (50 mL) for 30 min before addition of the titanium isopropoxide (10 mL). The mixture was stirred to form the CNT/titanium alcoholate solution. A solution of ammonium hydroxide (25%, 12 mL), the N source, containing the appropriate amount of the PGM dopant was then slowly added to the CNT/titanium alcoholate solution under stirring to form the hydrolysed sample. This sample was further stirred until a homogenous sol-gel was formed. The sol-gel was then dried at 80°C to form the amorphous powder which was then calcined to give the CNT/N, PGM co-doped TiO₂ nanocomposite material.

3.6 CHARACTERISATION OF MATERIALS

Nanoparticle characterisation is necessary to establish better understanding and control of nanoparticle syntheses and applications. Characterisation is done by using a variety of different techniques, mainly drawn from the materials science field (**Figure 3.2**).

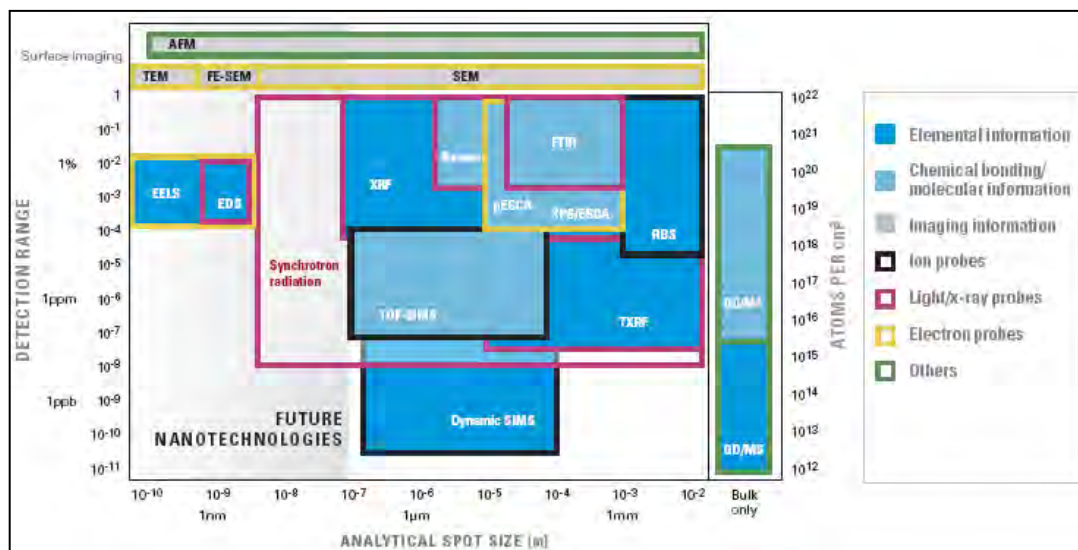


Figure 3.2 Elemental analysis techniques showing detection range, sensitivity and lateral resolution ⁵

3.6.1 Fourier transform infrared (FT-IR) spectroscopy

Infrared spectroscopy involves the use of photons that induce transitions between vibrational states in molecules and functional groups in the infrared frequency range ($10\,000\text{ cm}^{-1}$ to 100 cm^{-1}). The technique exploits the fact that molecules and functional groups have specific frequencies at which they absorb energy, thereby enabling determination of a sample's composition from its IR spectrum. The entire IR spectrum of a sample can be obtained simultaneously over a large frequency range. In Fourier transform infrared (FT-IR) spectroscopy, an interferometer is used. This consists of fixed and movable mirrors that reflect the incident light before it passes through the sample. The resulting time-domain interferogram is converted into a frequency domain spectrum by using Fourier transformation. Multiple scans are used to improve the signal-to-noise ratio.⁶ The technique is widely used to identify the functional groups in organic and inorganic compounds. Signals arise from the vibrational and rotational excitation of atoms and groups of atoms within a molecule. Because of the variety of symmetry of atomic groups and their differences in atomic masses and electronic structures, the absorption patterns for a specific species will be unique, which allows for their identification.⁷

FT-IR spectra were obtained on a Perkin Elmer Spectrum 100 FT-IR spectrometer at a resolution of 4 cm^{-1} , averaging 30 scans. Samples were analysed in their powder form using a ZnSe/diamond composite as the key component of the universal attenuated total reflectance sample holder. In other cases a NaCl window was used to mount the samples.

3.6.2 Raman spectroscopy

Raman spectroscopy is based on the Raman effect (also known as Raman scattering), which is the inelastic scattering of photons after their interaction with vibrating molecules of a given material. During this interaction, photons either transfer energy to (Stokes) or receive energy from (anti-Stokes) molecular vibrations, i.e., phonons. Thus, the energy change of the scattered photons corresponds to the vibrational energy levels of the molecules in the sample. Since the vibrational energy spectrum depends on the chemical composition of the sample (type of atoms, bond strength, bond angles, crystallographic symmetry and so on), a Raman spectrum is chemically very specific and provides an excellent chemical fingerprint of the sample.

The Raman system typically consists of a laser that provides the optical signal used to produce the Raman effect, a fibre that collects optical signals exiting the sample, and a spectrograph connected to a data-processing unit. As the scattered light consists of radiation of the same frequency as the laser frequency (Rayleigh scattering), as well as sidebands at lower (Stokes) and higher (anti-Stokes) frequencies, Raman signals usually require powerful lasers and sensitive detectors. Its applications include chemical fingerprinting, crystallite examination in ceramics and the examination of structure and strain rates in polycrystalline ceramics, glasses, fibres, gels and thin and thick films. Vibrational information as well as impurity concentration can also be determined from Raman data.⁶

Raman spectra, excited by a high performance line-narrowed laser (785 nm), were recorded on a Raman microscope (Perkin Elmer RamanMicro 200) equipped with a cooled charged coupled device (CCD) detector set at -50°C and an Olympus

BX51M confocal microscope. Measurements were performed with the beam path set at 50X magnification at various exposure times. Instrument control as well as data acquisition, processing and analysis were performed using Spectrum software.

3.6.3 Ultraviolet-visible (UV-Vis) spectroscopy

The UV-Vis spectrophotometer consists of the following elements: (i) a light source (usually a deuterium lamp for the UV spectral range and a tungsten lamp for the Vis and IR spectral ranges) that is focused on the entrance to (ii) a monochromator, which is used to select a single frequency (wavelength) from all of those provided by the lamp source and to scan over a desired frequency range; (iii) a sample holder; followed by (iv) a light detector (usually a photomultiplier for the UV-Vis range and an SPb cell for the IR range) to measure the intensity of each monochromatic beam after traversing the sample; and finally (v) a computer, to display and record the absorption spectrum.

3.6.3.1 Diffuse reflectance measurements

For diffuse reflectance measurements, an integrating sphere (a sphere with a fully reflective inner surface) is used (**Figure 3.3**). Such a sphere has a pinhole through which the light enters and is transmitted toward the sample. The diffuse reflected light reaches the detector after suffering multiple reflections in the inner surface of the sphere. The integrating spheres can be incorporated as an accessory into conventional spectrophotometers. The reflectance spectra can be very advantageous, as they manifest the singularities caused by the absorption process but with the possibility of using bulk samples. Diffuse reflectance is generally applicable to unpolished or powdered samples.

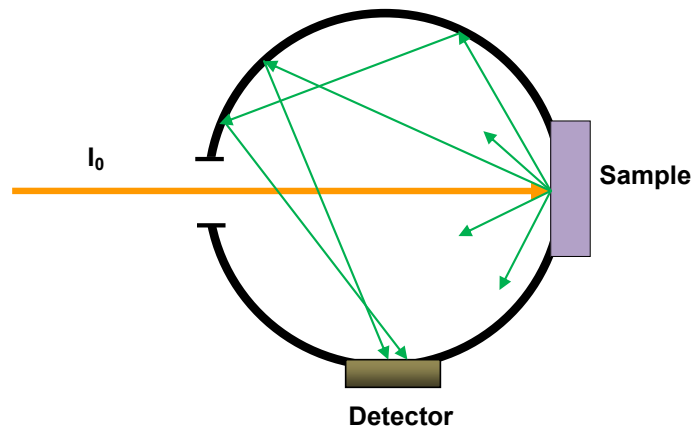


Figure 3.3 A 0° incident light integrating sphere attachment

The percentage diffuse reflectance data can be transformed to Kubelka-Munk units, for an infinitely thick layer, by applying the Kubelka-Munk algorithm according to the equation:

$$K = \frac{(1-R)^2}{2R} = F(R) \quad (3.4)$$

where:

K is reflectance transformed according to Kubelka-Munk

R is reflectance (%)

$F(R)$ is the remission or the Kubelka-Munk function

The band gap, E_g and the absorption coefficient, α , are related according to the equation:

$$\alpha h\nu = A(h\nu - E_g)^n \quad (3.5)$$

where:

α is the absorption coefficient

A is a constant

$h\nu$ is the energy of light

E_g is the band gap

n is a constant depending on the nature of the band-gap transition mode.⁸

For an indirect allowed transition, $n = 2$ whilst for a direct allowed transition, $n = 1/2$. Values of n can be $3/2$ for a direct forbidden transition and 3 for an indirect forbidden transition. In the case of TiO_2 , the fundamental absorption has an indirect transition ($n = 2$). However, the type of transition may change slightly due to doping, leading to other types of transitions.

3.6.3.2 Determination of material band gaps from absorption coefficient

The study of optical absorption provides useful information for understanding the optically induced transitions and optical band gaps of materials. For crystalline solids that scatter light in a perfectly diffuse manner, K becomes equal to α . In this case, Equation (3.5) can be re-written as;

$$[F(R)hv]^{1/n} = A(h\nu - E_g)^n \quad (3.6)$$

Band gaps of the nanoparticles were deduced from the “Tauc plot”, a plot of $[F(R)hv]^n$ vs. photon energy. The zero intercept of $[F(R)hv]^n$ vs. photon energy plot to the x-axis provides the band-gap energy which corresponds to the absorption edge of the material (**Figure 3.4**). The value of n depends on the specific type of transition of the material.^{9,10,11}

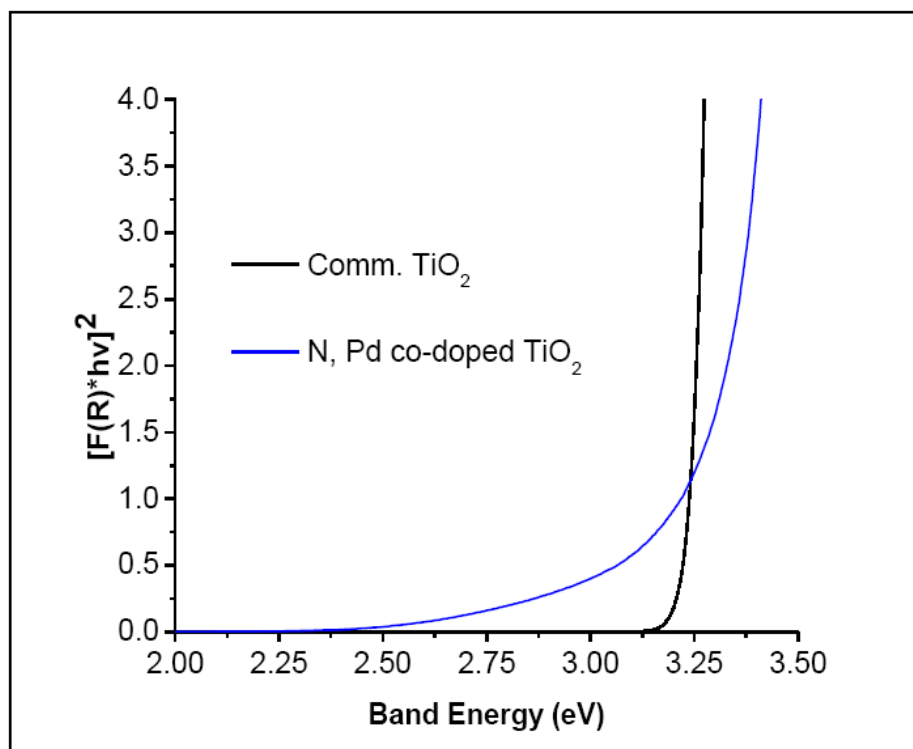


Figure 3.4 Tauc plots for Commercial TiO₂ (P25) and N,Pd co-doped TiO₂ ($n = 2$)

Optical properties were investigated using diffuse reflectance UV-Vis absorption spectrophotometry on a Shimadzu UV - 2540 (Japan) equipped with an IRS 240A integrating sphere attachment. BaSO₄ was used as the reflectance standard.

3.6.4 X-ray Diffraction (XRD)

In XRD, a collimated beam of X-rays is directed at the sample and the angles at which the beam is diffracted are measured. When the beam interacts with an arbitrarily chosen material, its atoms may scatter the rays into all possible directions resulting in a diffraction pattern. In a crystalline solid, however, the atoms are arranged in a periodic array. The diffraction pattern contains a range of peaks of different relative intensities at specific angles of diffraction and this diffraction pattern is unique to a specific crystal structure. This periodicity imposes strong constraints on the resulting X-ray diffraction pattern, so much so that it is possible to determine the crystallographic structure from an analysis of the diffraction pattern. Bragg's Law is used to explain the interference pattern of X-

rays scattered by the material. As such, XRD is an important quantitative and qualitative technique which is used for the 'fingerprint' characterisation of crystalline materials and their crystal structures. In addition to the determination of the crystalline structure of nanomaterials, XRD can provide information on nanocrystal sizes, micro-stresses, micro-strains, types of crystal structure, inter-planar differences, Miller indices, charge distribution around atoms and orientation distribution.⁶

XRD measurements were performed using on a Philips PANalytical X^{pert} diffractometer operated at 40 kV and 40 mA. The Cu K α radiation ($\lambda = 0.15406$ nm), Ni filtered (0.02 mm) and masked (11.6mm), was collimated with Soller slits (0.04 rad). Measurements were performed in the range 20° to 80° (2θ). Samples in their powder form were mounted on a Si sample holder using a bracket sample stage. Data analysis was performed using X^{pert} Data Collector software.

3.6.4.1 Crystallite phases and sizes

The ratio (x_A) of anatase in the TiO₂ samples was estimated using the equation:

$$x_A = [1 + 1.26 (I_R/I_A)]^{-1} \quad (3.7)$$

where:

I_A and I_R are the integral intensities of the anatase (101) and rutile (110) reflections, respectively

The crystallite sizes, (D), were estimated by applying the Scherrer equation to the FWHM of the (101) peak of the anatase phase or the (110) peak of the rutile phase:

$$D = \frac{0.9\lambda}{B \cos\theta} \quad (3.8)$$

where:

λ is the X-ray wavelength corresponding to Cu-K α radiation (0.15406 nm)


B is the broadening (in radians) of the anatase (101) or rutile (110) peak

0.9 is a constant

θ is the angle of diffraction corresponding to the peak broadening.^{12,13}

3.6.5 Thermogravimetric analysis(TGA)

Thermal analysis may be defined as the measurement of the physical and chemical properties of materials as a function of temperature, time and atmosphere (inert or oxidising). In TGA, the mass change of a substance is measured as a function of temperature whilst the substance is subjected to a controlled temperature programme. A mass loss is noted during heating if the substance contains a volatile fraction. Modern instrumentation used for thermal analysis usually consists of four parts:

- 
- (i) A sample pan/sample holder.
 - (ii) Sensors to detect/measure a property of the sample and the temperature.
 - (iii) An enclosure within which the experimental parameters may be controlled.
 - (iv) A computer to control data collection and processing.

TGA data can detect and quantify the presence of bulk water and/or associated water in the samples analysed. It is also important in identifying the temperature at which molecular decomposition occurs. Information on the composition of the material as well as its thermal or oxidative stability is also obtained. The change in weight measured by TGA is quantitative; however, no information on the chemistry of evolved gases is obtained. Chemical knowledge on the evolved gases can only be obtained by coupling TGA to other techniques such as FT-IR or mass spectrometry (MS). TGA measurements are important in materials science because the end-use properties (functionality) of a material at a specific

temperature are dependent on the structure of the components at that temperature.¹⁴

TGA analyses were performed on a Perkin Elmer TGA 4000 thermogravimetric analyser at a heating rate of 10°C/min under nitrogen flow over a range of 30°C to 800°C. Samples (10 mg to 15 mg) were loaded into the sample pan. Data were converted to their derivatives whenever necessary. The Pyris software was used for all data processing.

3.6.6 Scanning electron microscopy (SEM)

SEM is a powerful technique for examining material surfaces. In the microscope, electrons are directed through a series of condenser and objective lenses that condense and constrict them to eliminate high-angle electrons before they are focused onto a sample. The number of backscattered electrons and/or the secondary electrons generated by the beam that emerges from the sample depends on the local composition and topography of the sample. These electrons are collected by an electron detector and an image is formed by plotting the detector signal as a function of the beam location.

With the recent developments in the electron source and the advancement in the detector technologies, higher resolutions have been achieved that can be utilised to examine beam-sensitive materials, nanomaterials and grain structures. Some applications of SEM include determining structure-property relationships for a wide range of materials, including metals, alloys, semi- and superconductors, ceramics, carbon nanotubes, nanoporous supports and polymers. Topographical data and morphological properties such as surface features and shape and size of particles in these materials can be obtained.⁶

3.6.6.1 Energy dispersive X-ray spectroscopy (EDS)

SEM can have a wide range of attachments (detectors) such as the energy dispersive X-ray spectroscopy (EDS) and the wavelength dispersive X-ray spectroscopy (WDS). Using these techniques, the composition of a sample can be

measured as well as mapped. In addition to these detectors, there is also an electron back-scattered diffraction detector (EBSD). This can be used to investigate and map crystal grain boundaries in materials down to about 0.1 μm . Energy dispersive X-ray spectroscopy (EDS or EDX) is a chemical microanalysis technique used in conjunction with either TEM or SEM. The EDS technique detects X-rays emitted from the sample during bombardment by an electron beam to characterise the elemental composition of the analysed volume. Features or phases as small as 1 μm or less can be analysed.

Scanning electron microscopy (SEM) images were obtained on a NOVA FEI/FIB Instrument, equipped with an INCA EDS analyser. Samples were loaded in their powder form on the carbon tape and mounted on the sample holder, ready for imaging.

3.6.7 Transmission electron microscopy (TEM)

Electron microscopy is an extremely important technique for the analysis of characteristic spatial features of nanostructures at high resolution, since it provides direct images from which morphological details can be extracted. TEM utilises a collimated beam of electrons that is accelerated by high voltages and focused through a series of electrostatic or magnetic lenses. The electron beam then travels through the sample and is focused on a detector plate. Images are formed because different atoms interact with and absorb electrons to different extents. Since electrons interact much more strongly with matter than do X-rays or neutrons with comparable energies or wavelengths, the best results are obtained for sample thicknesses that are comparable to the mean free path of the electrons (the average distance travelled by the electrons between scattering events). The recommended thickness varies from a few nanometres for samples containing light elements to tens or hundreds of nanometres for samples made of heavy elements. The theoretical resolving power of high-resolution TEM is theoretically subatomic, although resolutions of around 0.1 nm have been achieved in practice. Additionally TEM allows generation of diffraction patterns for determining the crystallographic structures of samples. Digital micrographs and diffraction patterns

can be obtained with a digital camera and dedicated software. Image processing can be used to increase the information obtained from TEM, thus enhancing some features close to the noise level.

TEM can provide micro-structural details down to an atomic level and can be utilised to examine crystal structures and crystalline defects. TEM finds applications in determining structure-property relationships for a wide range of materials such as metals, alloys, semiconductors, ceramics, carbon nanotubes and polymers. TEM can provide information pertaining to size and shape of particles, detection of atomic scale defects, elemental composition and information on phases (lattice spacing measurement) as well as sample orientation. The EDS analyser attachment allows qualitative/quantitative elemental composition analysis.⁶

TEM analyses were performed under bright field on a Tecnai G² Spirit TEM at 120 kV. Images were collected on a Gatan Digital Imaging system with the Power Mac 8600 computer Digital Micrograph software. Samples were prepared for TEM analysis by sonicating them in methanol for 10 min and then depositing small drops of the material suspension on the TEM lacy copper grids. The grids were allowed to dry before being mounted on the TEM sample holder.

3.6.8 X-ray photoelectron spectroscopy (XPS)

XPS involves the irradiation of a specimen by a beam of usually monochromatic low energy X-rays. Absorption of a high energy X-ray photon causes the ionisation of an electronic level. A part of the photon's energy is used for the ionisation, while the excess appears as the kinetic energy of the photoelectron. Depending on the ionisation energy of the electronic level, the kinetic energy is large or small. The energy spectrum of the electrons is determined with an electrostatic energy analyser and a peak appears for each electronic level. The binding energy of each core-level electron (approximately equal to its ionisation energy) is characteristic of the atom and the specific orbital to which it belongs. Since the energy of the incident X-rays is known, the measured kinetic energy of a core-level

photoelectron peak can be related directly to its characteristic binding energy. The binding energies of the various photoelectron peaks (i.e. 1s, 2s, 2p, etc.) have been tabulated and are available in databases. Therefore, XPS provides a means of elemental identification that can also be quantified via measurement of integrated photoelectron peak intensities and the use of a standard set of sensitivity factors to give a surface atomic composition.

XPS is currently the most widely used surface-analysis technique. Depth profiling can provide information about the material a few nanometres from the surface. It provides information about the elemental and chemical composition of a material surface. It can determine the surface concentration of elements present, chemical states, the molecular environment, binding states and/or oxidation state of metals. All elements, except hydrogen and helium, can be analysed. Elemental and chemical mapping across the surface is also possible. XPS is therefore a key research method for nanostructured materials like metals, semiconductors and insulators, where the nano-effect is related to the surface activity and properties.^{6,15}

XPS surface elemental analysis was performed on a Physical Electronics (PHI) (Quantum2000) X-ray photoelectron spectrometer (XPS) with Al K α (1 486 eV) as the excitation source. The instrument was set to an X-ray power of 30 W, 100 μ m beam diameter, 117.4 eV pass energy (wide), 29.35 eV pass energy (narrow) and a take-off angle of 45°. The binding energy was referenced to C1s line at 284.76 eV for calibration. The atomic concentrations of these elements were obtained by comparing the peak areas of their spectra.

3.7 PHOTODEGRADATION EXPERIMENTS

The photocatalytic performance of the materials was evaluated by measuring the rate of photodegradation of a dye Eosin Yellow (EY) and/or natural organic matter (NOM) under visible-light irradiation. The powdered material (0.1 g) was suspended in 100 ml of the Eosin Yellow solution (100 ppm) For NOM photodegradation tests; the material (0.02 g) was suspended in 20 ml of the NOM

solution. This amount was chosen after preliminary tests were carried out on the effect of catalyst amount on the degradation efficiency of the dye. It was assumed that at this concentration, monolayer coverage of the catalyst is attained. Two sources of radiation were used; a 150 W tungsten filament lamp (Eurolux), kept at a distance of 10 cm from the reaction vessel (**Figure 3.5**) and a solar simulator (Oriel, Newport), equipped with an Oriel 500 W Xenon. The power output of the solar simulator was set to 300 W in order to give an irradiance of 1 000 W/m² at about 25°C, using an Air Mass1.5 Global Spectral Filter (**Figure 3.6**). An Oriel PV reference cell system equipped with a 2 cm × 2 cm monocrystalline silicon photovoltaic cell and a Type K thermocouple was used to set the simulator irradiance to 1 sun and to monitor the temperature of the system. Prior to photocatalytic reactions, the suspensions were ultra-sonicated for 10 min and then magnetically stirred in the dark for an hour to allow for adsorption equilibrium before visible-light illumination. Aliquots of the suspension (2 ml) were withdrawn at constant time intervals using a 5 ml Neomedic disposable syringe and filtered through a 0.22µm PVDF membrane filter for various periods of irradiation up to 180 min. Variations in the concentrations of EY or NOM were monitored on a UV-Vis spectrophotometer (Shimadzu UV-2450, Japan) at $\lambda = 517$ nm.

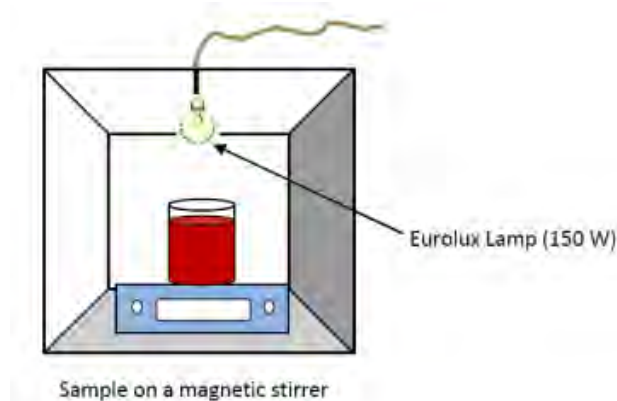


Figure 3.5 Experimental setup for photodegradation experiments using a 150 W Eurolux lamp

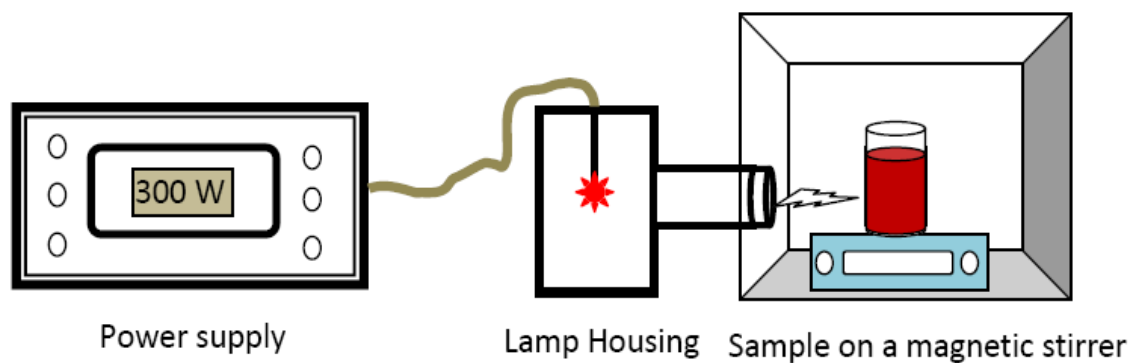


Figure 3.6 Experimental setup for photodegradation experiments using a solar simulator

Figures 3.7 and 3.8 show the irradiances of the solar simulator and the normal solar spectrum at sea level on a clear day respectively.

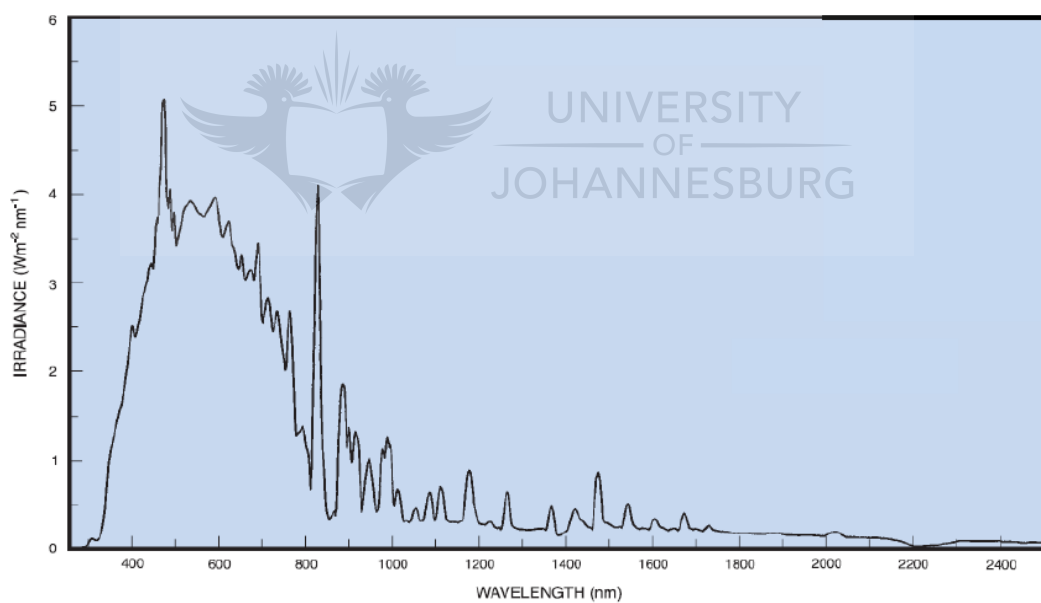


Figure 3.7 Output of the solar simulator with an AM 1.5 Global Filter

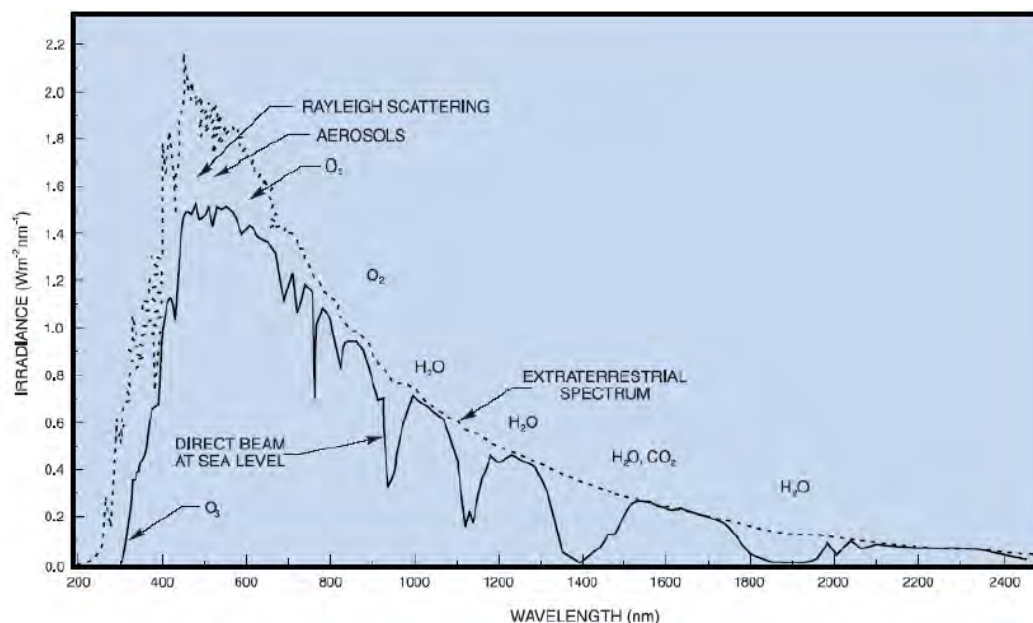


Figure 3.8 Normal incident solar spectra at sea level on a clear day

3.8 PHOTODEGRADATION KINETICS

3.8.1 Kinetic model

Reaction kinetics gives information about the reaction rates and the mechanisms by which the reactants are converted to the products. In general, first- and second-order Langmuir–Hinshelwood models are more common. Evaluation of solar photocatalytic reactors for water decontamination requires an accurate analysis of the dynamics of molecular processes occurring at the catalyst/solution interface. The primary processes include the photo-generation of electron–hole pairs, their transport and capture by species adsorbed on the catalyst surface (such as water molecules, molecular oxygen and hydroxyl ions), charge recombination, the formation of hydroxyl and superoxide radicals and the attack of substrate molecules through redox reactions. Controversies regarding both the mechanism of photoactivation have led to the formulation of many different empirical and semi-predictive kinetics rate law models for the kinetics of photocatalytic degradation of organic pollutants.¹⁶ Some researchers have proposed a mechanism based on attack of the organic compounds through

cleavage of the C-H bond by the hydroxyl radicals generated by the oxidation of the adsorbed water and hydroxyl ions in which the photocatalytic degradation rate of a species i per catalyst particle in an aqueous suspension of catalyst is can be given as;¹⁷

$$-r_p = \alpha'_1 \left\{ \left(\frac{E(R_i, R_j)}{1+E(R_i, R_j)} \right) - \sqrt{\left(\frac{E(R_i, R_j)}{1+E(R_i, R_j)} \right)^2 + \frac{\alpha'_2}{C_{cat}} \int_{\lambda} e_{\lambda}^a d\lambda} \right\} \alpha_{3,i} \times \frac{[R_i]}{(1+E(R_i, R_j))} \quad (3.9)$$

$$E(R_i, R_j) = \sum_{k=1}^N \alpha_{3,k} [R_k] = \alpha_{3,i} [R_i] + \sum_{\substack{j=1 \\ j \neq i}}^{N_c} \alpha_{3,j} [R_j] \quad (3.10)$$

where α'_1 , α'_2 , $\alpha_{3,i}$, $\alpha_{3,k}$, $\alpha_{3,j}$ are adjustment constant of the model, $E(R_i, R_j)$ is the global adsorption function for i and j compounds, C_{cat} is the catalyst concentration, e_{λ}^a is the local volumetric rate of photon absorption and R_i , R_j , R_k refer to the molecules adsorbed.

The quantum yield of the photodegradation process is affected by the process conditions, the type and geometry of photoreactor, the scale of operation and the properties of the catalyst. For species i in a heterogeneous system, the quantum yield can only be defined in local terms as the quotient of the reaction rate at a specific location in the reactor and the local volumetric rate of photon absorption (LVRPA).

Turch et al.¹⁷ proposed a generalised model for the evaluation of photocatalytic degradation of water pollutants in heterogeneous solar photoreactors using slurry TiO_2 suspensions, assuming a steady state concentration of water molecules and hydroxyl ions adsorbed on the catalyst surface and slow adsorption of organic substrates in comparison with the total reaction time.

For $E(R_i, R_j) \gg 1$, then;

$$-r_p = \alpha'_1 \left\{ -1 + \sqrt{1 + \frac{2}{\alpha'_1} R_g} \right\} \alpha_{3,i} \frac{[R_i]}{(1+E(R_i, R_j))} \quad (3.11)$$

The term $-1 + \sqrt{1 + \frac{2}{\alpha'_1} R_g}$ contains the effects of the incident photon flux, catalyst concentration and quantum yield and is extrinsic to the prevalent kinetic mechanism expressed by the Langmuir–Hinshelwood term.

The reaction rate for the i th component in a solution can be expressed for all the N_v catalytic particles suspended in the liquid as;

$$r_i = v_i \frac{S_g}{a_s} C_{cat} \alpha'_1 \left\{ -1 + \sqrt{1 + \frac{2}{\alpha'_1} R_g} \right\} \alpha_{3,i} \frac{[R_i]}{(1+E(R_i, R_j))} \quad (3.12)$$

where v_i is the stoichiometric coefficient for component i in the oxidation reaction, S_g is the catalyst specific surface area (m^2/kg), C_{cat} is the catalyst concentration (kg/m^3), a_s is the superficial area per catalyst particle ($\text{m}^2/\text{particle}$), r_i is the volumetric reaction rate ($\text{mol}/\text{m}^3\text{s}$), $[R_i]$ is the concentration of component i (mol/m^3), $E(R_i, R_j)$ is a global adsorption function from i and j compounds, and R_g is the rate of electron–hole generation for the activation step.

For an irradiated heterogeneous catalytic system in which the electron - hole pairs are generated with a primary quantum yield (ϕ_λ), the accepted model for the reaction rate at the initial stage for N_v catalyst particles suspended in the volume v_R is given by;

$$R_g = \frac{1}{N_v} \int_\lambda \phi_\lambda \hat{e}_\lambda^a d\lambda \quad (3.13)$$

$$N_v = \frac{C_{cat}}{v_p \rho_p} \quad (3.14)$$

where \hat{e}_λ^a is the local volumetric rate of photon absorption (LVRPA, $\text{Einstein}/\text{m}^3\text{s}$), v_p is the particle volume and ρ_p is the particle density, assuming that the absorption of radiation is a volumetric phenomenon that is carried out by the

catalytic particles in suspension only. For solar irradiation with polychromatic radiation, the reaction rate is represented by;

$$R_g = \frac{v_p \rho_p}{C_{cat}} \Phi_g^{Eff} \hat{E}_g^a(\lambda \rightarrow \lambda') \quad (3.15)$$

$$\Phi_g^{Eff} = \frac{\int_{\lambda} \phi_{\lambda} \hat{e}_{\lambda}^a d\lambda}{\int_{\lambda} \hat{e}_{\lambda}^a d\lambda} \quad (3.16)$$

$$\hat{E}_g^a(\lambda \rightarrow \lambda') = \frac{1}{v_R} \int_v \hat{e}_{\lambda}^a dv \quad (3.17)$$

where Φ_g^{Eff} is the overall effective quantum yield (mol/Einstein) of the process and $\hat{E}_g^a(\lambda \rightarrow \lambda')$ is the overall volumetric rate of photon absorption (OVRPA) (Einstein/m³s). The OVRPA corresponds to the LVRPA averaged over the entire volume of the reactor. The approximation of constant global parameters is valid only if pseudo-isotropic systems are considered, in which the physical properties (optical parameters, concentration of species and hydrodynamics) are calculated as functions of integrated variational parameters.

Introducing the global parameters (Φ_g^{Eff} and OVRPA) into the new reaction rate equation (assuming that the reaction is limited by the substrate of interest), and if $[R_i]$ is the substrate concentration c_i (mol/m³), $E(R_i, R_j) = (\alpha_{3,i} c_i)$, $\alpha_1 = \alpha'_1/a_s$, $\alpha_{3,i} = k_A^{L-H}$, $\alpha_2 = 1/\alpha_1$ and defining a particle constant, \mathcal{K}_p (m³/m²) as;

$$\mathcal{K}_p \equiv \frac{2}{S_g C_{cat}} \quad (3.18)$$

Then the reaction rate r_i (mol/m³s) for the oxidation of component i th in solution in an irradiated catalyst suspension is will be;

$$r_i = -2 \frac{\alpha_1}{\mathcal{K}_p} \left[-1 + \sqrt{1 + \frac{\mathcal{K}_p}{\alpha_1} \Phi_g^{Eff} \hat{E}_g^a(\lambda \rightarrow \lambda')} \right] \theta_i^{L-H} \quad (3.19)$$

where

$$\theta_i^{L-H} = \frac{k_A^{L-H} c_i}{1 + k_A^{L-H} c_i} \quad (3.20)$$

k_A^{L-H} (m^3/mol) is an absorption and α_1 ($\text{mol}/\text{m}^2\text{s}$) a kinetic reaction rate constant.

Equation 3.20 takes the general form of the Langmuir-Hinshelwood model when

$$\frac{\mathcal{K}_p}{\alpha_1} \Phi_g^{Eff} \hat{E}_g^a(\lambda \rightarrow \lambda') \ll 1:$$

$$R = \frac{-dC_0}{dt} = \frac{k_r K C_0}{1 + K C_0} \quad (3.21)$$

where:

R represents the initial rate of disappearance of the EY

C_0 the initial concentration

K the equilibrium constant for the adsorption of the dye on nanomaterial

k_r reflects the limiting rate of the reaction at the maximum coverage at the experimental conditions.

Integrating Equation (3.21) gives:

$$t = \left(\frac{1}{k_r K} \right) \ln \left(\frac{C_0}{C} \right) + \frac{C_0 - C}{k_r} \quad (3.22)$$

where:

t is the time in minutes required for the degradation of the dye from the initial concentration C_0 to equilibrium concentration C .

At low initial concentration of the dye, the second term in the equation (Equation (3.22)) becomes insignificant and hence it can be neglected. This will yield the equation:

$$\ln\left(\frac{C_0}{C}\right) = k_r K t = k' t \quad (3.23)$$

where:

k' is the apparent rate constant (min^{-1}) of the photodegradation

A plot of $\ln\left(\frac{C_0}{C}\right)$ vs. irradiation time gives a straight line whose slope represents the apparent first-order rate constant, k' .¹⁸

$$\text{When } \frac{C_0}{C} = 0.5, \text{ then } t_{1/2} = \frac{0.693}{k'} \quad (3.24)$$

The half-life, $t_{1/2}$, is a useful indication of the rate of a first-order chemical reaction of a substance. It describes the time taken for the concentration of a reactant to fall to half of its initial value.¹⁹

3.8.2 Global effective quantum yield model, ϕ_g^{Eff}

Quantum yields can be calculated based on some assumptions:¹⁷

- (i) The semiconductor photo-activation depends on the irradiation source, the electronic properties of the material and the characteristics of the energy levels of the semiconductor- solution interface (pH effect).
- (ii) The quantum yield is considered within the catalyst band gap activation energies with maximum values (not null) and minimum value (zero).

$$\text{eg. } \phi_{g,min}^{Eff} \leq \phi_g^{Eff} \leq \phi_{g,max}^{Eff} = 0 \text{ for TiO}_2 - \text{P25}$$

- (iii) The activation of the catalyst depends on the amount of energy available in the system and the catalyst absorption capacity.

(iv) For optimal conditions of irradiation, there is an „ideal“ value of the quantum yield, which corresponds to maximum generation of electron–hole pairs and zero charge recombination.

(v) The effective value $\phi_{g,max}^{Eff}$ is a constant value associated with the intrinsic nature of the catalyst.

$$\phi_{g,max}^{Eff} = \phi_g^{Id} \cdot P_\phi^a \quad (3.25)$$

where, $P_\phi^a \equiv \frac{\mathcal{K}_\lambda(\lambda \rightarrow \lambda')}{\beta_\lambda(\lambda \rightarrow \lambda')}$, with the interval $\lambda \rightarrow \lambda'$ corresponding to the absorption spectrum of the catalyst (i.e. band gap), \mathcal{K}_λ is the specific scattering coefficient, β_λ is the extinction coefficient and $\phi_g^{Id} \equiv 1$ (mol/Ein).

The observed quantum yields ϕ_g^{Eff} vary with the experimental conditions such as substrate type, pH, radiation field, catalyst load and reactor geometry the effects of these operational parameters can be decoupled from ϕ_g^{Eff} by introducing a new function ψ , which takes into account these effects:

$$\psi = \delta' A_\phi \quad (3.26)$$

$$A_\phi = f(\psi_E) e^{-\xi_\phi} \quad (3.27)$$

$$\xi_\phi = -p(\kappa_{ads}) M_{w,i} S_g \frac{C_{cat}}{\rho_{cat}} \left(\frac{C_{O_2}}{C_{i,0}} \right) \left(\frac{pH_{solution}}{zpc_{cat}} \right) \quad (2.28)$$

$$\psi_E = \frac{\hat{E}_{g(\lambda \rightarrow \lambda')}^a}{\hat{E}_{g(\lambda \rightarrow \lambda'),0}^a} \quad (3.29)$$

where ρ_{cat} , C_{cat} and zpc_{cat} are the density, concentration and point of zero charge of the catalyst, respectively, $p\kappa_{ads}$ is a probability function of the molecular adsorption for the i th component in equilibrium per unit of molecular weight, pH is the initial pH for the reaction, $C_{i,0}$ is the initial substrate concentration, C_{O_2} is the overall concentration of oxygen, δ' is the Kronecker delta function and $\hat{E}_{g(\lambda \rightarrow \lambda'),0}^a$ is

the volumetric rate of photon absorption (VRPA) at the reactor wall exposed to the incident radiation.

The value of the solar effective quantum yield for the photocatalytic process that are independent of operating conditions and reactive substance is given by:

$$\phi_g^{Eff} = \phi_{g,max}^{Eff} \cdot \psi \quad (3.30)$$

$$\delta' = \begin{cases} 1 & 3.2 \leq hv \leq 4.1 \text{ eV} \\ 0 & hv < 3.2 \text{ eV}, hv > 4.1 \text{ eV} \end{cases} \quad (3.31)$$

3.9 REFERENCES

1. Arayne M.S., Sultana N. and Sabah N.U. (2007). Fabrication of solid nanoparticles for drug delivery. *Pak. J. Pharm. Sci.* 20, (3), 251 – 259.
2. Factorovich M., Guz L. and Candal R. (2011). N-TiO₂: Chemical synthesis and photocatalysis. *Adv. Phys. Chem.* Article ID 821204, DOI:10.1155/2011/821204
3. Chen X. and Mao S.S. (2007). Titanium dioxide nanomaterials: Synthesis, properties, modifications and applications. *Chem. Rev.* 107, 2891 – 2959.
4. Flahaut E., Peigney A., Bacsa W.S., Bacsa R.R. and Laurent Ch. (2004). CCVD synthesis of carbon nanotubes from (Mg, Co, Mo)O catalysts: Influence of the proportions of cobalt and molybdenum. *J. Mater. Chem.* 14, 646 – 653.
5. Dosch H. and Van de Voorde M.H. (2009). GENNESYS White Paper. A New European Partnership between Nanomaterials Science and Nanotechnology and Synchrotron Radiation and Neutron Facilities. Max-Planck-Gesellschaft, Stuttgart. ISBN 978-3-00-027338-4, 262.

6. Palma R.J.M. and Lakhtakia A. (2010). *Nanotechnology: A Crash Course*. SPIE, Bellingham, Washington, USA.
7. Griffiths P.R. (1983). Fourier transform infrared spectrometry. *Sci.* 21, 297-302.
8. Marcos J.S., Ochando I.M., Galindo R.E., Morillas R.M. and Prieto C. (2010). Optical and transport properties of Ti-doped In_2O_3 thin films prepared by electron beam physical vapour deposition. *Phys. Status Solidi A* 207, (7), 1549 – 1553.
9. Zhu L., Meng Z.D. and Oh W.C. (2012). MWCNT-based $\text{Ag}_2\text{S-TiO}_2$ nanocomposites photocatalyst: Ultrasound-assisted synthesis, characterisation and enhanced catalytic efficiency. *J. Nanomater.* Article ID 586526, DOI:10.1155/2012/586526
10. Murphy A.B. (2007). Band-gap determination from diffuse reflectance measurements of semiconductor films and application to photo-electrochemical water splitting. *Solar Energ. Mater. Solar Cells* 91, 1326 – 1337.
11. Chimalawong P., Kaewkhao J. and Limsuwan P. (2010). Optical investigation and electronic polarizability of Nd^{3+} doped soda-lime-silicate glasses. *Energ. Res. J.* 1 (2): 176 – 181.
12. Maicu M., Hidalgo M.C., Colon G. and Navio J.A. (2011). Comparative study of the photodeposition of Pt, Au and Pd on pre-sulphated TiO_2 for the photocatalytic decomposition of phenol. *J. Photochem. Photobiol. A: Chem.* 217, 275 – 283.
13. Panagiotopoulou P. and Kondarides D.I. (2004). Effect of morphological characteristics of TiO_2 -supported noble metal catalysts on their activity for the water–gas shift reaction. *J. Catal.* 225, 327 – 336.

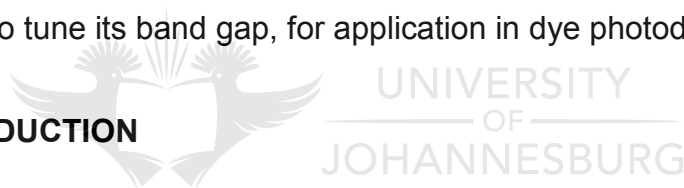
14. Nielsen S.S. (2009). *Food Analysis: Food Science Text Series*. Springer, New York. DOI: 10.1007/978-1-4419-1478-1, 555 – 573.
15. Marcus P. and Mansfeld F. (eds). (2005). *X-Ray Photoelectron Spectroscopy in Corrosion Research in Analytical Methods in Corrosion Science and Technology*. Taylor & Francis Group, New York. pp 2 – 36.
16. Mueses M. A., Martinez F. M. and Puma L.G. (2013). Effective quantum yield and reaction rate model for evaluation of photocatalytic degradation of water contaminants in heterogeneous pilot-scale solar photoreactors. *Chemical Engineering Journal* 215 - 216, 937 – 947.
17. Turchi C. and Ollis D. (1990). Photocatalytic degradation of organic water contaminants: mechanisms involving hydroxyl radical attack, *J. Catal.* 122, 178 – 192.
18. Rupa A.V., Manikandan D., Divakar D. and Sivakumar T. (2007). Effect of deposition of Ag on TiO₂ nanoparticles on the photodegradation of Reactive Yellow-17. *J. Hazard. Mater.* 147, 906 – 913.
19. Zainal Z., Hui L.K., Hussein M.Z., Abdullah A.H. and Hamadneh I.R. (2009). Characterisation of TiO₂-chitosan/glass photocatalyst for the removal of a monoazo dye via photodegradation-adsorption process. *J. Hazard. Mater.* 164, 138 – 145.

CHAPTER 4

NITROGEN, PALLADIUM CO-DOPED TiO₂ FOR EFFICIENT VISIBLE-LIGHT PHOTOCATALYTIC DYE DEGRADATION[†]

South Africa has about 80% of the world's reserves of platinum group metals (PGMs), which include palladium and osmium. The platinum metals have outstanding catalytic properties. They are highly resistant to wear and tarnish, making platinum, in particular, well suited for fine jewellery. Other distinctive properties include resistance to chemical attack, excellent high temperature characteristics and stable electrical properties. These properties can be exploited in fabrication of materials with desirable qualities for various applications. In the study described in this chapter nitrogen and palladium are introduced onto TiO₂ nanoparticles, to tune its band gap, for application in dye photodegradation.

4.1 INTRODUCTION



In the past few years, there has been tremendous research and development in the area of photocatalysis. Photocatalysis using semiconductor particles has found increasing interest in solving global pollution problems. One of the major applications of this technology is the degradation of organic pollutants in water.¹ Compared to other semiconductor photocatalysts, titania (TiO₂) has so far been shown to be the most promising material used for both fundamental research and practical applications because of its high activity, good chemical inertness, safeness, non-toxicity and low cost. However, pure TiO₂ is only active under ultraviolet (UV) light irradiation ($E_g = 3.2$ eV), limiting its practical application in the visible region.^{2,3}

[†] Contents of this chapter were published in a slightly modified form in:

Kuvarega A.T., Krause R.W.M. and Mamba B.B. (2011). Nitrogen/palladium co-doped TiO₂ for efficient visible light photocatalytic dye degradation. *J. Phys. Chem. C*, 2011, 115, 22110 - 22120

Several strategies have been attempted to improve the activity of TiO₂ in the visible region, including doping with other species.⁴⁻¹⁰ Anionic species such as nitrogen, carbon and sulphur were identified to potentially form new impurity levels close to the valence or conduction band of TiO₂ thereby lowering the band gap and shifting the absorption edge to the visible region.¹¹ One conventional method for preventing recombination is utilisation of platinum group metal (PGM) catalysts, e.g. platinum, osmium, palladium and rhodium, which are capable of collecting a large number of electrons and enhance the photoactivity by increasing the lifetime of holes. However, the use of noble metals as co-catalysts is a problem from the viewpoint of cost and availability.¹² Moreover, much controversy still exists on the modification mechanism of TiO₂ doped with metals or non-metals.

Despite the development of effective visible-light-induced photocatalysts in the past few decades, there have been only a limited number of reports on environmental applications of non-metal, platinum-group metal co-doped TiO₂. The non-metal, platinum-group metal co-doping of TiO₂ may result in a material with excellent photocatalytic performance compared to singly doped TiO₂. In this chapter, nitrogen, palladium co-doped TiO₂ nanoparticle photocatalysts were synthesised by a modified sol-gel method and investigated for their visible-light-induced photocatalytic degradation effect on Eosin Yellow (EY) (**Figure 4.1**).

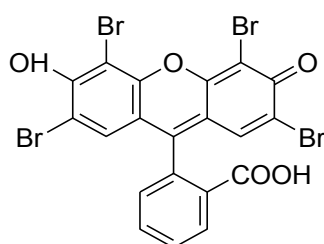


Figure 4.1 Chemical structure of Eosin Yellow

4.2 EXPERIMENTAL DETAILS

4.2.1 Preparation of materials

N, Pd co-doped TiO₂ was prepared by a modified sol-gel method using ammonium hydroxide as a source of nitrogen, solvent for the Pd precursor and a hydrolysing

reagent. An aliquot of 10 mL of titanium isopropoxide, Ti(OC₃H₇)₄, (97%, Sigma Aldrich, Germany), was added to 50 mL of 2-propanol, C₃H₈O, (99.8%, Sigma Aldrich, Germany) and stirred for about 10 min. An appropriate amount of palladium diamine dichloride, Pd(NH₃)₂Cl₂, (45% Pd, PGM Chemicals, RSA) to give a Pd:Ti proportion of 0.2%, 0.4%, 0.6%, 0.8% and 1.0%, was dissolved in 3 mL of 25% ammonia, NH₃, (Merck, Germany). The ammoniacal solution was then slowly added to the isopropoxide/propanol solution with vigorous stirring for about half an hour. Stirring was continued for 1 h. The resulting sol was dried in air at 80°C for 12 h to obtain a white powder. The powder was calcined for 2 h at 500°C in air in an electric furnace and characterised by various methods. The 0% Pd sample was prepared by the same method without the addition of Pd(NH₃)₂Cl₂.

4.2.2 Material characterisation

Materials were characterised using various techniques as described in **Section 3.6**.

4.2.3 Evaluation of photocatalytic activity

The photocatalytic performance of the N, Pd co-doped TiO₂ (0.0% to 1.0% Pd) was quantified by measuring the rate of degradation of EY under visible-light irradiation using a 150 W tungsten filament lamp (Eurolux), kept at a distance of 10 cm from the reaction vessel (**Section 3.7**).

4.3 RESULTS AND DISCUSSION

4.3.1 FT-IR studies

FT-IR studies were performed in order to determine the presence of functional groups as well as to study the surface changes on the particles at different Pd dopant levels (**Figure 4.2**). The presence of OH groups and water on the surface of the particles is evidenced by the appearance of a broad band between 3 400 cm⁻¹ and 3 210 cm⁻¹ for all samples. Another peak associated with O-H bending also appears around 1 644 cm⁻¹. There is an increase in the intensity of the O-H

peaks with increasing amounts of Pd, showing the increase in surface OH groups. A very intense peak centred around 520 cm⁻¹ appears for all samples. This peak is attributed to the Ti-O bond. The peak at around 2340 cm⁻¹, which appears only for the N-doped sample, may be due to out-of-phase stretching of the -N=C=O or -N=C-C bond. The peak disappears with the introduction of Pd due to the preferential formation of PdO enhanced by heat treatment in air.

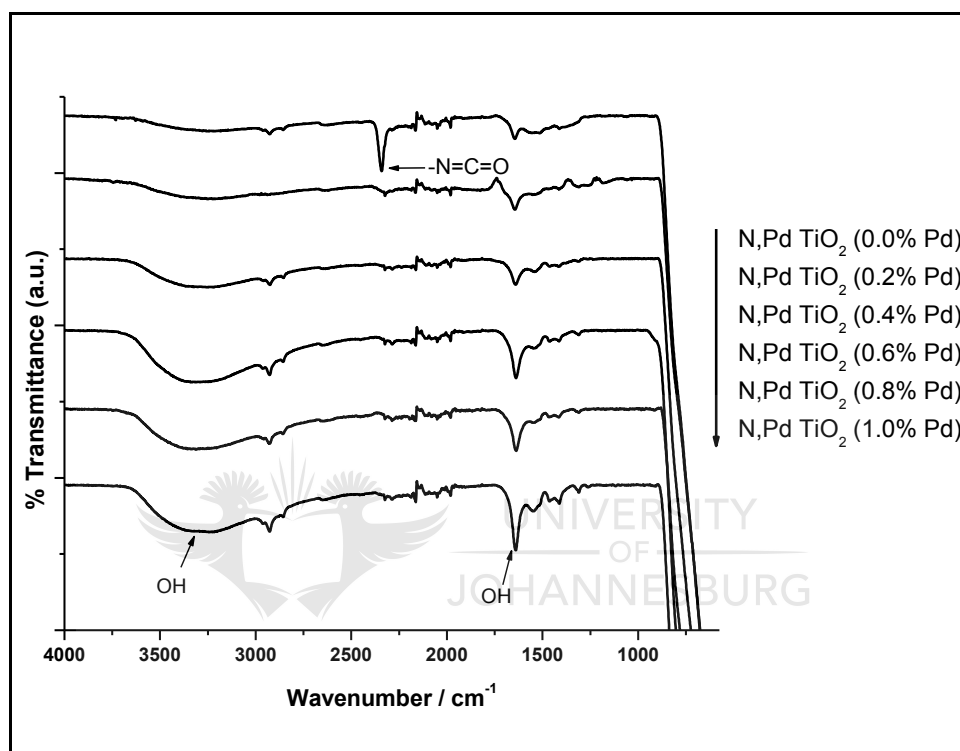


Figure 4.2 FT-IR spectra of N, Pd co-doped TiO₂ with different palladium concentrations

4.3.2 Raman analysis

Raman analysis of the samples was carried out on a Perkin Elmer Raman microscope in the 100 cm⁻¹ to 800 cm⁻¹ frequency range with laser excitation of 785 nm (**Figure 4.3**). Anatase TiO₂ shows six Raman-active fundamental modes at 144 cm⁻¹ (E_g), 197 cm⁻¹ (E_g), 397 cm⁻¹ (B_{1g}), 518 cm⁻¹ (A_{1g} + B_{1g}) and 640 cm⁻¹ (E_g).⁷ Well-resolved Raman peaks were observed at 146 cm⁻¹ (E_g), 198 cm⁻¹ (E_g), 397 cm⁻¹ (B_{1g}), 516 cm⁻¹ (A_{1g} + B_{1g}) and 636 cm⁻¹ (E_g) in the spectra of all the samples calcined at 500°C, indicating that anatase was the predominant phase.

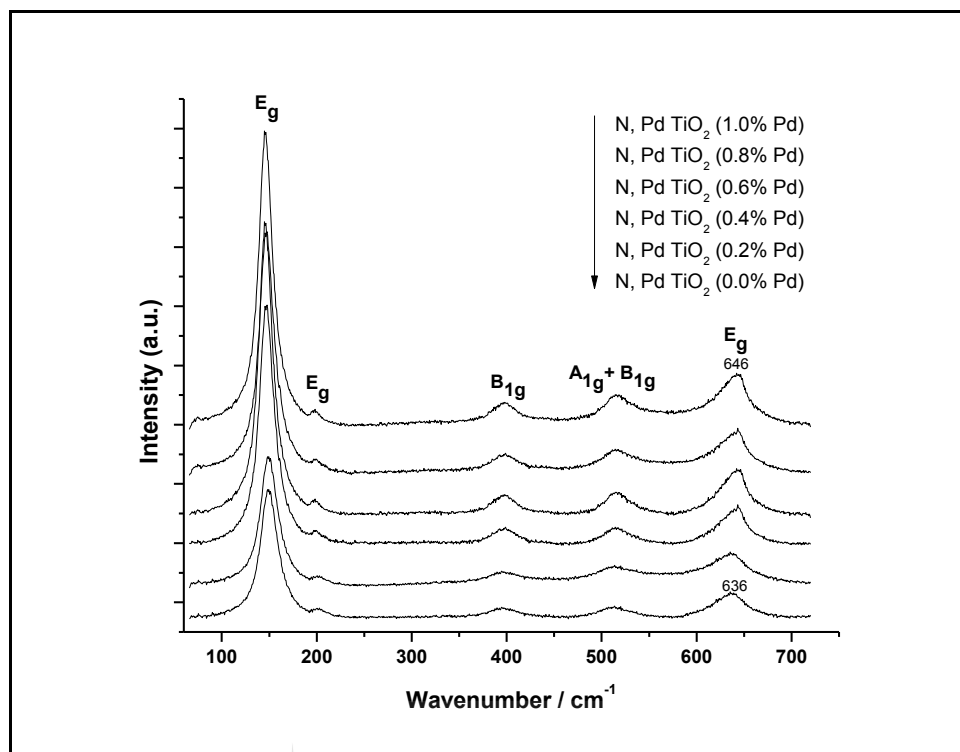


Figure 4.3 Raman spectra of N, Pd co-doped TiO₂ with different palladium concentrations

PdO has two Raman-active modes ($B_{1g} + E_g$). The allowed Raman modes are assigned to lines at 651 cm^{-1} (B_{1g}) and 445 cm^{-1} (E_g), respectively. The highly intense B_{1g} mode is due to scattering from the (001) face and the E_g mode from the (110) face.¹³ There is a shift in the position of the high-frequency anatase E_g with an increasing amount of Pd, with the N, Pd TiO₂ (0.0% Pd) appearing at 636 cm^{-1} whilst that of N, Pd TiO₂ (1.0% Pd) appeared at 646 cm^{-1} . This shift may indicate the presence of PdO in high Pd level samples. No Raman lines due to PdO E_g mode appeared in all the samples because of the low intensity, confirming the presence of the dopant in low concentrations on the crystal lattice. Sharp, narrow intense peaks at low wave numbers confirmed the presence of the particles in the crystalline state. The TiO₂ crystalline structure was not changed by the doping procedure.

4.3.3 XRD analysis

Figure 4.4 shows XRD patterns of the N-doped and N, Pd co-doped TiO₂ subjected to heat treatment at 500°C for 2 h. Post-synthesis treatment by thermal annealing resulted in increased crystallinity with anatase as the principal phase in agreement with Raman spectra. Peaks at 2θ values of 25.3, 37.6, 48.2, 53.9, 54.8, 62.7 and 75.2 corresponding to the (101), (004), (200), (105), (211), (204) and (215) planes, respectively, are all anatase signature peaks. Calcination resulted in intense and sharp anatase peaks. This is clearly indicative of an improvement in the degree of crystallinity corresponding to the formation of larger particles with fewer defects. No obvious diffraction peaks attributed to the N or Pd dopants were observed at low dopant levels. However, a PdO peak (101) at 2θ value of 33.8 appears at Pd levels greater than 0.4%. Another PdO peak can be observed for the 1% Pd sample at a 2θ value of about 42. The absence of nitrogen or nitrogen-related compound XRD peaks could be explained by the low nitrogen dopant levels or it could be an indication that the nitrogen atoms were well-dispersed in/on the TiO₂ particles. This resulted in the TiO₂ maintaining its anatase polymorph.

In N-doped TiO₂, the nitrogen atoms can substitute the O atoms in the lattice because of the similarity in the atomic radii of the two atoms. Pd will most likely be located in interstitial positions on the lattice rather than directly on Ti⁴⁺ sites because of the relatively large size difference between the ions (0.86 Å for Pd²⁺ and 0.68 Å for Ti⁴⁺).¹⁴

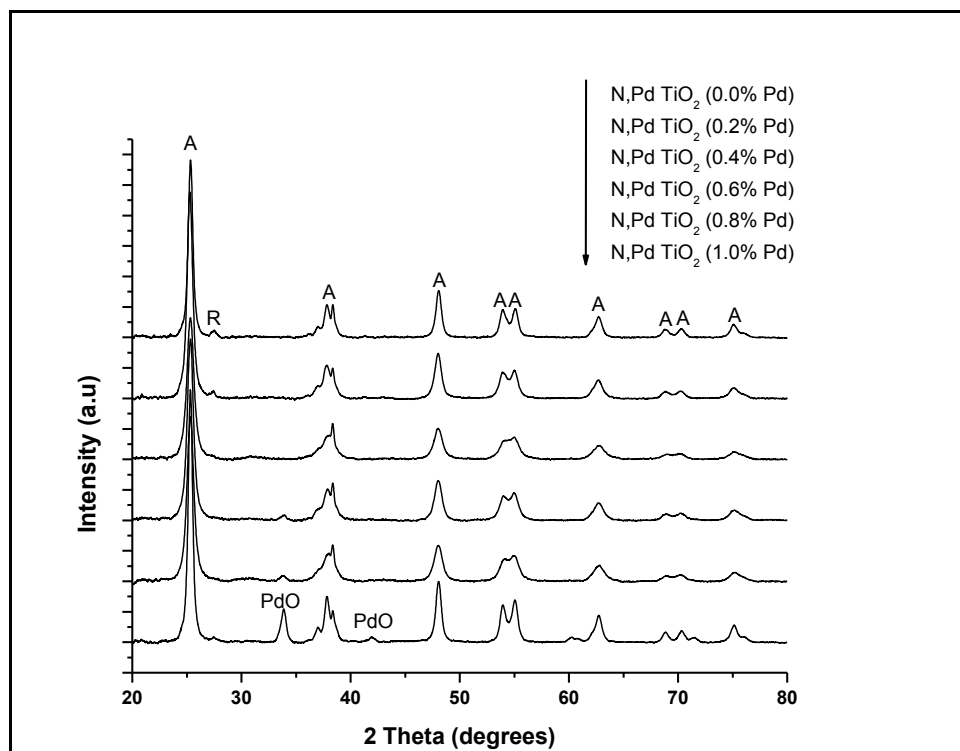


Figure 4.4 XRD patterns of N, Pd co-doped TiO₂ with different palladium concentrations (A – anatase)

The presence of Pd ions inhibited the anatase to rutile transformation as shown by the increase in the anatase phase with increasing Pd content (**Table 4.1**). This is ascribed to the fact that defects are formed on the grain boundaries of the TiO₂ resulting in distortion of ordering, consequently reducing the anatase to rutile transformation.

The crystallite size was calculated by X-ray line broadening analysis using the Scherrer equation (**Equation 3.8, Section 3.6.4.1**) Results of the particle sizes and phase composition are shown in **Table 4.1**. There is generally a slight increase in particle size with increasing amount of Pd. At concentrations lower than 0.4%, Pd is incorporated in the TiO₂ structure (probably in interstitial positions). As Pd concentration increases, it becomes segregated from the TiO₂ structure. This allows growth of TiO₂ crystallites, leading to slightly bigger sizes. Maicu *et al.* reported on a particle size of 17 nm for Pd-doped TiO₂ (1.5% Pd) using the Scherrer equation.¹⁵ All the samples consisted of mainly the anatase phase.

Table 4.1 Effect of Pd dopant level on average crystallite size and phase composition

Sample	Crystallite size (nm)	Phase content (% anatase)
N, Pd co-doped TiO ₂ (0.0% Pd)	18	96
N, Pd co-doped TiO ₂ (0.2% Pd)	15	97
N, Pd co-doped TiO ₂ (0.4% Pd)	17	98
N, Pd co-doped TiO ₂ (0.6% Pd)	18	100
N, Pd co-doped TiO ₂ (0.8% Pd)	16	100
N, Pd co-doped TiO ₂ (1.0% Pd)	20	100

4.3.4 Optical properties

The UV-Vis diffuse reflectance spectra of the photocatalysts are shown in **Figure 4.5**. The absorption edges of the light yellowish N-doped and light brownish N, Pd co-doped samples were shifted to a longer wavelength region as compared to that of commercial TiO₂. The shift in absorption intensity at wavelengths longer than 400 nm was enhanced with an increasing amount of Pd.⁶ A broad band between 450 nm and 550 nm centred at 500 nm was observed in the absorption spectrum of N, Pd co-doped TiO₂ containing 1.0% Pd, owing to d–d transitions of PdO particles.¹⁶ The spectrum of P25 showed single intense absorption around 400 nm due to a charge-transfer transition between the lattice oxygen ligands (O²⁻) and a central titanium ion (Ti⁴⁺).¹⁴ It can be seen that the N, Pd TiO₂ (0.0% Pd) sample presents a significant absorption in the visible region between 400 nm and 700 nm. This could be due to the excitation of electrons from localised nitrogen 2p levels in the band gap to the vacant CB, confirming the presence of Ti-N bonds.¹⁷ Qiu and Burda reported that N doping, even with significantly high doping levels, may not cause significant band-gap narrowing effects.¹⁸ The major effect of N doping on the absorption spectra is the greatly enhanced absorption at long wavelength regions (>400 nm) in the N-doped TiO₂, which might be useful in

enhancing the photocatalytic visible-light activities of these materials. Increasing amount of Pd led to higher absorbancies in the visible region, emphasising the synergistic effect of co-doping in enhancing visible-light activity.

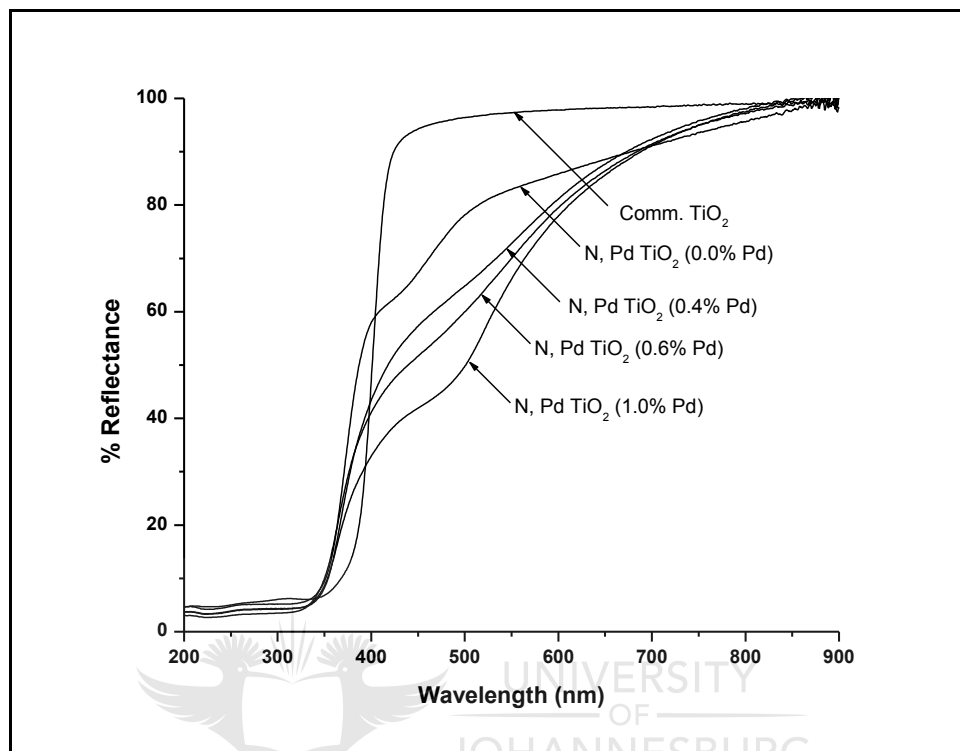


Figure 4.5 Diffuse reflectance UV-Vis spectra of N, Pd co-doped TiO₂ with different palladium concentrations

The diffuse reflectance spectra were plotted as the Kubelka–Munk function, $F(R)$, vs. wavelength, (**Figure 4.6**), based on the Kubelka–Munk equation (**Equation 3.4, Section 3.6.3.1**). The type of transition in TiO₂ is not clear.¹⁹ For a direct allowed band-gap semiconductor the plot with $n = 2$ will show a linear Tauc region just above the optical absorption edge. Extrapolation of this line to the photon energy axis yields the semiconductor band gap, a key indicator of its light-harvesting efficiency under solar illumination. Indirect allowed band-gap materials show a Tauc region with $n = 1/2$ (**Section 3.6.3.2**).²⁰

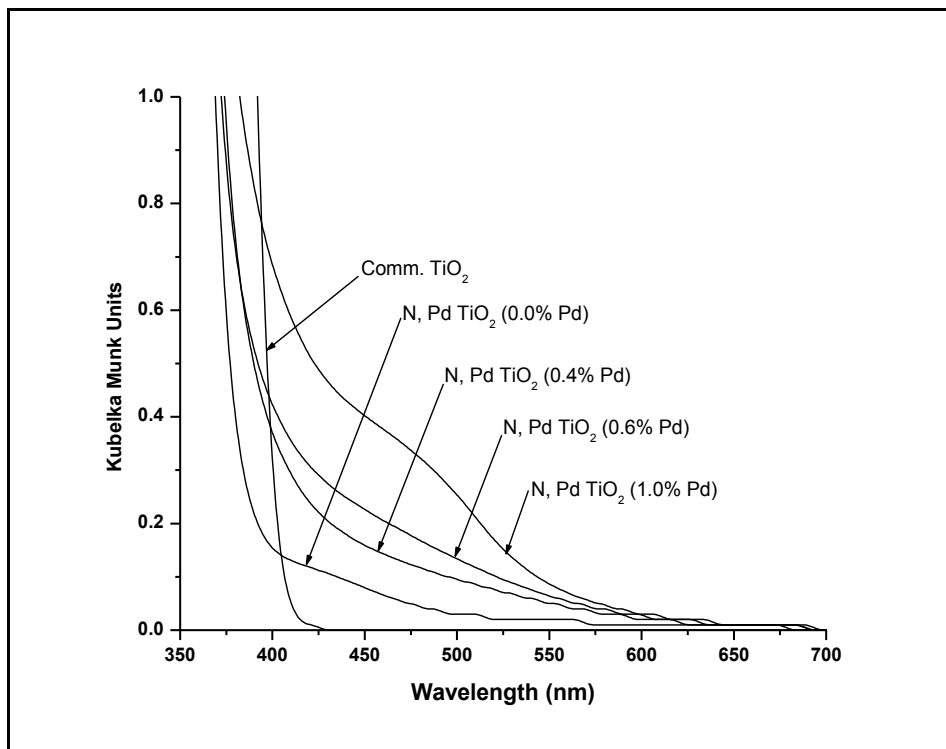


Figure 4.6 Kubelka-Munk plots of N, Pd co-doped TiO₂ with different palladium concentrations

Comparison of the spectra of commercial and co-doped samples show no notable differences in the UV region, with the strong, broad absorption observed below 400 nm associated with charge-transfer from the valence to the conduction band of the TiO₂.¹⁵ As the palladium doping amount is increased, band tailing becomes evident, with the onset of absorption at lower energy. The doping smears out the linear region making a more rounded shape (**Figure 4.7**).

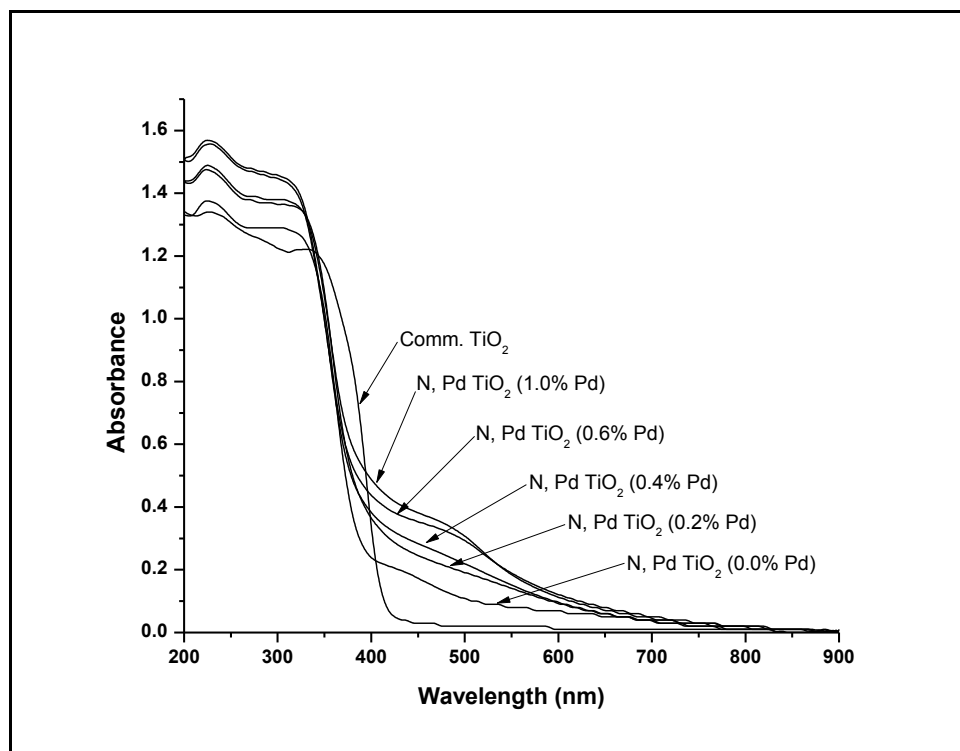


Figure 4.7 UV-Vis absorption spectra of N, Pd co-doped TiO₂ with different palladium concentrations

The character of the band gap may be becoming more indirect with added palladium. The red shift in the absorption edges is typically attributed to the sp - d exchange between the TiO₂ band electrons and localised d-electrons associated with the doped Pd ions. The absorption at low energy in higher dopant samples may indicate the formation of palladium-derived states near the band edge. Band tails can arise from perturbations in the band structure caused by impurities and disorder. States introduced by impurities overlap at high concentrations and evolve into impurity bands. The tails' intensity increases with increasing palladium levels. The tails are most likely related to the increase of impurity states.²¹ Therefore, the low-energy absorption onset is likely an electron transition from the valence band to palladium-derived impurity states.

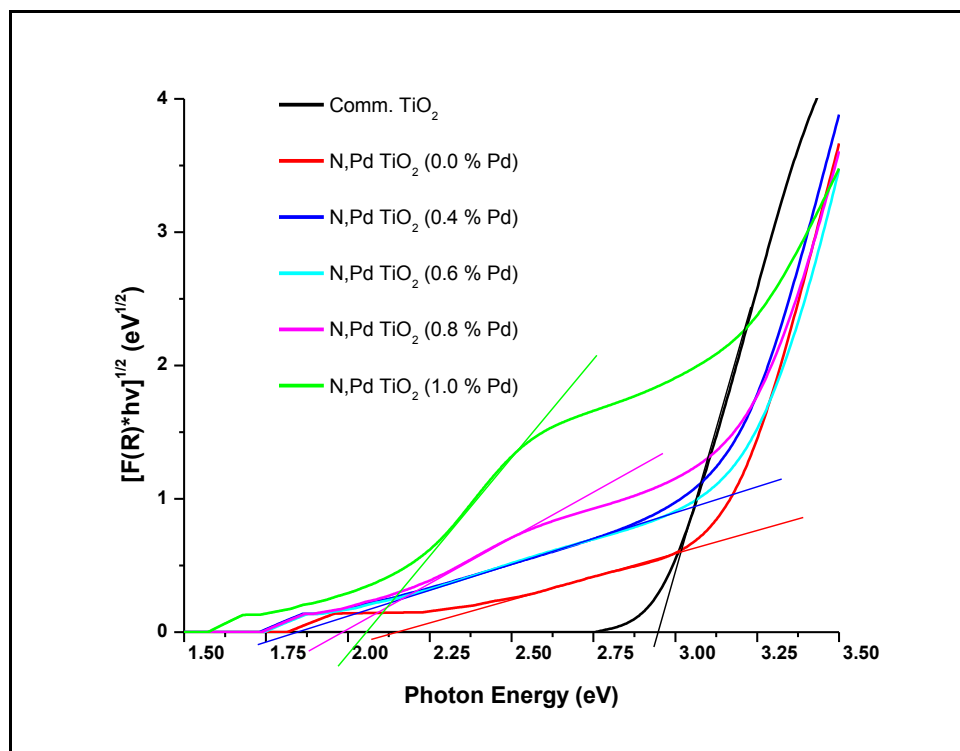


Figure 4.8 Tauc plots of N, Pd co-doped TiO₂ with different palladium concentrations

The band gaps (E_g) for all the catalysts were determined from the extrapolation of the linear fit for the Tauc plot onto the low-energy axis (**Figure 4.8**).²² Commercial TiO₂ shows a well-defined absorption edge that can be fit reliably to the energy axis. Assuming an indirect allowed band gap for all the samples, there is generally a gradual reduction in band gap with increasing amount of Pd. However, at much higher Pd content (1.0%), the band gap increases due to the dominance of the d-d transitions over the sp-d transitions (**Table 4.2**). This might also be due to the preferential formation of PdO at higher Pd levels, confirmed by XRD.

Table 4.2 Effect of Pd dopant level on band gap

Sample	Indirect band gap (eV)	λ_{\max}
Commercial TiO ₂ (Degussa P25)	2.95	439
N, Pd co-doped TiO ₂ (0.0% Pd)	2.16	599
N, Pd co-doped TiO ₂ (0.4% Pd)	1.87	691
N, Pd co-doped TiO ₂ (0.6% Pd)	1.85	699
N, Pd co-doped TiO ₂ (0.8% Pd)	1.99	650
N, Pd co-doped TiO ₂ (1.0% Pd)	2.06	627

4.3.5 SEM, TEM and EDS analyses

A SEM image of one of the thermally treated N, Pd co-doped TiO₂ samples is shown below (**Figure 4.9(a)**). The sample consists of small, nearly spherical and larger elongated particles. The size of the particles is in the nanometre range. The particles show some degree of aggregation. TEM images confirm the presence of Pd deposits on the surface of the N-doped TiO₂ (**Figure 4.9(b) and 4.9(c)**). Pd deposits are well dispersed on many of the TiO₂ particles with diameters predominantly ranging from 1 nm to 2 nm. The size of the TiO₂ particles is approximately in the range of 15 nm to 20 nm consistent with XRD measurements. This is in agreement with results reported by Wu *et al.*²³

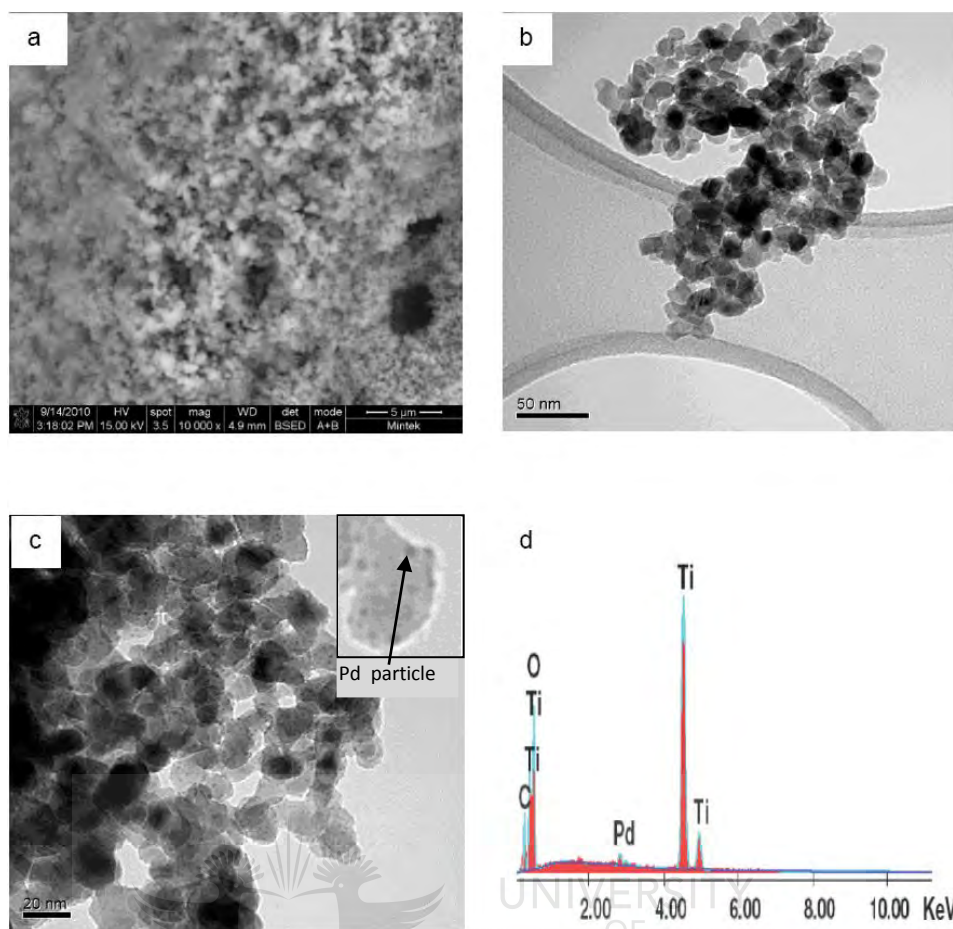


Figure 4.9 (a) SEM image; (b) and (c) TEM images; and (d) EDX spectrum of N, Pd co-doped TiO₂ (0.6% Pd)

The elemental composition of the various samples was estimated by EDX. The EDX spectra of the co-doped TiO₂ show signals directly related to the dopants (**Figure 4.9(d)**). The spectrum indicates that the main components are O and Ti with low levels of Pd. This confirms the formation of N, Pd co-doped TiO₂. Low-intensity peaks due to Pd, a co-dopant, are also visible. A carbon tape was used so the C peak also appears on the EDX spectrum. However, there is possibility of C doping of TiO₂ from the organic precursors that were used in the synthesis of the materials.

4.3.6 Thermal analysis

Figure 4.10 shows the thermogram obtained for some N, Pd co-doped TiO₂ nanoparticles heated at 500°C. The mass loss at around 100°C is attributed to the

loss of water adsorbed onto the particle surface. A small weight loss from 100°C up to about 900°C could be due to loss of nitrogen or carbon-related materials entrapped within the nanoparticles. The total mass loss of between 2.0% and 5.5% shows the exceptionally high thermal stability of the materials. This confirms that much of the nitrogen and carbon material was lost through calcination at 500°C.

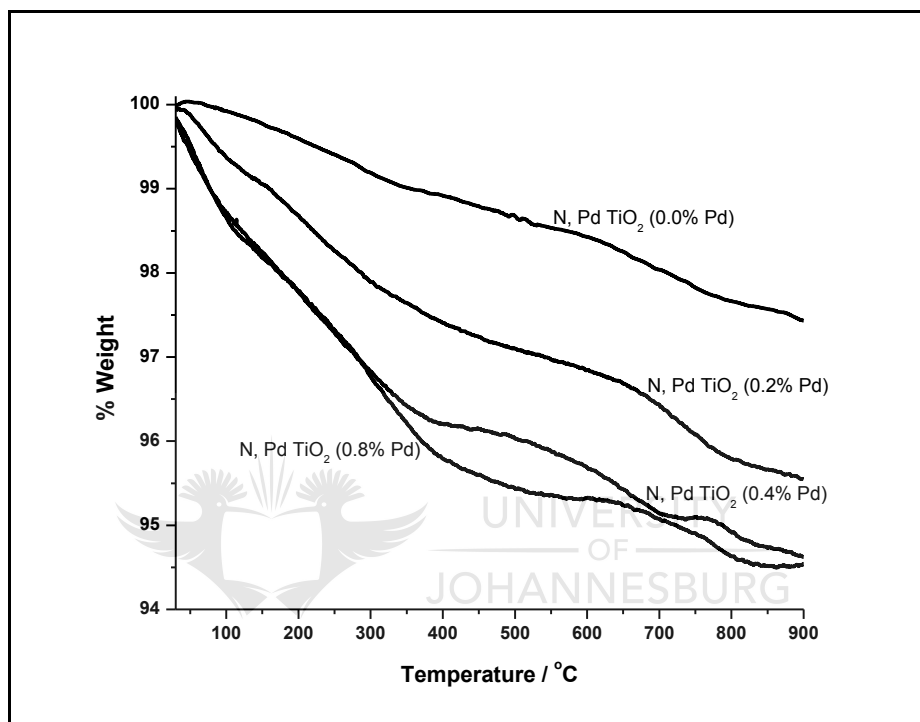


Figure 4.10 TGA curves of N, Pd co-doped TiO₂ with different palladium concentrations

4.3.7 XPS studies

The surface compositions of the catalysts were confirmed by XPS analysis. Samples were analysed without any sputtering using an instrument with a detection limit of 0.1 at.%. **Figure 4.11(a)** shows representative XPS survey spectra of N, Pd co-doped TiO₂ (0.6% Pd) and **Figure 4.11(b)** shows an XPS survey scan of N-doped TiO₂ powders. Photoelectron peaks of Ti 2p and O 1s are clearly visible for both samples. In **Figure 4.11(a)**, the presence of Pd in the N, Pd co-doped TiO₂ (0.6%) sample was confirmed by the appearance of Pd 3d and Pd 3s peaks. Also a B 1s peak appeared in both samples and can be attributed to

impurities from the glass reaction vessel used in preparing the samples. S was also detected in the N-doped sample.

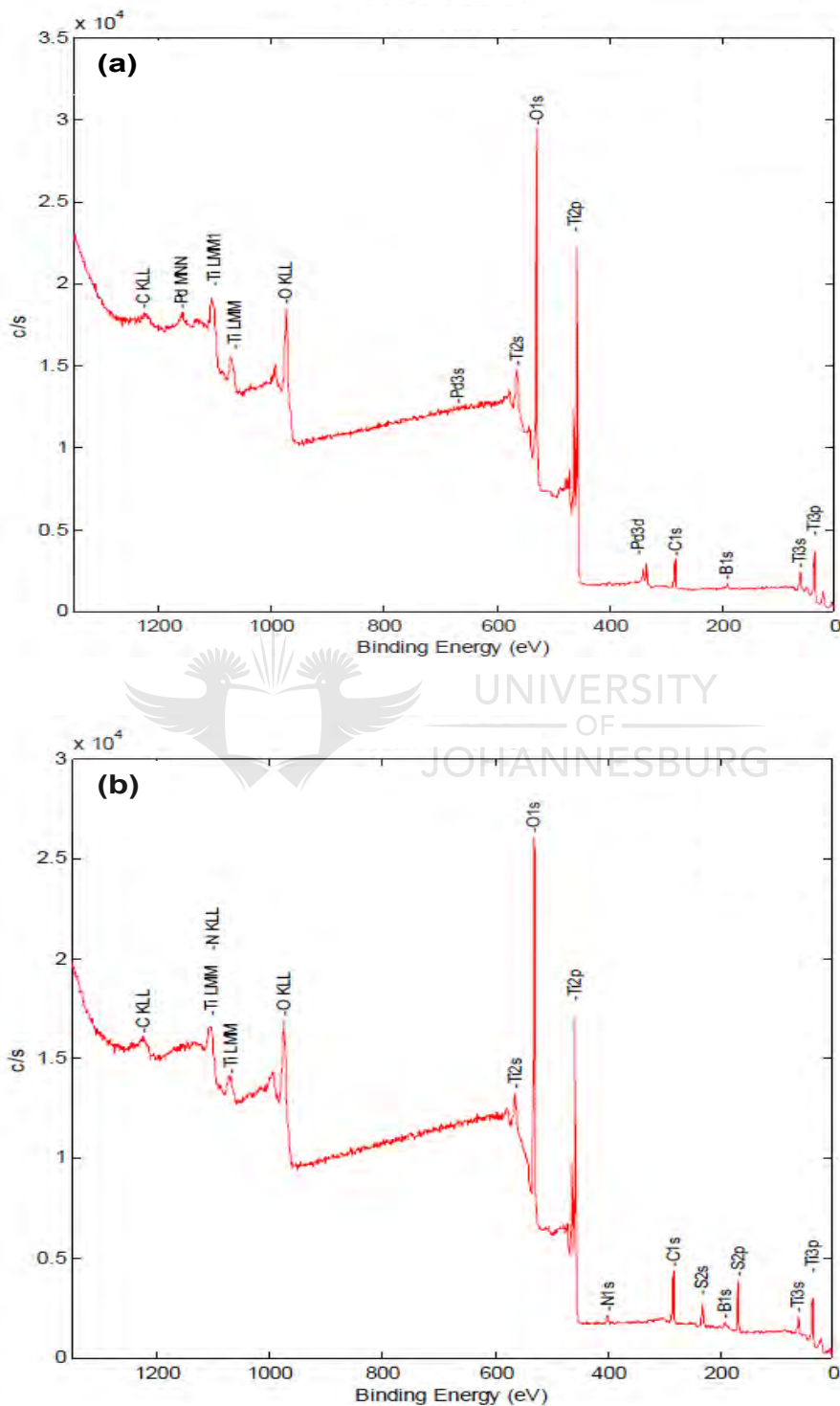


Figure 4.11 XPS survey scan of (a) N, Pd co-doped TiO₂ (0.6% Pd); and (b) N-doped TiO₂

No observable N 1s photoelectron peaks appeared for N, Pd co-doped TiO₂ (0.6% Pd) due to the low levels of doped nitrogen after calcination at 500°C or the peaks could have been below the detection limit. It is also possible that the Pd could be sitting on the N defect sites on the TiO₂ particles, thereby reducing the chances of emission from N. Samples were not sputter-cleaned with argon prior to analysis. This might have caused poor emission from the N 1s due to superficial contaminants.

Figure 4.12 shows the high-resolution XPS scans over the Pd 3d, Ti 2p, O 1s and N 1s peak regions. The binding energies of Pd 3d_{5/2} (335.6 eV) and 3d_{3/2} (341.6 eV) revealed that palladium was in the form of PdO or metallic Pd for N, Pd co-doped TiO₂.⁶ Loaded Pd was oxidised to PdO in the preparation procedure in agreement with Raman, SEM and XRD observations. Another peak at around 671.2 eV (Pd 3s) signals the presence of a small amount of Pd⁰ in the co-doped samples. Two peaks around 458.3 eV and 464.3 eV were observed for both samples. These peaks can be assigned to the spin orbit doublet of Ti 2p_{3/2} and Ti 2p_{1/2}, respectively, indicating the presence of TiO₂. This is in agreement with Raman and XRD results. Other peaks associated with Ti were observed at about 37.5 eV (Ti 3p), 61.0 eV (Ti 3s) and 561.0 eV (Ti 2s) (**Figure 4.11**). The peak at 37.5 eV confirmed the presence of Ti⁴⁺ as an oxide whilst the one at 61.0 eV could possibly be due to the presence of Ti³⁺ again in the oxide form, indicating possible formation of oxygen vacancies (defects) on the TiO₂ surface. The peak at 530.2 eV for both samples is attributed to the O²⁻ ion (O 1s_{1/2}) in the TiO₂ lattice or PdO. This peak shows a shoulder that stretches up to about 335.0 eV. This shoulder could be due to OH groups from Ti-OH bonds. Presence of N in the N-doped TiO₂ was confirmed by the appearance of an N 1s peak around 400 eV (**Figure 4.12(d)**). Asahi and co-workers (2001) reported three N 1s peaks with binding energies of 402 eV, 400 eV and 396 eV which were assigned as atomic β-N (396 eV) and molecularly chemisorbed γ-N₂ (400 eV and 402 eV).⁵ This could also indicate the presence of NO species since the N 1s is attributed to NH₃ or NO_x species²⁴. The presence of Ti-N bonds cannot be ruled out. The N in this bond is also expected to appear in the same region.

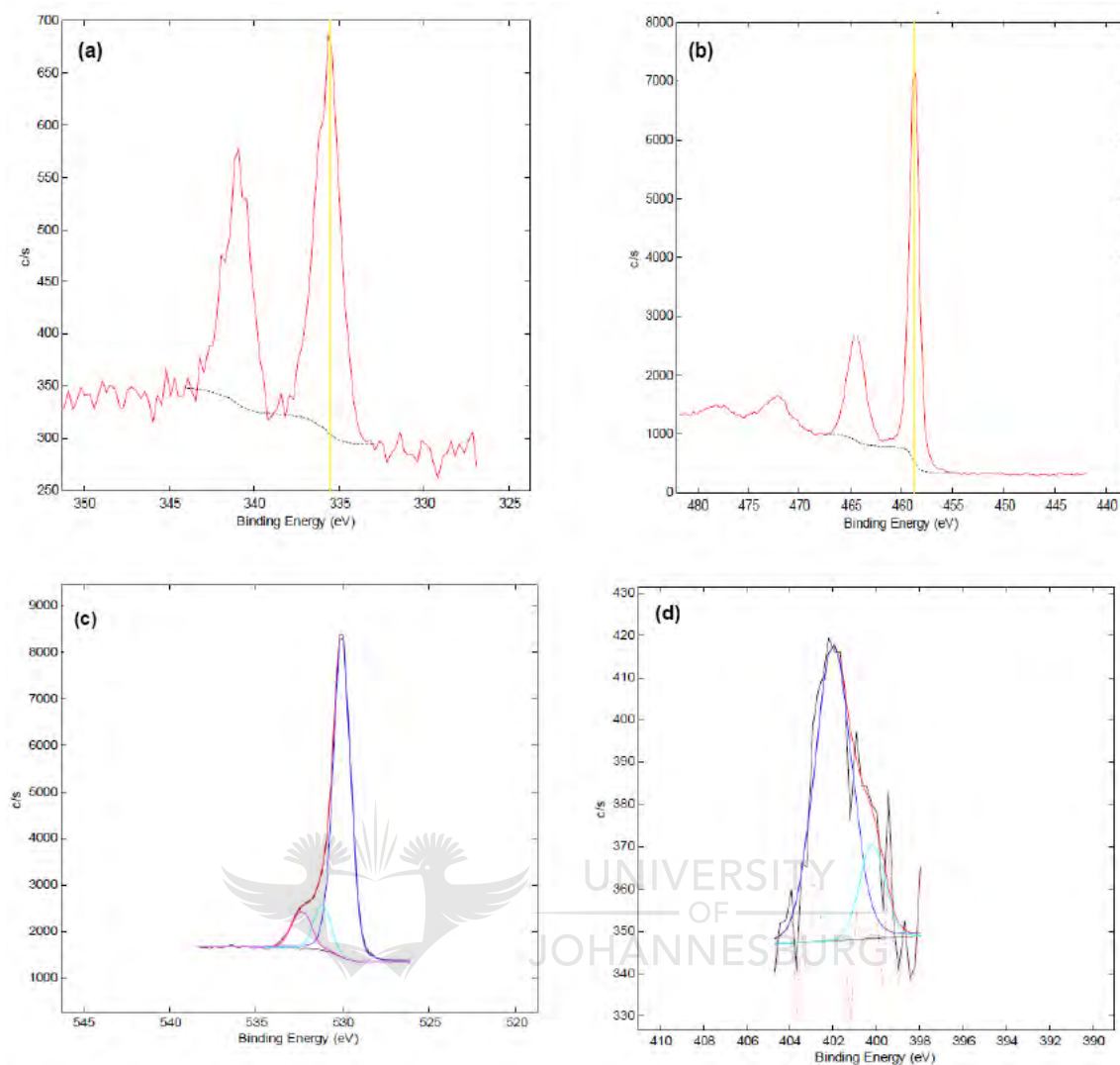


Figure 4.12 High resolution XPS scan over (a) Pd 3d; (b) Ti 2p; (c) O 1s in N, Pd TiO₂; and (d) N 1s in N TiO₂

Table 4.3 shows the relative atomic element composition of the materials from XPS scans over N 1s, O 1s, Pd 3d, and Ti 2p spectral regions for both samples. There are very small differences in the amount of Ti and O in the samples. However, introduction of Pd appeared to lower the nitrogen content. The amount of Pd in the co-doped sample was within the expected range for the sample.

Table 4.3 Core-level XPS elemental analysis results for the N-doped TiO₂ and N, Pd co-doped TiO₂

Sample	Atomic percentages				
	Ti	O	Pd	N	C
N-doped TiO ₂	20.8	56.9	-	1.6	18.6
N, Pd co-doped TiO ₂	21.1	59.5	0.8	-	14.8

4.4 DYE PHOTODEGRADATION STUDIES

The amount of EY was plotted as a function of irradiation time. From the results it is clear that the photodegradation of EY in the presence of the semiconductor powders led to the disappearance of the compound (**Figure 4.13**). The disappearance of the 515 nm absorption band suggests that the chromophore responsible for the characteristic colour of the dye was being broken down. Complete dye degradation was realised after 180 min for the N, Pd TiO₂ (0.6% Pd) sample.

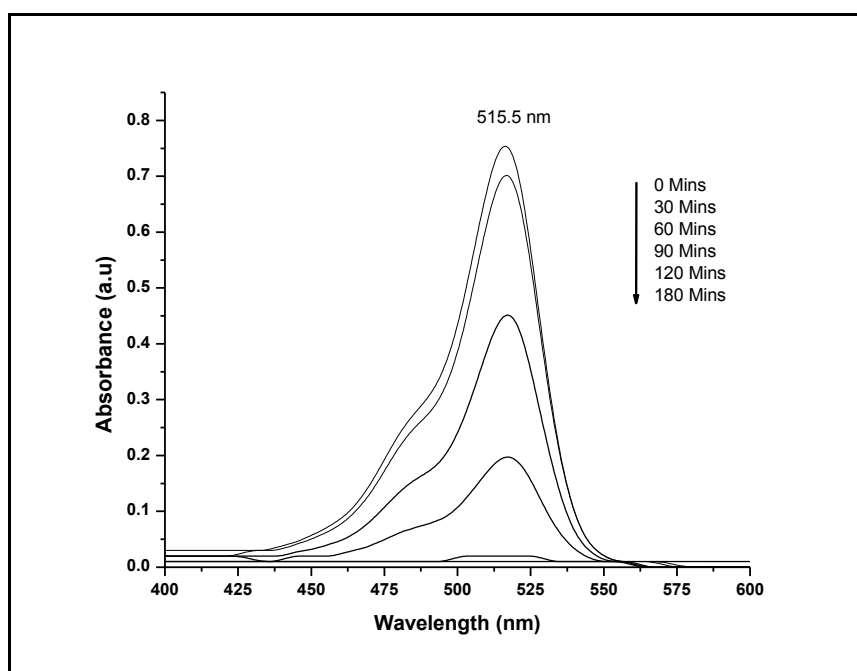


Figure 4.13 Eosin Yellow degradation profile using N, Pd TiO₂ (0.6% Pd)

The apparent rate constants obtained with various catalyst samples with different palladium content are shown in **Table 4.3**. The EY degradation rate on the commercial TiO₂ under visible-light irradiation is very low (18.2%). After 3 h of illumination, no detectable decolourisation was observed for the commercial TiO₂. In contrast, N-doped and N, Pd co-doped TiO₂ nanostructures exhibited substantial photocatalytic activity within the time frame of the tests. Recent research studies have shown that the desired band-gap narrowing of TiO₂ can be better achieved by using non-metal elements such as N.²⁵ Liu *et al.* prepared N-doped TiO₂ by using titanium isopropoxide and ammonia as precursors. The calcined photocatalyst (10 mg/l) was tested for the degradation of 15 ml of 0.03 mM Acid Orange 7 (AO7), Procion® Red MX-5B and Reactive Black 5 (RB5) under sunlight irradiation. They observed 70% degradation of AO7 in 1 h, 100% degradation of MX-5B in 3 h and 80% total organic carbon (TOC) removal in RB5 in 4 h.²⁶

The higher photocatalytic activity observed for N, Pd co-doped TiO₂ (0.6% Pd) compared to commercial TiO₂ (Degussa P25) may be attributed to the Pd effectively capturing the photo-induced electrons, which inhibited their recombination with holes and improved the photocatalytic activity. It is believed that the metal induces greater enhancements in the photocatalytic activity of TiO₂ by creating a Schottky junction between metal and semiconductor. The metal particle acts as a sink for photogenerated electrons, reducing the rate of their recombination with holes.¹⁵ There is an increase in the degradation efficiency with increasing Pd content up to 0.6% Pd, then a decrease to 65.8% for the sample with the highest Pd content (**Figure 4.14**). A similar trend was reported for the oxidation of benzene using Pd-doped TiO₂.²⁷ The dosage level is an important factor in influencing the enhancement effect of noble metals. Below an optimum dosage level platinum-group metals can act as electron-hole separation centres, improve the charge separation, and thus enhance the photocatalytic efficiency of modified TiO₂. However, as dosage levels exceed optimum loading, they can act as electron-hole recombination centres which are detrimental to the photocatalytic activity.²⁵ This may also be due to shading of the photosensitive surface of TiO₂ by the metal dopant. The differences may also be explained by differences in the

optical thicknesses of each catalyst sample. Some catalysts may perform better in the reactor due to more photons being absorbed by the catalyst suspension. This observation led to the conclusion that the optimum amount of dopant for effective photoactivity is 0.6% Pd. Higher Pd levels, (1.0%), led to lower photodegradation rates as these become recombination centres, thus short-circuiting the system.

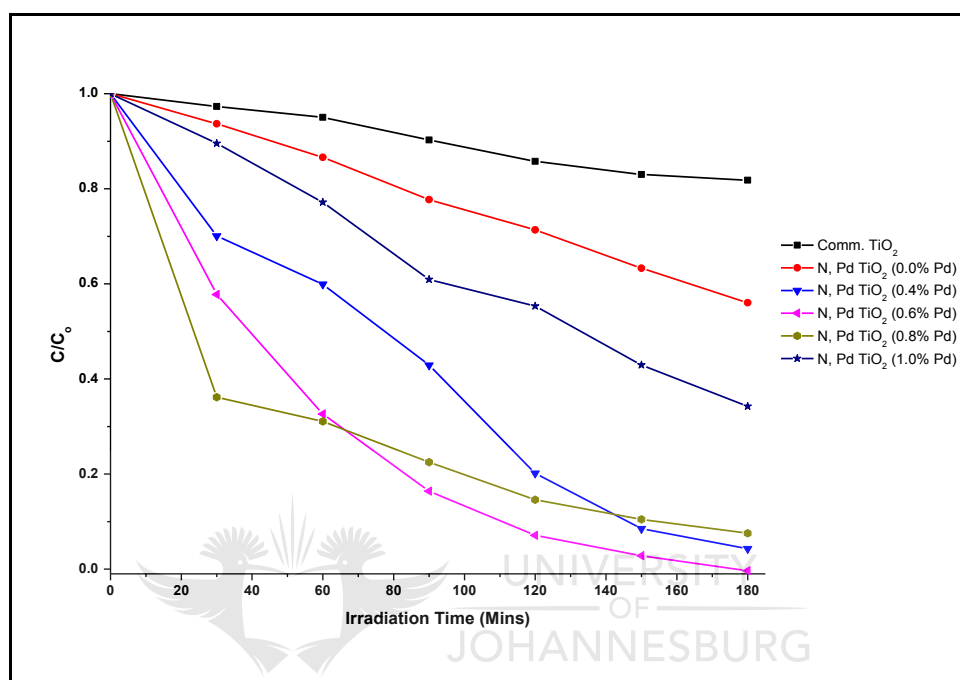


Figure 4.14 Eosin Yellow degradation by various photocatalysts

Table 4.4 Percentage degradation after exposure to visible radiation

Sample	% degradation after 180 min
Commercial TiO ₂ (Degussa P25)	18.2
N, Pd co-doped TiO ₂ (0.0% Pd)	44.0
N, Pd co-doped TiO ₂ (0.4% Pd)	95.7
N, Pd co-doped TiO ₂ (0.6% Pd)	100.0
N, Pd co-doped TiO ₂ (0.8% Pd)	92.5
N, Pd co-doped TiO ₂ (1.0% Pd)	65.8

Nitrogen and palladium have synergistic effects on improving the photocatalytic activity under visible-light irradiation. Under visible-light irradiation, substitutional nitrogen dopant can create intra-band-gap states close to the valence-band edges leading to a narrower band gap than P25 TiO₂. **Figure 4.15** shows the proposed possible mechanism for the synergistic effects of nitrogen and palladium on the co-doped photocatalysts. Under UV light illumination, electrons (e^-) are excited from the valence band (VB) to the conduction band (CB), creating holes (h^+) in the VB. Normally, these charge carriers quickly recombine and only a fraction of the electrons and holes participate in the photocatalytic reaction, resulting in low reactivity. Introduction of substitutional or interstitial nitrogen in the TiO₂ will result in the formation of impurity states close to the valence band. This enhances the visible-light activity of the nanoparticles as electrons can be excited from the nitrogen 2p orbitals to the conduction band.⁵ In the presence of Pd, the photogenerated electrons are trapped, leading to electron-hole separation. The holes can scavenge surface-adsorbed water or hydroxyl molecules generating highly reactive hydroxyl radical species. The electrons on the other hand scavenge the oxygen molecules to form very reactive superoxide radicals.²⁸ Both radicals are highly reactive towards the degradation of the organic compounds such as EY used in the present study.

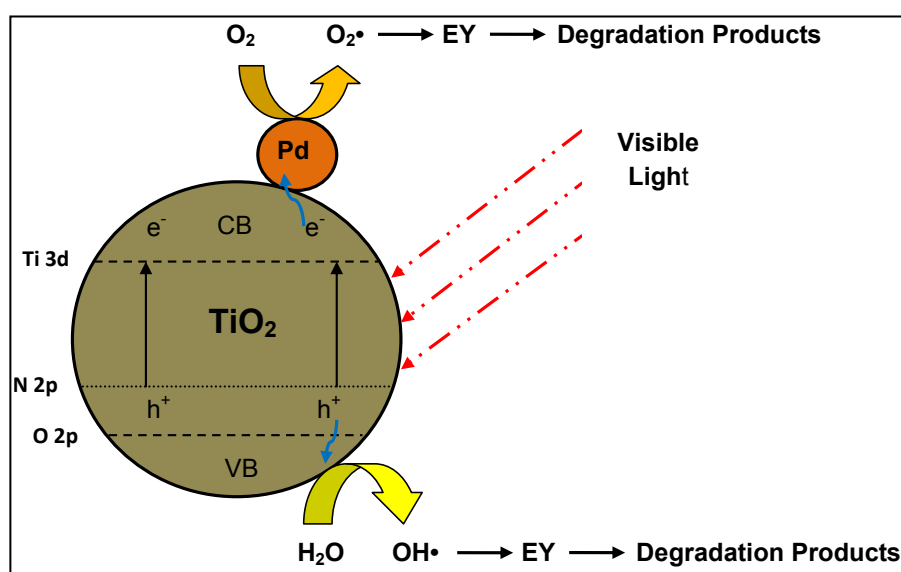


Figure 4.15 Proposed visible-light-induced photocatalytic mechanism of N, Pd co-doped TiO₂ photocatalyst

The kinetics of EY degradation are presented in **Figure 4.16** by plotting the logarithm of the normalised dye concentration against irradiation time for the first 60 min. Fairly good linear relationships were observed, indicating that all reactions followed first-order kinetics. Sun *et al.* reported a k value of $1.6 \times 10^{-3} \text{ min}^{-1}$ for N-doped TiO₂ prepared at a pH of 5.5.²⁴ This value is lower than the k value of $2.35 \times 10^{-3} \text{ min}^{-1}$ observed for N, Pd (0.0% Pd). N, Pd co-doped TiO₂ (0.8% Pd) showed the highest initial rate ($2.238 \times 10^{-2} \text{ min}^{-1}$), indicating faster dye decolourisation and higher catalytic activity. However, the rate decreased after 60 min, probably due to pseudo first-order kinetics. The initial rate for the N, Pd co-doped TiO₂ (0.8% Pd) was higher than that reported for Co, Cu, Os, Pt, Fe, Cr, V, Ni, Ru, Ag, Rb, Y and La doped TiO₂ for the degradation of methylene blue under visible-light irradiation.²⁹ Li *et al.* reported on the visible-light activity of palladium-modified nitrogen-doped TiO₂ (TiON/PdO) nanoparticles synthesised by a sol-gel process for photocatalytic degradation of humic acid. They realised an increase in the reaction rate constant from 0.0002 min^{-1} for TiON to 0.0003 min^{-1} for TiON/PdO containing 0.5% PdO. When the palladium concentration was further increased, an inverse effect was observed, wherein the rate constant decreased to 0.00015 min^{-1} for TiON/PdO with 2.0% PdO.⁶ These rates are several orders lower than the ones observed for the N, Pd co-doped TiO₂. The better performance of N, Pd co-doped nanoparticles could be explained by the possible synergistic effects of co-doping, though the difference in the photocatalytic activity can be influenced by the differences in material preparation method.

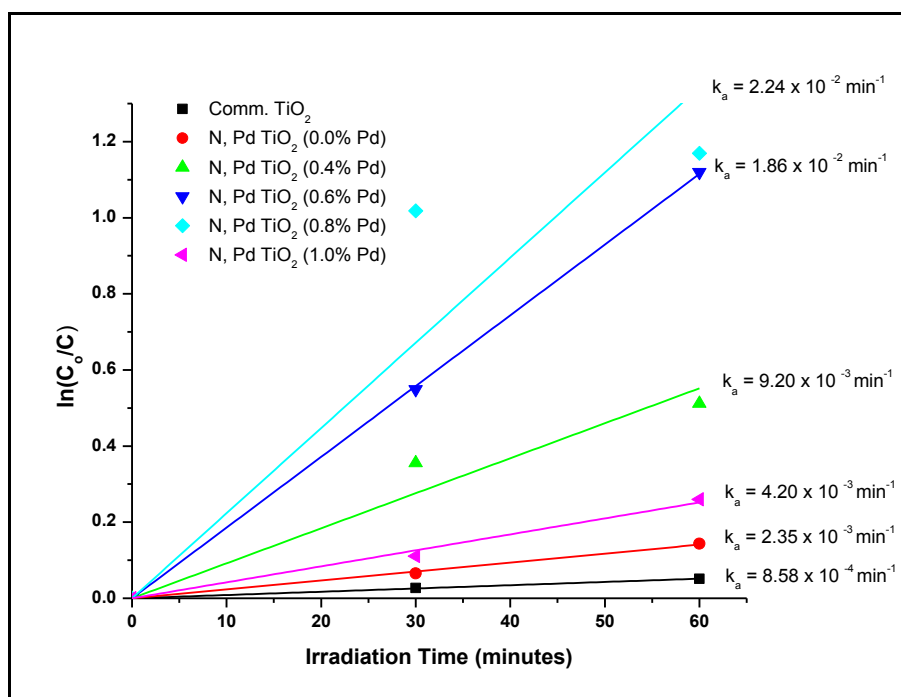


Figure 4.16 Kinetics of EY degradation in the first 60 min of visible-light irradiation

4.5 CONCLUSION

A simple method was developed for the preparation of highly visible active nanocrystalline N-doped and N, Pd co-doped TiO₂ photocatalysts by calcination of the hydrolysis product of titanium isopropoxide with ammonia solution. According to the XRD and Raman analysis, the photocatalysts were crystalline and consisted of mainly the anatase phase of TiO₂. UV-Vis spectra indicated that the nitrogen and nitrogen-palladium co-doping causes the absorption edge of TiO₂ to shift to a lower energy region, evidenced by the reduction in the band gaps. The highest photocatalytic activity was observed for the N, Pd co-doped TiO₂ (0.6% Pd) sample. Un-doped TiO₂ and P25 as well as N, Pd co-doped TiO₂ (1.0% Pd) showed the lowest degradation efficiency. Control of the dopant amount is very important as higher levels may result in the dopants becoming recombination centres. The synergistic effects of N and Pd co-doping led to enhanced utilisation of solar energy through narrowing of the band gaps. The presence of Pd sufficiently promoted the separation of photogenerated holes and electrons by

acting as electron traps leading to high photodegradation efficiency of EY under visible-light irradiation.

4.6 REFERENCES

1. Malato S., Ibanez P.F., Maldonado M.I., Blanco J. and Gernjak W. (2009). Decontamination and disinfection of water by solar photocatalysis: Recent overview and trends. *Catal. Today* 147, 1 – 59.
2. Song K., Zhou J., Bao J. and Feng Y. (2008). Photocatalytic activity of (copper, nitrogen)-codoped titanium dioxide nanoparticles. *J. Am. Ceram. Soc.* 91, (4), 1369 – 1371.
3. Mills A. and Hunte S.L. (1997). An overview of semiconductor photocatalysis. *J. Photochem. Photobiol. A: Chem.* 108, 1 – 35.
4. Nosaka Y., Matsushita M., Nishino J. and Nosaka A.Y. (2005). Nitrogen-doped titanium dioxide photocatalysts for visible response prepared by using organic compounds. *Sci. Technol. Adv. Mater.* 6, 143 – 148.
5. Asahi R., Morikawa T., Ohwaki T., Aoki K. and Taga Y. (2001). Visible-light photocatalysis in nitrogen-doped titanium oxides. *Sci.* 293, 269 – 271.
6. Li Q., Xie R., Mintz E.A. and Shang J.K. (2007). Enhanced visible-light photocatalytic degradation of humic acid by palladium-modified nitrogen-doped titanium oxide. *J. Am. Ceram. Soc.* 90, (12), 3863 – 3868.
7. Morikawa T., Ohwaki T., Suzuki K., Moribe S. and Kubota S.T. (2008). Visible-light-induced photocatalytic oxidation of carboxylic acids and aldehydes over N-doped TiO₂ loaded with Fe, Cu or Pt. *Appl. Catal. B: Environ.* 83, 56 – 62.
8. Wang J., Tafen D.N., Lewis J. P., Hong Z., Manivannan A., Zhi M., Li M. and Wu N. (2009). Origin of photocatalytic activity of nitrogen-doped TiO₂ nanobelts. *J. Am. Chem. Soc.* 131, 12290 – 12297.

9. Li D., Chen Z., Chen Y., Li W., Huang H., He Y. and Fu X. (2008). A new route for degradation of volatile organic compounds under visible light: Using the bifunctional photocatalyst Pt/TiO_{2-x}N_x in H₂-O₂ atmosphere, *Environ. Sci. Technol.* 42, 2130 – 2135.
10. Sivalingam G., Nagaveni K., Hegde M.S. and Madras G. (2003). Photocatalytic degradation of various dyes by combustion synthesised nano anatase TiO₂. *Appl. Catal. B* 45, 23 – 38.
11. Lin Z., Orlov A., Lambert R.M. and Payne M.C., (2005). New insights into the origin of visible light photocatalytic activity of nitrogen-doped and oxygen-deficient anatase TiO₂. *J. Phys. Chem. B.* 109, 20948 – 20952.
12. Lee S.K. and Mills A. (2003). Platinum and palladium in semiconductor photocatalytic systems. *Platinum Metals Rev.* 41, (2), 61 – 72.
13. McBride J. R., Hass K. C. and Weber W. H., (1991). Resonance-Raman and lattice-dynamics studies of single-crystal PdO. *Phys. Rev. B* 44, (10), 5016 – 5028.
14. Shah S.I., Li W., Huang C.P. and Jung O.C. (2002). Study of Nd³⁺, Pd²⁺, Pt⁴⁺, and Fe³⁺ dopant effect on photoreactivity of TiO₂ nanoparticles. *Proc. Natl. Acad. Sci. USA* 99, (9), 6482 – 6486.
15. Maicu M., Hidalgo M.C., Colon G. and Navio J.A. (2011). Comparative study of the photodeposition of Pt, Au and Pd on pre-sulphated TiO₂ for the photocatalytic decomposition of phenol. *J. Photochem. Photobiol. A: Chem.* 217, 275 – 283.
16. Zhang Z., Mestl G., Knozinger H. and Sachtler W.M.H. (1992). Effects of calcination program and rehydration on Pd dispersion in zeolites NaY and 5 A. *Appl. Catal. A.* 89, 155 – 168.

17. Cong Y., Zhang J.L., Chen F., Anpo M. and He D. (2007). Preparation, photocatalytic activity, and mechanism of nano-TiO₂ co-doped with nitrogen and iron (III). *J. Phys. Chem. C* 111, 10618 – 10623.
18. Qiu X. and Burda C. (2007). Chemically synthesized nitrogen-doped metal oxide nanoparticles. *Chemical Physics*. 339, 1 – 10.
19. Li Q., Xie R. and Shangw J.K. (2007). Effect of precursor ratio on synthesis and optical absorption of titanium photocatalytic nanoparticles. *J. Am. Ceram. Soc.* 90, (4), 1045 – 1050.
20. Serpone N., Lawless D. and Khairutdinov R. (1995). Size effects on the photophysical properties of colloidal anatase TiO₂ particles: Size quantization versus direct transitions in this indirect semiconductor. *J. Phys. Chem.* 99, 16646 – 16654.
21. Kittilstved K.R., Liu W.K. and Gamelin D.R. (2006). Electronic structure origins of polarity-dependent high-TC ferromagnetism in oxide-diluted magnetic semiconductors. *Nat. Mater.* 5, 291 – 297.
22. Wu Y., Zhang J., Xiao L. and Chen F. (2010). Properties of carbon and iron modified TiO₂ photocatalyst synthesised at low temperature and photodegradation of acid orange 7 under visible light. *Appl. Surf. Sci.* 256, 4260 – 4268.
23. Wu Z., Sheng Z., Liu Y., Wang H., Tang N. and Wang J. (2009). Characterization and activity of Pd-modified TiO₂ catalysts for photocatalytic oxidation of NO in gas phase. *J. Hazard. Mater.* 164, 542 – 548.
24. Sun H., Bai Y., Liu H., Jin W., Xu N., Chen G. and Xu B. (2008). Mechanism of nitrogen-concentration dependence on pH value: Experimental and theoretical studies on nitrogen-doped TiO₂. *J. Phys. Chem. C* 112, 13304 – 13309.
25. Han F., Kambala V. S. R., Srinivasan M., Rajarathnam D. and Naidu R. (2009). Tailored titanium dioxide photocatalysts for the degradation of

- organic dyes in wastewater treatment: A review. *Appl. Catal. A: Gen.* 359, 25 – 40.
26. Liu Y., Chen X., Li J. and Burda C. (2005). Photocatalytic degradation of azo dyes by nitrogen-doped TiO₂ nanocatalysts. *Chemosphere* 61, 11 – 18.
27. Zhong J.B., Lu Y., Jiang W.D., Meng Q.M., Xi Yang He X.Y., Li J. Z. and Chen Y.Q. (2009). Characterization and photocatalytic property of Pd/TiO₂ with the oxidation of gaseous benzene. *J. Hazard. Mater.* 168, 1632 – 1635.
28. Yu J., Ma T. and Liu S. (2011). Enhanced photocatalytic activity of mesoporous TiO₂ aggregates by embedding carbon nanotubes as electron-transfer channel, *Phys. Chem. Chem. Phys.*, 13, 3491 – 3501.
29. Choi J., Park H. and Hoffmann M.R. (2010). Effects of single metal-ion doping on the visible-light photoreactivity of TiO₂. *J. Phys. Chem. C* 114, 783 – 792.



CHAPTER 5

SYNTHESIS AND CHARACTERISATION OF Pd MODIFIED N- DOPED TiO₂ FOR PHOTOCATALYTIC DEGRADATION OF NATURAL ORGANIC MATTER (NOM) FRACTIONS[†]

Dyes are commonly used as model pollutants to evaluate the photoactivity of visible-light-activated photocatalysts. However, they absorb visible light, and thus might sensitise photocatalysts and make it difficult to evaluate the “real” photoactivity of these photocatalysts. In this chapter NOM, which absorbs at 254 nm, was chosen as a probe pollutant. Nitrogen, palladium co-doped TiO₂ nanoparticles, with an optimum Pd concentration of 0.6%, were synthesised by a modified sol-gel method and investigated for their visible-light-induced photocatalytic degradation of NOM fractions using simulated solar radiation. Comparisons were made with commercial TiO₂ (Degussa P25).

5.1 INTRODUCTION

The photocatalytic degradation of pollutants in water has attracted much attention in the past several decades as more and new emerging pollutants are detected in the environment.¹ Water-availability problems are expected to grow in the coming decades even in regions currently considered water-rich. These challenges call for intensive research to identify effective, robust new methods of purifying water at lower cost using less energy, while at the same time minimising usage of chemicals and impact on the environment. Among many semiconductor photocatalysts, TiO₂ has received the most attention due to its high photocatalytic

[†] Contents of this chapter were published in a slightly modified form in:

Nkambule T.I., Kuvarega A.T., Krause R.W., Mamba B.B and Haarhoff J. (2012). Synthesis and characterization of Pd-Modified N-doped TiO₂ for photocatalytic degradation of natural organic matter. *Environ. Sci. Pollut. Res.* 19, 4120 – 4132.

activity, chemical and biological stability, insolubility in water, acidic and basic media, non-toxicity, availability and low cost.^{2,3}

An emerging pollutant in water treatment is natural organic matter (NOM) which is a mixture of organic compounds, having diverse chemical properties, that occurs in all natural water sources when animal and plant material breaks down.⁴ Natural organic matter affects water quality in the following ways:

- It could be responsible for the colour, undesirable taste and odour of natural waters.
- It is a source of nutrients for heterotrophic bacteria.
- It inhibits precipitative processes which form the backbone of drinking water treatment.
- It is a major membrane foulant, as it promotes bacterial re-growth in the distribution system, which compromises water quality, accelerates corrosion of the distribution network, increases turbidity at the consumer end and causes high disinfectant demand.
- In addition, it has recently become obvious that the interaction of NOM with disinfectants can form carcinogenic and mutagenic disinfection by-products.⁵

All these problems, combined or individually, negatively affect human life and that of other aquatic organisms.

Since NOM emanates from many different sources, it can be predicted that the composition of NOM in different water sources may not be uniform and characterisation studies are therefore necessary. Many authors have suggested that the character of NOM varies per geographic location of the water source. Some papers have even suggested that the character of NOM is also dependent on the climatic conditions of that particular locality while some have also

suggested that the character of NOM per water source is dependent on the type of agricultural/industrial activities occurring in the surrounding catchment area. It is therefore crucial to understand the composition of the NOM in the source water, especially as applied to the local NOM conditions. Fractionating the NOM into different fractions based on their polarity is one of the many NOM characterisation techniques that can give an idea about its nature. Once the character of the NOM in the water source has been understood, methods aimed at effectively removing the NOM from the water source can then be developed. The need to characterise the NOM before attempting to remove it is based on the fact that its aromaticity, functional group distribution, molecular weight and elemental composition have a great influence on how NOM can be effectively removed from water.⁶ The presence of NOM in drinking water sources influences both the efficiency of water-treatment steps and the processes in the distribution network. Hence methods aimed at effectively removing NOM from water are highly sought after. Among the different NOM-removal processes, coagulation and or enhanced coagulation are the most commonly used methods; however, total removal is not achievable. Photocatalysis may provide solutions to this wide spectrum of problems associated with presence of NOM in water.

An important drawback of TiO₂ photocatalysis is its wide band gap of 3.0 eV to 3.2 eV, which results in only a small fraction of the solar spectrum ($\lambda < 380$ nm, UV region) being utilised in sensitising the TiO₂. Utilising natural energy sources such as the sun as an economically and ecologically sensible light source would lead to cheaper and more sustainable wastewater treatment options.⁷⁻¹³ Many studies have shown insignificant differences on the rate of photodegradation of pollutants when UV-Vis and UV only were compared. This can be attributed to the improper tuning on the electronic properties of the semiconductor material. Novel non-metal/PGM co-modified TiO₂ may result in a material with excellent photocatalytic performance compared to singly doped or mono-doped TiO₂.

5.2 METHODOLOGY

5.2.1 Preparation of material

The Pd modified N-doped TiO₂ was prepared by a modified sol-gel method as detailed in **Section 4.2.1**, using an appropriate amount of palladium diamine dichloride, Pd(NH₃)₂Cl₂, (45% Pd, PGM Chemicals, RSA) to give a Pd:Ti proportion of 0.6%.

5.2.2 Characterisation of materials

The materials were characterised using various physicochemical techniques as detailed in **Section 3.6**.

5.3 WATER SAMPLING AND CHARACTERISATION

5.3.1 Sample collection

Raw water samples were collected three times from the Plettenberg Bay Water Treatment Plant in the Southern Cape, South Africa. These samples were named P1, P2 and P3. The P water is from the Keurbooms River. This type of water is highly coloured (e.g. water found on the south-western coast), usually due to the presence of humic and fulvic substances.

5.3.2 Bulk water characterisation

On site, the pH, the turbidity, conductivity and temperature of all samples taken were determined using a Hanna 98129 multimeter, in order to establish the NOM characteristics in the samples.

5.3.3 Organic carbon analysis

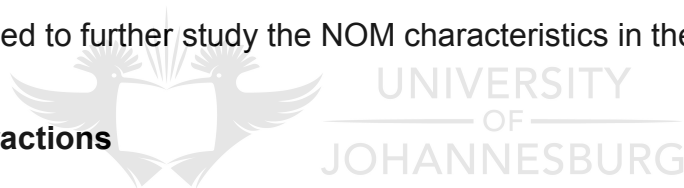
The dissolved organic carbon (DOC) analyses were carried out using a total organic carbon (TOC) analyser (Teledyne Tekmar, TOC fusion). Prior to analysis

all samples were filtered through 0.45 µm filter paper. DOC is the organic constituent that can pass through 0.45 µm filter paper, while TOC is the measure of all organic molecules present in a water sample. Standards of 1 mg/l, 5 mg/l, 10 mg/l, 20 mg/l and 30 mg/l carbon were prepared with potassium hydrogen phthalate (KHP) and deionised water and were then run prior to analysis of samples to calibrate the instrument.

5.3.4 Ultraviolet-visible (UV-Vis) spectrophotometric analysis

A Shimadzu UV-2450 Spectrophotometer was used to analyse the samples in the UV range over the following four wavelengths: 214 nm (indicative of nitrites and nitrates); 254 nm (indicative of humic substances and aromatics); 272 nm (reported in the literature to be the best predictor of trihalomethane (THM) formation¹⁴; and 300 nm (used by Rand Water and other treatment plants as a measure of DOC). A full wavelength spectrum (200 nm to 900 nm) of each sample was also obtained to further study the NOM characteristics in the samples.

5.3.5 NOM fractions



The NOM fractions of dissolved organic materials are usually defined by the physical or chemical isolation procedure. According to Marhaba and Van, the chemical description of the hydrophobic (HPO), hydrophilic (HPI) and transphilic (TPI) NOM fractions obtained after polarity rapid assessment method (PRAM) is given as follows:¹⁵

- (i) Hydrophobic (HPO): These are carboxylic acids of five to nine carbons, one- and two-ring aromatic carboxylic acids, aromatic acids, one- and two-ring phenols and tannins, proteins with one- and two-ring aromatic amines except for pyridine and high-molecular-weight acids.
- (ii) Hydrophilic (HPI): Aliphatic acids of less than five carbons, hydroxyl acids, sugars, low-molecular-weight alkyl monocarboxylic

acids and dicarboxylic acids, amphoteric proteinaceous materials containing amino acids, amino sugars, peptides and proteins.

- (iii) Transphilic (TPI): A mixture of hydrocarbon and carboxyl compounds, aliphatic amides, alcohols, aldehydes, esters, polysaccharides and ketones with less than five carbons.

The significance of these fractions is that some are more problematic than others (e.g. in forming DBPs). The hydrophilic fraction has more affinity for water and is composed mainly of low-molecular-weight carbohydrates, proteins and amino acids. The hydrophobic fraction has less affinity for water making it more soluble in organic solvents and consists mainly of humic and fulvic acids. Not all the samples were fractionated using the PRAM as this method first had to be modified and optimised to be able to give a good fractionation. There is a fundamental difficulty in using UV₂₅₄ to define HPO, HPI and TPI fractions. This difficulty emanates from the fact that the HPI fractions and to a lesser extent the TPI fractions do not generally have a very high UV absorbance, so they are likely to be significantly under-represented using this method.

5.3.5.1 Fractionation of NOM

Due to the chemical complexity and heterogeneous nature of NOM, a fractionation step can help reduce the molecular heterogeneity of NOM and provide more insight into its chemical composition.¹⁶ The characterisation techniques based on fractionation isolates the group of compounds present in the NOM based on physical properties. The fractionation of NOM into various fractions was done using the polarity rapid assessment method (PRAM).

5.3.5.2 Polarity rapid assessment method (PRAM)

The experimental conditions of this method have been reported and were discussed in detail by Rosario-Ortiz *et al.*¹⁷ The characterisation of NOM with PRAM is based on preferential adsorption of dissolved organic matter (DOM) fractions onto solid-phase extraction (SPE) sorbents. Three different types of

sorbents were used, namely polar sorbents, non-polar sorbents and anion-exchange resins.

Table 5.1 shows the different cartridges with the various types of sorbents used. The use of different SPE cartridges sequentially allows for a multidimensional characterisation of the polarity of NOM. **Figure 5.1** shows the experimental setup, including the SPE cartridges used for PRAM analysis.

Table 5.1 The different SPE cartridges and various types of sorbents used

SPE cartridge	Type of sorbent
C18, C8, C2	Non-polar
CN, Silica, Diol	Polar
NH ₂	Weak anion exchange
SAX	Strong ion exchange

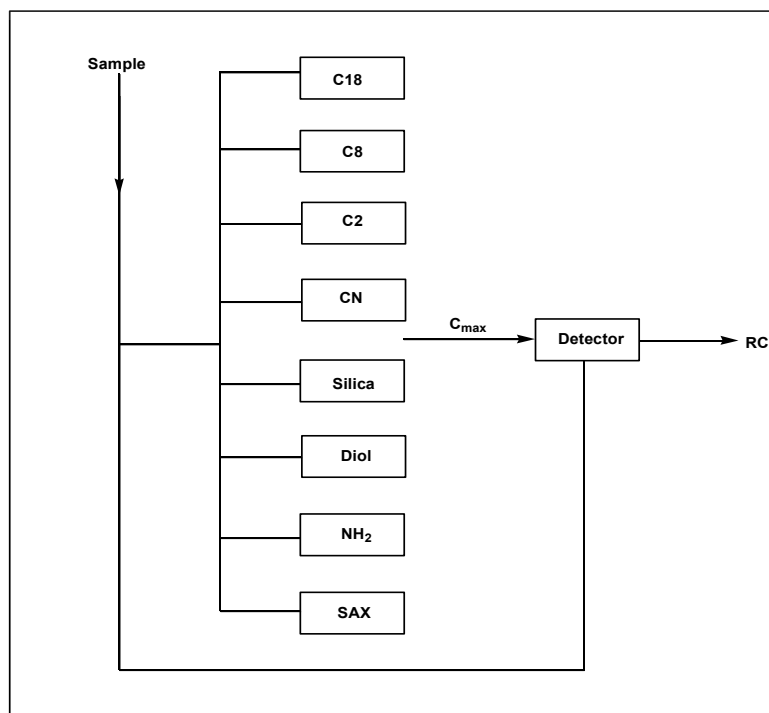


Figure 5.1 Experimental setup for PRAM

The SPE cartridges were rinsed by flushing with deionised water until a steady UV₂₅₄ signal was obtained (approximately 15 min) in order to remove any UV-absorbing organic residue on the SPE sorbent. The breakthrough was then measured by UV₂₅₄ and DOC. The retention coefficient (RC) (**Equation (5.1)**) is defined as one minus the maximum breakthrough level achieved and describes the capacity of each SPE sorbent for specific NOM components.¹⁷

$$RC = 1 - \frac{C_{\max}}{C_0} \quad (5.1)$$

where:

C_0 and C_{\max} refer to the initial sample concentration and maximum breakthrough concentrations, respectively.

5.3.5.3 The modified PRAM

The modified PRAM, instead of producing all six NOM fractions, only gives three fractions and thus is a very rapid method for NOM characterisation. This method results only in the hydrophobic NOM fraction (HPO), the hydrophilic NOM fraction (HPI) and the transphilic NOM fraction (TPI). All three fractions provide good information for the characterisation of the NOM based on its composition as these three fractions best represent the composition of the NOM with respect to its aromaticity.

In this modified method, the PRAM methodology should be followed as discussed earlier, the exception being the use of only three SPE cartridges to collect the three fractions. The C18 cartridge is used to generate the hydrophobic (HPO) NOM fraction, the CN SPE cartridge elutes the hydrophilic (HPI) NOM fraction while the NH₂ SPE cartridge generates the transphilic (TPI) NOM fraction. Sufficient amounts of 0.1M NaOH (approximately 10 ml) are used to elute the HPO and HPI fractions retained by the C18 and CN SPE cartridges, respectively; the TPI fraction is thus collected as the fraction that passes through the NH₂ SPE cartridge as shown in **Figure 5.2**.

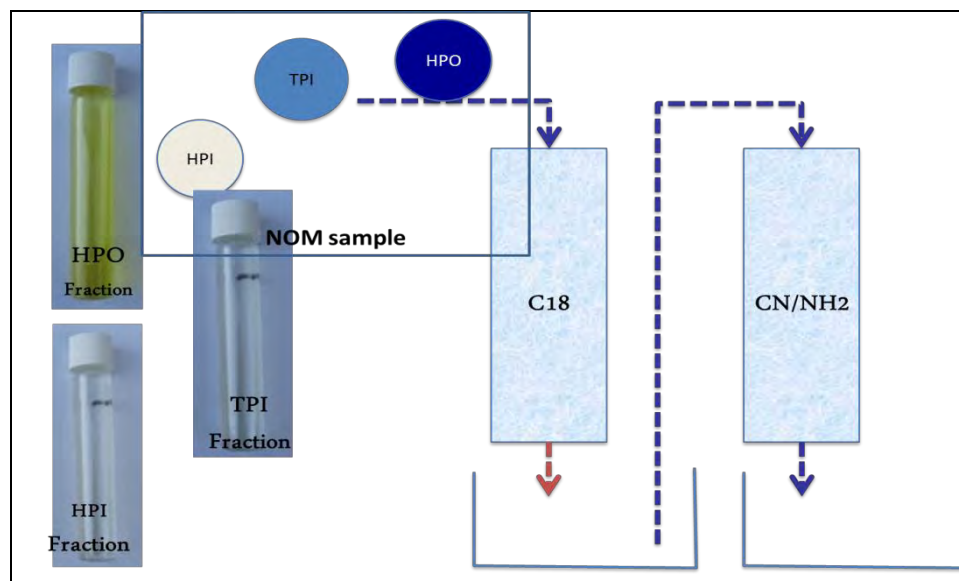


Figure 5.2 Experimental setup for the modified PRAM

5.4 PHOTOCATALYTIC DEGRADATION EXPERIMENTS

Photocatalytic degradation experiments were performed as described in **Section 3.7** using a solar simulator as a radiation source.

5.5 RESULTS AND DISCUSSION

5.5.1 FT-IR characterisation

FT-IR studies were performed in order to determine the presence of functional groups as well as to study the surface changes on the nanoparticles (**Figure 5.3**). OH groups and water on the surface of the particles were confirmed by appearance of a broad band at about $3\ 354\ \text{cm}^{-1}$ and at $1\ 629\ \text{cm}^{-1}$, respectively. The OH peak at $1\ 629\ \text{cm}^{-1}$ is associated with O-H bending of the adsorbed water. A highly intense peak centred around $640\ \text{cm}^{-1}$ is due to the Ti-O stretching vibrations.

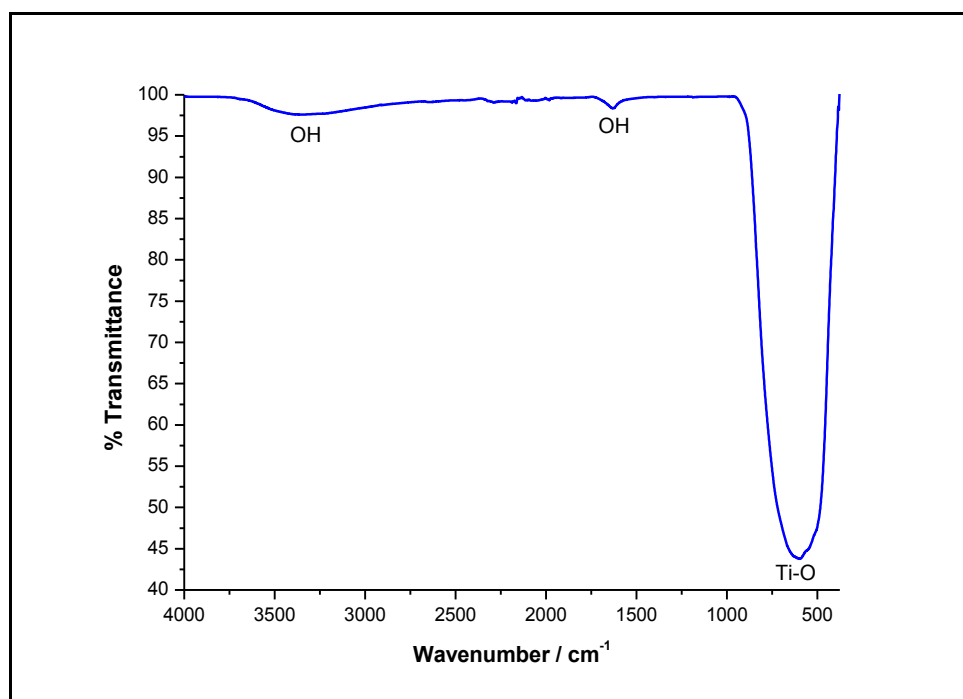


Figure 5.3 FT-IR spectrum of N, Pd co-doped TiO₂ (0.6% Pd)

5.5.2 Raman characterisation

Raman analysis was carried out on a Perkin Elmer Raman microscope in the 800 cm⁻¹ to 50 cm⁻¹ frequency range using the 785 nm laser exciting line (**Figure 5.4**). Anatase TiO₂ shows six Raman-active fundamental modes at 144 cm⁻¹ (E_g), 197 cm⁻¹ (E_g), 397 cm⁻¹ (B_{1g}), 518 cm⁻¹ (A_{1g} + B_{1g}) and 640 cm⁻¹ (E_g).¹⁸ Well-resolved Raman peaks were observed for the N, Pd TiO₂ at 141 cm⁻¹ (E_g), 397 cm⁻¹ (B_{1g}), 517 cm⁻¹ (A_{1g} + B_{1g}) and 639 cm⁻¹ (E_g), indicating that anatase was the predominant phase. The rutile TiO₂ polymorph has five Raman-active modes; B_{1g}, multi-photon process, E_g, A_{1g} and B_{2g} appearing at 140 cm⁻¹, 250 cm⁻¹, 425 cm⁻¹, 609 cm⁻¹, and 825 cm⁻¹, respectively.^{19,20} The commercial Degussa P25 TiO₂ is a mixture of the anatase and rutile forms. Broad peaks were observed at 239 cm⁻¹, 445 cm⁻¹ and 612 cm⁻¹ together with the anatase peak at 144 cm⁻¹. The broad peaks at 445 cm⁻¹ and 612 cm⁻¹ were due to the overlap of the anatase and rutile bands. No Raman lines due to palladium appeared in the N, Pd co-doped sample as they were shadowed by the more intense TiO₂ peaks.²¹ Sharp, narrow intense peaks at low wave numbers confirmed the presence of the particles in the

crystalline state. The TiO₂ crystalline structure was not altered by the doping procedure.

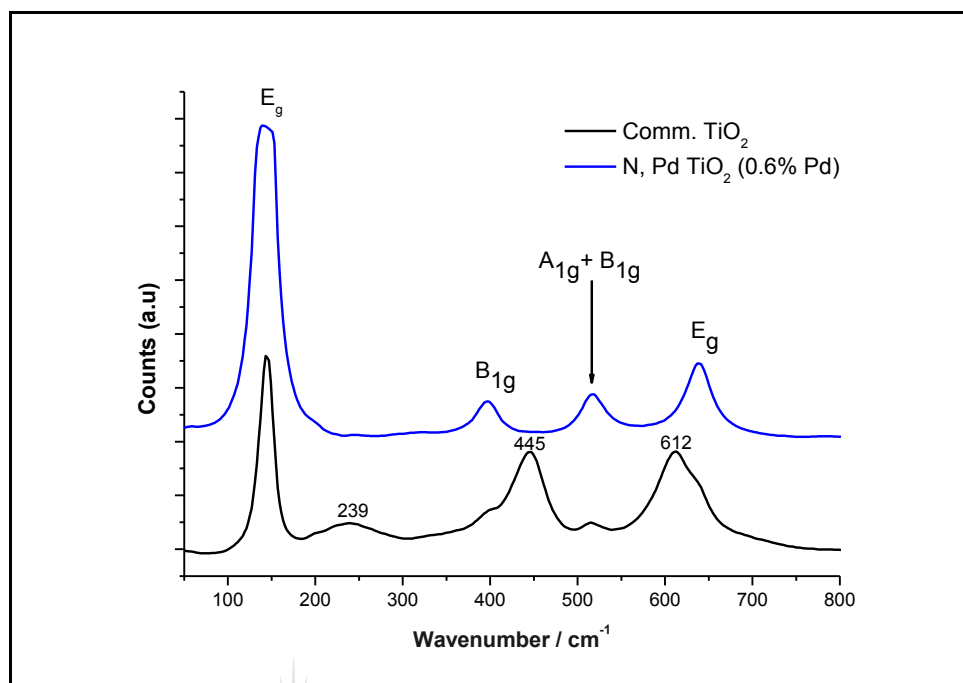


Figure 5.4 Raman spectrum of commercial and N, Pd co-doped TiO₂

5.5.3 XRD characterisation

XRD patterns of the N, Pd co-doped TiO₂ subjected to heat treatment at 500°C for 2 h are shown in **Figure 5.5**. Post-synthesis treatment by thermal annealing resulted in increased crystallinity with anatase as the principal phase in agreement with Raman spectra. Resolved peaks at 2 θ values of 25.3, 37.6, 48.2, 53.9, 54.8, 62.7 and 75.2 for the N, Pd TiO₂ corresponding to the (101), (004), (200), (105), (211), (204) and (215) planes, respectively, are attributed to the anatase phase of TiO₂.²¹ Calcination resulted in intense and sharp anatase peaks. This is clearly indicative of an improvement in the degree of crystallinity corresponding to the formation of larger particles with fewer defects. A PdO peak (101) at 2 θ value of 33.8 confirmed the presence of Pd in the oxide form. Degussa P25 gave peaks associated with the anatase and rutile phases. Rutile peaks appeared at 2 θ values of 27.45, 36.09, 41.19, 44.61, 56.57, 68.97 and 76.49 due to the (110), (101), (200), (210), (220), (301) and (202) mirror planes, respectively, again in

agreement with the literature values for the rutile phase structure.²² The crystallite size was calculated using the Scherrer equation (**Section 3.6.4.1**). Results of the particle size determination gave an average value of 16 nm.

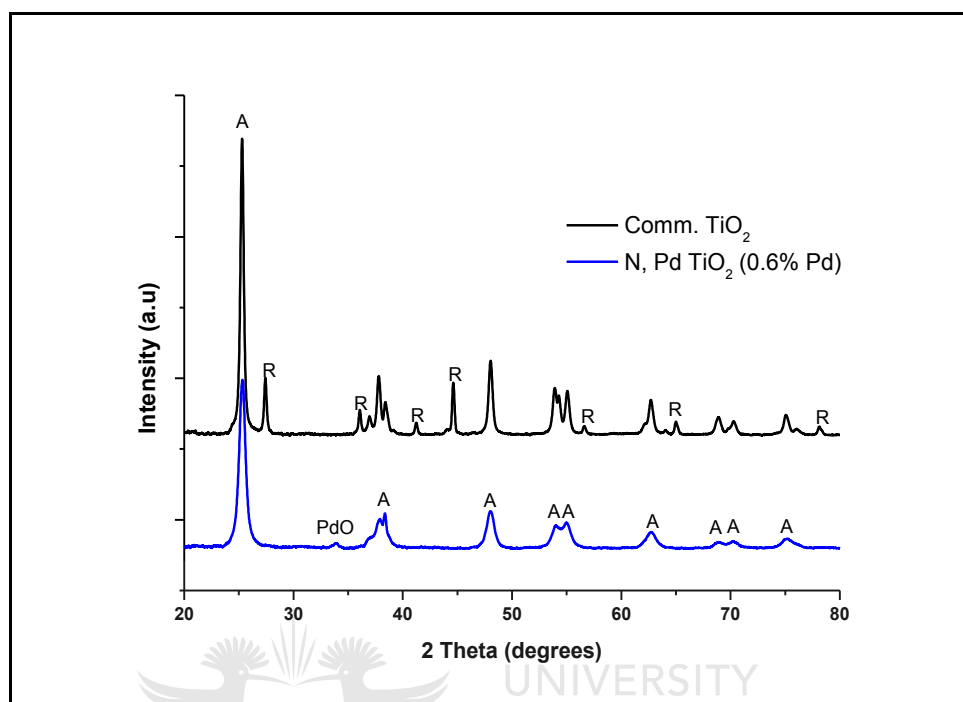


Figure 5.5 XRD pattern of commercial TiO₂ and N, Pd co-doped TiO₂ (A - anatase; R - rutile)

5.5.4 Optical properties

The optical properties of the material are shown in **Figure 5.6**. The spectra are characterised by an intense fundamental absorption due to anatase TiO₂ in the region between 300 nm and 400 nm (**Figure 5.6(a)** and **Figure 5.6(b)**). There is a red shift in the absorption edge for N, Pd co-doped TiO₂ compared to Degussa P25 that can be attributed to the presence of Pd and N in the TiO₂. Commercial TiO₂ gave a well-defined absorption with an edge of about 380 nm whilst the co-doped TiO₂ showed tailing of the fundamental TiO₂ band into the high-wavelength region with an absorption edge at about 750 nm. Increased absorption in the visible-light region by the N, Pd co-doped TiO₂ could be due to d–d transitions of PdO particles,²³ corresponding to the brown colour of the powders. Degussa P25 is characterised by the transition from the oxygen 2p orbital to the Ti 3p orbital,

which occurs well into the UV region. The presence of N could also have led to a red shift in the absorption edge due to the excitation of electrons from localised nitrogen 2p levels in the band gap to the vacant conduction band of the TiO₂. The absorption around 400 nm for the Degussa P25 is due to a charge transfer transition between the lattice oxygen ligands (O²⁻) and a central titanium ion (Ti⁴⁺).¹⁰ A plot of the absorption coefficient vs. wavelength (Kubelka-Munk plot) showed increased absorption by the co-doped TiO₂ in the high-energy UV region (Figure 5.6(c)) compared to the Degussa P25. The reflectance spectral data were converted to the Kubelka-Munk function (Section 3.6.3.1). The Kubelka-Munk function can be transformed to a Tauc plot - a plot of $[F(R).hv]^n$ vs. $h\nu$ (Figure 5.6(d)).²¹

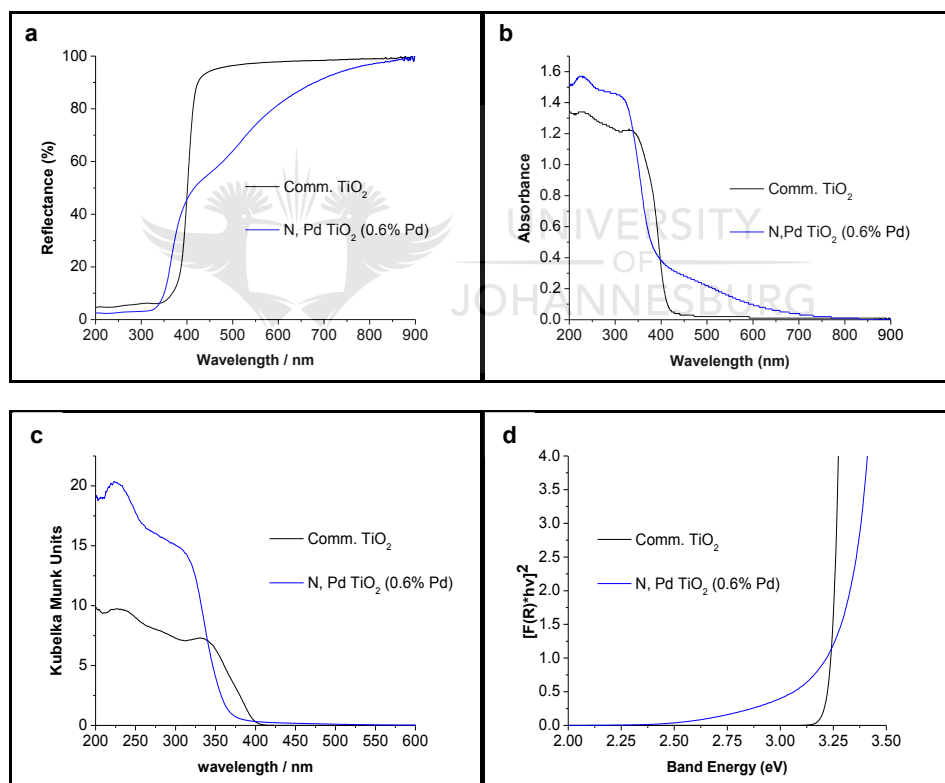


Figure 5.6 (a) Diffuse reflectance spectra; (b) absorption spectra; (c) Kubelka-Munk plots; and (d) Tauc plots of N, Pd co-doped TiO₂ and commercial TiO₂ (Degussa P25)

A direct band-gap semiconductor was assumed for the N, Pd co-doped TiO₂ since a linear region just above the gap edges was observed with $n = 2$ (Section

3.6.3.2). A band gap of about 2.48 eV for the N, Pd co-doped TiO₂ was realised from the Tauc plot. Commercial TiO₂ gave a band gap of about 3.15 eV. The red-shift in the absorption edge for the N, Pd TiO₂ is typically attributed to the sp - d exchange interaction between the TiO₂ band electrons and localised d-electrons associated with the doped Pd ions. Band tailing is evidence of the presence of impurities and disorder in the band structure of the material leading to inter-band gap states. Therefore, the low-energy absorption onset is likely an electron transition from the valence band to the nitrogen- or palladium-derived impurity states.²¹ This tailing was not observed in the Degussa P25.

5.5.5 Morphological properties

The SEM image of N, Pd co-doped TiO₂ shows that the material consists of small, nearly spherical particles (**Figure 5.7(a)**). Particles are not of uniform size and show a high degree of agglomeration. The size of the particles is in the nanometre range. TEM images confirmed the presence of Pd deposits on the surface of the N-doped TiO₂ (**Figure 5.7(b)**) with particles that are nearly spherical and some showing elongated morphologies. Pd deposits are well dispersed on many of the TiO₂ particles and show diameters predominantly in the 1 nm to 2 nm range. This was confirmed by EDX analysis since Pd was the only other detectable element besides Ti and O. The size of the TiO₂ particles is approximately in the range of 15 nm to 20 nm consistent with XRD measurements. This is in agreement with reported results.²⁴

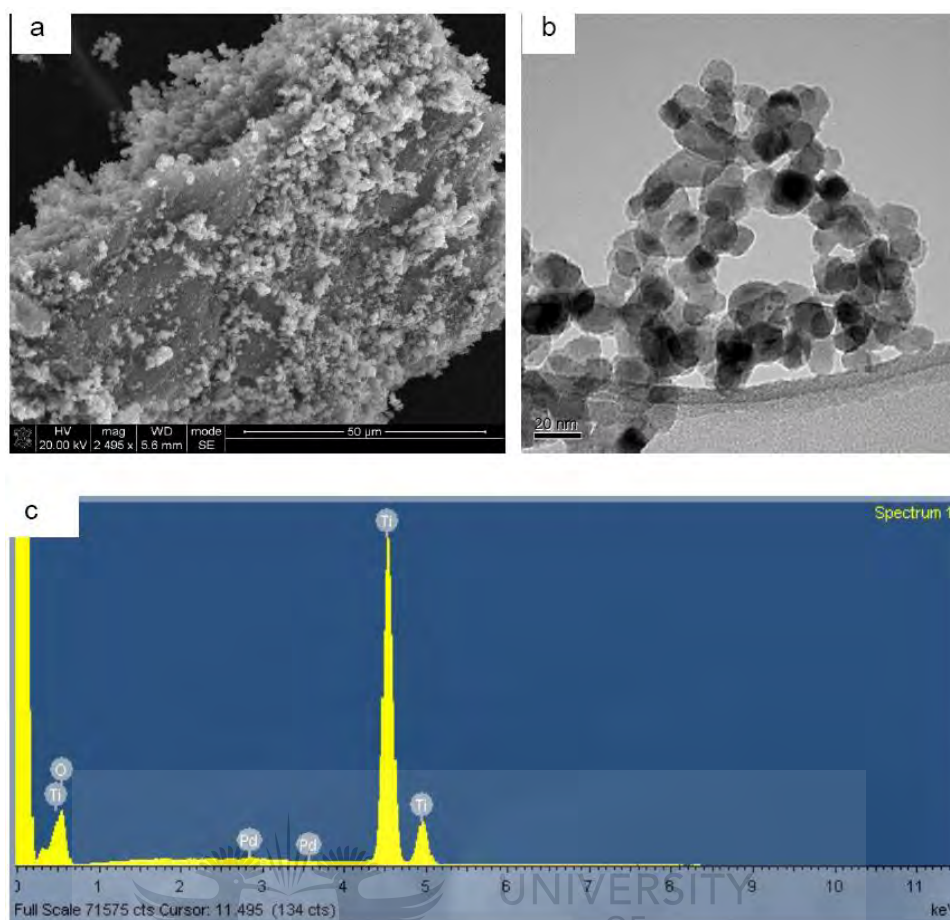


Figure 5.7 (a) SEM image; (b) TEM images; and (c) EDX spectrum of N, Pd co-doped TiO₂ (0.6% Pd)

The elemental composition of the various samples was estimated by EDX analysis. The EDX spectra of the co-doped TiO₂ showed signals closely related to the elemental composition of the material (**Figure 5.7(c)**). Ti and O appeared as the main components with low levels of Pd. This confirmed the formation of N, Pd co-doped TiO₂. However, N cannot be detected by EDX. EDX confirmed the presence of Pd on the TiO₂.

5.5.6 Thermal properties

The thermogram of N, Pd co-doped TiO₂ heated at 500°C showed a small mass loss around 100°C, attributed to the loss of water adsorbed onto the particle surfaces (**Figure 5.8**). A continuous small weight loss from 100°C up to about 900°C could be due to the loss of some of the volatile nitrogen or carbon-related

materials entrapped within the nanoparticles. The total mass loss of about 4.5% shows the exceptionally high thermal stability of the material. It also confirms that some of the nitrogen and carbon material was lost through calcination at 500°C.²¹

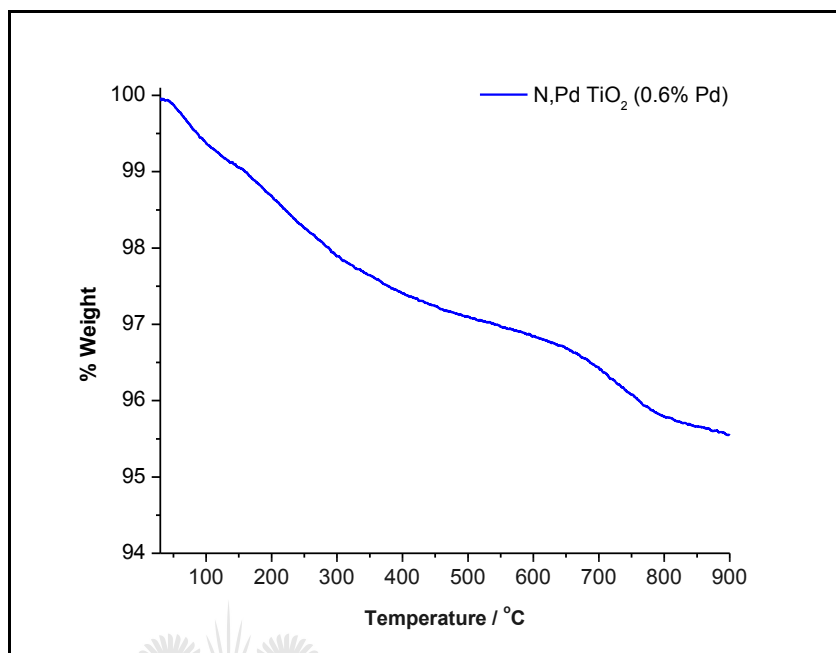


Figure 5.8 TGA curve of N, Pd co-doped TiO₂

5.5.7 Bulk water characterisation of samples

Table 5.2 gives the characterisation of the bulk NOM sample, the determinants being DOC, specific UV absorbance (SUVA), turbidity, conductivity and pH.

Table 5.2 Bulk characteristics of the NOM samples from plant P

	DOC (mg/ℓ)	SUVA (ℓ/mg·m)	Turbidity (NTU)	Conductivity (mS/cm)	pH
P1	14.04	5.20	14.6	0.12	6.73
P2	9.64	4.67	1.87	0.12	6.73
P3	2.38	4.62	0.27	0.12	6.39

The **P** sample water is characteristic of the organically coloured surface water found on the south-west coast in South Africa; its brownish colour is usually due to humic and fulvic substances. These samples have high DOC values (14.04 mg/l, 9.64 mg/l and 2.38 mg/l for the first, second and third sampling respectively). The turbidity of the raw water sample is also high (ranging from 14.64 NTU to 0.27 NTU), indicative of a high content of colloids and clay particles in these samples.

The SUVA values of all the samples (**Table 5.2**) are greater than 4 l/mg·m, implying that the NOM consists mostly of hydrophobic NOM, thus a greater percentage of the samples comprises humic substances.

5.5.8 Ultraviolet-visible (UV-Vis) spectrophotometric analysis

UV absorbance is usually measured at a wavelength of 254 nm and absorbance at this wavelength is used as an industrial standard for the maximum UV absorption of NOM samples. The absorption at this wavelength has been reported to represent the aromatic character of the organic species. **Figure 5.9** shows a UV scan obtained for the bulk characterisation of the samples.

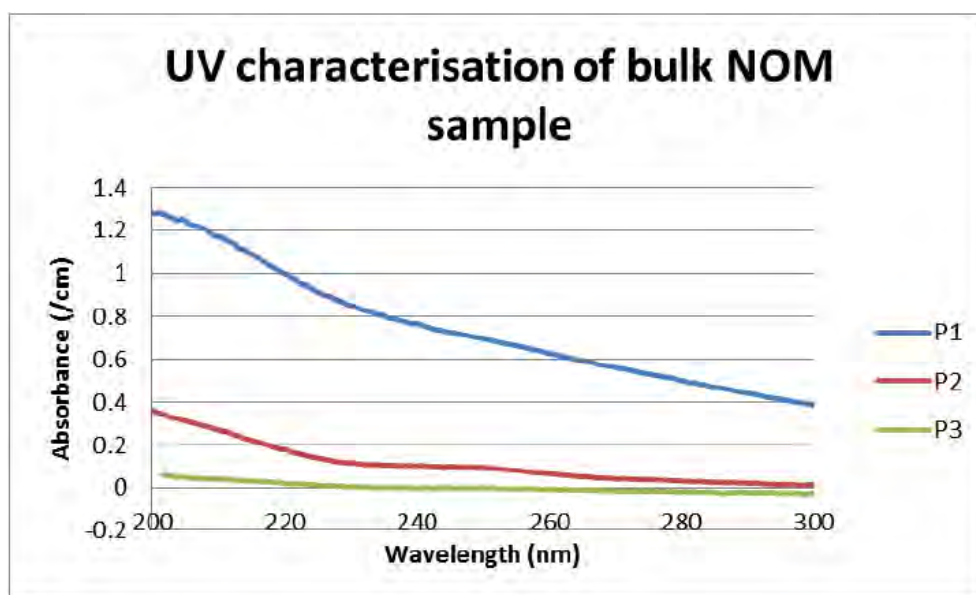


Figure 5.9 UV scan of samples

The bulk UV characterisation of the NOM in all three samples was then used to compare the photodegradation of the NOM in the samples by the commercial TiO₂ and the N, Pd co-doped TiO₂ to evaluate the efficiency together with the extent of photodegradation by the two nanomaterials.

5.6 NOM PHOTODEGRADATION STUDIES

5.6.1 Bulk NOM

The UV photodegradation scans for the samples P1, P2 and P3 are shown in **Figure 5.10**, **Figure 5.11** and **Figure 5.12**, respectively, using commercial TiO₂ and the N, Pd co-doped TiO₂. Changes in NOM concentration were monitored before solar light illumination and 2 h after illumination.

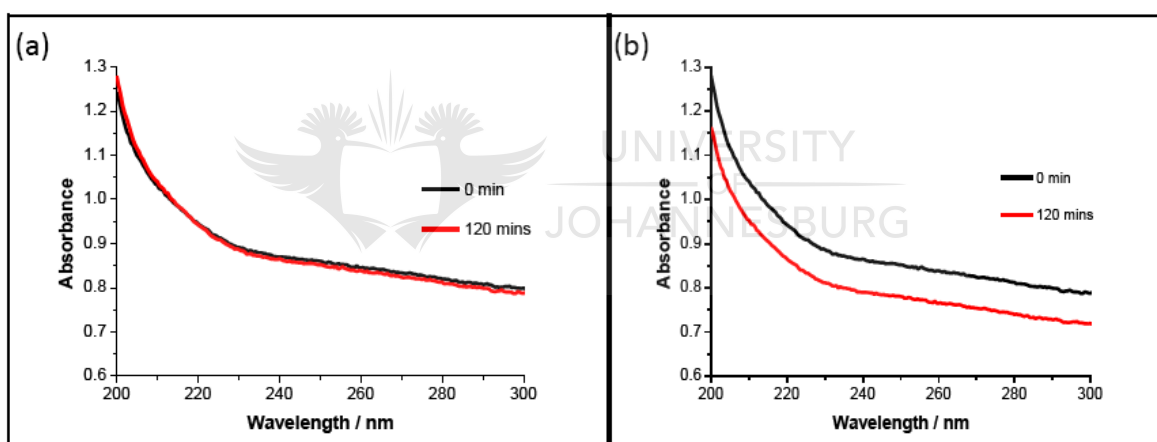


Figure 5.10 UV scan over time for the P1 sample using (a) P25; and (b) N, Pd co-doped TiO₂

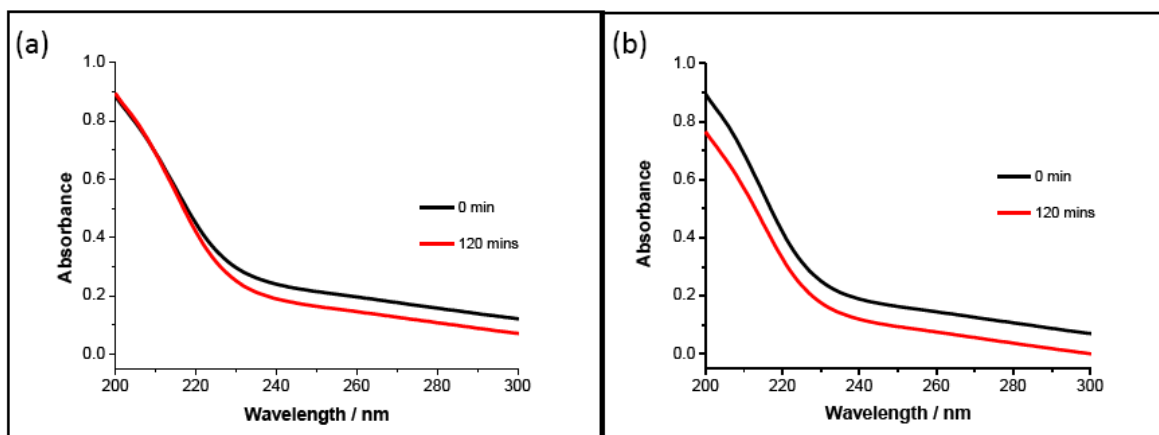


Figure 5.11 UV scan over time for the P2 sample using (a) P25; and (b) N, Pd co-doped TiO₂

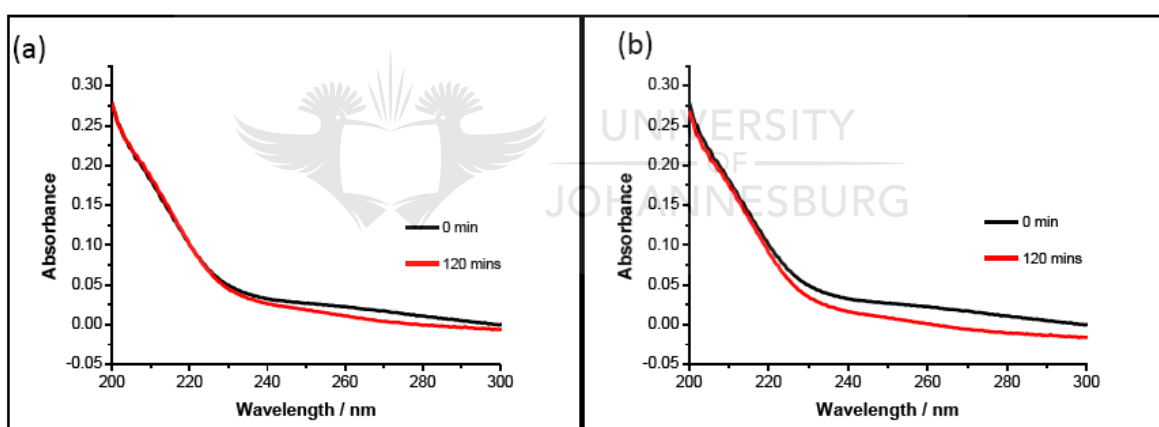


Figure 5.12 UV scan over time for the P3 sample using (a) P25; and (b) N, Pd co-doped TiO₂

Results of bulk NOM photodegradation using commercial Degussa P25 show a very small change in the NOM concentration compared to the initial amounts. Besides adsorption of the NOM onto the nanoparticles, the low activity can be explained by the wide band gap of the P25 and its inability to be activated by low-energy visible light. The N, Pd co-doped TiO₂ gave considerable photodegradation as shown by the slight decrease in the absorbancies at 254 nm for all the samples. Bekbolet and Ozkosemen performed a preliminary investigation into the

photocatalytic degradation of model humic acid using titanium dioxide as the photocatalyst and Black Light Fluorescent Lamp as the irradiation source. 40 % TOC and 75% Color₄₀₀ removals were attained for 50 mg/L humic acid solution in the presence of 1.0 mg/mL TiO₂ after illumination for 1 hr. Destructive removal of humic acid was effective enough to keep the THM levels below the maximum contaminant level of 0.10 mg/L (USEPA).²⁵ In another study, Uyguner and Bekbolet investigated the removal efficiency of humic acid by TiO₂ in the presence of copper (II) ions. The presence of copper ions significantly altered the photocatalytic degradation kinetics of humic acids in relation to the concentration effects of humic acid. Batch equilibrium adsorption experiments revealed a distinct Langmuirian-type adsorptive behaviour of humic acid onto TiO₂ both in terms of UV₂₅₄ and Color₄₃₆.²⁶ The degradation of humic acid in the river water was followed with respect to time by monitoring UV₂₅₄, colour and TOC using a TiO₂ photoelectrocatalytic (PEC) system. For comparison purposes the photocatalytic removal of humic acid was also studied on the same photo anode. Results showed that the PEC system was much more effective than the photocatalytic method. The effect of other important reaction variables, such as external potential, oxygen and UV intensity on humic acid degradation were also investigated. For all the external applied potential conditions and UV intensity range over 90% removal of UV₂₅₄ and colour were obtained with the PEC system while TOC removal was between 58-80%.²⁷ The N, Pd co-doped TiO₂ thus performed much better compared to the P25 under simulated solar irradiation.

5.6.2 NOM fractions

The susceptibility of NOM fractions to undergo photocatalytic degradation by commercial TiO₂ and N, Pd co-doped TiO₂ is thus investigated herein. **Table 5.3** shows results for the degradation of NOM fractions using commercial TiO₂.

Table 5.3 Percentage UV₂₅₄ reduction of the three NOM samples using commercial TiO₂

NOM fraction	Per cent UV ₂₅₄ reduction (%)		
	P1	P2	P3
HPO	34	23	20
HPI	8	11	9
TPI	5	6	7

Photodegradation percentages lower than 50% were realised for all the samples. This can also be attributed to the wide band gap of TiO₂. Theoretically, the P25 cannot be activated by visible light; however, visible light consists of a very small percentage (less than 5%) of the UV component. This small UV component is not sufficient to fully activate wide band P25 (band gap = 3.0 – 3.2 eV) for enhanced photoactivity. Contrary to these observations, N, Pd co-doped TiO₂ gave much higher NOM-removal percentages. An enhancement factor of close to 3 times was observed for the HPO whilst TPI gave an enhancement factor of about 2 for P1, P2 and P3 samples. The enhanced performance of N, Pd TiO₂ can be explained by the synergistic effects of the co-dopants on the separation of electrons and holes. **Figure 5.13**, **Figure 5.14** and **Figure 5.15** show the photocatalytic behaviour of the three NOM fractions over a period of 120 min of simulated solar irradiation in the presence of N, Pd co-doped TiO₂.

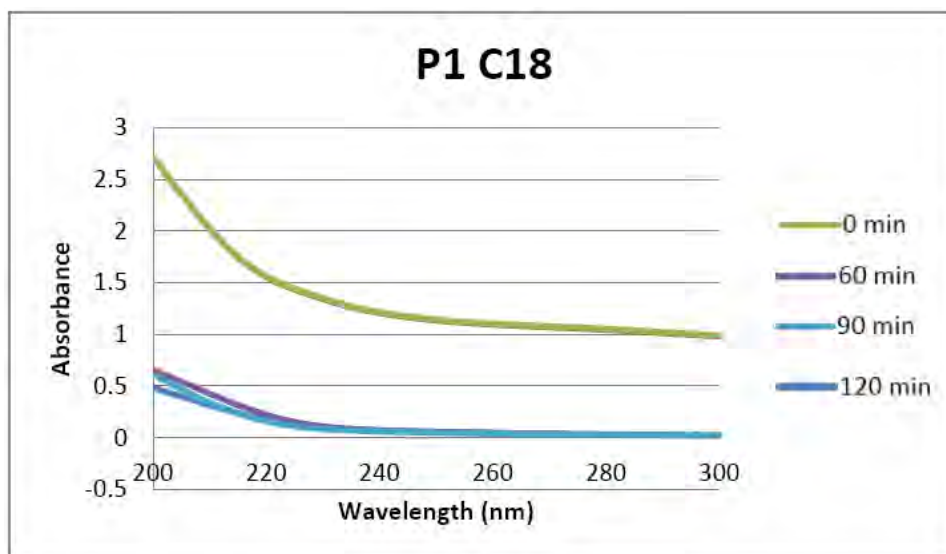


Figure 5.13 UV scans over time of hydrophobic (HPO) NOM fraction

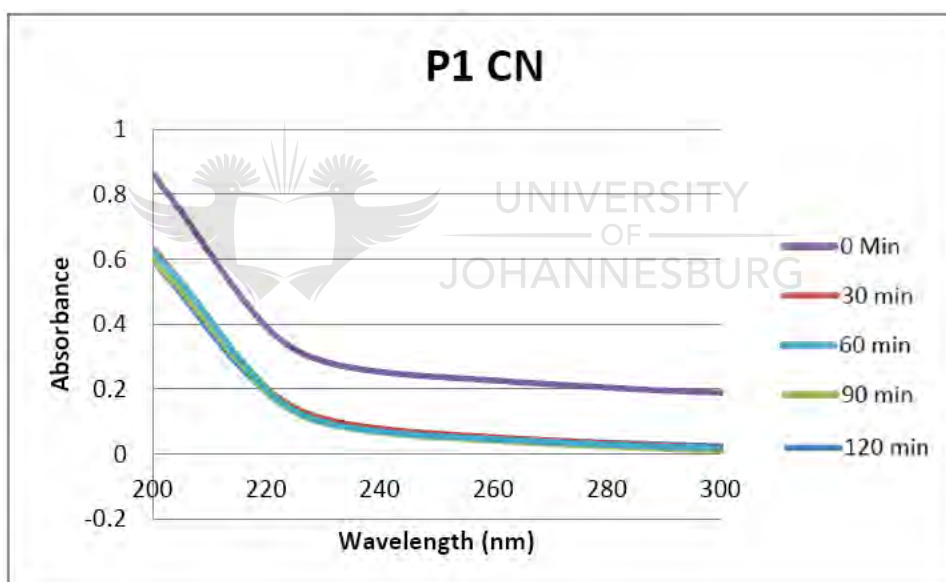


Figure 5.14 UV scans over time for the hydrophilic (HPI) NOM fraction

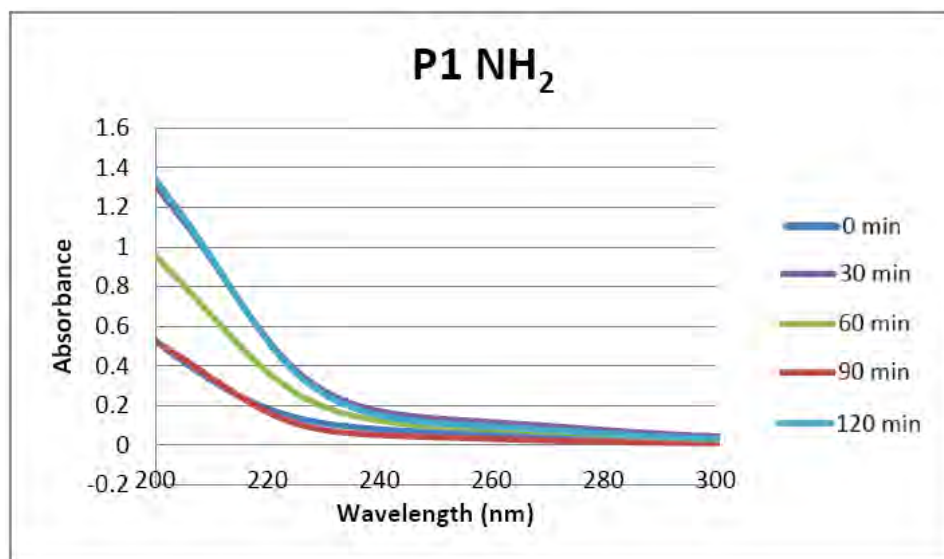


Figure 5.15 UV scans over time for the transphilic (TPI) NOM fraction

The hydrophobic fraction (**Figure 5.13**) underwent the highest photodegradation, with a 96% UV₂₅₄ reduction and the transphilic NOM fraction (**Figure 5.15**) was the least photo-degraded with a 14% UV₂₅₄ reduction. The hydrophilic NOM fraction had a 19% UV₂₅₄ reduction of the NOM content (**Figure 5.14**). A summary of UV absorbance results of the NOM fractions photodegradation experiments is shown in **Table 5.4**. It is worth noting that for the HPO (P1C18) fraction, there is almost no difference in photoactivity between 0 min and 30 min and then a large increase in photoactivity from 30 min to 60 min. This was probably due to the hydrophobic nature of the NOM interacting with the hydrophilic material resulting in delayed attack by the reactive radical species. The opposite was observed for the HPI (P1CN) and the TPI (P1NH₂) fractions, where the activity was uniform, most likely due to a similar polarity between the NOM fractions and the material.

Table 5.4 UV absorbance over time for the different NOM fraction samples

	Time	UV ₂₅₄ (/m)		
		P1	P2	P3
C18 (hydrophobic)	0	112.4	23.3	12.7
	30	111.8	5.9	10.3
	60	4.5	5.6	5.9
	90	4.5	5.1	6.1
	120	4.2	4.9	3.7
CN (hydrophilic)	0	3.7	3.2	3.7
	30	3.2	3.0	3.3
	60	3.2	2.9	3.2
	90	3.2	2.9	2.9
	120	3.0	2.0	2.4
NH₂ (transphilic)	0	8.6	5.9	5.3
	30	7.9	5.5	5.2
	60	7.9	5.4	4.9
	90	7.6	5.3	4.5
	120	7.4	5.0	4.5

5.6.3 Photodegradation mechanism

The proposed mechanism for the photo-degradation of NOM by the N, Pd co-doped TiO₂ is shown in **Figure 5.16**. Under UV radiation, photons excite electrons (e⁻) from the valance band (VB) of TiO₂ to the conduction band (CB), creating holes (h⁺) in the VB. The created charge carriers quickly recombine and only a fraction of the electrons and holes participate in the photocatalytic reaction, resulting in low reactivity for the commercial TiO₂. Introduction of nitrogen and palladium in the TiO₂ will result in the formation of impurity states close to the

valence band. This enhances the visible-light activity of the nanoparticles as electrons can be excited from the inter-gap nitrogen 2p orbitals to the TiO₂ conduction band.²¹ In the presence of Pd, a Schottky barrier is formed at the interface. These Schottky barriers at the interface can act as electron-trap-sites for the photo-generated electrons, leading to electron-hole separation. The holes, in the presence of surface-adsorbed water or hydroxyl groups, react to generate highly reactive hydroxyl radicals. The electrons on the other hand scavenge the oxygen molecules to form superoxide radicals.²¹ The radicals are highly reactive towards the degradation of the organic compounds such as NOM. The NOM is most likely degraded to less complex products, and eventually carbon dioxide and water.

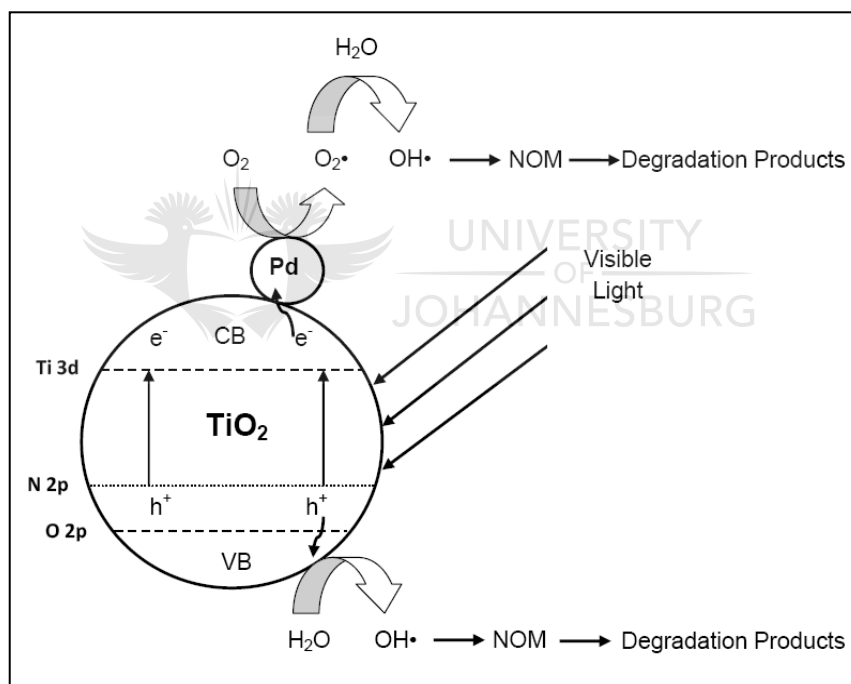


Figure 5.16 Proposed photocatalytic degradation mechanism of NOM by N, Pd co-doped TiO₂

Pollutant removal by different water-treatment processes is primarily dependent on both the chemical and physical properties of particular fractions of NOM. Hydrophobic and higher-molecular-weight NOM fractions are more effectively removed by coagulation than the other fractions, i.e. hydrophilic and lower-molecular-weight NOM.^{15,28}

The overall photocatalysis reaction as portrayed in **Figure 5.16** can be divided into seven steps.²⁹

- (i) Mass transfer of the organic contaminants in the liquid phase to the co-doped TiO₂ surface.
- (ii) Adsorption of the organic contaminants onto the photon-activated co-doped TiO₂ surface.
- (iii) Generation of charge carriers through photo-irradiation.
- (iv) Generation of reactive radicals from the charge carriers.
- (v) Photodegradation of the adsorbed phase on the co-doped TiO₂ surface.
- (vi) Desorption of the intermediates from the TiO₂ surface.
- (vii) Mass transfer of the intermediates from the interface region to the bulk fluid.

Table 5.5 is a summary of the percentage UV₂₅₄ reduction of the three NOM samples. Reduction in UV₂₅₄ absorbance was after exposure of the samples to visible light was assumed to indicate removal or photodegradation of NOM. The highest photodegradation of the NOM fractions was achieved in the hydrophobic fraction (71% to 96%) supporting literature observations that the hydrophobic NOM fraction is the more easily removed by NOM treatment protocols. The least NOM reduction occurred in the transphilic fraction (14% to 15%). However, these results are still far better than those achieved by most NOM removal methods such as coagulation, whose NOM removal efficiencies are in the range of about 75% compared to the 96% reduction achieved for the hydrophobic (HPO) NOM fraction (as evidenced by the 96% UV₂₅₄ reduction). In a study on the degradation of NOM by Degussa P25 TiO₂, NOM removal of about 90% was achieved within 120 min at a dose of 1.0 g/l on a 10 mg/l NOM solution using a UV light source.³⁰ Similar studies by a different group showed 70% NOM removal using a high intensity (75W) UV source.³¹ The high NOM-removal efficiencies

were attributed to the high intensity UV radiation. Liu *et al.* used commercial Degussa P25 TiO₂ for NOM degradation and reported more than 95% reduction of UV₂₅₄ and more than 80% reduction of the DOC after 150 min of UVA (365 nm)/TiO₂ treatment. They concluded that the higher percentage of UV₂₅₄ removal compared to DOC removal indicated an incomplete mineralisation of the organics after the break-up of large aromatic structures.³² The high NOM photodegradation efficiency using visible light for the hydrophobic fraction can be explained by the stronger interaction with the N, Pd co-doped TiO₂ nanoparticles leading to preferential attack by the HO[•] radicals.

Table 5.5 Percentage UV₂₅₄ reduction of the three NOM samples by photocatalytic degradation

NOM fraction	Per cent UV ₂₅₄ reduction (%)		
	P1	P2	P3
HPO	96	78	71
HPI	19	38	35
TPI	14	15	15

5.7 CONCLUSION

Photodegradation percentages of lower than 50% were realised for all the samples using the commercial TiO₂. This can be attributed to the wide band gap of TiO₂. Co-doping reduced the band gap of TiO₂ and shifted the absorption edge to the visible-light region. This resulted in successful application of visible light for activating the co-doped TiO₂ for NOM photodegradation. The nanocatalyst was found to be efficient in NOM degradation compared to conventional NOM treatment methods. Improved photoactivity was attributed to the synergistic effects of N and Pd co-doping of TiO₂. The hydrophobic fraction (HPO) showed the highest degradation efficiency of 96% because of the increased interaction with the nanoparticles while only a 35% reduction was obtained for the same fraction using the commercial TiO₂. This value is higher compared to similar systems

tested under high energy UV radiation. Results from this study showed that N, Pd co-doped TiO₂ is a promising photocatalytic material for NOM removal in water-treatment systems and can be considered a good candidate for future photocatalytic applications.

5.8 REFERENCES

1. Bolong N., Ismail A.F., Salim M.R. and Matsuura T. (2009). A review of the effects of emerging contaminants in wastewater and options for their removal. *Desalination* 239, 229 – 246.
2. Sojic D., Despotovic V., Abramovic B., Todorova N., Giannakopoulou T. and Trapalis C. (2010). Photocatalytic degradation of mecoprop and clopyralid in aqueous suspensions of nanostructured N-doped TiO₂. *Molecules* 15, 2994 – 3009.
3. Martins A.F., Mayer F., Confortin E.C. and Frank C.S. (2009). A study of photocatalytic processes involving the degradation of the organic load and amoxicillin in hospital wastewater. *Clean* 37, (4-5), 365 – 371.
4. Kim H. and Yu M. (2005). Characterization of natural organic matter in conventional water treatment processes for selection of treatment processes focused on DBPs control. *Water Res.* 39, 4779 – 4789.
5. Kim H.C., Hong J.H. and Lee S. (2006). Fouling of microfiltration membrane by natural organic matter after coagulation treatment: A comparison of different initial mixing conditions. *J. Membr. Sci.* 283, 288-272.
6. Nkambule T.I., Krause R.W., Mamba B.B. and Haarhoff J. (2009). Removal of natural organic matter from water using ion-exchange resins and cyclodextrin polyurethanes. *J. Phys. Chem. Earth* 34, 812 – 818.

7. Malato S., Ibanez P.F., Maldonado M.I., Blanco J. and Gernjak W. (2009). Decontamination and disinfection of water by solar photocatalysis: Recent overview and trends. *Catal. Today* 147, 1 – 59.
8. Mills A. and Hunte S.L. (1997). An overview of semiconductor photocatalysis. *J. Photochem. Photobiol. A: Chem.* 108, 1 – 35.
9. Obare S.O. and Meyer G.J. (2004). Nanostructured materials for environmental remediation of organic contaminants in water. *J. Environ. Sci. Health* 39, (10), 2549 – 2582.
10. Han F., Kambala V.S.R., Srinivasan M., Rajarathnam D. and Naidu R. (2009). Tailored titanium dioxide photocatalysts for the degradation of organic dyes in wastewater treatment: A review. *Appl. Catal. A: Gen.* 359, 25 – 34.
11. Asahi R., Morikawa T., Ohwaki T., Aoki K. and Taga Y. (2001). Visible-light photocatalysis in nitrogen-doped titanium oxides. *Sci.* 293, 269 – 276.
12. Li Y., Ma G., Peng S., Lu G. and Li S. (2008). Boron and nitrogen co-doped titania with enhanced visible-light photocatalytic activity for hydrogen evolution. *Appl. Surf. Sci.* 254, 6831 – 6836.
13. Li Y., Yuan Y., Peng S. and Jiang F. (2010). Nitrogen-doped TiO₂ modified with NH₄F for efficient photocatalytic degradation of formaldehyde under blue light-emitting diodes. *J. Hazard. Mater.* 182, 90 – 96.
14. Liu W., Cheng L., Yang X. and Shang C. (2006). THM, HAA and CNCl formation from UV irradiation and chlor(am)ination of selected organic waters. *Water Res.* 40, (10), 2033 – 2043.
15. Marhaba T.F. and Van D. (2000). The variation of mass and disinfection by-product formation potential of dissolved organic matter fractions along a conventional surface water treatment plant. *J. Hazard. Mater.* A74, 133 – 147.

16. Cornelissen E.R., Morean N., Siegers W.G., Abrahamse A.J., Rietveld L.C., Grefte A., Dignum M., Amy G. and Wessels L.P. (2008). Selection of anionic exchange resins for removal of natural organic matter (NOM) fractions. *Water Res.* 42, 413 – 423.
17. Rosario-Ortiz F.L., Snyder S. and Suffet I.H. (MEL). (2007). Characterization of the polarity of natural organic matter under ambient conditions by the polarity rapid assessment method (PRAM). *Environ. Sci. Technol.* 41, (14), 4895 – 4900.
18. Morikawa T., Ohwaki T., Suzuki K., Moribe S. and Kubota S.T. (2008). Visible-light-induced photocatalytic oxidation of carboxylic acids and aldehydes over N-doped TiO₂ loaded with Fe, Cu or Pt. *Appl. Catal. B: Environ.* 83, 56 – 62.
19. Ma H.L., Yang J.Y., Dai Y., Zhang Y.B., Lu B. and Ma G.H. (2007). Raman study of phase transformation of TiO₂ rutile single crystal irradiated by infrared femtosecond laser. *Appl. Surf. Sci.* 253, 7497 – 7500.
20. Yang X., Cao C., Erickson L., Hohn K., Maghirang R. and Klabunde K. (2008). Synthesis of visible-light-active TiO₂-based photocatalysts by carbon and nitrogen doping. *J. Catal.* 260, 128 – 133.
21. Kuvarega A.T., Krause R.W.M. and Mamba B.B. (2011). Nitrogen/palladium-codoped TiO₂ for efficient visible light photocatalytic dye degradation. *J. Phys. Chem. C* 115, 22110 – 22120.
22. Yan M.C., Chen F., Zhang J.L. and Anpo M. (2005). Preparation of controllable crystalline titania and study on the photocatalytic properties. *J. Phys. Chem. B* 109, 8673 – 8678.
23. Choi J., Park H. and Hoffmann M.R. (2010). Effects of single metal-ion doping on the visible-light photoreactivity of TiO₂. *J. Phys. Chem. C* 114, 783 – 792.

24. Weishaar J.L., Aiken R.G., Bergamaschi B.A., Fram M.S., Fujii R., Wu Z., Sheng Z., Liu Y., Wang H., Tang N. and Wang J. (2009). Characterization and activity of Pd-modified TiO₂ catalysts for photocatalytic oxidation of NO in gas phase. *J. Hazard. Mater.* 164, 542 – 548.
25. Bekbolet M. and Ozkosemen G. (1996). A preliminary investigation on the photocatalytic degradation of a model humic acid. *Water Sci Technol.* 33, 189 – 194.
26. Uyguner C.S. and Bekbolet M. (2010). TiO₂-assisted photocatalytic degradation of humic acids: effect of copper ions. *Water Sci Technol.* 61, (10), 2581 – 2590.
27. Selcuk H., Sene J.J., Sarikaya H.Z., Bekbolet M. and Anderson M.A. (2004). An innovative photocatalytic technology in the treatment of river water containing humic substances. *Water Sci Technol* 49, (4), 153 – 158.
28. Hammes F.A. and Egli T. (2005). New method for assumable organic carbon determination using flow-cytometric enumeration and a natural microbial consortium as inoculums. *Environ. Sci. Technol.* 39, 3289 – 3294.
29. Chong M.N., Jin B., Chow C.W.K. and Saint C. (2010). Recent developments in photocatalytic water treatment technology: A review. *Water Res.* 44, 2997 – 3027.
30. Huang X., Leal M. and Qilin Li Q. (2008). Degradation of natural organic matter by TiO₂ photocatalytic oxidation and its effect on fouling of low-pressure membrane. *Water Res.* 42, 1142 – 1150.
31. Le-Clech P., Lee E.K. and Chen V. (2006). Hybrid photocatalysis/membrane treatment for surface waters containing low concentrations of natural organic matters. *Water Res.* 40, 323 – 330.
32. Liu S., Lim M., Fabris R., Chow C., Chiang K., Drikas M. and Amal R. (2008). Removal of humic acid using TiO₂ photocatalytic process –

Fractionation and molecular weight characterisation studies. *Chemosphere*
72, 263 – 271.



CHAPTER 6

PHOTOCATALYTIC PERFORMANCE OF NITROGEN, OSMIUM CO-DOPED TiO₂ FOR REMOVAL OF EOSIN YELLOW IN WATER UNDER VISIBLE-LIGHT IRRADIATION[†]

In this chapter, osmium, a much cheaper PGM, is introduced as one of the co-dopants in N, PGM co-doped TiO₂. Osmium tetroxide, OsO₄, a volatile crystalline solid and a product of the oxidation of metallic osmium is a well-known oxidising agent. It has found application as an organic reagent in the conversion of alkenes to diols and this is almost the only use. Its application is hampered by its volatility and toxicity. Formation of osmium dioxide, OsO₂, a less volatile and non-toxic product, from OsO₄ could open up new avenues in the search for cheaper, more efficient and affordable materials for water decontamination. This chapter reports on the synthesis of N, Os co-doped TiO₂ for dye photodegradation under simulated solar radiation.

6.1 INTRODUCTION

One of the problems affecting people throughout the world is inadequate access to clean water and sanitation. In recent years, environmental legislation has imposed increasingly stringent targets for permitted levels of water pollutants.¹ The presence of carcinogenic emerging pollutants such as dyes has received particular attention as they cannot easily be removed from water using current conventional water-treatment technologies. Photo-oxidation using TiO₂ photocatalysis is being widely studied as a relatively new technique for water-pollution abatement.²⁻⁴ In recent years, a great effort has been made to develop TiO₂-based photocatalysts sensitive to visible light in order to make use of solar energy more efficiently in

[†] Contents of this chapter were based on:

Kuvarega A.T., Krause R.W.M. and Mamba B.B. Photocatalytic performance of nitrogen, osmium co-doped TiO₂ for removal of eosin yellow in water under visible-light irradiation. *J. Nanosci. Nanotechnol.* (Accepted)

practical applications.^{5,6} Substitutional doping with metals or non-metals are some of the most promising modification attempts that have been reported.⁷⁻¹² Metal ions such as Os⁴⁺ with an ionic radius of 0.63 Å compared to Ti⁴⁺ or Ti³⁺ will most likely substitute Ti³⁺ or Ti⁴⁺ sites within TiO₂ to occupy some of the Ti lattice sites. Os is a favourable candidate for doping due to its ionic radius and the presence of a half-filled electronic configuration.¹³ However, it has been observed that some metals on the TiO₂ surface can have no influence or may even have a detrimental effect on the photocatalytic degradation of investigated organic pollutants.¹⁴⁻¹⁶

This chapter reports on the sol-gel synthesis of N, Os co-doped TiO₂ nanomaterials using osmium tetroxide as the Os precursor, taking advantage of the formation of the crystalline rutile phase OsO₂ at high temperatures, and evaluation of their photocatalytic characteristics towards the degradation of Eosin Yellow (EY) in aqueous medium using visible light.

6.2 MATERIALS AND METHODS

6.2.1 Preparation of materials

N, Os co-doped TiO₂ nanoparticles were prepared by a modified sol-gel method using osmium tetroxide as the osmium precursor and ammonium hydroxide as a source of nitrogen as well as the hydrolysing reagent. Osmium tetroxide, OsO₄, (1 g) (Sigma, USA) was dissolved in 2-propanol (50 mL) to give a pale-yellow solution (2% OsO₄) [solid OsO₄ produces toxic vapours at room temperature]. An appropriate amount of this solution was added to a mixture of 2-propanol C₃H₈O, (50 mL), (99.8%, Sigma Aldrich, Germany) and titanium isopropoxide, Ti(OC₃H₇)₄, (10 mL), (97%, Sigma Aldrich, Germany) to give an Os:Ti percentage of 0.5%. The mixture was stirred for about 10 min. Aqueous ammonia, (3 mL) (25%, Merck, Germany) was then added drop-wise to the isopropoxide/propanol solution with vigorous stirring for about 30 min and stirring was continued for 1 h. The resulting sol-gel was dried in air at 80°C for 12 h to obtain a pale-yellow powder. Separate samples of the powder were calcined for 2 h at 350°C, 500°C, 650°C and 800°C in air in an electric furnace and characterised by various methods.

6.2.2 Material characterisation

The synthesised materials were characterised using various physicochemical techniques as described **Section 3.6**.

6.2.3 Evaluation of photocatalytic activity

Photocatalytic activity evaluations were performed on a model dye as described in **Section 3.7** using simulated solar radiation.

6.3 RESULTS AND DISCUSSION

6.3.1 FT-IR analysis

FT-IR spectra in the region 450 cm⁻¹ to 4 000 cm⁻¹ for IR-active fundamental vibrations of N, Os co-doped TiO₂ are shown in **Figure 6.1**. Bending vibrations associated with surface-adsorbed water (1 640 cm⁻¹) were observed for all the samples. A broad OH vibrational mode associated with the surface groups on the materials appeared at around 3 400 cm⁻¹. The intensity of these bands diminished with increasing calcination temperature due to preferential formation of volatile non-metal oxides resulting in more stable metal oxides. The fundamental vibrations of TiO₂ appeared in the 400 cm⁻¹ to 1 000 cm⁻¹ range. The intense broad bands were ascribed to the stretching vibrations of Ti–O bonds (651 cm⁻¹), visible for the amorphous oven-dried sample and the Ti–O–Ti bonds (580 cm⁻¹), common for all the calcined samples.^{17,18,19} The oven-dried sample also gave a band at 1 385 cm⁻¹, which was assigned to the vibrational mode of hyponitrite. This new band may suggest formation of coordinated nitrogen species.²⁰ The band disappeared with increasing calcination temperature due to loss of carbon- and nitrogen-related material. A new band appeared at about 2 350 cm⁻¹ for the samples calcined at 350°C and 500°C. The peak may be assigned to the out-of-phase stretching of the –N=C=O or –N=C–C– bond. The peak disappeared with increasing calcination temperature, again due to loss of more carbon and nitrogen material. High-temperature calcination resulted in increased scattering of radiation

as observed from the highly tilted spectral baseline for the 650°C and 800°C samples. This may be evidence of increasing particle size.

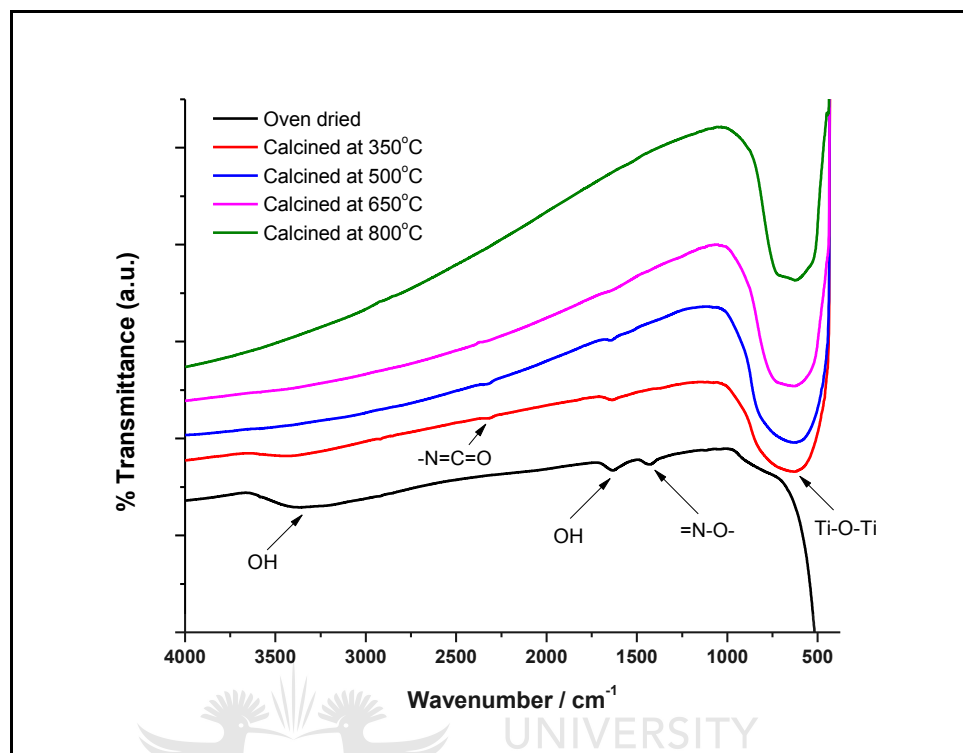


Figure 6.1 FT-IR spectra of N, Os co-doped TiO₂ calcined at different temperatures

6.3.2 Raman analysis

Anatase TiO₂ shows six Raman-active fundamental vibrations; three E_g modes centred around 144 cm⁻¹, 197 cm⁻¹, and 636 cm⁻¹ (designated as E_{g(1)}, E_{g(2)}, and E_{g(3)}, respectively), two B_{1g} modes at 399 cm⁻¹ and 519 cm⁻¹ (designated as B_{1g(1)} and B_{1g(2d)}, respectively), and an A_{1g} mode at 513 cm⁻¹.²¹ The rutile TiO₂ polymorph has five Raman-active modes; B_{1g}, multi-photon process, E_g, A_{1g} and B_{2g} appearing at 140 cm⁻¹, 250 cm⁻¹, 425 cm⁻¹, 609 cm⁻¹, and 825 cm⁻¹, respectively.^{22,23} Well-resolved Raman peaks were observed for the calcined samples with a phase transformation at above 500°C (**Figure 6.2**). The non-crystalline oven-dried sample hardly showed any Raman peaks. N, Os co-doped TiO₂ calcined at 350°C and 500°C gave peaks characteristic of the anatase phase of TiO₂ whilst the sample calcined at 650°C confirmed a mixed anatase-rutile

phase. Calcination at 800°C confirmed complete transformation to the rutile phase. The most intense anatase E_{g(1)} mode showed a red shift whilst the peaks for the sample calcined at 650°C were broader due to peak overlap between the anatase and the rutile vibrational modes as well as the different crystallite sizes after calcination. The broad multi-photon process peak at 254 cm⁻¹ is clearly visible for the rutile-phase samples calcined at 650°C and 800°C.

Calcination of the N, Os co-doped TiO₂ at high temperature in air could have led to the formation of crystalline OsO₂ which, like TiO₂ has a tetragonal rutile structure belonging to the space group P4₂/mnm. OsO₂ has been shown to have four Raman-active modes with symmetries A_{1g} (685 cm⁻¹), B_{1g} (187 cm⁻¹), B_{2g} (726 cm⁻¹), and E_g (544 cm⁻¹). The first three are singlets and the last one is a doublet.²⁴ OsO₂ vibrational modes could not be detected due to possible overlap with the highly intense rutile TiO₂ peaks. Peaks at 694 cm⁻¹ and 718 cm⁻¹ could be due to the A_{1g} and B_{2g} modes of the OsO₂, respectively. These peaks are only present for the high-calcination-temperature samples confirming the formation of OsO₂.

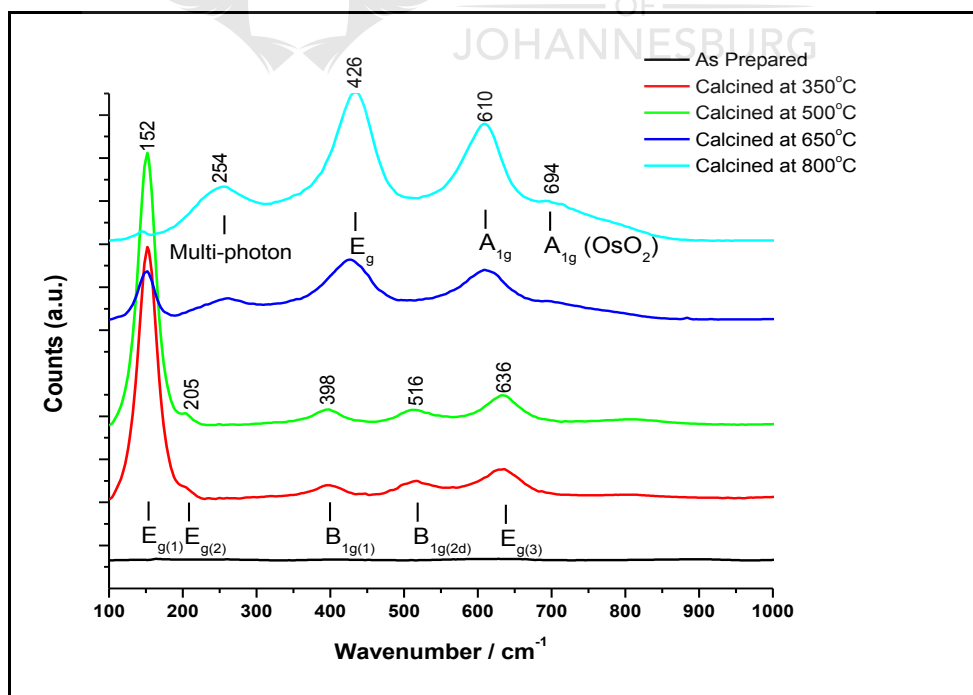
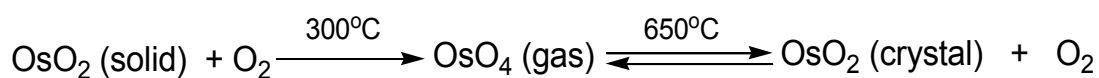


Figure 6.2 Raman spectra of N, Os co-doped TiO₂ calcined at different temperatures

6.3.3 XRD analysis

X-ray diffraction patterns of the N, Os co-doped TiO₂ are displayed in **Figure 6.3**. The presence of both anatase and rutile phases in the samples was confirmed. OsO₂ and TiO₂ fall within the family of transition metal dioxides with rutile-type structure. Little is known about the fundamental properties of OsO₂. This may be due to the highly toxic nature of the readily formed and volatile tetroxide of the material. The formation of crystalline OsO₂ from the amorphous phase occurs at high temperatures. The following reactions take place:²⁵



The diffraction patterns of OsO₂ and TiO₂ in the rutile phase cannot be differentiated. However, the low Os composition led to low-intensity rutile peaks. The oven-dried sample did not show any peaks because of its amorphous nature. Samples calcined at 350°C and 500°C gave characteristic anatase-phase peaks with a small percentage of the rutile phase for the higher-calcination-temperature sample. The presence of Os (0.5%) favours the formation of the rutile phase at calcination temperature of 500°C most probably due to the crystalline structure of OsO₂. Peaks at 2θ values of 25.24 , 37.87, 48.05, 54.03, 55.13, 62.77, 68.85 , 70.29 and 75.05 corresponding to the (101), (004), (200), (105), (211), (204), (116), (220) and (215) planes, respectively, were observed for the anatase-phase TiO₂, in agreement with values given in the literature.²⁶ Samples calcined at 650°C and 800°C gave intense peaks associated with the rutile phase. Peaks appeared at 2θ values of 27.45, 36.09, 39.19, 41.19, 44.61, 54.36, 56.57, 62.77, 64.09, 68.97, 69.85 and 76.49 due to the (110), (101), (111), (200), (210), (211), (220), (002), (310), (301), (112) and (202) mirror planes, respectively, again in agreement with literature values given for the rutile-phase structure.^{25,27}

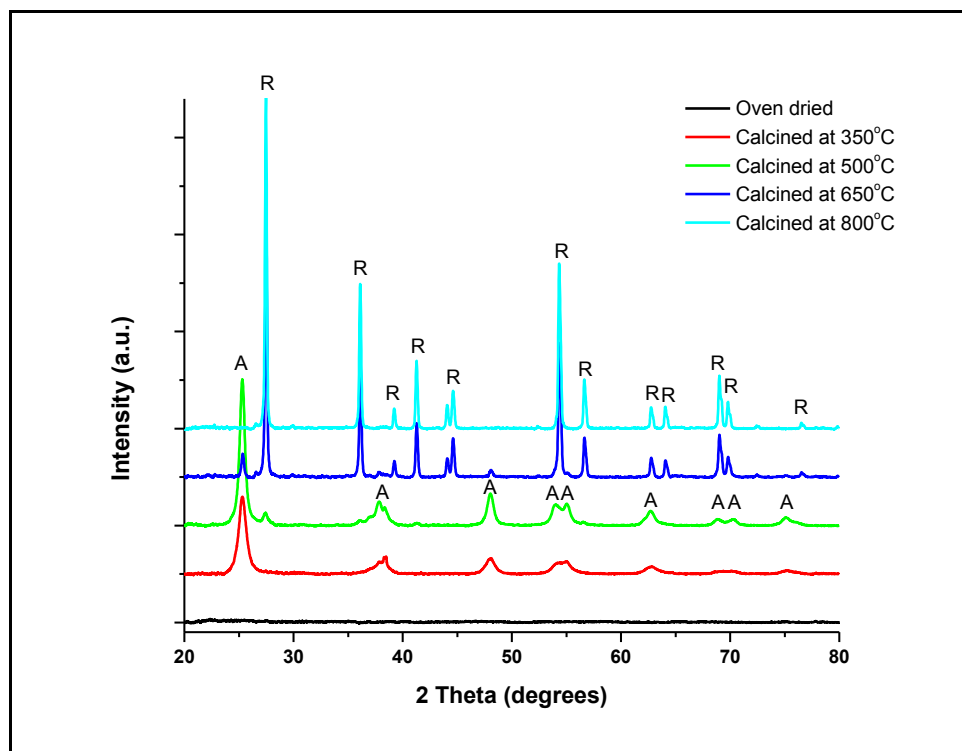


Figure 6.3 XRD spectra of N, Os co-doped TiO₂ calcined at different temperatures (A = anatase; R = rutile)

The anatase- and rutile-phase percentages were deduced from the integrated intensity of the peaks at 2θ values of 25.3 for anatase and 27.4 for rutile (**Section 3.6.4.1**). Average crystal sizes of the nanoparticles were calculated from the full width at half maximum (FWHM) of the most intense peaks using the Scherrer equation (**Table 6.1**). There was an increase in particle size associated with the transformation from the anatase to the rutile phase. This transformation was associated with an increase in crystallinity which may be enhanced by the simultaneous formation of TiO₂ and OsO₂.

Table 6.1 Crystallite size and phase composition of N, Os co-doped TiO₂ calcined at different temperatures [A = Anatase, R = Rutile]

Calcination temperature (°C)	Crystallite size (nm)	Phase composition
Oven-dried	-	-
Calcined at 350°C	7.77	100% A
Calcined at 500°C	14.04	91.9% A, 8.1% R
Calcined at 650°C	14.04	6.6% A, 93.4% R
Calcined at 800°C	15.46	100% R

6.3.4 Optical properties

Changes in the optical properties of the N, Os co-doped TiO₂ nanoparticles calcined at different temperatures were investigated using diffuse reflectance ultraviolet visible (DRUV-Vis) analysis. Samples displayed the typical TiO₂ absorption with an intense transition in the UV region of the spectra, which is assigned to the intrinsic band-gap absorption of TiO₂ due to the electron transitions from the valence band to conduction band (O_{2p} - Ti_{3d}).¹⁷ The commercial TiO₂ (rutile) showed no absorption above its fundamental absorption edge (around 400 nm) (**Figure 6.4**). In contrast, the N, Os co-doped TiO₂ exhibited increasing absorption in the visible region with an increasing calcination temperature, which is in agreement with the colour change from pale yellow to golden brownish. The extent of the red shift depended on the calcination temperature. The oven-dried sample showed the highest absorption in the UV region with some tailing well into the visible region.

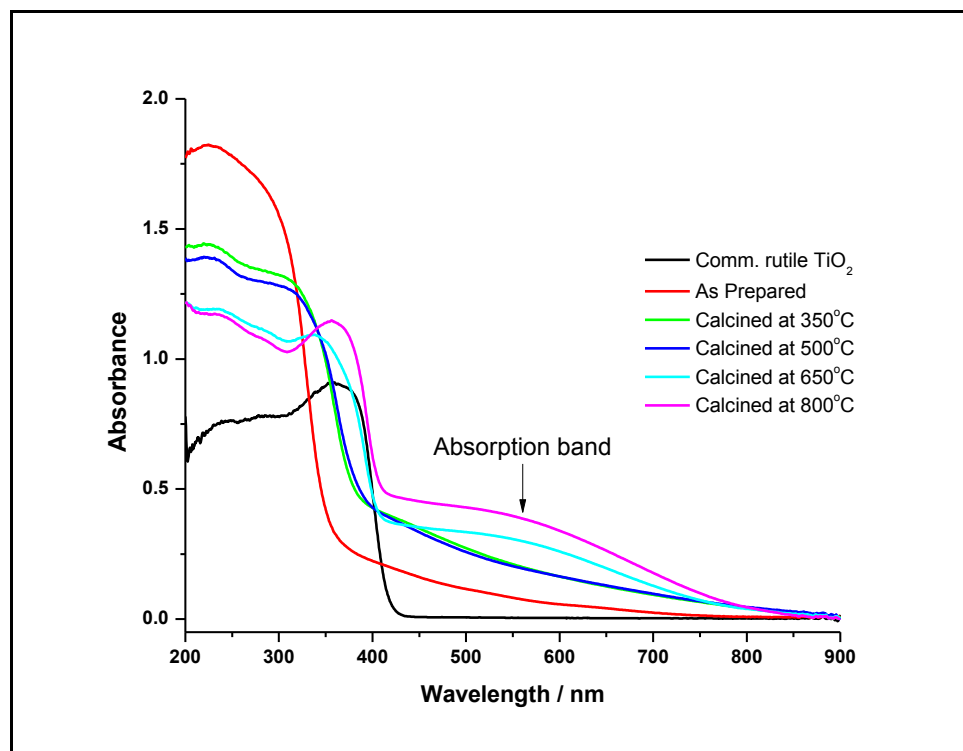


Figure 6.4 UV-Vis absorption spectra of N, Os co-doped TiO₂ calcined at different temperatures

Calcination resulted in a decrease in the UV absorption, increased tailing as well as increased absorption in the visible region. The order of the effectiveness in the red shift was found to be as follows; sample calcined at 800°C > sample calcined at 650°C > sample calcined at 500°C > sample calcined at 350°C > oven-dried (Figure 6.5). This red shift can be attributed to the charge-transfer transition between either the N p or Os d electrons of the dopants and the CB (or VB) of TiO₂. Enhanced absorption in the visible region can also be attributed to the excitation of 5d electrons of Os⁴⁺ to the TiO₂ conduction band (charge transfer-transition) giving rise to a band centred at about 550 nm for higher calcination temperature samples. Besides charge-transfer transitions, d-d transition of Os⁴⁺ can also give rise to absorption in the visible region. The significant enhancement of light absorption in the 400 nm to 800 nm range could point to the effective utilisation of visible light in activating the co-doped photocatalysts. Commercial TiO₂ showed very little tailing with a well-defined absorption edge at about 425 nm.

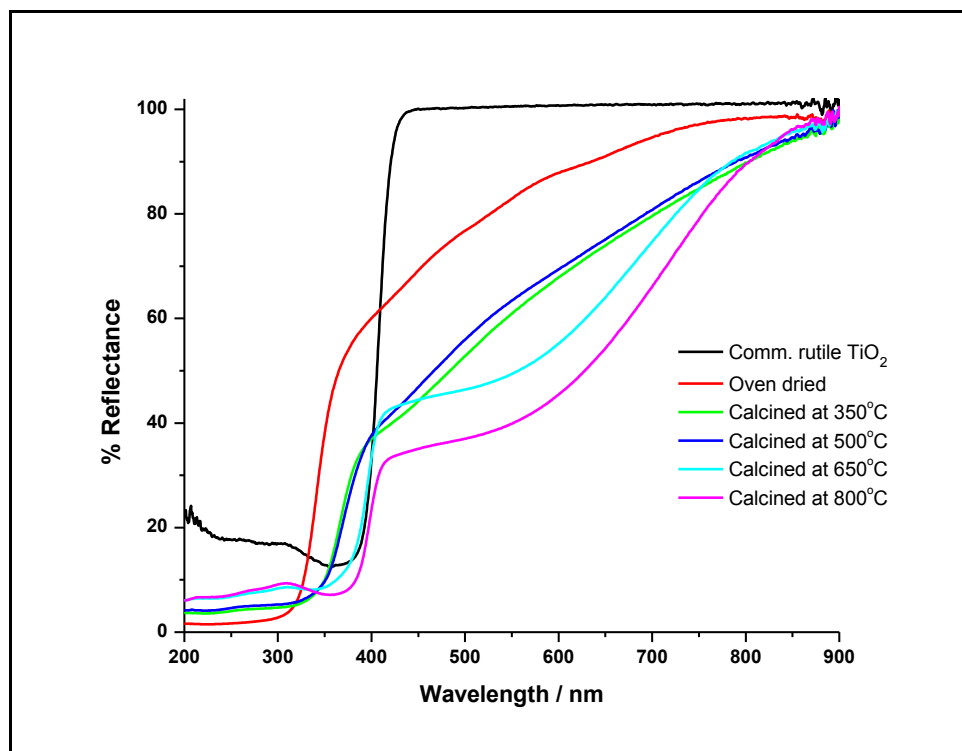


Figure 6.5 Diffuse reflectance UV-Vis spectra of N, Os co-doped TiO₂ calcined at different temperatures

The main mechanism of light absorption in pure semiconductors is direct inter-band electron transitions. This absorption is especially small in indirect semiconductors like TiO₂, where the direct electron transitions between the band centres are prohibited by the crystal symmetry.²¹ The presence of non-metals (e.g. N) and metals such as Os in TiO₂ does not modify the position of the valence-band edge of TiO₂. Instead new energy levels of the non-metal or noble metal are introduced into the band gap of TiO₂ thereby shifting the absorption edges towards longer wavelengths as electronic transitions occur from the dopant energy level to the conduction band of TiO₂. Further enhancement of the absorption occurs due to an increase in electron density of states closer to the valence band. Interface absorption becomes the main mechanism of light absorption for the crystallites that are smaller than 20 nm.²¹

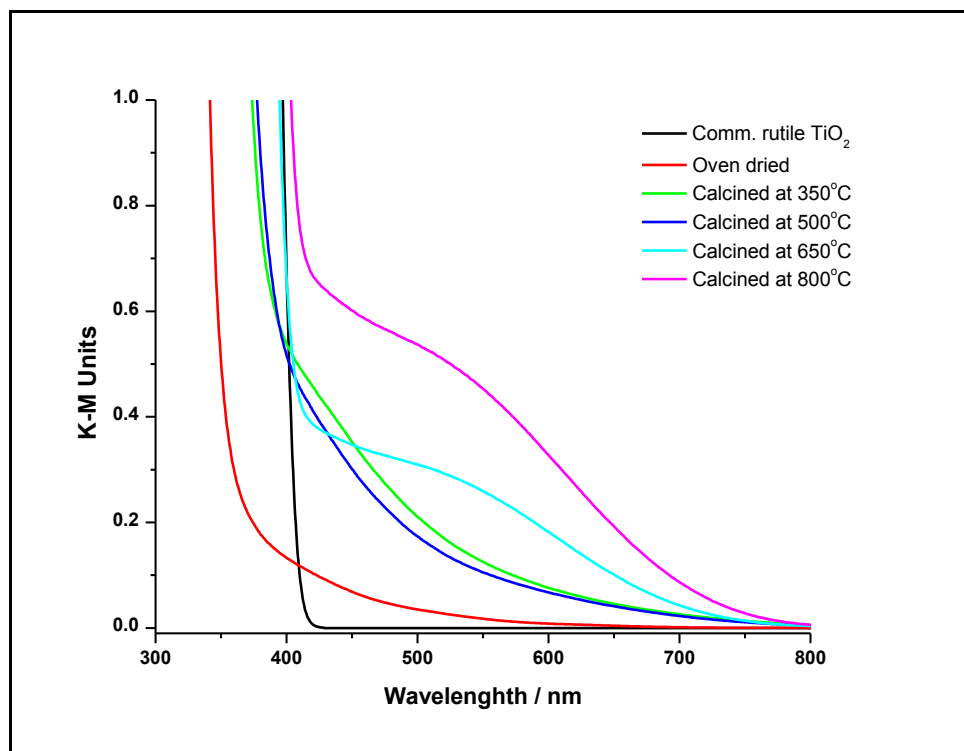


Figure 6.6 Kubelka-Munk spectra of N, Os co-doped TiO₂ calcined at different temperatures

The reflectance data were converted to Kubelka–Munk units and the absorption coefficient data were plotted as a function of wavelength (**Figure 6.6**).

The Tauc plot data were found to fit more satisfactorily the $[F(R) \cdot hv]^2$ vs. photon energy than the $[F(R) \cdot hv]^{1/2}$ vs. photon energy, suggesting a direct band-gap transition (**Figure 6.7**).

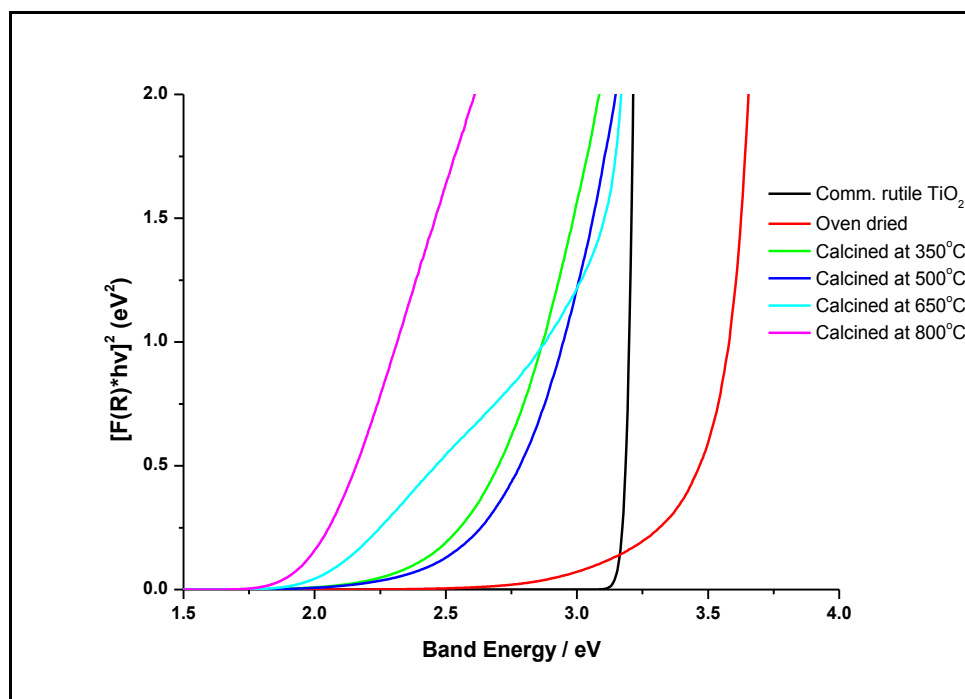


Figure 6.7 Diffuse reflectance UV-Vis spectra of N, Os co-doped TiO₂ calcined at different temperatures

The band gap for pure commercial rutile TiO₂ was found to be 3.11 eV, while that for the oven-dried N, Os co-doped TiO₂ was higher (3.50 eV). There was a continuous decrease in band-gap energy to 1.76 eV with an increase in the calcination temperature (**Table 6.2**). The changes in the phases of the TiO₂ from amorphous through anatase to rutile and of OsO₂ from amorphous to rutile were associated with this reduction in band gaps. Band-gap reduction also points to the formation of inter-band gap states on the TiO₂. The decrease in band gaps may lead to better utilisation of visible light in photocatalytic dye degradation.

Table 6.2 Direct band-gap values for N, Os co-doped TiO₂ calcined at different temperatures

Sample	Direct band gap (eV)
Comm. rutile TiO ₂	3.11
Oven-dried	3.50
Calcined at 350°C	2.60
Calcined at 500°C	2.62
Calcined at 650°C	1.84
Calcined at 800°C	1.76

6.3.5 SEM and EDS analyses

SEM analysis was performed in order to obtain information on the shape and surface structure of the material. Images revealed particle agglomerations to form large nanoclusters (**Figure 6.8(a)** and **Figure 6.8(b)**). These agglomerates are assemblies of aggregates held together by weak bonds that may be due to Van der Waals forces or by ionic/covalent bonds operating over very small contact areas. Similar observations were reported for Pt and Au/TiO₂ synthesised using a sol-gel method.²⁸ Particles appeared spherical and were in the nanometre range. It was difficult to estimate the actual size of single particles due to aggregation.

The elemental composition of the various samples was estimated by EDS (**Figure 6.8(c)**). EDS spectra of the co-doped TiO₂ showed signals directly related to the dopants. Results confirmed the presence of Ti, O and Os indicating the formation of N, Os co-doped TiO₂ nanoparticles. Low dopant amounts of Os resulted in correspondingly weak EDS peaks.

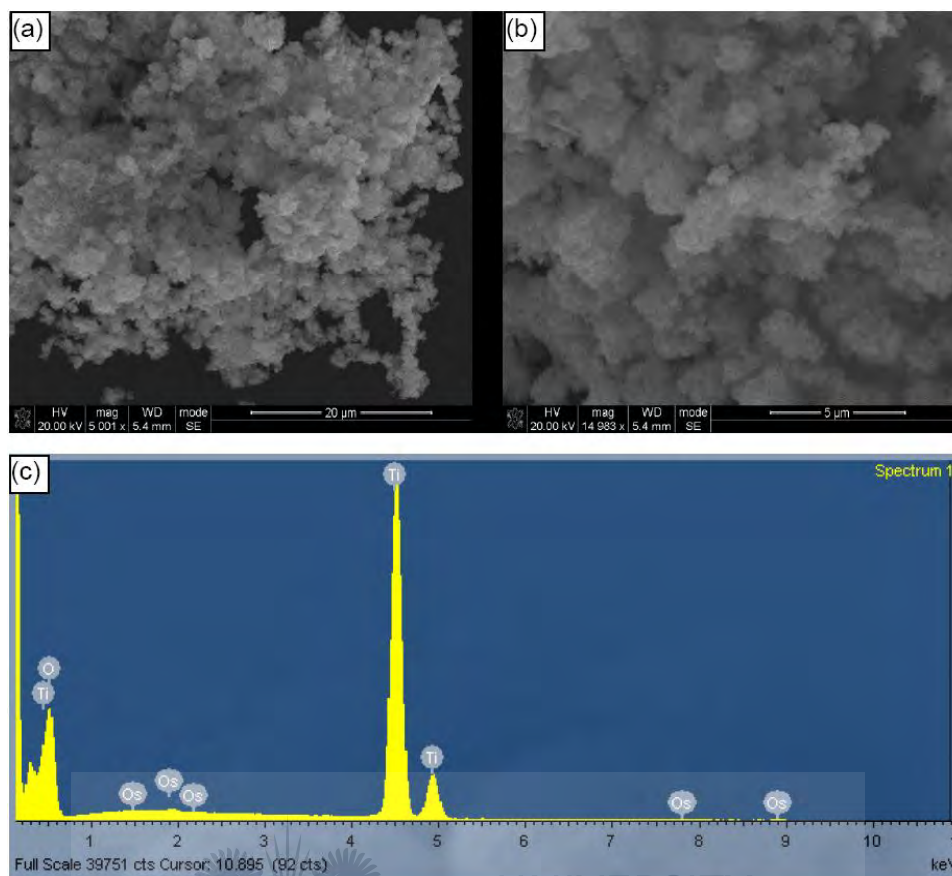


Figure 6.8 (a) and (b) SEM images; and (c) EDS spectrum of N, Os co-doped TiO₂ calcined at 500°C

6.3.6 TEM analysis

TEM analysis revealed that the morphology of N, Os co-doped TiO₂ nanoparticles was temperature dependent and ranged from spherical to cuboidal, with some showing elongated ellipsoidal shapes (**Figure 6.9**). There was an increase in particle size and crystallinity with increasing calcination temperature. Calcination at 350°C led to small, slightly crystalline particles with an approximate size of about 10 nm. Calcination at 500°C resulted in particles with a size range of 10 - 20 nm showing increased crystallinity. OsO₂ particles could not be observed since they appear in the amorphous phase at temperatures below 650°C. Also there is no way to know if the OsO₂ will form particles or just substitute the Ti. Agglomeration and crystallite stacking is evident. Samples calcined at 650°C were bigger and showed regular spherical to cuboidal structures. These particles ranged in size

from about 20 nm to 50 nm. Tiny particles, possibly of OsO₂ could be observed on the TiO₂ surface but these could not be confirmed. After calcination at 800°C, the TiO₂ nanoparticles maintained their crystalline structure, but their size visibly increased to about 100 nm due to agglomeration and change in the phase from anatase to rutile.²⁹ The calcination at high temperature not only led to a further increase in particle size but also resulted in the formation of crystalline OsO₂ in the rutile phase, observed as small spherical dots (about 5 nm) on the surfaces of the TiO₂ nanoparticles calcined at 800°C.²⁵

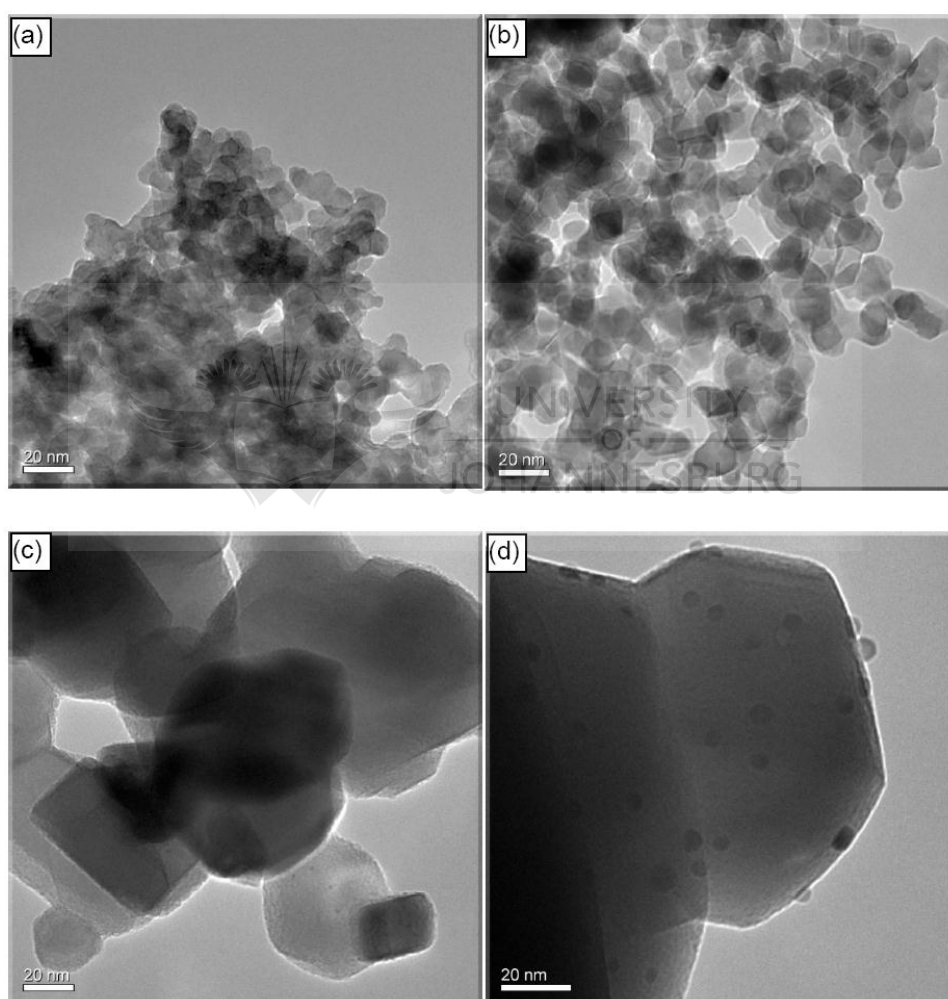


Figure 6.9 TEM images of N, Os co-doped TiO₂ calcined at (a) 350°C; (b) 500°C; (c) 650°C; and (d) 800°C

These observations are contrary to the XRD results, where very small differences in crystallite size with increasing calcination temperature were noted. This might be due to the presence of much smaller OsO₂ particles dispersed on the large rutile

TiO₂ crystallites. Rutile TiO₂ is a semiconductor whilst rutile OsO₂ shows metallic properties. There is an intimate contact between the two rutile phases. Rutile TiO₂ nanoparticles can therefore act as supports for rutile OsO₂ particles, a system that is attractive for visible-light photochemistry due to synergistic effects or inter-particle charge migration.

6.3.7 Thermal properties

Thermograms of the oven-dried sample together with samples calcined at 350°C and 800°C are shown in **Figure 6.10**. A mass loss of about 25% attributed to the loss of water adsorbed onto the particle surface and precursor material, both nitrogenous as well as carbonaceous, was observed for the oven-dried sample between 30°C and 250°C. Between 250°C and 650°C, a further mass loss of about 5% was observed. This can be attributed to the decomposition of OsO₂ into the volatile OsO₄ and metallic Os together with more nitrogen- or carbon-related materials entrapped within the nanoparticles. The sample calcined at 350°C showed a small weight loss of about 5% from 30°C up to about 800°C, due to loss of nitrogen- or carbon-related materials. At a calcination temperature of 350°C, very little OsO₂ could have remained on the nanoparticles as the amorphous OsO₂ decomposes to the volatile OsO₄ without forming the crystalline OsO₂. The sample calcined at 800°C showed an even smaller weight loss of about 2%. This is attributed to the formation of the much more stable rutile TiO₂ and crystalline rutile OsO₂. All carbon- and nitrogen-related materials were lost by calcination at 800°C. The total mass loss of between 2.0% and 5% shows the exceptionally high thermal stability of the materials calcined at 350°C and 800°C.

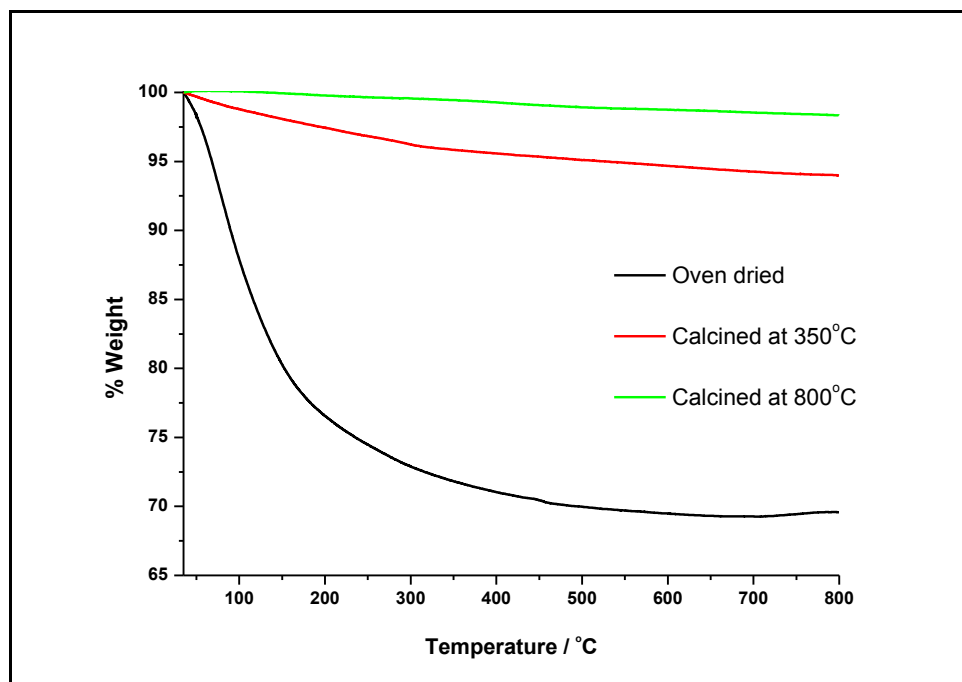


Figure 6.10 TGA curves of N, Os co-doped TiO₂

6.4 DYE PHOTODEGRADATION STUDIES

Results of the degradation of Eosin Yellow under simulated solar irradiation in the presence of N, Os co-doped TiO₂ calcined at different temperatures are shown in **Figure 6.11**. There is an increase in the degradation efficiency with increasing calcination temperature. The phase change from anatase to rutile is normally associated with a decrease in photocatalytic activity due to increased electron-hole recombination rate and large crystallite size.³⁰ Increased light-harvesting capability of the rutile N, Os co-doped TiO₂ can be explained by the presence of OsO₂ acting as an electron sink for the photogenerated electrons. Previous work on TiO₂ photocatalysts suggested that TiO₂ with the anatase structure exhibits substantially higher photocatalytic activity than TiO₂ in the amorphous or rutile phases as a result of its slightly higher Fermi level, lower capacity to adsorb oxygen and higher degree of hydroxylation. It was also reported that highly crystalline anatase had a higher adsorptive affinity for organic compounds and exhibited a lower recombination rate than rutile TiO₂.³¹ A number of research groups have tried to unravel the mystery of the synergetic effect between anatase and rutile forms of TiO₂ by comparing samples with varying polymorph compositions. Synergetic effects were observed for anatase compositions ranging

from 20% to 90%. Another factor that may explain the differences in the photoactivity relates to optical thickness of the catalyst sample. A catalyst that absorbs more photons in the suspension may perform better. However, pure rutile TiO₂ was found to be less effective in photocatalysis.³² This is in contrast to our work where the rutile phase show very good activity.

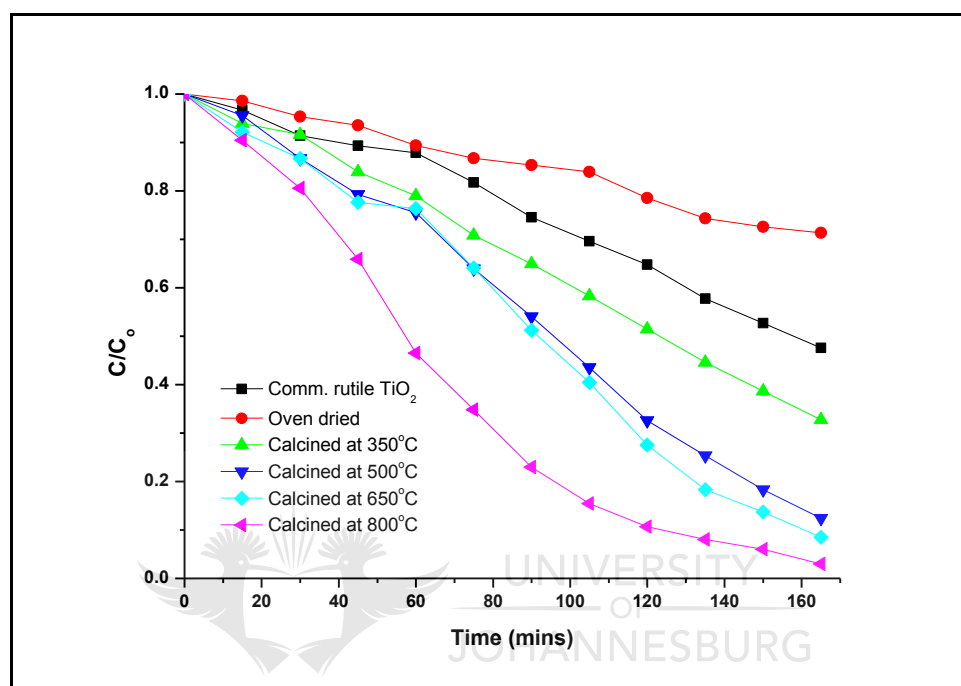


Figure 6.11 EY photodegradation by N, Os co-doped TiO₂ calcined at different temperatures

The highest photocatalytic activity was observed for the N, Os co-doped TiO₂ calcined at 800°C under visible-light irradiation. This sample consisted of the rutile phases of TiO₂ and possibly OsO₂. Rutile TiO₂ alone hardly shows any photocatalytic activity under ultraviolet or visible light because of the high rate of electron-hole recombination. Contrary to our observation, Wang *et al.* reported a decline in photocatalytic activity of TiO₂ treated at temperatures of above 600°C.³³ Chen *et al.* synthesised N-doped TiO₂ by post-nitridation annealing at various temperatures and assessed its photocatalytic activity for ethylene decomposition under visible light. They reported an increase in activity with increasing annealing temperature up to 400°C followed by a decrease as the temperature was increased to 600°C. The decrease was attributed to the change in TiO₂ phase from anatase to rutile associated with an increase in particle size.¹⁶ The synergistic

effects of TiO₂ and OsO₂ could have led to the observed rutile photocatalytic stretch. The smaller size of the dispersed OsO₂ particles probably leads to an overall increase in surface area and improved adsorption and subsequently degradation of the eosin yellow dye.²³ Formation of OsO₂ on the rutile TiO₂ surface led to an enhancement in the photocatalytic reactivity due to enhanced charge separation of the electrons and holes generated by visible-light irradiation. The presence of small amounts of platinum-group metals on semiconducting TiO₂ has been reported to enhance electron-hole separation in photocatalysis.³⁴

There was a general decrease in dye adsorption with increasing calcination temperature, consistent with the observed increase in particle size and consequently decreased surface area for dye adsorption (**Table 6.3**). There was no correlation between dye adsorption and dye degradation implying that photodegradation is controlled by electron-transfer processes and not surface area.

Table 6.3 EY adsorption and degradation by different N, Os co-doped TiO₂ samples

Sample	Dye adsorption (%)	Degradation after 165 min (%)
Comm. rutile TiO ₂	5.9	52.43
Oven-dried	11.7	28.65
Calcined at 350°C	10.0	67.25
Calcined at 500°C	7.6	87.58
Calcined at 650°C	3.2	91.54
Calcined at 800°C	4.3	97.02

A plot of $\ln(C_0/C)$ vs. time gave nearly a straight line, the slope of which upon linear regression approximates the overall apparent first-order rate constant, k_a .^{35,36} (**Figure 6.12**). Good linear relationships were observed at low calcination temperatures, indicating that the reactions followed first-order kinetics. At

calcination temperatures of 650°C and 800°C, pseudo first-order kinetics were observed, an indication that OsO₂ played a part in the degradation of the dye. The deviation from first order kinetics at higher calcination temperatures can be attributed to the increase in particle size as evidenced by TEM images. The larger the particle size, the lower the surface area and consequently the lower the photon absorption. This may have effects on the kinetics of the photoreactions.

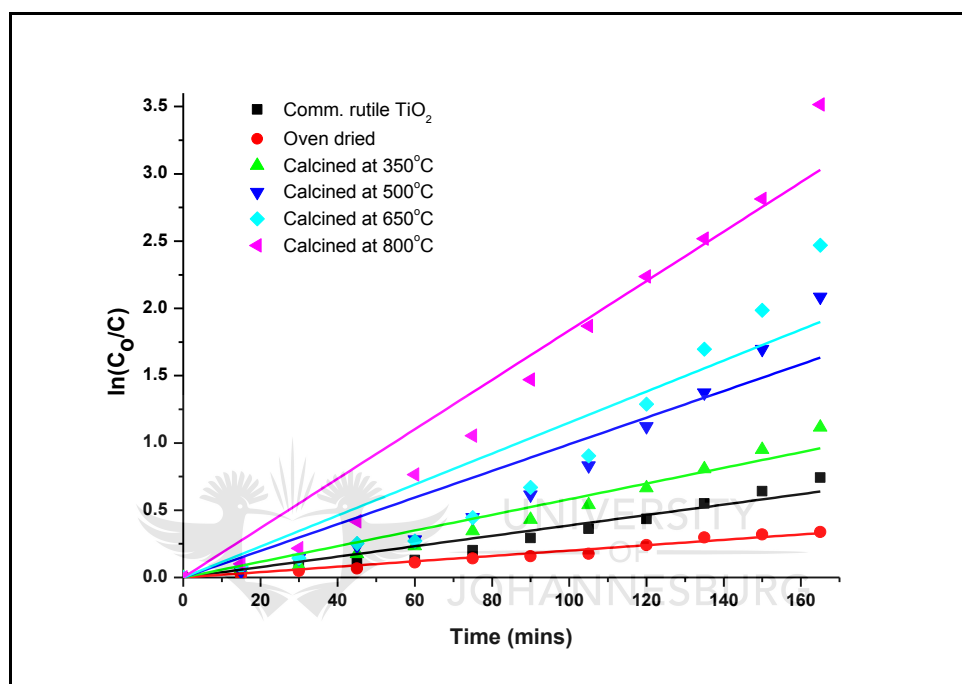


Figure 6.12 EY photodegradation kinetics by N, Os co-doped TiO₂ calcined at different temperatures

First-order rate constants of N, Os co-doped TiO₂ nanoparticles calcined at different temperatures are shown in **Table 6.4**. The rate constants increased with calcination temperature. The oven-dried sample showed the lowest rate of $2.00 \times 10^{-3} \text{ min}^{-1}$ whilst the sample calcined at a temperature of 800°C gave a rate constant of $1.84 \times 10^{-2} \text{ min}^{-1}$. A system consisting of carbon, nitrogen co-doped TiO₂ prepared by the sol-gel method was tested for the degradation of methylene blue dye. It was found that the degradation activity drops sharply with an increase in calcination temperature. The sample calcined at 300°C was found to be the most efficient in dye degradation (97.14% removal) under visible-light irradiation.³⁷ In another study on photodegradation of Bisphenol A (BPA) under visible-light irradiation using praseodymium (Pr), nitrogen co-doped titania (Pr/N-TiO₂)

photocatalysts prepared by the modified sol-gel process, the optimal dopant amount of Pr was found to be 1.2 mol% for samples calcined at 500°C. An apparent rate constant of $(4.56 \pm 0.11) \times 10^{-3} \text{ min}^{-1}$ was reported for the best photocatalytic activity. An increase in calcination temperature to 600°C and 800°C resulted in reduced photocatalytic rate constants as the TiO₂ transformed from the anatase to the rutile phase. Pr/N-TiO₂ samples exhibited enhanced visible-light photocatalytic activity compared to N-doped TiO₂, un-doped TiO₂ and commercial P25.³⁵ A rate constant of $1.38 \times 10^{-4} \text{ min}^{-1}$ was reported for carbon, vanadium co-doped TiO₂ prepared by a sol-gel method for the degradation of acetaldehyde under visible radiation ($\lambda > 450 \text{ nm}$).³⁸ The N, Os co-doped TiO₂ particles exhibited much higher photodegradation rates compared to these similar co-doped systems.

Table 6.4 Apparent first-order rate constants of N, Os co-doped TiO₂ nanoparticles calcined at different temperatures

Sample	Apparent first-order rate constant, k_a (min ⁻¹)
Comm. rutile TiO ₂	3.87×10^{-3}
Oven-dried	2.00×10^{-3}
Calcined at 350°C	5.82×10^{-3}
Calcined at 500°C	9.90×10^{-3}
Calcined at 650°C	1.15×10^{-2}
Calcined at 800°C	1.84×10^{-2}

The apparent rate constant values were normalised to the rate constant, k_R of the commercial pure rutile TiO₂. Values for the normalised rate constant, $K = k_a/k_R$ were plotted as a function of the calcination temperature (**Figure 6.13**). The amorphous oven-dried sample exhibited the lowest photoactivity. Activity increased with increasing calcination temperature with the maximum activity observed for the sample calcined at 800°C. There is an exponential increase in photoactivity with increasing calcination temperature up to 650°C. This is most

probably due to the phase transformation from the amorphous to anatase form as well as an increase in crystallinity of the particles. At 650°C a mixture of anatase and rutile TiO₂ was observed. Mixed anatase-rutile phase TiO₂ has been reported to show increased photoactivity due to synergistic effects of the rutile form (with the lower band gap) on the anatase form with respect to electron-hole recombination as well as higher adsorption affinity for organic molecules by the smaller anatase particles.³² The sample calcined at 800°C showed the highest activity due to the synergistic effects of the rutile TiO₂ and OsO₂. The rate constant is about 4.5 times higher than that of commercial rutile TiO₂ and nearly twice that of the anatase samples calcined at 350°C and 500°C. This constitutes a significant improvement in the photoactivity of the material. Although the measurement does not reveal what exactly caused the synergism, it seems plausible to assume that electrons that are photoexcited in rutile TiO₂ migrated to the vacant d orbitals of Os, thereby effectively suppressing recombination.³⁸ These observations are contrary to many reports published on the photoactivity of rutile TiO₂ on pollutant removal from water.³²

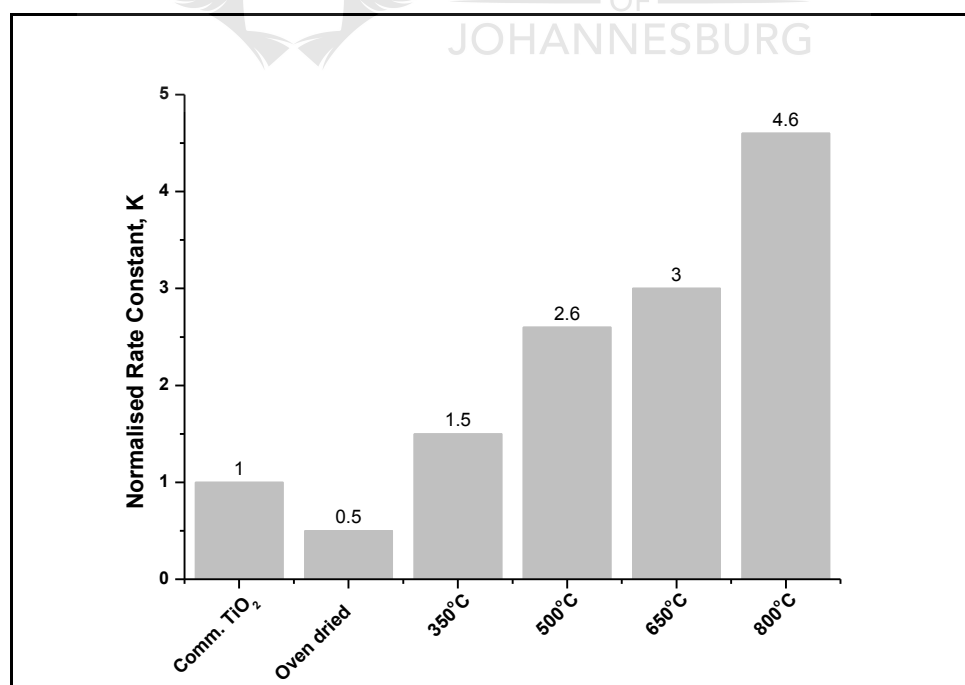


Figure 6.13 Normalised rate constants of N, Os co-doped TiO₂ calcined at different temperatures

The proposed mechanism for the EY photodegradation under simulated solar irradiation is shown in **Figure 6.14**. The enhanced visible light activity is pretty much due to reasons mentioned earlier, except that in this case a Schottky barrier is formed between the rutile TiO₂ and the rutile OsO₂.

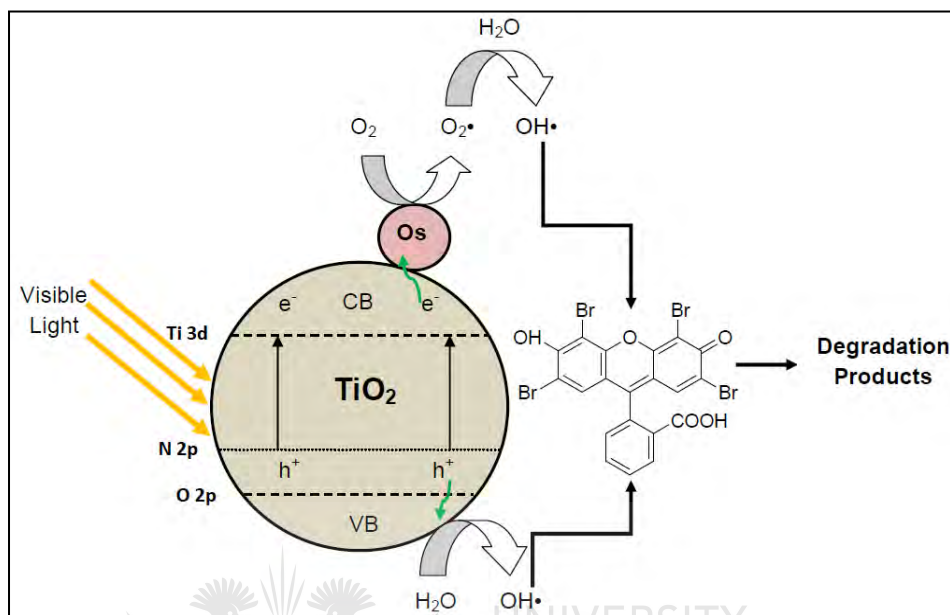


Figure 6.14 Proposed mechanism for EY photodegradation under visible-light irradiation

A proposed explanation for the enhanced effect in the presence of Os, is that the photogenerated electrons are trapped in vacant d orbitals, leading to electron-hole separation. A Schottky barrier could be formed at the interface of TiO₂ and Os when their Fermi levels are equal. The barrier height is the energy difference between the work function of the Os (4.8 eV) and the electron affinity of the TiO₂ (3.9 eV). Driven by this Schottky barrier, photogenerated electrons transfer directionally, from the outer TiO₂ layer to the inner Os network resulting in an enhanced separation of photogenerated charge carriers.^{39,40}

6.5 CONCLUSION

N, Os co-doped TiO₂ catalysts were successfully synthesised by the sol-gel process. Increasing calcination temperature resulted in phase transformation from amorphous through anatase to rutile for the TiO₂, whilst the amorphous OsO₂ was

transformed to the rutile phase. The rutile phase N, Os co-doped TiO₂ calcined at 800°C showed high activity compared to the anatase phase for the photodegradation of Eosin Yellow under visible-light irradiation. The Os appeared as crystalline OsO₂ and was uniformly dispersed on the rutile TiO₂ surface. Os acted as an electron sink for the photogenerated electrons thereby increasing the lifetime of holes which are highly reactive towards adsorbed organic molecules. 97.02% Eosin Yellow photodegradation was achieved in 165 min with the rutile N, Os TiO₂ calcined at 800°C compared to 87.58% with the anatase phase calcined at 500°C. It was observed that the photodegradation rate increased 1.77 fold for the sample calcined at 800°C relative to the anatase sample calcined at 500°C. Results from this study showed that rutile N, Os co-doped TiO₂ is more efficient in degrading EY compared to the anatase phase, contrary to the general observation that the anatase phase TiO₂ is more active than the rutile phase under UV or visible-light irradiation.

6.6 REFERENCES

1. Garcia T.B., Solsona B., Murphy D.M., Antcliff K.L. and Taylor S.H. (2005). Deep oxidation of light alkanes over titania-supported palladium/vanadium catalysts. *J. Catal.* 229, 1 – 11.
2. Sonawane R.S. and Dongare M.K. (2006). Sol-gel synthesis of Au/TiO₂ thin films for photocatalytic degradation of phenol in sunlight. *J. Mol. Catal. A: Chem.* 243, 68 – 76.
3. Li Y., Wen B., Ma W., Chen C. and Zhao J. (2012). Photocatalytic degradation of aromatic pollutants: A pivotal role of conduction band electron in distribution of hydroxylated intermediates. *Environ. Sci. Technol.* 46, 5093 – 5099.
4. Han F., Kambala V.S.R., Srinivasan M., Rajarathnam D. and Naidu R. (2009). Tailored titanium dioxide photocatalysts for the degradation of organic dyes in wastewater treatment: A review. *Appl. Catal. A: Gen.* 359, 25 – 40.

5. Gao B., Ma Y., Cao Y., Yang W. and Yao J. (2006). Great enhancement of photocatalytic activity of nitrogen-doped titania by coupling with tungsten oxide. *J. Phys. Chem. B* 110, (29), 14391 – 14397.
6. Wang J., Tafen D.N., Lewis J.P., Hong Z., Manivannan A., Zhi M., Li M. and Wu N. (2009). Origin of photocatalytic activity of nitrogen-doped TiO₂ nanobelts. *J. Am. Chem. Soc.* 131, 12290 – 12297.
7. Zou Z., Ye J., Sayama K. and Arakawa H. (2001). Direct splitting of water under visible light irradiation with an oxide semiconductor photocatalyst. *Nature* 424, 625.
8. Yamashita H., Harada H., Misaka J., Takeuchi M., Ikeue K. and Anpo M. (2002). Degradation of propanol diluted in water under visible light irradiation using metal ion-implanted titanium dioxide photocatalysts. *J. Photochem. Photobiol. A* 148, 257 – 261.
9. Asahi R., Morikawa T., Ohwaki T., Aoki K. and Tao Y. (2001). Visible-light photocatalysis in nitrogen-doped titanium oxides. *Sci.* 293, 269 – 271.
10. Khan S.U.M., Al-Shahry M. and Ingler Jr, W.B. (2002). Efficient photochemical water splitting by a chemically modified n-TiO₂. *Sci.* 297, 2243 – 2245.
11. Kowalska E., Abe R. and Ohtani B. (2009). Visible light-induced photocatalytic reaction of gold-modified titanium (IV) oxide particles: Action spectrum analysis. *Chem. Commun.* 2, 241 – 243.
12. Hufschmidt D., Bahnemann D., Testa J.J., Emilio C.A. and Litter M.I. (2002). Enhancement of the photocatalytic activity of various TiO₂ materials by platinisation. *J. Photochem. Photobiol. A* 148, (1–3) 223 – 231.
13. Ciesla P., Kocot P., Mytych P. and Stasicka Z. (2004). Homogeneous photocatalysis by transition metal complexes in the environment. *J. Mol. Catal. A: Chem.* 224, 17 – 33.

14. Sivalingam G., Nagaveni K., Hegde M.S. and Madras G. (2003). Photocatalytic degradation of various dyes by combustion synthesised nano anatase TiO₂. *Appl. Catal. B* 45, 23 – 38.
15. Lin Z., Orlov A., Lambert R.M. and Payne M.C. (2005). New insights into the origin of visible light photocatalytic activity of nitrogen-doped and oxygen-deficient anatase TiO₂. *J. Phys. Chem. B.* 109, 20948 – 20952.
16. Chen X., Wang X., Hou Y., Huang J., Wu L. and Fu X. (2008). The effect of postnitridation annealing on the surface property and photocatalytic performance of N-doped TiO₂ under visible light irradiation. *J. Catal.* 255, 59 – 67.
17. Yu J., Ma T. and Liu S. (2011). Enhanced photocatalytic activity of mesoporous TiO₂ aggregates by embedding carbon nanotubes as electron-transfer channel. *Phys. Chem. Chem. Phys.* 13, 3491 – 3501.
18. Lu G., Linsebigler A. and Yates J. (1994). Ti³⁺ Defect Sites on TiO₂ (110): Production and Chemical Detection of Active Sites. *J. Phys. Chem.* 98, 11733 – 11738.
19. Kumar P.M., Badrinarayanan S. and Sastry M. (2000). Nanocrystalline TiO₂ Studied by Optical, FTIR and X-ray Photoelectron Spectroscopy: Correlation to Presence of Surface States. *Thin Solid Films* 358, 122 – 30
20. Debeila M.A., Coville N.J., Scurrill M.S. and Hearne G.R. (2005). The effect of calcination temperature on the adsorption of nitric oxide on Au-TiO₂: Drifts studies. *Appl. Catal. A Gen.* 291, 98 –115.
21. Chen X. and Mao S.S. (2007). Titanium dioxide nanomaterials: Synthesis, properties, modifications and applications. *Chem. Rev.* 107, 2891 – 2959.
22. Ma H.L., Yang J.Y., Dai Y., Zhang Y.B., Lu B. and Ma G.H. (2007). Raman study of phase transformation of TiO₂ rutile single crystal irradiated by infrared femtosecond laser. *Appl. Surf. Sci.* 253, 7497 – 7500.

23. Yang X., Cao C., Erickson L., Hohn K., Maghirang R. and Klabunde K. (2008). Synthesis of visible-light-active TiO₂-based photocatalysts by carbon and nitrogen doping. *J. Catal.* 260, 128 – 133.
24. Yen P.C., Chen R.S., Huang Y.S., Chia C.T., Chen R.H. and Tjong K.K. (2003). The first-order Raman spectra of OsO₂. *J. Phys.: Condens. Matter* 15, 1487 – 1494.
25. Yen P.C., Chen R.S., Chen C.C., Huang Y.S. and Tjong K.K. (2004). Growth and characterization of OsO₂ single crystals. *J. Cryst. Growth* 262, 271 – 276.
26. Panagiotopoulou P. and Kondarides D.I. (2004). Effect of morphological characteristics of TiO₂-supported noble metal catalysts on their activity for the water–gas shift reaction. *J. Catal.* 225, 327 – 336.
27. Ge M., Li W., Liu L. and Zhou Z. (2011). Template-free synthesis and photocatalytic application of rutile TiO₂ hierarchical nanostructures. *Ind. Eng. Chem. Res.* 50, 6681 – 6687.
28. Rosseler O., Shankar M.V., Le Du M.K., Schmidlin L., Keller N. and Keller V. (2010). Solar light photocatalytic hydrogen production from water over Pt and Au/TiO₂ (anatase/rutile) photocatalysts: Influence of noble metal and porogen promotion. *J. Catal.* 269, 179 – 190.
29. Wang Y., Zhang L., Deng K., Chen X. and Zou Z. (2007). Low temperature synthesis and photocatalytic activity of rutile TiO₂ nanorod superstructures. *J. Phys. Chem. C* 111, 2709 – 2714.
30. Sun J., Gao L. and Zhang Q. (2003). Synthesizing and comparing the photocatalytic properties of high surface area rutile and anatase titania nanoparticles. *J. Am. Ceram. Soc.* 86, 1677 – 1682.
31. Junin C., Thanachayanont C., Euvananont C., Inpor K. and Limthongkul P. (2008). Effects of precipitation, sol-gel synthesis conditions, and drying

- methods on the properties of nano-TiO₂ for photocatalysis applications. *Eur. J. Inorg. Chem.* (6), 974 – 979.
32. Su R., Bechstein R., So L., Vang R.T., Sillassen M., Esbjornsson B., Palmqvist A. and Besenbache, F. (2011). How the anatase-to-rutile ratio influences the photoreactivity of TiO₂. *J. Phys. Chem. C* 115, 24287 – 24292.
33. Wang J., Li R.H., Zhang Z.H., Sun W., Wang X.F., Xing Z Q., Xu R. and Zhang X.D. (2008). Heat treatment of nanometer anatase powder and its photocatalytic activity for degradation of acid red B dye under visible light irradiation. *Inorg. Mater.* 44, 608 – 614.
34. Anpo M. and Takeuchi M. (2003). The design and development of highly reactive titanium oxide photocatalysts operating under visible light irradiation. *J. Catal.* 216, 505 – 516.
35. Yang J., Dai J. and Li. J. (2011). Synthesis, characterization and degradation of Bisphenol A using Pr, N co-doped TiO₂ with highly visible light activity. *Appl. Surf. Sci.* 257, 8965 – 8973.
36. Guo C., Ge M., Liu L., Gao G., Feng Y. and Wang Y. (2010). Directed synthesis of mesoporous TiO₂ microspheres: Catalysts and their photocatalysis for Bisphenol A degradation. *Environ. Sci. Technol.* 44, 419 – 425.
37. Silija P., Yaakob Z., Yarmo M.A., Sugunan S. and Binith N.N. (2011). Visible light active anion codoped sol gel titania photocatalyst for pollutant degradation. *J. Sol-Gel Sci. Technol.* 59, 252 – 259.
38. Yang X., Cao C., Hohn K., Erickson L., Maghirang R., Hamal D. and Klabunde K. (2007). Highly visible-light active C- and V-doped TiO₂ for degradation of acetaldehyde. *J. Catal.* 252, 296 – 302.

39. Chen H., Chen S., Quan X. and Zhang Y. (2010). Structuring a TiO₂-based photonic crystal photocatalyst with Schottky junction for efficient photocatalysis. *Environ. Sci. Technol.* 44, 451 – 455.
40. Kuvarega A.T., Krause R.W.M. and Mamba B.B. (2011). Nitrogen/palladium co-doped TiO₂ for efficient visible light photocatalytic dye degradation. *J. Phys. Chem. C* 115, 22110 – 22120.



CHAPTER 7

MULTIWALLED CARBON NANOTUBES DECORATED WITH NITROGEN, PALLADIUM CO-DOPED TiO₂ (MWCNT/N, Pd CO-DOPED TiO₂) FOR VISIBLE-LIGHT PHOTOCATALYTIC DEGRADATION OF EOSIN YELLOW IN WATER[†]

Carbon nanotube-titanium dioxide (CNT-TiO₂) nanocomposite systems are currently being considered for many applications including their potential use to address environmental problems. This chapter then highlights the synthesis, characterisation and photocatalytic activity of MWCNT/N, Pd co-doped TiO₂ nanocomposites for degradation of a model dye in water. The chapter also provides deeper insight into the MWCNT junction with TiO₂ and how this enhances the photoactivity of the nanocomposite.

7.1 INTRODUCTION

Carbon nanotubes (CNTs) exhibit excellent mechanical, electrical and magnetic properties as well as nanometre-scale diameter and high aspect ratio, which make them suitable candidates to mitigate the ever-increasing environmental challenges. They can be considered as good supports for semiconductors with photocatalytic properties because of their chemical stability, high mechanical strength and nanoporous character, which favour the diffusion of reacting agents. They also show great potential for sensor application, composites and as membrane materials.^{1,2} To date, many types of inorganic and organic molecules have been successfully employed to decorate CNTs using various methods. These

[†] Contents of this chapter were published in a slightly modified form in:

Kuvarega A.T., Krause R.W.M. and Mamba B.B. (2012). Multiwalled carbon nanotubes decorated with nitrogen, palladium co-doped TiO₂ (MWCNT/N, Pd co-doped TiO₂) for visible light photocatalytic degradation of eosin yellow in water. *J. Nanopart. Res.* 14, 776. DOI: 10.1007/s11051-012-0776-x.

composites not only exhibit unique intrinsic properties, such as electronic, mechanical, adsorption and thermal properties, but also display cooperative or synergetic effects.³

The published literature on CNT/TiO₂ nanocomposites has attracted the attention of scientists because of their many and varied applications, *inter alia*, the purification of contaminated water.³⁻⁵ CNTs can efficiently adsorb pollutants in water and also increase the photocatalytic activity of TiO₂ by acting as electron traps, thus stabilising the charge carriers and suppressing the rate of electron-hole recombination.^{4,6} Photocatalysis by TiO₂-based semiconductors has received much attention in the past few decades with the final goal of efficiently converting solar light energy into useful chemical energy. The effective utilisation of clean, safe and abundant solar energy should lead to promising solutions not only for energy issues due to the exhaustion of natural energy sources, but also for environmental pollution remediation.⁷⁻¹⁰

There are a number of methods that can be used to fabricate CNT/TiO₂ composite materials, including mechanical mixing of TiO₂ and CNTs, sol-gel synthesis of TiO₂ in the presence of CNTs, electro-spinning methods, electrophoretic deposition and chemical vapour deposition.^{4,6,11-13} The uniformity of the oxide coating and the physical properties of the composite materials may vary depending on the preparation method used. Though uniform coating of TiO₂ on CNTs may be achieved by chemical vapour deposition and electro-spinning methods, these techniques are not simple. They require specialised equipment and it may be difficult to quantify the ratio between composite compounds. Sol-gel methods are still the most preferred, although they usually lead to a heterogeneous, non-uniform coating of CNTs by TiO₂, showing bare CNT surfaces and random aggregation of TiO₂ onto the CNT surfaces.⁴

The photocatalytic properties of CNT/TiO₂ composite photocatalysts still remain largely unexplored although considerable efforts have been devoted to the coating of TiO₂ nanoparticles on CNTs. There are only a few reports on coating non-metal-metal co-doped TiO₂ on CNTs^{6,14} for applications in water decontamination.¹⁵ To

the best of our knowledge, there are no reports on supporting N, Pd co-doped TiO₂ on MWCNTs. Such nanocomposites have the potential to show the synergetic effect of the combination of N, Pd and MWCNTs on the catalytic performance of the TiO₂ on oxidative decomposition of organic pollutants in water using solar radiation. In this chapter, MWCNT/N, Pd co-doped TiO₂ composite photocatalysts were prepared by a modified sol-gel method. The photocatalytic degradation efficiency of the composite catalysts for a model synthetic dye was evaluated using EY in aqueous solution as a probe molecule.

7.2 EXPERIMENTAL DETAILS

7.2.1 Preparation of MWCNTs

MWCNTS were prepared, purified and functionalised as detailed in **Section 3.5**.

7.2.2 Preparation of the nanocomposites

The following method was used to prepare 0.5% MWCNT/N, Pd co-doped TiO₂ (0.5% Pd): An appropriate weighed amount of purified MWCNTs was dispersed in a mixture of 2-propanol C₃H₈O, (50 mL), (99.8%, Sigma Aldrich, Germany) and titanium isopropoxide, Ti(OC₃H₇)₄, (10 mL), (97%, Sigma Aldrich, Germany) to give a MWCNT:TiO₂ percentage of 0.5%. The mixture was sonicated for 30 min to improve MWCNT dispersion. An appropriate amount of palladium diamine dichloride, Pd(NH₃)₂Cl₂, (45% Pd, PGM Chemicals, RSA), to give a Pd:Ti ratio of 0.5% was dissolved in aqueous ammonia (3 mL) (25%, Merck, Germany). The solution was added drop-wise to the MWCNT/2-propanol/titanium isopropoxide mixture while stirring vigorously for 30 min. After a further hour of stirring, the suspension was dried overnight in an oven set at 80°C. The resulting light-grey powder was calcined for 2 h at 500°C in air in an electric furnace and characterised by various techniques. In addition, 1%, 2%, 5% and 10% MWCNT samples were prepared by following the same procedure and weighing appropriate amounts of functionalised MWCNTs, respectively. A sample without MWCNTs was prepared for comparison. The proposed synthetic route for formation of MWCNT/N, Pd co-doped TiO₂ nanocomposites is shown in **Figure 7.1**

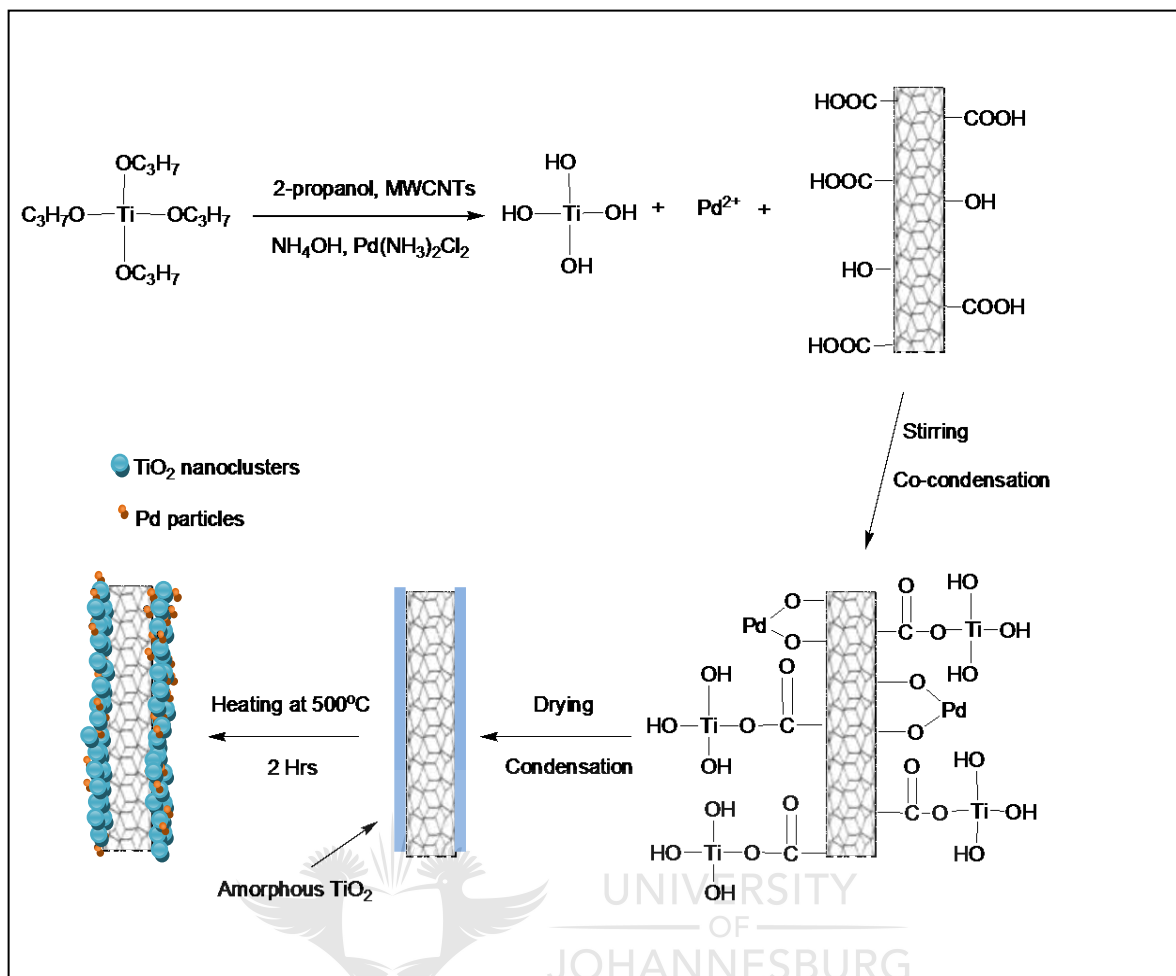


Figure 7.1 Illustration of the synthesis of N, Pd co-doped TiO₂ decorated MWCNTs

7.2.3 Material characterisation

The synthesised materials were characterised using various techniques as described in **Section 3.6**.

7.2.4 Evaluation of photocatalytic activity

The photocatalytic performances of the synthesised materials were evaluated for the degradation of Eosin Yellow under simulated solar irradiation. Experimental details are given in **Section 3.7**.

7.3 RESULTS AND DISCUSSION

7.3.1 FT-IR studies

FT-IR studies were performed in order to determine the presence of functional groups and to study the surface changes on the nanocomposites (**Figure 7.2**). The presence of OH groups and water on the surface of the particles was confirmed by the appearance of a broad band at 3 360 cm⁻¹ for all samples. Another peak associated with O-H bending appeared around 1 640 cm⁻¹. The presence of hydroxyl groups on composite surfaces plays an important role in photocatalytic degradation. The functional groups on the composites were mainly from surface groups on the TiO₂. No characteristic peaks of the carbon nanotubes were observed due to the low percentage of MWCNTs in the nanocomposites. The band due to stretching and bending modes of Ti-O and O-Ti-O appeared as a highly intense broad band centred at approximately 500 cm⁻¹.¹⁶

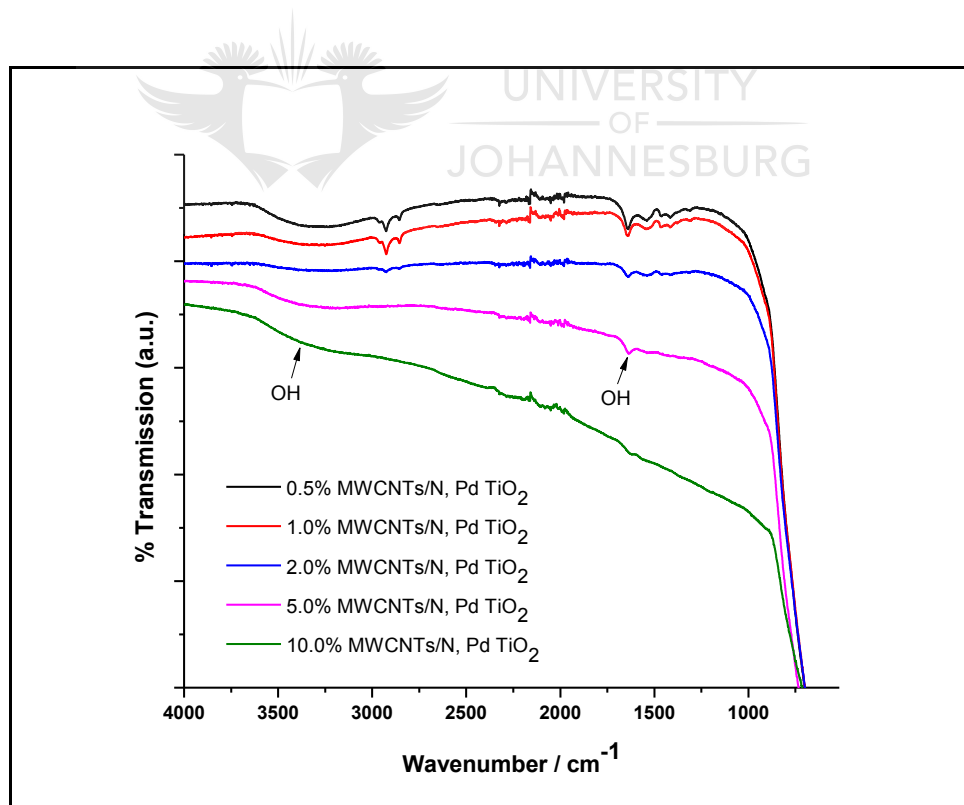


Figure 7.2 FT-IR spectra of MWCNT/N, Pd co-doped TiO₂ with different MWCNT ratios

7.3.2 Raman studies

Raman analyses confirmed the presence of TiO₂ and MWCNTs in the nanocomposites (**Figure 7.3**). Anatase TiO₂ shows six Raman-active fundamental modes at 144 cm⁻¹ (E_g), 197 cm⁻¹ (E_g), 397 cm⁻¹ (B_{1g}), 518 cm⁻¹ (A_{1g} + B_{1g}) and 640 cm⁻¹ (E_g).⁷ Well-resolved Raman peaks were observed at 145 (E_g), 399 (B_{1g}), 517 (A_{1g} + B_{1g}) and 640 (E_g) cm⁻¹ in the spectra of all the samples calcined at 500°C indicating the presence of anatase as the predominant phase.¹⁷

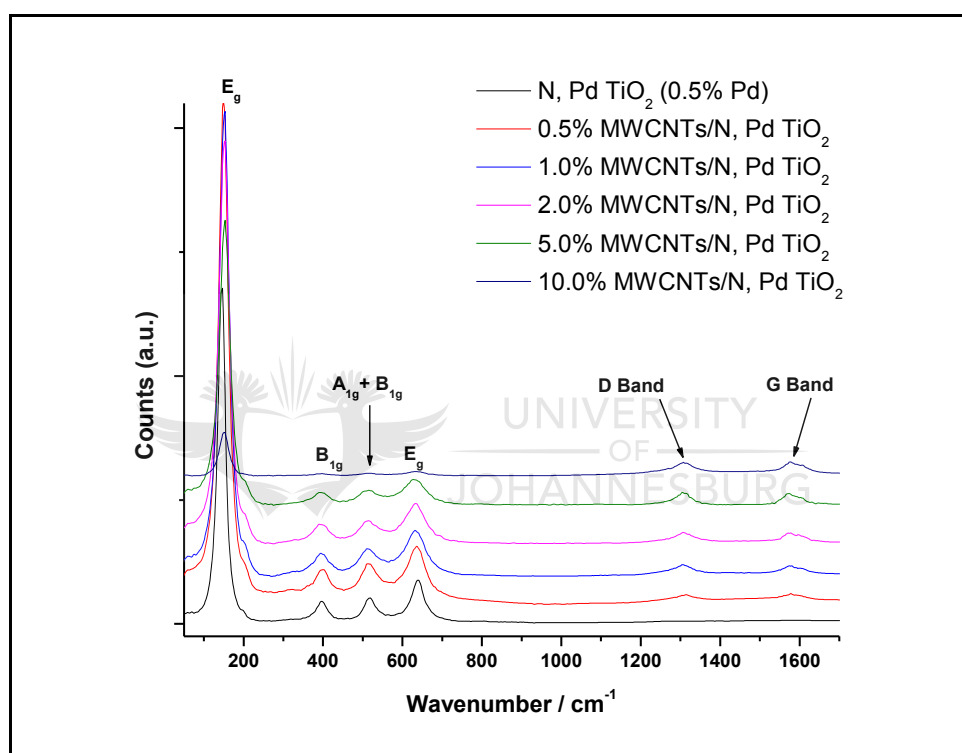


Figure 7.3 Raman spectra of MWCNT/N, Pd co-doped TiO₂ with different MWCNT ratios

Peaks characteristic of MWCNTs also appeared at about 1311cm⁻¹ (D band) and at 1578cm⁻¹ (G band or E_{2g})¹⁸ in the nanocomposites (**Figure 7.4**). The D band corresponds to defect sites in the hexagonal framework of the MWCNTs due to disorder induced by sp³ hybridisation, whereas the G band indicates the presence of ordered sp² hybridisation, a feature related to the structural integrity of the nanotubes. The ratio of D-band (*I_D*) to G-band (*I_G*) intensities is sensitive to the surface character of MWCNTs. The intensity ratio (*I_D*/*I_G*) values for 2% MWCNT/N, Pd co-doped TiO₂ and 5% MWCNT/N, Pd co-doped TiO₂ were found to be 0.986

and 0.942, respectively. These values suggest increased defects on CNTs resulting in increased D-band intensity, signalling the change of the hybridisation of C atoms on the nanotubes from sp² to sp³. A weak shoulder (D'' band), which is also associated with the defects and disorder in the MWCNTs appears at about 1613 cm⁻¹ in the nanostructure.¹⁹ These observations provide evidence for covalent functionalisation of N, Pd TiO₂ nanoparticles on MWCNTs.¹⁵

The intensity of these Raman peaks increases with increasing amounts of MWCNTs in the nanocomposites. The low Raman intensity at low MWCNT percentages may be explained by the total coverage of the CNTs by the co-doped TiO₂ particles. At high MWCNT levels, the coverage by co-doped TiO₂ was lower due to aggregation and poor dispersion in 2-propanol, thus some of the MWCNTs were bare leading to more intense Raman peaks. These results are in agreement with SEM and TEM observations.

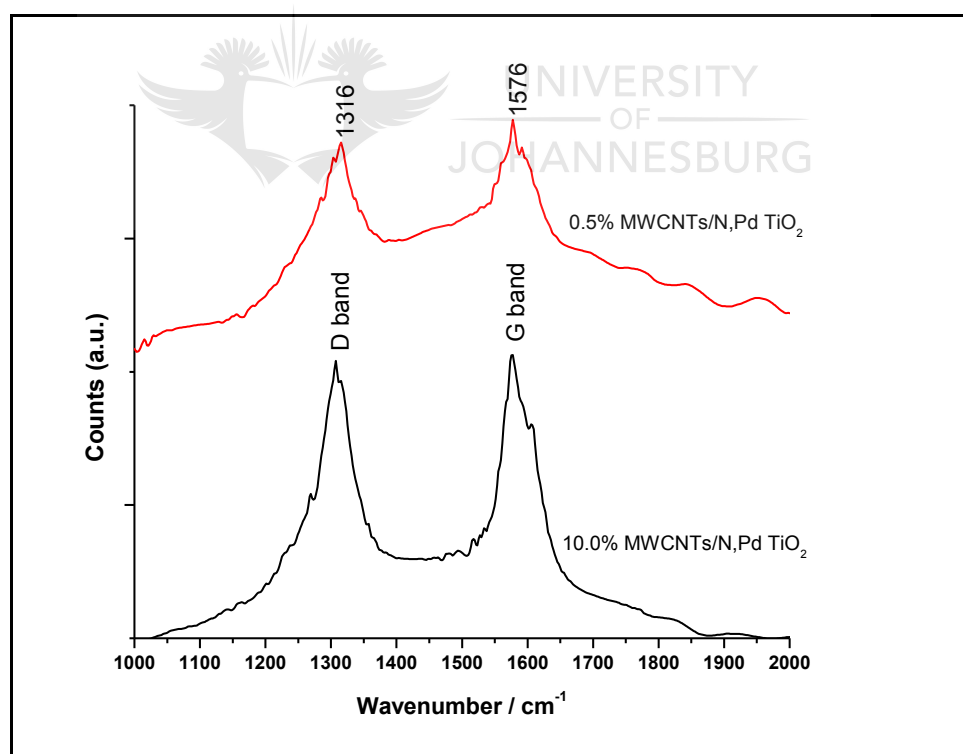


Figure 7.4 Raman spectra of MWCNT/N, Pd co-doped TiO₂ showing the D and G bands

7.3.3 XRD analysis

XRD analysis was performed to investigate the effect of MWCNTs on the crystallisation of different samples (**Figure 7.5**). The XRD patterns of the nanocomposites may be as a result of the formation of pure anatase crystallites in the composites. Peaks at 2θ values of 25.3, 37.6, 48.2, 53.9, 54.8, 62.7 and 75.2 corresponding to the (101), (004), (200), (105), (211), (204) and (215) planes, respectively, can be indexed to the anatase phase.¹⁷ The characteristic peaks of the MWCNTs can hardly be identified from the pattern of the nanocomposite catalysts at low MWCNT percentages. The absence of aggregated MWCNTs in the composites containing low percentages of MWCNT led to a homogeneous dispersion of N, Pd TiO₂ on MWCNTs, further confirming the absence of the MWCNT characteristic peaks in the XRD patterns. There is a possibility of overlap of the intense peak of the MWCNTs (101) with the anatase (101) reflection.⁴ This feature is clearly visible by the appearance of a shoulder on the (101) anatase reflection of the 5% MWCNT/N, Pd co-doped TiO₂ and 10% MWCNT/N, Pd co-doped TiO₂. The crystallite size was calculated by X-ray line-broadening analysis using the Scherrer equation.

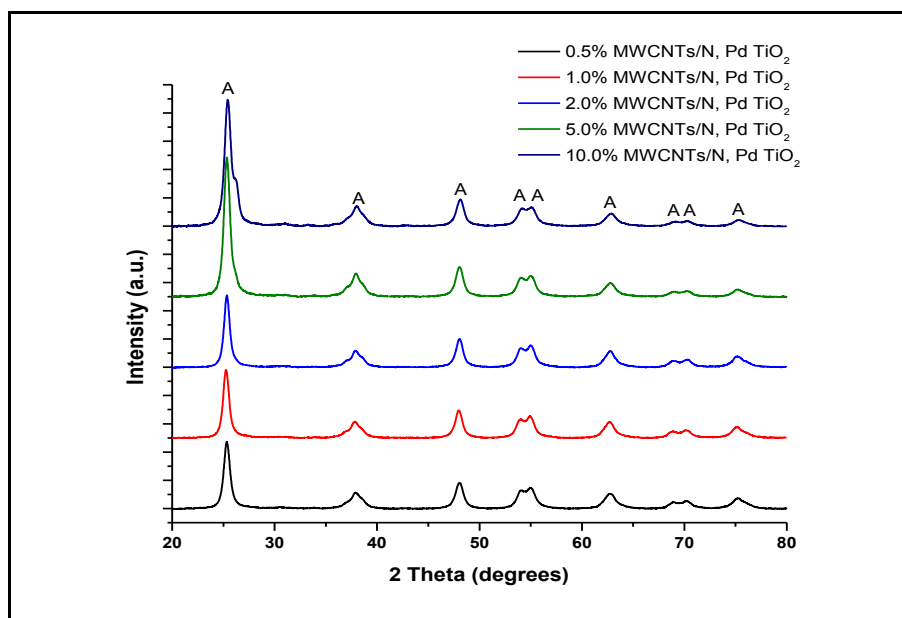


Figure 7.5 XRD patterns of MWCNT/N, Pd co-doped TiO₂ with different MWCNT ratios (A = anatase phase)

Results of particle sizes are shown in **Table 7.1**. There are no major differences in particle size with increasing amounts of MWCNTs. A general slight increase in particle size with increasing MWCNT content may be attributed to the rate of hydrolysis and condensation reactions on the support. At low MWCNT levels, the condensation reaction gets complete within a short period of time as few carboxylate sites are available for the reaction. The rapid hydrolysis of the titanium precursor may occur prior to or while the reaction products are anchored onto the nanotube supports leading to smaller particle sizes.⁴ An average particle sizes of 5 nm for MWCNT/TiO₂ composites prepared by the sol-gel method has been reported.^{19,20} All the samples were still 100% in the anatase phase after calcination at 500°C.

Table 7.1 Effect of MWCNTs on average particle size

Sample	Particle size (nm)
N, Pd co-doped TiO ₂ (0.5% Pd)	16.41
0.5% MWCNT/N, Pd co-doped TiO ₂ (0.5% Pd)	17.92
1.0% MWCNT/N, Pd co-doped TiO ₂ (0.5% Pd)	15.21
2.0% MWCNT/N, Pd co-doped TiO ₂ (0.5% Pd)	17.89
5.0% MWCNT/N, Pd co-doped TiO ₂ (0.5% Pd)	18.64
10.0% MWCNT/N, Pd co-doped TiO ₂ (0.5% Pd)	19.60

7.3.4 SEM and EDS analyses

SEM images of the MWCNT/N, Pd co-doped TiO₂ nanocomposites (**Figure 7.6**) show coverage of the MWCNTs with N, Pd TiO₂. **Figure 7.6(a)** shows coated MWCNTs in clusters of highly agglomerated N, Pd TiO₂ nanoparticles. Coverage is not continuous for some of the nanocomposites (**Figure 7.6(b)**), with small bare gaps in the nanometre range on the MWCNTs. This might be due to the calcination leading to loss of water, carbon and nitrogenous material. This creates a strain on the nanoclusters resulting in a gap being created. The nanoclusters are

formed by the hydrolysis and co-condensation of isopropyl titanate under alkaline conditions in the presence of MWCNT-COOH and Pd ions. The amorphous N, Pd TiO₂ obtained at room temperature was transformed to crystalline anatase after heat treatment at 500°C. At higher MWCNT levels, aggregation becomes a problem, leading to poor dispersion of MWCNTs in 2-propanol and eventually poor coverage by the nanoparticles (**Figure 7.6(d)**).

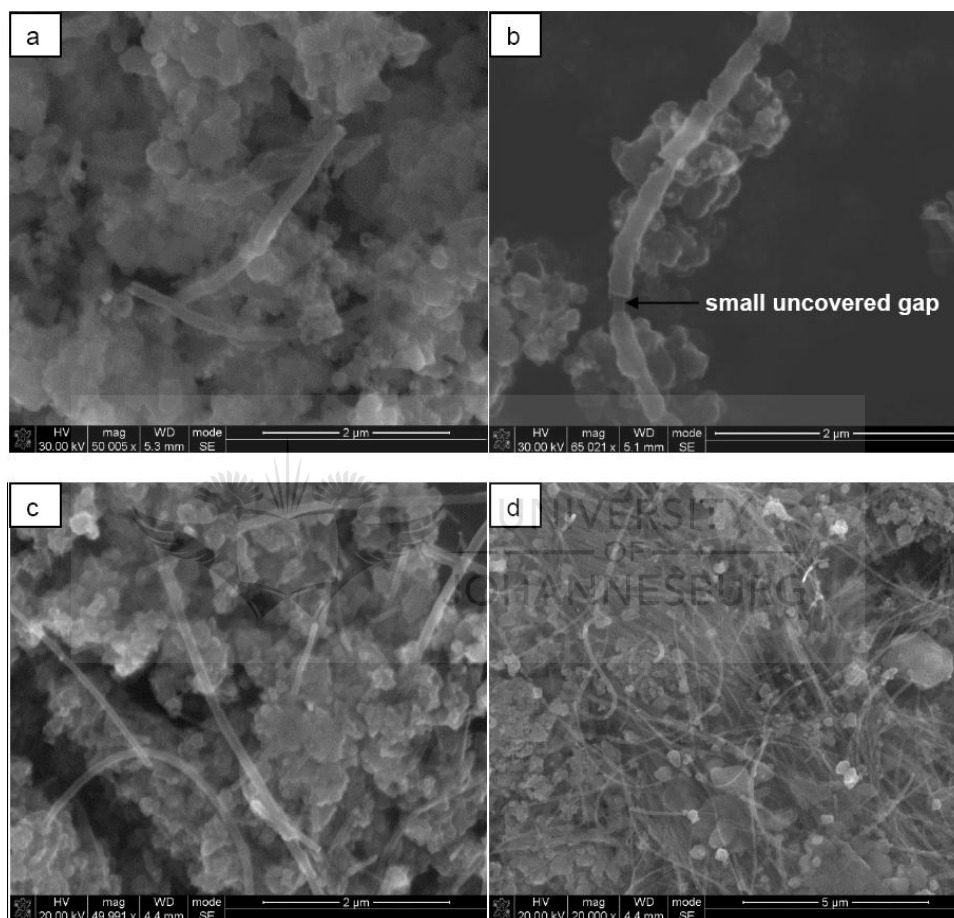


Figure 7.6 SEM images of (a) 0.5% MWCNT/N, Pd TiO₂; (b) N, Pd TiO₂ decorated MWCNT showing a small uncovered gap; (c) 5% MWCNT/N, Pd TiO₂; and (d) aggregation in 10% MWCNT/N, Pd TiO₂

Elemental composition of the nanocomposites was probed and confirmed by EDS analysis (**Figure 7.7**). Results indicated the presence of Ti, O, C and Pd. Presence of Na and S was also detected which may have originated from containers or

sample-handling contamination. The C signal most certainly emanates from the MWCNTs.

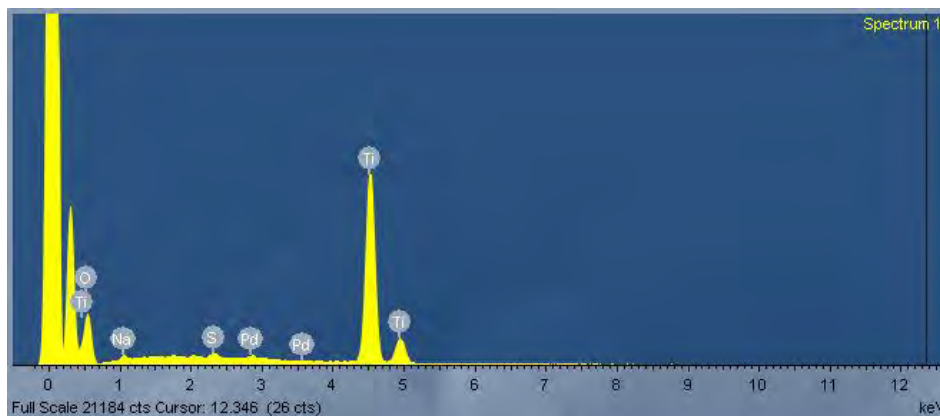


Figure 7.7 Full-scale EDS scan of 2% MWCNT/N, Pd co-doped TiO₂

7.3.5 TEM analysis

Figure 7.8 shows the TEM images of the N, Pd co-doped TiO₂ alone and of MWCNT/N, Pd co-doped TiO₂ nanocomposites. TEM images confirm the presence of Pd deposits on the surface of the N-doped TiO₂ (**Figure 7.8(a)**). Pd deposits are well dispersed on many of the TiO₂ particles and have diameters ranging from 1 nm to 2 nm. The particles are agglomerated and nearly spherical in shape. The size of the TiO₂ particles is approximately in the range of 15 nm to 20 nm, consistent with XRD measurements. The images also reveal a composite microstructure consisting of TiO₂ agglomerates covering the MWCNTs, confirming the intimate contact between the MWCNTs and co-doped TiO₂. All the carbon nanotubes were covered uniformly with a layer of co-doped TiO₂ at low MWCNT/co-doped TiO₂ ratio (**Figure 7.8(b)** and **Figure 7.8(c)**). However at 5% MWCNT/co-doped TiO₂ and 10% MWCNT/co-doped TiO₂, the distribution of the clusters is far from being homogeneous. Some of the MWCNTs are completely bare or show poor coverage (**Figure 7.8(d)** and **Figure 7.8(f)**). Small Pd particles, in addition to the TiO₂ are clearly visible on the poorly covered MWCNTs (**Figure 7.8(f)**). The aggregation of co-doped TiO₂ nanoparticles on MWCNTs indicates the supporting role of the MWCNTs as centres for the deposition and growth of hydrolysis products as well as support for spatial confinement of the co-doped TiO₂ clusters.⁴ The thickness of the N, Pd TiO₂ layer on the MWCNTs was

estimated to be 10 nm to 20 nm (at least one layer). Furthermore, it can be noted that the open ends of the tubular structure are also covered by co-doped TiO₂, suggesting the presence of functional groups on the sidewalls and at the open ends of the functionalised MWCNTs (**Figure 7.8(e)** and **Figure 7.8(f)**).

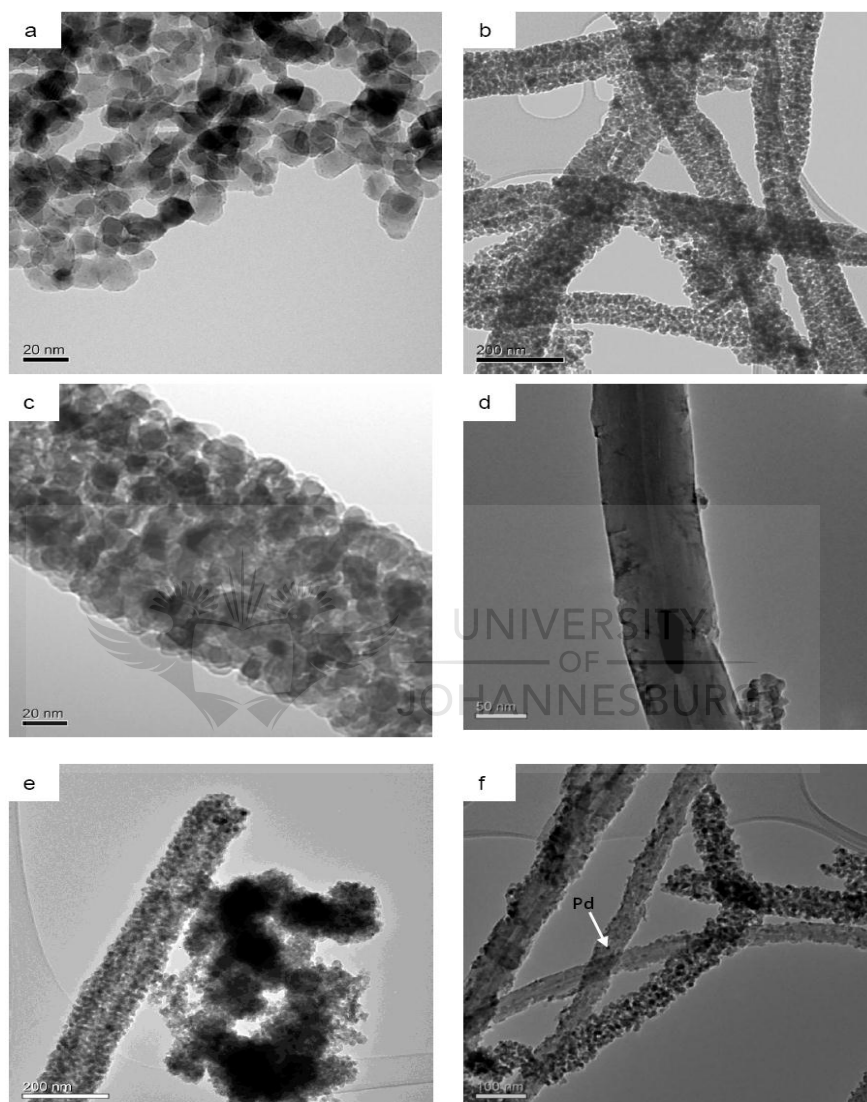


Figure 7.8 TEM images of (a) N, Pd co-doped TiO₂ (0.5% Pd); (b) and (c) 0.5% MWCNT/ N, co-doped Pd TiO₂ showing MWCNTs completely covered with N, Pd co-doped TiO₂; (d) MWCNT with N, Pd co-doped TiO₂ particle as well as aggregates; (e) MWCNT covered with N, Pd co-doped TiO₂ and N, Pd co-doped TiO₂ aggregates; and (f) unevenly covered MWCNTs (5.0% MWCNT/N, Pd co-doped TiO₂) showing some Pd particles

7.3.6 TGA studies

TGA analysis was carried out to investigate the thermal stability and to estimate the carbon nanotube content in the nanocomposites. The results of weight loss as a function of temperature for 0.5% MWCNT/N, Pd co-doped TiO₂ to 10.0% MWCNT/N, Pd co-doped TiO₂ nanocomposites are shown in **Figure 7.9**. A weight loss at a temperature of between 50°C and 100°C is attributed to the loss of water adsorbed onto the surface of the nanocomposites. Another weight loss at about 250°C could be due to loss of any carbon or nitrogen-related material. The weight loss above 500°C indicates the decomposition of carbon nanotubes. The weight ratio of MWCNTs over TiO₂ was estimated by correlating the mass loss with temperature. The weight loss above 500°C, of approximately 1%, 2%, 5% and 12% for the 1%, 2% 5% and 10% MWCNT/N, Pd co-doped TiO₂, respectively, suggests that the MWCNT/N, Pd co-doped TiO₂ ratios used during synthesis of the nanocomposites are in close agreement with results obtained from TGA analyses. This observation points to negligible losses of MWCNTs during the composite-preparation procedure. The decomposition temperature of functionalised MWCNTs was found to be 570°C. It occurs over a narrow temperature range of between 520°C and 580°C. However, the decomposition of nanocomposites occurs at a higher temperature of about 600°C and over a wider temperature range with the onset at nearly 530°C for the 5% MWCNT/N, Pd co-doped TiO₂ sample, ending at about 680°C. The decomposition starts at 540°C for the 2% MWNCT/N, Pd co-doped TiO₂ and at 560°C for the 1% MWCNT/N, Pd co-doped TiO₂, respectively. This shift in the onset of the decomposition appears to be related to the level of coating of N, Pd TiO₂ on the MWCNTs as shown by the TEM images. The shift may be ascribed to the presence of the co-doped TiO₂ coated on the MWCNTs which may slightly restrain heat transfer resulting in delayed oxidation of MWCNTs.

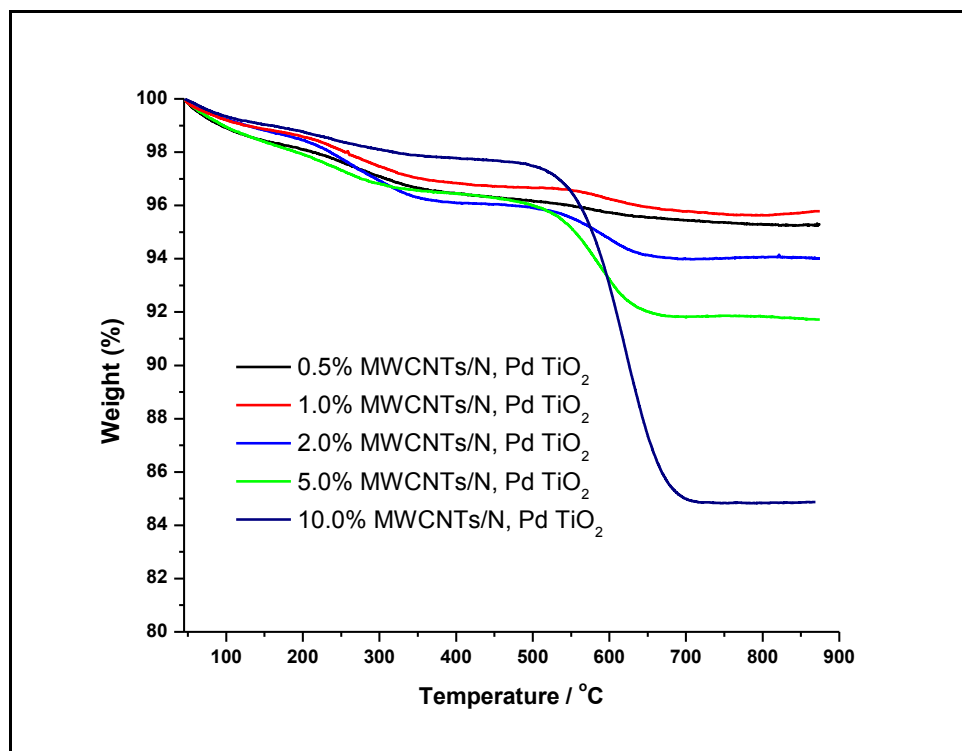


Figure 7.9 TGA curves of MWCNT/N, Pd co-doped TiO₂ with different MWCNT ratios

7.3.7 Optical properties

The diffuse reflectance UV-Vis spectra of the different nanocomposites are shown in **Figure 7.10**. The spectra are characterised by an intense fundamental absorption due to anatase TiO₂ in the region of between 350 nm and 400 nm. There is a red shift in the absorption edge for MWCNT/N, Pd co-doped TiO₂ nanocomposites that can be correlated to the amount of MWCNTs in the high-wavelength visible region. There is an increase in the absorption edge for the 0.5% and 1.0% MWCNT/N, Pd co-doped TiO₂ centred on 475 nm. At 2.0%, 5.0% and 10% MWCNT/N, Pd co-doped TiO₂ there is a decrease in the absorption at around 475 nm but an increase in the absorption band between 700 nm and 900 nm is observed.

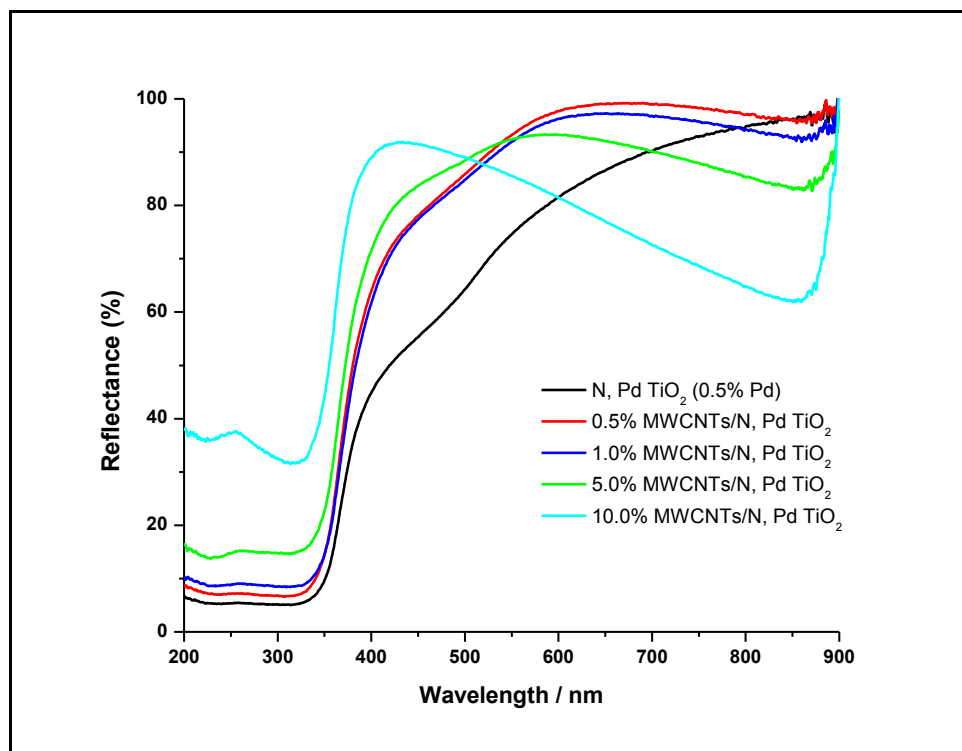


Figure 7.10 UV-Vis diffuse reflectance spectra of different MWCNT/N, Pd co-doped TiO₂ nanocomposites

An increase in the percentage of MWCNTs was accompanied by a decrease in absorbance in the UV region (200 nm to 350 nm). This is due to a decrease or non-uniform coverage of MWCNTs in agreement with TEM and SEM observations. The nanocomposites showed the combined features of MWCNTs and co-doped TiO₂ with new properties, which are favourable for applications in the visible-light region. The characteristics of the co-doped TiO₂ and MWCNTs were altered due to the interaction of TiO₂ nanoparticles with the MWCNTs, which may modify the process of the electron/hole pair formation under visible-light irradiation.^{5,14} This unique structure of the MWCNT/TiO₂ composites might have led to the high catalytic activity reported for phenol degradation.³

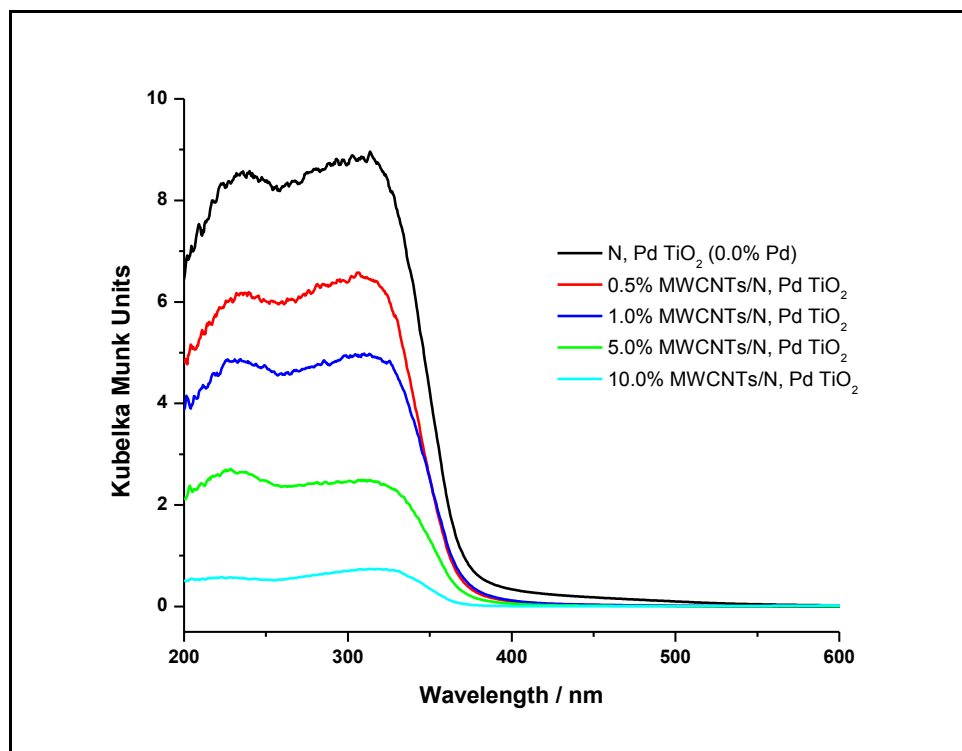


Figure 7.11 Kubelka-Munk plots of different MWCNT/N, Pd co-doped TiO₂ nanocomposites

The diffuse reflectance spectra were plotted as the Kubelka-Munk function, $F(R)$, vs. wavelength (**Figure 7.11**). The plot shows a decrease in the absorption coefficient with increasing amounts of MWCNTs in the UV region. The type of transition in TiO₂-based semiconductors is not well understood;²¹ however, for a direct band-gap semiconductor, the plot with $n = 2$ gives a linear Tauc region just above the optical absorption edge. Extrapolation of this straight line to the photon energy axis yields the semiconductor band gap, a key indicator of its light-harvesting efficiency under solar illumination.²²

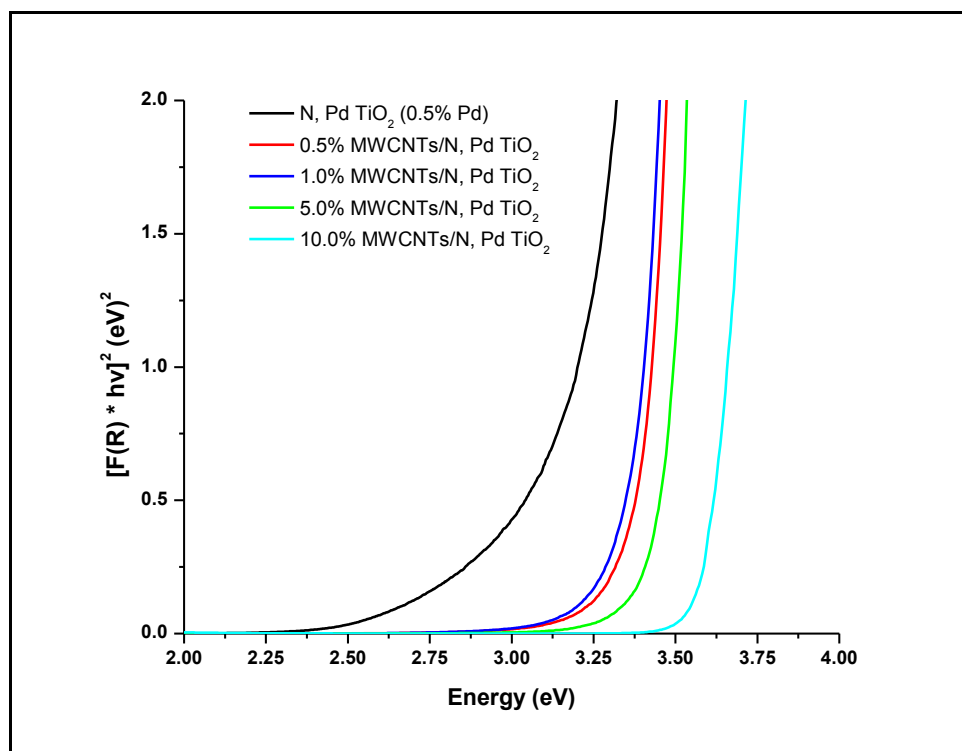


Figure 7.12 Tauc plots of MWCNT/N, Pd co-doped TiO₂ nanocomposites

The band gaps (eV) for all the nanocomposites were determined from the lines' point of contact with the energy axis²³ (**Figure 7.12**). Assuming a direct band gap for all the samples, there was an increase in band-gap energy with increasing amounts of MWCNTs (**Table 7.2**). This can be ascribed to low levels of N and Pd available for doping with TiO₂. The N and Pd tend to associate more with the CNTs than with the TiO₂, causing an increase in band gap with increased loadings of MWCNTs.

Table 7.2 Effect of MWCNTs on band gap in MWCNT/N, Pd co-doped TiO₂ nanocomposites

Sample	Direct band gap (eV)
N, Pd co-doped TiO ₂ (0.5% Pd)	2.30
0.5% MWCNT/N, Pd co-doped TiO ₂ (0.5% Pd)	2.84
1.0% MWCNT/N, Pd co-doped TiO ₂ (0.5% Pd)	2.93
5.0% MWCNT/N, Pd co-doped TiO ₂ (0.5% Pd)	3.06
10.0 % MWCNT/N, Pd co-doped TiO ₂ (0.5% Pd)	3.42

7.4 PHOTODEGRADATION STUDIES

Figure 7.13(a) shows the results of the degradation of Eosin Yellow under simulated solar irradiation, in the presence of N, Pd TiO₂ alone and with the MWCNT/TiO₂ composites. There is a decrease in the degradation efficiency of the nanocomposites with increasing amounts of MWCNTs. Reduced efficiency in the nanocomposites could be explained by partial agglomeration of the N, Pd TiO₂ on the MWCNTs as shown in the SEM and TEM images (**Figure 7.6** and **Figure 7.8**). The remarkable thickness of the coating layer on some MWCNTs can be attributed to the continuous adsorption of titania particles on the initially formed TiO₂ coating layer, forming multi-layers on the MWCNT surfaces resulting in compromised photodegradation efficiency. Heterogeneous, non-uniform coating of N, Pd TiO₂ on MWCNTs, showing bare CNT surfaces and random aggregation of the nanoparticles onto the MWCNTs surface could also explain the observed trend.⁴ However, the supporting role of the MWCNTs as centres for the deposition and growth of hydrolysis products as well as support for spatial confinement of the TiO₂ clusters was noted.

The photodegradation of EY using visible light is shown in **Figure 7.13(b)**. Simulated solar irradiation gave higher degradation rates compared to visible-light irradiation because of the presence of a small percentage, (3% to 5%), of high-

energy UV radiation in solar radiation. Irradiation of the composites with radiation of wavelengths greater than 450 nm resulted in reduced light-harvesting capability by TiO₂, with the MWCNTs acting as photosensitisers for the photocatalytic process. MWCNTs themselves tend to absorb very well in the visible region because of their colour. Their synergistic effects are governed by the ability to trap electrons before channelling them to the conduction band of the TiO₂.

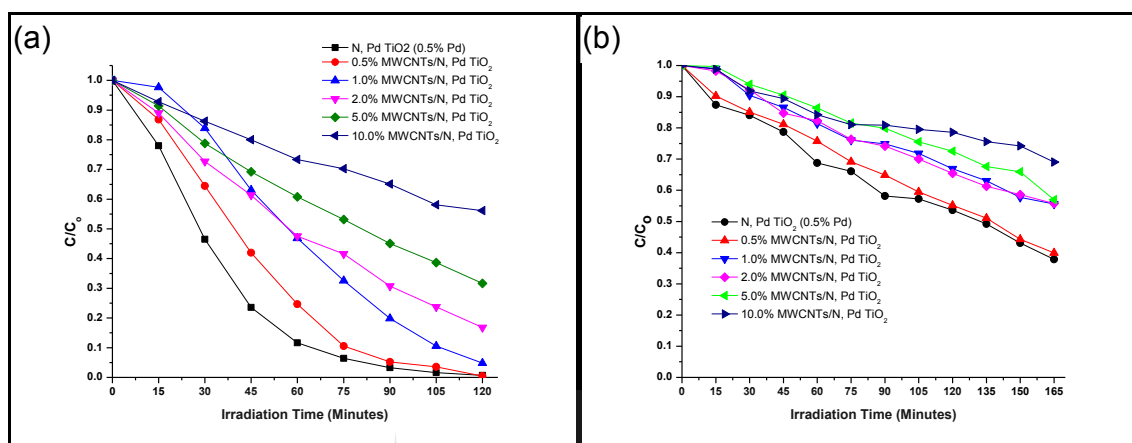


Figure 7.13 Photodegradation of EY on N, Pd TiO₂ and MWCNT/N, Pd co-doped TiO₂ nanocomposites under (a) simulated solar light irradiation; and (b) visible-light irradiation ($\lambda > 450$ nm)

The highest degradation efficiency under simulated solar irradiation was observed for the 0.5% MWCNT/N, Pd co-doped TiO₂ composite (99.55%). As the amount of MWCNTs was increased, the exposed surface area of TiO₂ was reduced due to formation of aggregates between TiO₂ particles and the MWCNTs. This phenomenon may explain the reduction in dye adsorption. When the concentration of the MWCNTs is high enough, the bare surfaces of the MWCNTs start to adsorb the dye and adsorption increases again. However, with high MWCNT concentration, co-doped TiO₂ becomes less active. There was a decrease in the degradation efficiency of the nanocomposites with increasing amounts of MWCNTs, with the 1.0%, 2.0%, 5.0% and 10% MWCNT/N, Pd co-doped TiO₂ composites showing values of 95.21%, 83.18%, 68.36% and 43.84%, respectively (Table 7.3). This trend correlates very well with the increase in band gaps

observed in the Tauc plots (**Figure 7.12**). The presence of low levels of MWCNTs caused a slight but insignificant increase in dye-degradation efficiency probably due to the synergistic effects of MWCNTs and N, Pd TiO₂ on the entire photodegradation process. There was no correlation between dye adsorption and photodegradation as observed with the 10% MWCNT/N, Pd co-doped TiO₂ which could adsorb 27.09% of the dye but only showed a degradation efficiency of 43.84%, a value lower than that for 0.5% MWCNT/N, Pd co-doped TiO₂ which showed an adsorption of only 15.75%. This can be explained by the uneven coating of the MWCNTs as well as their aggregation at higher percentages. A similar trend was observed for experiments performed under visible radiation (**Table 7.4**).

Table 7.3 Dye adsorption and EY photodegradation under simulated solar radiation

Sample	Dye adsorption (%)	Degradation after 120 min (%)
N, Pd co-doped TiO ₂ (0.5% Pd)	23.39	99.30
0.5% MWCNT/N, Pd co-doped TiO ₂	15.75	99.55
1.0% MWCNT/N, Pd co-doped TiO ₂	15.36	95.21
2.0% MWCNT/N, Pd co-doped TiO ₂	13.40	83.18
5.0 % MWCNT/N, Pd co-doped TiO ₂	29.06	68.36
10.0 % MWCNT/N, Pd co-doped TiO ₂	27.09	43.84

Table 7.4 Dye adsorption and EY photodegradation under visible radiation ($\lambda > 450$ nm)

Sample	Dye adsorption (%)	Degradation after 165 min (%)
N, Pd co-doped TiO ₂ (0.5% Pd)	27.71	62.13
0.5% MWCNT/N, Pd co-doped TiO ₂	14.76	60.07
1.0% MWCNT/N, Pd co-doped TiO ₂	12.49	44.42
2.0% MWCNT/N, Pd co-doped TiO ₂	15.64	44.22
5.0 % MWCNT/N, Pd co-doped TiO ₂	18.49	43.03
10.0 % MWCNT/N, Pd co-doped TiO ₂	27.82	30.99

The photodegradation of EY in aqueous suspensions containing MWCNT/N, Pd co-doped TiO₂ nanocomposites obeyed first-order kinetics (**Figure 7.14**). The rate constants for EY photodegradation under simulated solar radiation are much higher than those for the experiments under visible radiation.

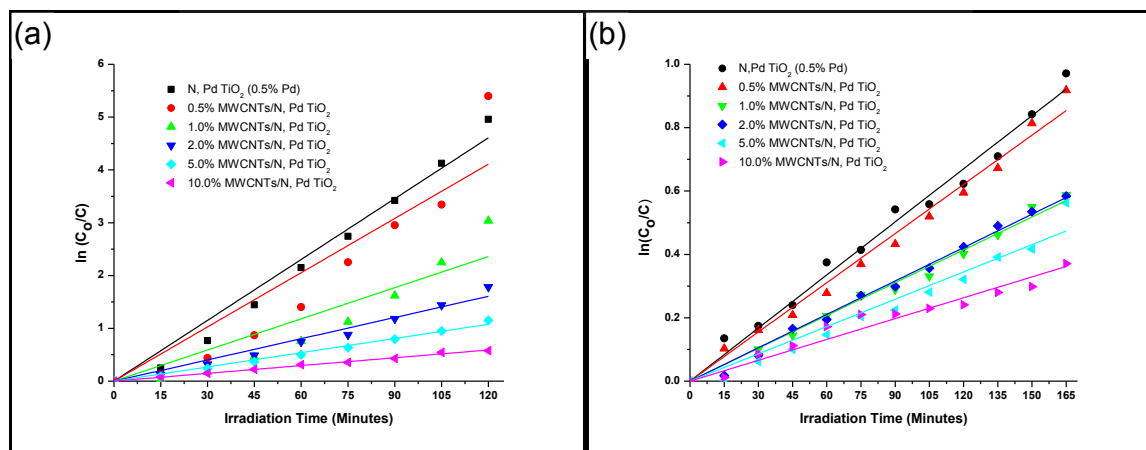


Figure 7.14 Kinetics of EY degradation under (a) simulated solar radiation; and (b) visible light

Incorporation of N and Pd had a profound effect on the degradation efficiency of the nanocomposites. N reduces the TiO₂ band gap by forming states in the inter-

gap region whilst Pd can trap photogenerated electrons, thereby enhancing electron-hole separation on the surface of the photocatalyst and increasing photocatalytic activity.

Wang and co-authors reported rate constants of $1.8 \times 10^{-3} \text{ min}^{-1}$ and $2.0 \times 10^{-3} \text{ min}^{-1}$ for neat TiO₂ and 5% MWCNT/TiO₂ composite catalyst, respectively.²⁴ These values are lower than the values shown in **Table 7.5** for nanocomposites containing lower levels of MWCNTs at $\lambda > 450 \text{ nm}$. In another study, Wang and co-authors reported on photodegradation of phenol using neat TiO₂ and 20% MWCNT/TiO₂ nanocomposites and obtained values of $0.68 \times 10^{-3} \text{ min}^{-1}$ and $1.55 \times 10^{-3} \text{ min}^{-1}$, respectively.⁵ Oh *et al.* reported on photocatalytic degradation of methylene blue (MB) in an aqueous solution containing 5% MWCNT/TiO₂ composite photocatalysts, under ultraviolet light irradiation and recorded a rate constant value of $9.5 \times 10^{-3} \text{ min}^{-1}$ which was higher than $8.0 \times 10^{-3} \text{ min}^{-1}$ for pristine TiO₂.²⁵ Tian *et al.* synthesised MWCNT/TiO₂ hybrid nanostructures via solvothermal synthesis and sol-gel method with benzyl alcohol as a surfactant and tested them for visible-light ($\lambda > 420 \text{ nm}$) MB degradation. The sol-gel MWCNT/TiO₂ (20%) significantly enhanced the degradation of MB, compared to the pure TiO₂ and the mechanical mixture of MWCNTs and TiO₂. However, owing to the uniform distribution of TiO₂ nanocrystals on the CNT surface, the MWCNT/TiO₂ (20%), prepared by solvothermal synthesis, showed even higher photocatalytic activity than the sol-gel MWCNT/TiO₂ (20%). A first-order rate constant of 0.001 min^{-1} was observed for the MWCNT/TiO₂ (20%) prepared by solvothermal synthesis at a catalyst loading of 0.2 g/l and an MB concentration of 10 mg/l .²⁶ Once again, these values are lower than those displayed in **Table 7.5**. These observations point to the increased efficiency of the nanocomposites prepared by the modified sol-gel method for EY degradation.

Table 7.5 EY photodegradation rate constants under simulated solar radiation and visible radiation

Sample	Rate constant, k (min ⁻¹) (solar simulator)	Rate constant, k (min ⁻¹) Visible light ($\lambda > 450$ nm)
N, Pd co-doped TiO ₂ (0.5% Pd)	3.84×10^{-2}	5.59×10^{-3}
0.5% MWCNT/N, Pd co-doped TiO ₂	3.42×10^{-2}	5.18×10^{-3}
1.0% MWCNT/N, Pd co-doped TiO ₂	1.97×10^{-2}	3.45×10^{-3}
2.0% MWCNT/N, Pd co-doped TiO ₂	1.34×10^{-2}	3.51×10^{-3}
5.0% MWCNT/N, Pd co-doped TiO ₂	8.98×10^{-3}	2.87×10^{-3}
10.0% MWCNT/N, Pd co-doped TiO ₂	4.92×10^{-3}	2.19×10^{-3}

A proposed mechanism for the enhanced photocatalysis of the MWCNT/N, Pd co-doped TiO₂ composites is shown schematically in **Figure 7.15**. Under visible-light illumination, photo-excited electrons from the dispersed MWCNTs are injected into the conduction band of the N, Pd TiO₂ through the Ti-C bonds. The generated positively charged MWCNTs will in turn capture electrons from the valence band of N, Pd TiO₂ leaving holes behind in the N, Pd TiO₂.

When N, Pd TiO₂ forms a heterojunction with another semiconductor or metal (e.g. MWCNT), a charge space ranging from several tens to hundreds of nanometres will be formed near the junction to equalise the Fermi levels. This will result in reduced band-gap energy within the MWCNT/N, Pd TiO₂ heterojunction. Formation of an interior electric field of the charge space within the nanocomposite can separate the photogenerated pairs which results in reduction of the recombination rate of the pairs. This mechanism suggests that the photocatalytic performance of MWCNT/N, Pd co-doped TiO₂ materials should be optimum at some specific value of the MWCNT content.^{27,28} Wang *et al.* recently reported 5

wt% of MWCNT content in MWCNT/TiO₂ composite photocatalysts as the optimum value for visible-light-induced photocatalytic degradation of 2,6-dinitro-p-cresol.²⁴

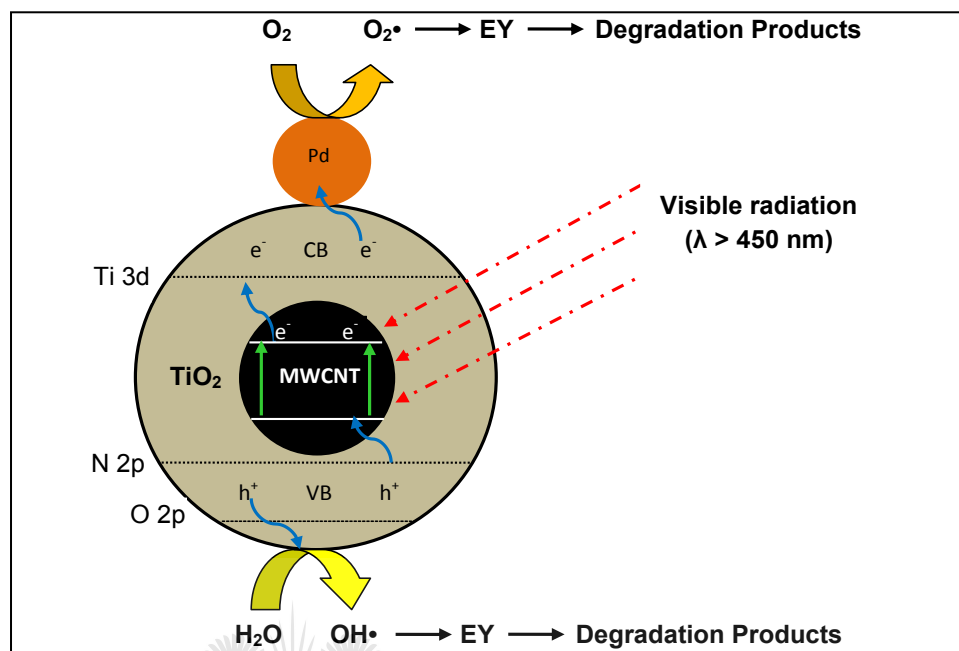


Figure 7.15 Proposed exciton processes for the MWCNT/N, Pd co-doped TiO₂ catalysts under visible-light irradiation

The superoxide radicals act as oxidising agents or as an additional source of hydroxyl radicals to catalyse the dye degradation.²⁰ The positive effect of N, Pd co-doping coupled with incorporation of MWCNTs leads to enhanced photoreactivity due to synergistic effects.

7.5 CONCLUSION

MWCNT/N, Pd co-doped TiO₂ composite materials prepared through a modified sol-gel route displayed a rather homogeneous coverage of N, Pd TiO₂ over MWCNT and less agglomeration of TiO₂ nanoparticles on the MWCNT surface. Particles were small (10 nm to 20 nm) and in the anatase form. At higher MWCNT levels, coverage was compromised by aggregation of the nanotubes. Incorporation of N led to reduced TiO₂ band gap whilst the Pd acted as a sink for photogenerated electrons. Consistent with the shift of the UV-Vis absorption of the

composites to longer wavelengths, there was a synergistic effect on the photocatalytic removal of EY at low MWCNT levels using visible-light irradiation source. This effect showed that MWCNTs can act as potential photosensitisers besides their role as adsorbents and dispersing agents. Simulated solar radiation gave higher degradation rates compared to visible-light irradiation ($\lambda > 450$ nm). The highest photodegradation efficiency was observed for the 0.5% MWCNT/N, Pd co-doped TiO₂ under simulated solar radiation. Higher MWCNT loadings led to reduced dye degradation efficiency with the 10% MWCNT/N, Pd co-doped TiO₂ degrading 43.84% in 2 h under simulated solar radiation. These observations confirm the unique properties of the MWCNT/N, Pd co-doped TiO₂ nanocomposites as potential functional water-purification materials.

7.6 REFERENCES

1. Baughman R.H., Zakhidov A.A. and de Heer W.A. (2002). Carbon nanotubes - the route toward applications. *Sci.* 297, (5582), 787 – 792.
2. Kim S., Jinschek J.R., Chen H., Sholl D.S. and Marand E. (2007). Scalable fabrication of carbon nanotube/polymer nanocomposite membranes for high flux gas transport. *Nano Lett.* 7, (9), 2806 – 2811.
3. An G., Ma W., Sun Z., Liu Z., Han B., Miao S., Miao Z. and Ding K. (2007). Preparation of titania/carbon nanotube composites using supercritical ethanol and their photocatalytic activity for phenol degradation under visible light irradiation. *Carbon* 45, 1795 – 1801.
4. Gao B., Chen G.Z. and Puma G. L. (2009) .Carbon nanotubes/titanium dioxide (CNTs/TiO₂) nanocomposites prepared by conventional and novel surfactant wrapping sol-gel methods exhibiting enhanced photocatalytic activity. *Appl. Catal. B: Environ.* 89, 503 – 509.
5. Wang W., Serp P., Kalck P. and Faria J.L. (2005). Visible light photodegradation of phenol on MWNT-TiO₂ composite catalysts prepared by a modified sol-gel method. *J. Mol. Catal. A: Chem.* 235, 194 – 199.

6. Woan K., Pyrgiotakis G., and Sigmund W. (2009). Photocatalytic carbon nanotube - TiO₂ composites. *Adv. Mater.* 21, 2233 – 2239.
7. Anpo M. and Takeuchi M. (2003). The design and development of highly reactive titanium oxide photocatalysts operating under visible light irradiation. *J. Catal.* 216, 505 – 516.
8. Kafizas A., Kellici S., Jawwad A. Darr J.A. and Parkin I.P. (2009). Titanium dioxide and composite metal/metal oxide titania thin films on glass: A comparative study of photocatalytic activity. *J. Photochem. Photobiol. A: Chem.* 204, 183 – 190.
9. Rupa A.V., Divakar D. and Sivakumar T. (2009). Titania and noble metals deposited titania catalysts in the photodegradation of Tartazine. *Catal. Lett.* 132, 259 – 267.
10. Lin Z., Orlov A., Lambert R.M. and Payne M.C. (2005). New insights into the origin of visible light photocatalytic activity of nitrogen-doped and oxygen-deficient anatase TiO₂. *J. Phys. Chem. B.* 109, 20948 – 20952.
11. Jitianu A., Cacciaguerra T., Benoit R., Delpeux S., Beguin F. and Bonnamy S. (2004). Synthesis and characterization of carbon nanotubes - TiO₂ nanocomposites. *Carbon* 42, (5–6), 1147 – 1151.
12. Fan W., Gao L. and Sun J. (2006). Anatase TiO₂-coated multi-wall carbon nanotubes with the vapor phase method. *J. Am. Ceram. Soc* 89, 731 – 733.
13. Yu Y., Yu J. C., Chan C. Y., Che Y. K., Zhao J. C., Ding L., Ge, W. K. and Wong P. K. (2005). Enhancement of adsorption and photocatalytic activity of TiO₂ by using carbon nanotubes for the treatment of azo dye. *Appl. Catal. B* 61, 1 – 11.
14. Kang S. Z., Cui Z. and Jin Mu J. (2007). Composite of carboxyl-modified multi-walled carbon nanotubes and TiO₂ nanoparticles: Preparation and photocatalytic activity. *J. Fuller. Nanotub. Car. N.* 15, 81 – 88.

15. Yadav S.K., Madeshwaran S.M. and Cho J.W. (2011). Synthesis of a hybrid assembly composed of titanium dioxide nanoparticles and thin multi-walled carbon nanotubes using „click chemistry“. *J. Colloid Interface Sci.* 358, 471 – 476.
16. Yu J., Ma T. and Liu S. (2011). Enhanced photocatalytic activity of mesoporous TiO₂ aggregates by embedding carbon nanotubes as electron-transfer channel. *Phys. Chem. Chem. Phys.* 13, 3491 – 3501.
17. Ou Y., Lin J., Fang S. and Liao D. (2006). MWNT–TiO₂:Ni composite catalyst: A new class of catalyst for photocatalytic H₂ evolution from water under visible light illumination. *Chem. Phys. Lett.* 429, 199 – 203.
18. Yan M.C., Chen F., Zhang J.L. and Anpo M. (2005). Preparation of controllable crystalline titania and study on the photocatalytic properties. *J. Phys. Chem. B*, 109, 8673 – 8678.
19. Hirano M., Nakahara C., Ota K., Tanaike O. and Inagaki M. (2003). Photoactivity and phase stability of ZrO₂-doped anatase-type TiO₂ directly formed as nanometer-sized particles by hydrolysis under hydrothermal conditions. *J. Solid State Chem.* 170, 39 – 47.
20. Zhang K. and Oh W.C. (2010). Kinetic study of the visible light-induced sonophotocatalytic degradation of MB solution in the presence of Fe/TiO₂-MWCNT catalyst. *Bull. Korean Chem. Soc* 31, (6), 1589 – 1595.
21. Li Q., Xie R. and Shangw J. K. (2007). Effect of precursor ratio on synthesis and optical absorption of TiON photocatalytic nanoparticles. *J. Am. Ceram. Soc.* 90, (4), 1045 – 1050.
22. Serpone N., Lawless D. and Khairutdinov R. (1995). Size effects on the photophysical properties of colloidal anatase TiO₂ particles: Size quantization versus direct transitions in this indirect semiconductor. *J. Phys. Chem.* 99, 16646 – 16654.

23. Wu Y., Zhang J., Xiao L. and Chen F. (2010). Properties of carbon and iron modified TiO₂ photocatalyst synthesised at low temperature and photodegradation of acid orange 7 under visible light. *Appl. Surf. Sci.* 256, 4260 – 4268.
24. Wang H., Wang H.L. and Jiang W.F. (2009). Solar photocatalytic degradation of 2,6-dinitro-p-cresol (DNPC) using multi-walled carbon nanotubes (MWCNTs)-TiO₂ composite photocatalysts. *Chemosphere* 75, 1105 – 1011.
25. Oh W.C., Jung A.R. and Ko W.B. (2009). Characterization and relative photonic efficiencies of a new nanocarbon/TiO₂ composite photocatalyst designed for organic dye decomposition and bactericidal activity. *Mater. Sci. Eng. C* 29, 1338 – 1347.
26. Tian L., Ye L., Deng K. and Zan L. (2011). TiO₂/carbon nanotube hybrid nanostructures: Solvothermal synthesis and their visible light photocatalytic activity. *J. Solid State Chem.* 184, 1465 – 1471.
27. Akhavan O., Azimirad R., Safa S. and Larijani M.M. (2010). Visible light photo-induced antibacterial activity of CNT-doped TiO₂ thin films with various CNT contents. *J. Mater. Chem.* 20, 7386 – 7392.
28. Wang W., Serp P., Kalck P. Silva C.G. and Faria J.L. (2008). Preparation and characterization of nanostructured MWCNT-TiO₂ composite materials for photocatalytic water treatment applications. *Mater. Res. Bull.* 43, 958 – 967.

CHAPTER 8

PEARL-BEAD-NECKLACE-STRUCTURED DOUBLE-WALLED CARBON NANOTUBE/NITROGEN, PALLADIUM CO-DOPED TiO₂ (DWCNT/N, Pd TiO₂) NANOCOMPOSITES FOR DYE DEGRADATION UNDER VISIBLE-LIGHT IRRADIATION[†]

In this chapter, details addressing the enhancement mechanism of the DWCNT/N, Pd co-doped TiO₂ systems and the proposed mechanisms for photocatalysis are discussed. An understanding of the fundamental processes leading to this enhancement may open new avenues for applications of these tailored nanocomposites for water decontamination. While studies on photocatalytic degradation of organic pollutants on MWCNT/TiO₂ composites have shown photocatalytic enhancement at certain optimum CNT levels, there are no reports on the application of DWCNTs in TiO₂ based nanocomposites. This chapter highlights the synthesis of DWCNTs and DWCNT/N,Pd TiO₂ nanocomposites and their photoactivity towards visible-light dye degradation.

8.1 INTRODUCTION

The 21st century has seen increasingly high amounts of pollutants being released into the environment as research and development industries unearth new raw materials and technologies aimed at improving people's lives. Among these pollutants are synthetic dyes from the textile and dyeing industries. It is estimated that over 10 000 different types of dyes and pigments are manufactured worldwide annually with 10 000 t of dyes being produced all over the world per year.¹ Due to

[†] Contents of this chapter were based on:

Kuvarega A.T., Krause R.W.M. and Mamba B.B. Pearl-bead-necklace structured double walled carbon nanotube/nitrogen, palladium co-doped TiO₂ (DWCNT/N,Pd TiO₂) nanocomposites for dye degradation under visible light irradiation. *Mater. Phys. Chem.* (Under review)

the large-scale production and extensive application, synthetic dyes have found their way into water bodies, some of which are sources for consumption by humans. Their release into the receiving water bodies is deleterious, not only because of their colour, but also because they are not easily degraded and form toxic, mutagenic or carcinogenic compounds upon partial degradation.² Dyes cannot be completely removed from water by well-established techniques like coagulation, flocculation, precipitation, adsorption, membrane separation and aerobic biological treatment.³ The inability of conventional wastewater treatment methods to effectively remove such pollutants calls for new, efficient, robust and cost-effective water-treatment systems.

Motivated by the need for economic and environmentally benign processes, there is a growing interest in the application of semiconductor photocatalytic methods for water decontamination. Titanium dioxide, a cheap, low-cost, non-toxic, photoactive and readily available semiconductor, has been widely used as photocatalytic material for solving environmental problems, including removal of toxic chemicals from wastewater.⁴⁻¹¹ Simultaneous introduction of non-metal and metal dopants may result in improved visible-light responsiveness and reduction in electron-hole recombination.

DWCNTs consist of two concentric graphene tubules that combine the structural and physical properties of single-walled carbon nanotubes (SWCNTs) and multi-walled carbon nanotubes (MWCNTs). They are promising materials for application as structural and functional materials. For structural composites, the outer shell of the DWCNTs can be functionalised to provide anchors for interface bonding with matrices while retaining the mechanical robustness of the inner shell. The outer shell can be loaded with electronically or optically active phases that integrate with the physical properties of the inner shell for the realisation of photoelectronic detections and energy conversions.¹²⁻¹⁴

The superior physical, mechanical and multifunctional properties of DWCNTs prompted an investigation into their application in photocatalytic pollutant removal from water. Currently, there are only a few reports on synthesis of high-quality

DWCNTs let alone their applications in visible-light-driven photodegradation of pollutants as DWCNT/TiO₂ hybrid materials. Utilisation of the larger portion of the spectrum of natural sunlight for photocatalysis is an important aspect for commercialisation of photocatalyst systems in sustainable environmental waste cleanup, including water purification.^{15,16} Optimisation of DWCNT usage in various applications including water purification requires assembling of nanostructures such as semiconductor photocatalysts onto their surfaces. A combination of DWCNTs and TiO₂ nanoparticles is expected to deliver exceptional performances in removal of organic pollutants from water. In this chapter, DWCNT/N, Pd co-doped TiO₂ nanocomposites were prepared by incorporating different amounts of DWCNTs (0.5% to 40.0%) in the titanium, palladium and nitrogen sol-gel precursor solution. The photocatalytic degradation efficiency of the nanocomposites was evaluated using an aqueous solution of EY.

8.2 MATERIALS AND METHODS

8.2.1 Synthesis of DWCNTs

DWCNTs were synthesised by the pyrolysis of methane gas over a mixed metal catalyst. The DWCNTs were acid purified and oxidised to enhance their solubility in aqueous solution as well as to impact functionalities on their walls. Details of the synthesis, purification and oxidation of the DWCNTs are given in **Section 3.4**.

8.2.2 Preparation of the nanocomposites

DWCNT(0.5%)/N, Pd co-doped TiO₂ (0.5% Pd) was prepared by the following method: An appropriate weighed amount of oxidised DWCNTs was dispersed in a mixture of 2-propanol C₃H₈O, (50 ml), (99.8%, Sigma Aldrich, Germany) and titanium isopropoxide, Ti(OC₃H₇)₄, (10 ml), (97%, Sigma Aldrich, Germany) to give a DWCNT:Ti percentage of 0.5%. The mixture was sonicated for 30 min to improve DWCNT dispersion. An appropriate amount of palladium diamine dichloride, Pd(NH₃)₂Cl₂, (45% Pd, PGM Chemicals, RSA), to give a Pd:Ti ratio of 0.5% was dissolved in 12 ml of aqueous ammonia (25%, Merck, Germany). The solution was added drop-wise to the DWCNT/2-propanol/titanium isopropoxide

mixture with vigorous stirring for 30 min. After a further hour of stirring, the suspension was dried overnight in air in an oven set at 80°C. The resulting light-grey powder was calcined for 2 h at 450°C in air in an electric furnace and characterised by various techniques. Then 1.0%, 2.0%, 5.0%, 10.0%, 20.0% and 40.0% DWCNT/N, Pd TiO₂ nanocomposite samples were prepared by following the same procedure, weighing appropriate amounts of oxidised DWCNTs, respectively.

8.2.3 Material characterisation

The synthesised materials were characterised using various techniques as described in **Section 3.6**.

8.2.4 Evaluation of photocatalytic activity

The activity of the nanocomposite photocatalysts was assessed by measuring the time-dependent concentration loss of a dye under simulated solar irradiation. Details of the experimental setup are given in **Section 3.7**.

8.3 RESULTS AND DISCUSSION

8.3.1 FT-IR studies

The presence of functionalities on DWCNTs and DWCNT/N, Pd TiO₂ nanocomposites was confirmed by FT-IR analysis (**Figure 8.1** and **Figure 8.2**). The spectrum of oxidised DWCNTs clearly shows the presence of OH groups centred at 3 351 cm⁻¹ due to acid oxidation. The band at 1 461cm⁻¹ present in both pristine and oxidised DWCNTs is ascribed to the C=C stretching vibrations. Further, two bands at 1 120 cm⁻¹ and 1 594 cm⁻¹ for the oxidised DWCNTs correspond to C–O and C=O stretching of carboxyl groups confirming the DWCNTs were –COOH functionalised. The presence of –COOH groups on DWCNTs promotes formation of physical or chemical interactions with other molecules through Van der Waals forces, hydrogen bonds and ester linkages.

TiO₂ can attach to the DWCNTs by forming C-O-Ti due to the esterification between the -COOH of DWCNTs-COOH and the -OH of TiO₂.^{17,18}

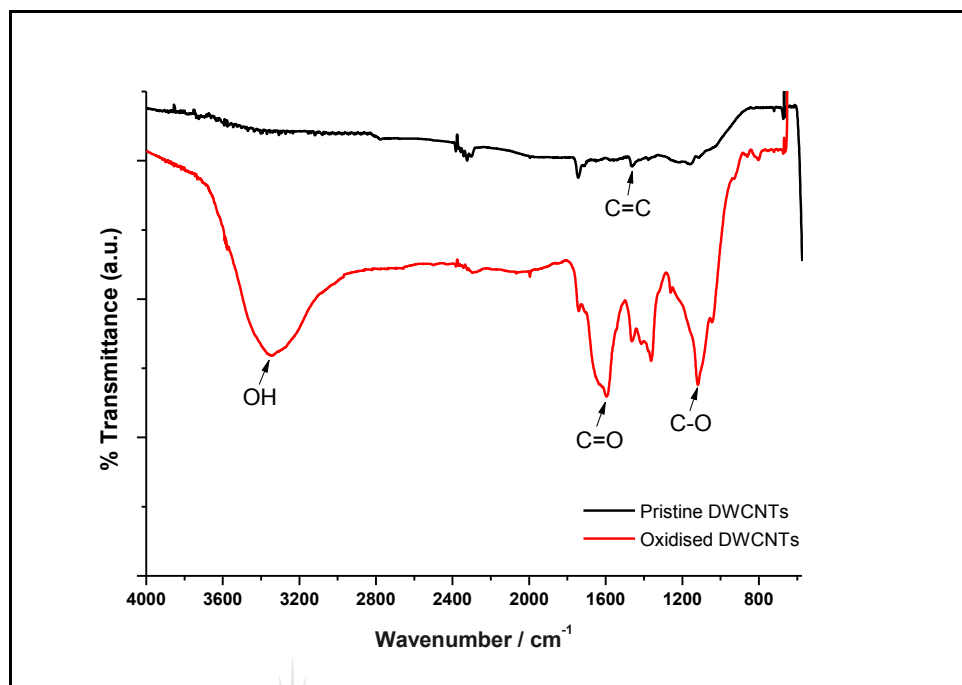


Figure 8.1 FT-IR spectra of pristine and oxidised DWCNTs

The DWCNT/N, Pd TiO₂ nanocomposites spectra were similar with the main peaks below 550 cm⁻¹, ascribed to the Ti-O, Ti-O-Ti and Ti-O-C vibrations. Broad-band peaks centred at around 3 390 cm⁻¹, and attributed to the OH stretching of physisorbed water on the nanocomposite surfaces, were observed for all samples. Relatively sharp bands at around 1 630 cm⁻¹ correspond to the OH bending modes of the water molecules. In addition, some samples gave peaks at 2 350 cm⁻¹ which were assigned to the N=C=O vibrations. Peaks associated with the functionalisation of DWCNTs were not observed in the nanocomposites. This could indicate good coverage of the DWCNTs by the TiO₂ as all -COOH functionalities were used in the condensation reaction.

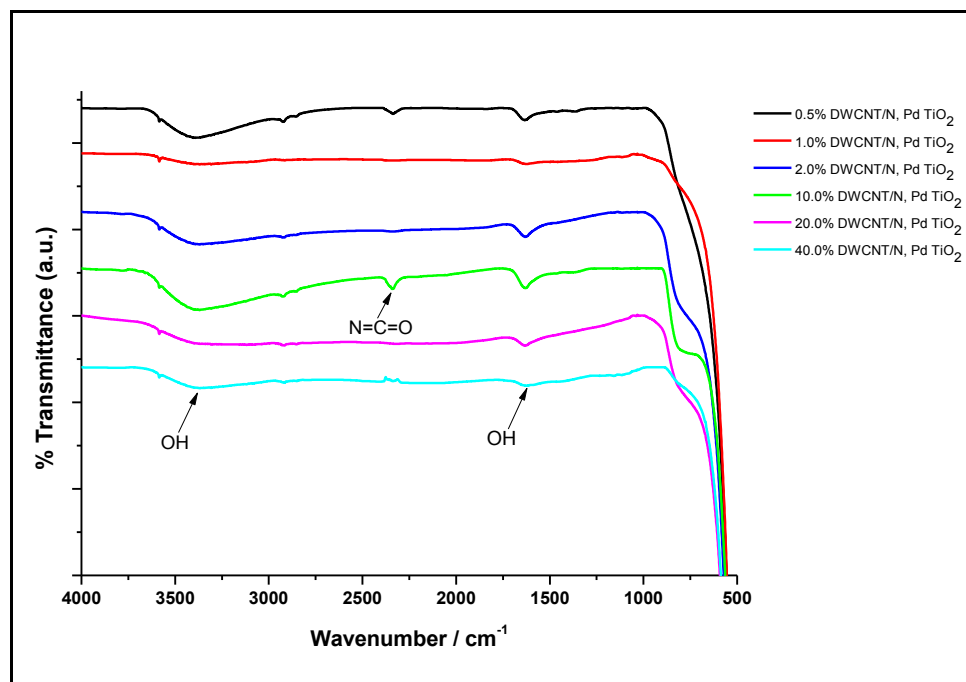


Figure 8.2 FT-IR spectra of DWCNT/N, Pd TiO₂ nanocomposites

8.3.2 Raman analysis

The Raman spectra of pristine and oxidised DWCNTs consisting of the radial breathing mode (RBM) signals at between 100 cm⁻¹ to 400 cm⁻¹, the D-band (1 305 cm⁻¹) and the G band (1 582 cm⁻¹) are shown in **Figure 8.3**. The D band corresponds to defect sites in the hexagonal framework of DWCNTs due to structural imperfections induced by sp³ hybridisation or amorphous carbon, whereas the G band indicates the presence of ordered sp² hybridisation.¹⁹

The ratio of the intensities of the G band and D band (I_G/I_D) can be used to show the extent of the structural defects induced by oxidation. The increase in defects on CNTs results in increased D band intensity and lowered G band intensity, reflecting the change in hybridisation of C atoms from sp² to sp³. Pristine DWCNTs gave an I_G/I_D ratio of 3.69, which was much higher than that of oxidised DWCNTs: ($I_G/I_D = 1.47$). The decrease in the ratio on oxidation confirmed the effects of the nitric acid/sulphuric acid treatment on the quality of the DWCNTs.

Radial breathing modes (RBMs) at the low-frequency range are strongly dependent on the diameters of the tubes. The frequencies of the RBM and DWCNT diameter are related by the expression;

$$\omega = 248/d$$

where:

ω is the RBM frequency in wave numbers

d is the tube diameter in nm.¹⁴

Two well-defined peaks are visible in the low-frequency region for both pristine and oxidised DWCNTs, one at 165.84 cm⁻¹ and another one at 263.2 cm⁻¹. These would give inner-tube diameters of 0.80 nm to 0.92 nm and outer tube diameters of about 1.06 nm to 1.52 nm in close agreement with the TEM observations. The Raman process is influenced by optical resonance and thus it is not possible to scan the whole population of CNTs present within a sample with only one wavelength (785 nm) because a specific excitation wavelength enhances the signal for only some of the CNTs. Earlier studies on DWCNTs have revealed that RBM peaks cannot be observed for much lower wave numbers, limiting the maximum diameter observation range.²⁰

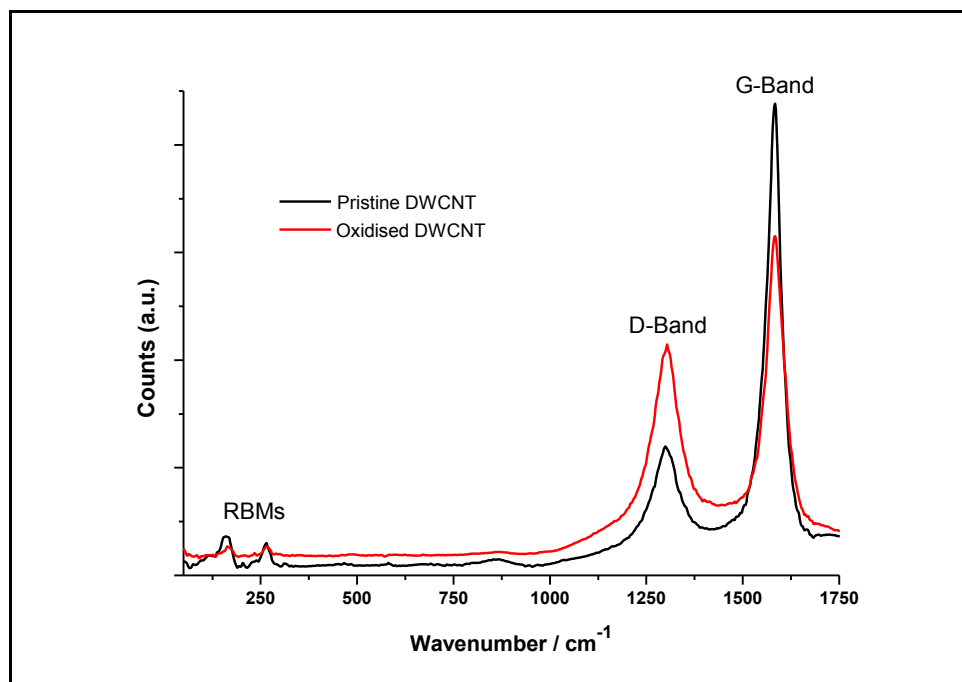


Figure 8.3 Raman spectra of pristine and oxidised DWCNT showing the D and G bands as well as the RBMs

Raman spectra of DWCNT/N, Pd TiO₂ are presented in **Figure 8.4**. DWCNT peaks could not be detected for low percentage DWCNT nanocomposites (0.5% to 2.0% DWCNT/N, Pd TiO₂) probably due to complete coverage of the DWCNTs by the TiO₂ as observed in the TEM images. The spectra show characteristic peaks for DWCNTs as well as anatase TiO₂. The fingerprint Raman features of the graphitic crystalline arrangement (G-band), arising from the Raman allowed optical mode and the disorder-activated band (D-band), centred respectively at 1 572 cm⁻¹ and 1 299 cm⁻¹, were observed in all spectra. The slight decrease in the peak frequencies of the DWCNT/N, Pd TiO₂ compared to the oxidised DWCNTs could be due to preferential bond formation with functional groups on the chemically oxidised DWCNTs. This is supported by the increase in the I_G/I_D ratios of the nanocomposites which showed higher values than those of the oxidised DWCNTs. The decrease in the disorder band provides evidence of possible bonding between oxidised DWCNTs and the TiO₂ as the defect sites are occupied by the TiO₂ particles. The lower frequency region is dominated by the TiO₂ bands.

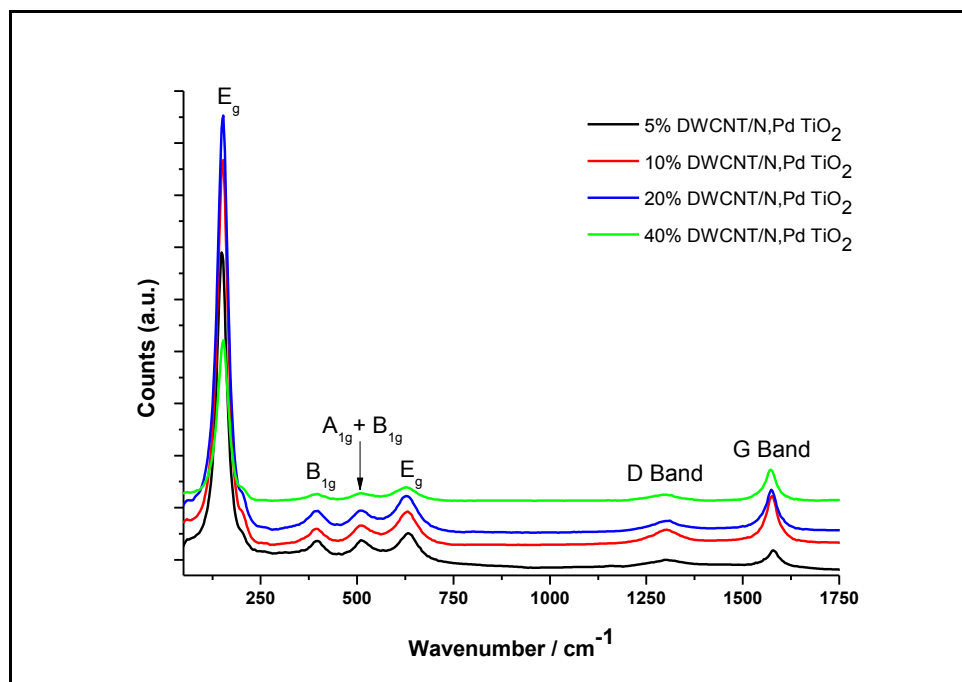


Figure 8.4 Raman spectra of DWCNT/N, Pd co-doped TiO₂ with different DWCNTs ratios

Peaks centred at 151 cm⁻¹, 395 cm⁻¹, 510 cm⁻¹ and 636 cm⁻¹ are ascribed to the E_g, B_{1g}, unresolved A_{1g}+B_{1g} and E_g Raman allowed modes of anatase TiO₂, respectively.^{15,18} The higher frequency E_g band shifts to lower frequencies at higher DWCNT percentages, indicating possible overlap due to formation of the rutile TiO₂, an observation supported by the XRD results.

8.3.3 XRD studies

XRD analysis was performed in order to investigate the effect of DWCNT content on the phase, crystallinity and particle size of the nanocomposites (**Figure 8.5**). The strong diffraction peaks at 2θ values of 25.29, 37.83, 48.07, 54.14, 55.07, 62.64, 68.94, 70.14 and 75.11 evidenced high crystallinity and can be indexed to the (101), (004), (200), (105), (211), (204), (116), (220) and (215) tetragonal crystal planes of the anatase phase of TiO₂.^{21,22} At high DWCNT percentages, traces of an extra TiO₂ phase, identified as rutile, were observed. The DWCNT peak was not detected probably due to the highly intense TiO₂ E_g peak that may have shielded the DWCNT (002) plane peak expected at 2θ = 25.6°. ¹⁵ The Scherrer equation was used to estimate the crystallite sizes.

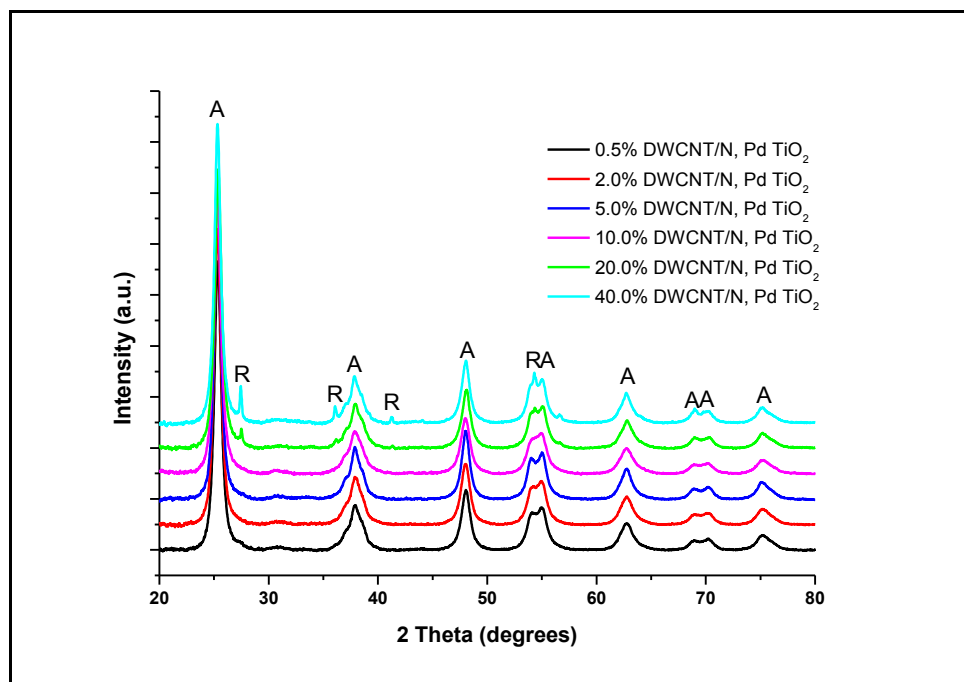


Figure 8.5 XRD patterns of DWCNT/N, Pd co-doped TiO₂ with different DWCNT ratios (A = anatase phase, R = rutile phase)

Results of particle sizes are shown in **Table 8.1**. There were no major differences in particle size with increasing amounts of DWCNTs. The particles were quite small and this may be attributed to the rate of hydrolysis and condensation reactions on the oxidised DWCNTs during the sol-gel process. The presence of DWCNTs led to faster reaction rates. The condensation reaction was complete within a short period of time as some carboxylate sites were available for the reaction, forming ester linkages with the functionalised DWCNTs. The rapid hydrolysis of the precursors occurred prior to or while the reaction products anchored on the nanotube supports leading to smaller particle sizes.¹⁶

Table 8.1 Effect of MWCNTs on average particle size

Sample	Particle size (nm)
0.5% DWCNT/N, Pd TiO ₂ (0.5% Pd)	10.9
2.0% DWCNT/N, Pd TiO ₂ (0.5% Pd)	10.3
5.0% DWCNT/N, Pd TiO ₂ (0.5% Pd)	11.8
10.0% DWCNT/N, Pd TiO ₂ (0.5% Pd)	10.5
20.0% DWCNT/N, Pd TiO ₂ (0.5% Pd)	11.6
40.0% DWCNT/N, Pd TiO ₂ (0.5% Pd)	10.9

8.3.4 Optical properties

Figure 8.6 shows the diffuse reflectance ultraviolet visible (DRUV-Vis) spectra of the DWCNT/N, Pd TiO₂ nanocomposites. All samples gave a fundamental absorption edge in the UV region, attributed to the presence of TiO₂ in the samples.²⁴ The strong UV absorption was accompanied by a tailing well into the visible region which decreases in the mid-range with increasing amounts of DWCNTs in the nanocomposites. The strongest absorption in the visible region was observed for the 0.5% DWCNT/ N, Pd TiO₂ centred at about 500 nm. Increasing percentages of DWCNTs resulted in a decrease in the absorption at around 500 nm but an increase was observed between 700 nm and 900 nm. The mid-range is associated with low absorbance from the TiO₂ which results in overall reduced absorbance in this region. The increase in visible-light absorption can be explained by the presence of N which forms inter-band-gap states in TiO₂, resulting in a lower band gap, consequently shifting the absorption edge to the visible region. The presence of Pd also shifts the absorption to the visible region due to d-d electron transitions. CNTs are known to absorb well in the entire visible region, so their presence in the nanocomposites also contributed to the red shift in the absorption edge, especially in the lower energy region (700 nm to 900 nm). A similar trend was observed for MWCNT/ N, Pd TiO₂ nanocomposites.²⁵

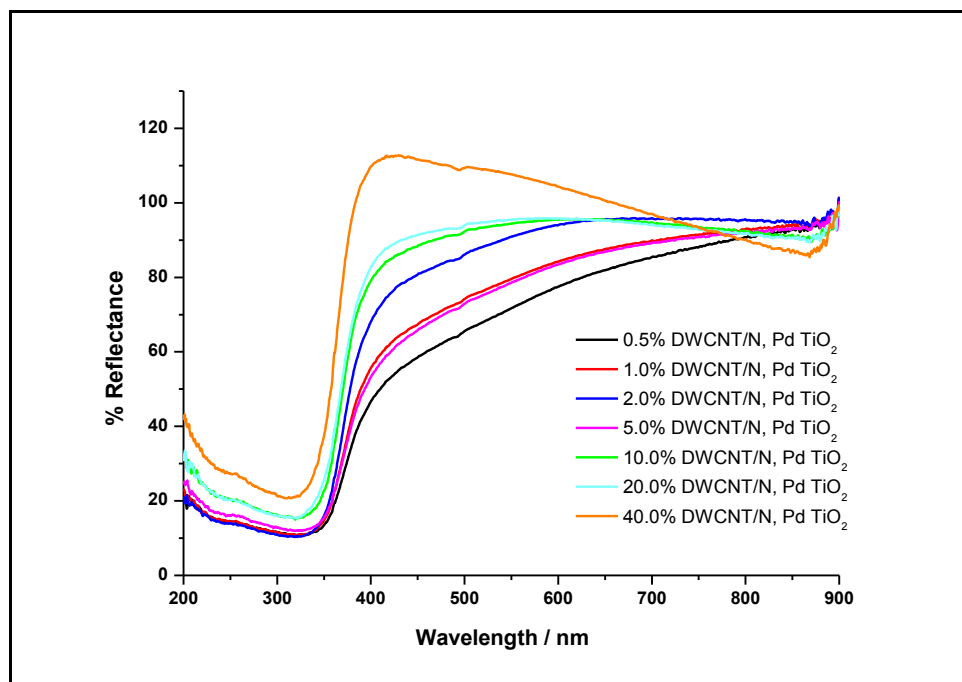


Figure 8.6 DRUV-Vis spectra of the DWCNT/N, Pd TiO₂ nanocomposites

Comparison of the spectra in the UV region reveals strong, broad absorption observed below 400 nm associated with charge transfer from the valence to the conduction band of the TiO₂ (Figure 8.7). There is a decrease in UV absorption peak intensity with increasing percentages of DWCNTs in the nanocomposites. The decrease in the UV absorbance intensity is associated with poor linkages between TiO₂ and the DWCNTs mainly due to aggregation of the CNTs, resulting in their poor coverage by the TiO₂.

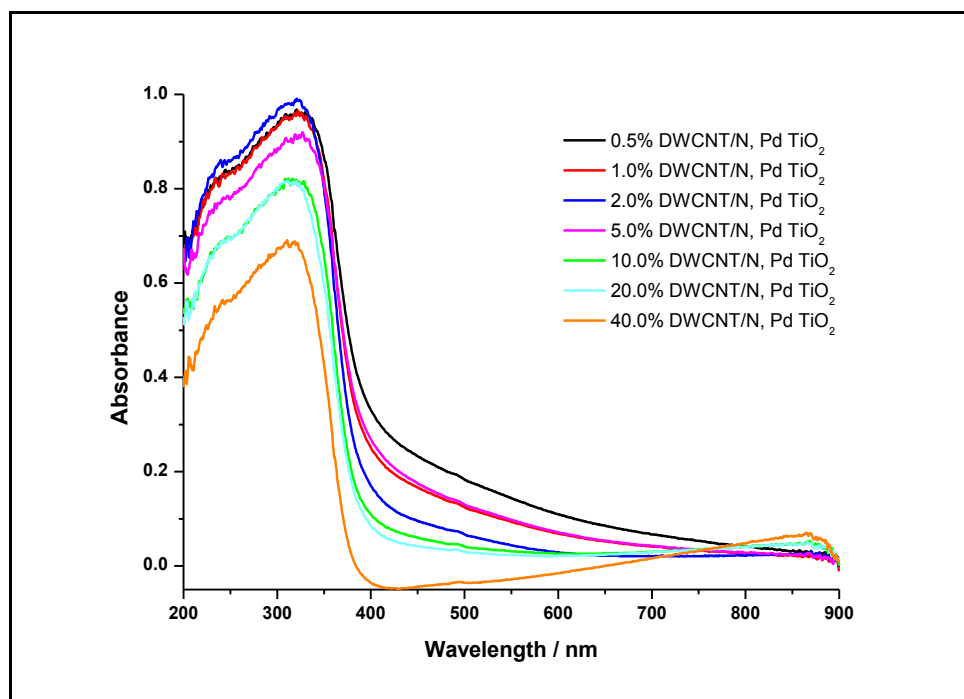


Figure 8.7 UV-Vis absorption spectra of the DWCNT/N, Pd TiO₂ nanocomposites

A plot of Kubelka-Munk data vs. wavelength is presented in **Figure 8.8**. The effect of higher percentages of DWCNTs on the absorption is clearly visible. The intense absorption band in the UV region can be ascribed to the charge transfer from O²⁻ to Ti⁴⁺ whilst the increased absorption in the visible range could be due to the synergistic effects of N and Pd co-doping as well as the DWCNTs. These observations suggest possible changes of the electronic properties of the nanocomposites due to DWCNT introduction, which may lead to modifications of the fundamental process of electron-hole pair formation during photocatalytic degradation.²⁶

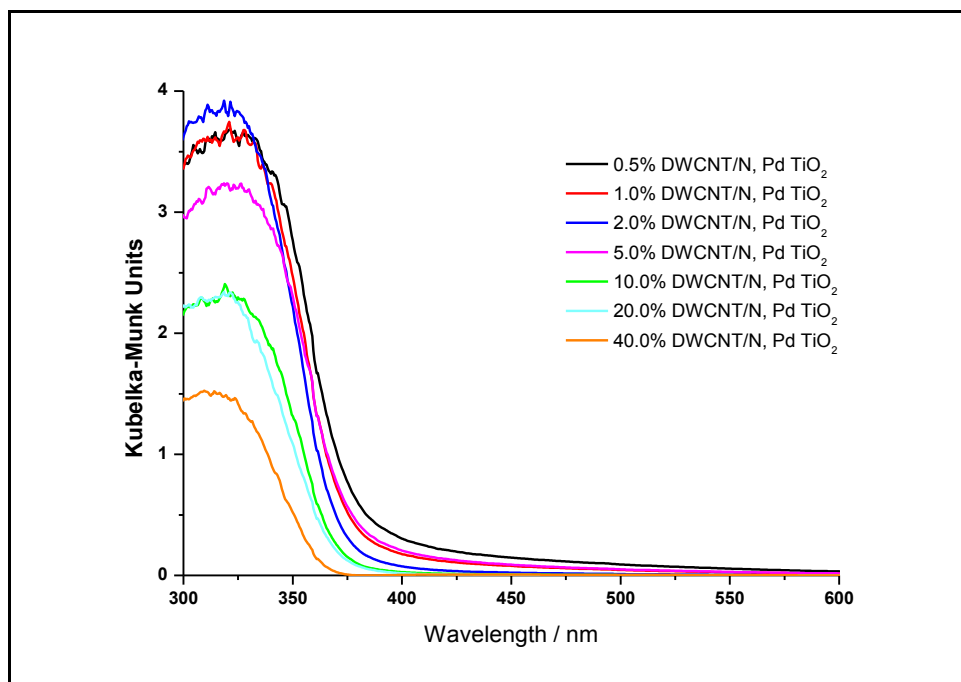


Figure 8.8 Kubelka-Munk spectra of the DWCNT/N, Pd TiO₂ nanocomposites

The band-gap energy (E_g) of the materials was estimated from the Tauc plots. Experimental results and theoretical calculations suggest TiO₂ has a direct forbidden band gap, which is almost degenerate with an indirect allowed transition. The indirect allowed transition dominates in the optical absorption just above the absorption edge due to weak strength of the direct forbidden transition.²⁷ Assuming a direct band-gap semiconductor, the plot with $n = 2$ gives a linear Tauc region that intersects with the photon energy axis yielding the semiconductor band gap (**Figure 8.9**).

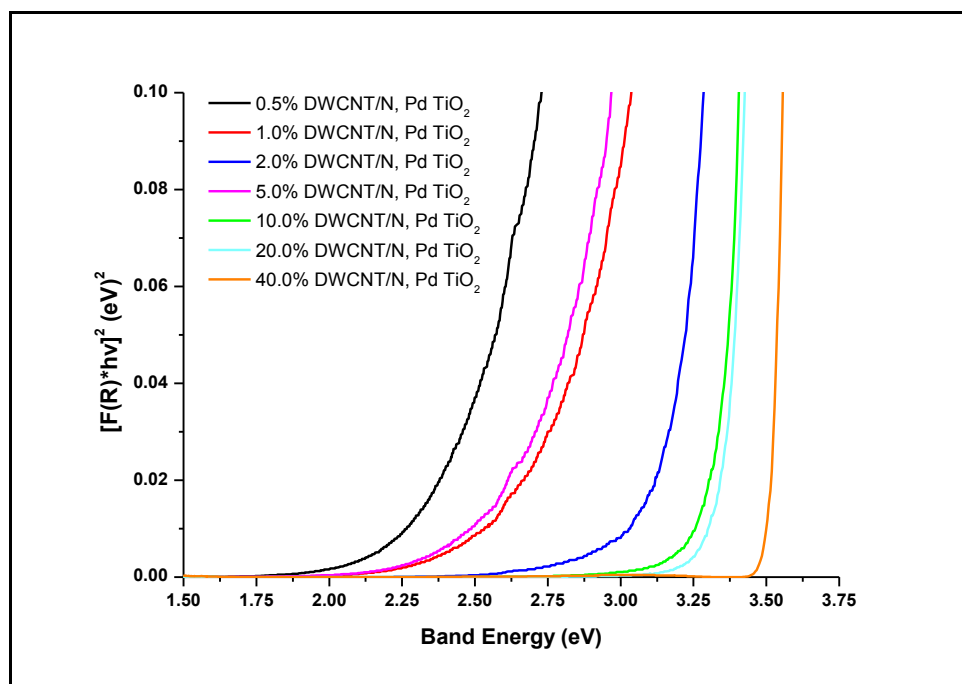


Figure 8.9 Tauc plots of the DWCNT/N, Pd TiO₂ nanocomposites

There was a general increase in band-gap energy with increasing percentages of DWCNTs in the nanocomposites (**Table 8.2**). Higher amounts of DWCNTs limit the available N and Pd for doping with TiO₂ as some of these elements may become associated with the DWCNTs, leading to an increase in band gap. The main role of DWCNT in the nanocomposites was to act as supports for the TiO₂ nanoparticles. The presence of DWCNTs also led to changes in the band-gap energy of the nanocomposites, favouring the application of the materials in pollutant degradation using solar energy.

Table 8.2 Band-gap energies of the DWCNT/N, Pd TiO₂ nanocomposites

Sample	Direct band gap (eV)
0.5% DWCNT/N, Pd TiO ₂ (0.5% Pd)	1.82
1.0% DWCNT/N, Pd TiO ₂ (0.5% Pd)	2.06
2.0% DWCNT/N, Pd TiO ₂ (0.5% Pd)	2.40
5.0% DWCNT/N, Pd TiO ₂ (0.5% Pd)	2.02
10.0% DWCNT/N, Pd TiO ₂ (0.5% Pd)	2.77
20.0% DWCNT/N, Pd TiO ₂ (0.5% Pd)	3.04
40.0% DWCNT/N, Pd TiO ₂ (0.5% Pd)	3.43

8.3.5 SEM and EDS analyses

Surface morphologies of pristine and oxidised DWCNTs were examined with SEM to assess the effect of oxidation on the general structure of DWCNTs (**Figure 8.10**). Pristine DWCNTs showed the presence of particles and impurities from the catalyst, support and carbonaceous material. The CNTs were several micrometres long and showed smooth, clean surfaces with small diameters (**Figure 8.10(a)**). The DWCNTs were treated with acid to remove the catalyst and support particles together with any other impurities. The amount of particles was reduced after purification; however, the length of the DWCNTs was reduced and their surfaces were rougher but the general structure of the DWCNTs was maintained (**Figure 8.10(b)**).

EDS analysis was performed on the pristine and oxidised DWCNTs to confirm the removal of catalyst particles and amorphous material by acid treatment. Pristine DWCNTs contained a substantial amount of Mg, Mo and Co which originated from the catalyst used in the synthesis of the DWCNTs (**Figure 8.10(c)**). After acid treatment, only a small amount of Co still remained on the DWCNTs (**Figure 8.10(d)**). A new S peak, most probably from the H₂SO₄ used in the oxidation process also appeared on the oxidised DWCNTs. These observations indicate that

the HNO₃-H₂SO₄ acid mixture totally dissolved the Mo and MgO catalyst support without causing much structural damage to the DWCNTs.

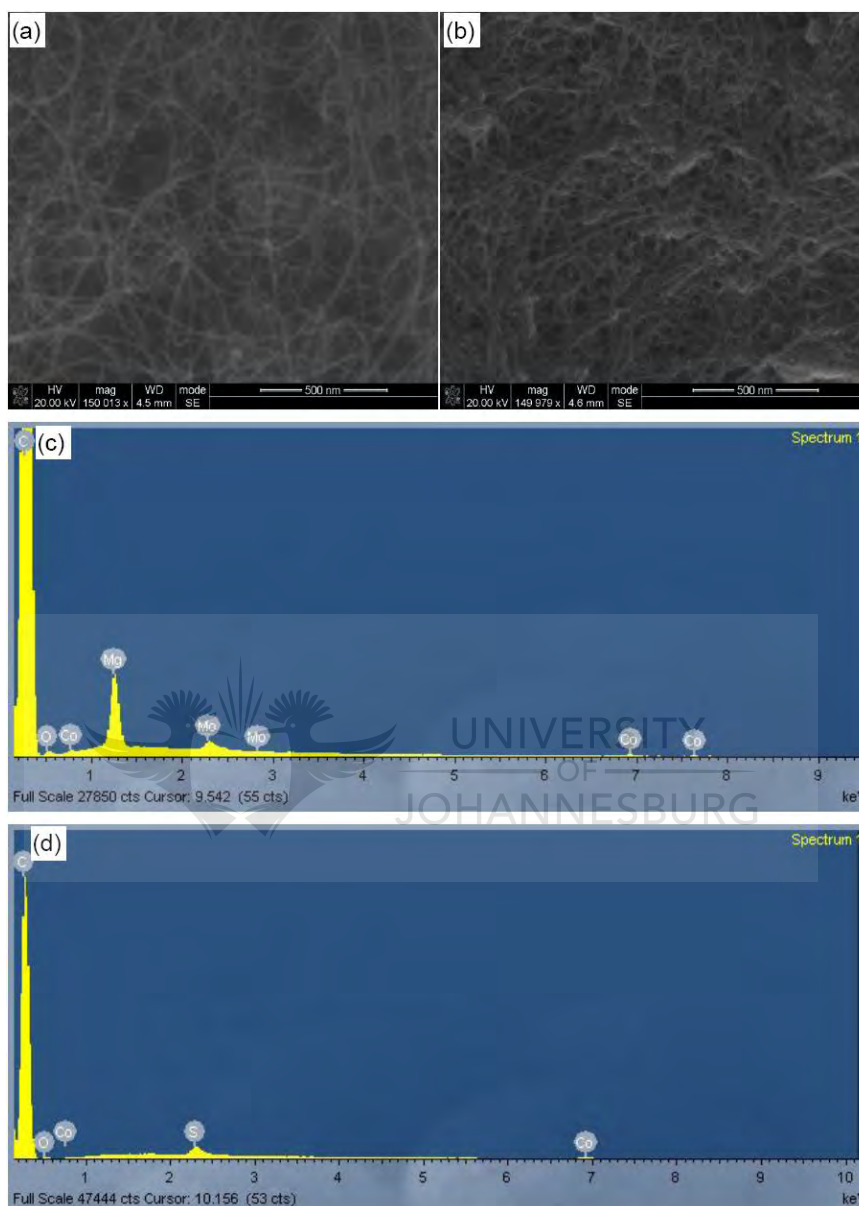


Figure 8.10 SEM images of (a) pristine; and (b) oxidised DWCNTs; and EDS spectra of (c) pristine; and (d) oxidised DWCNTs

8.3.6 TEM and EDS analyses

TEM images of pristine and oxidised DWCNTs are shown in (Figure 8.11). Pristine DWCNTs appeared as long, narrow-diameter, smooth-walled tubes with some catalyst particles and amorphous material (Figure 8.11(a)). Upon oxidation,

all the residual catalyst particles and impurities were removed to give dominantly rough-surfaced DWCNTs (**Figure 8.11(b)**). The DWCNTs had an average inner diameter of 2 nm and outer diameter of 4 nm in close agreement with the results from Raman calculations. Besides the DWCNTs some three and four-walled CNTs were also observed, but the amount was very small.

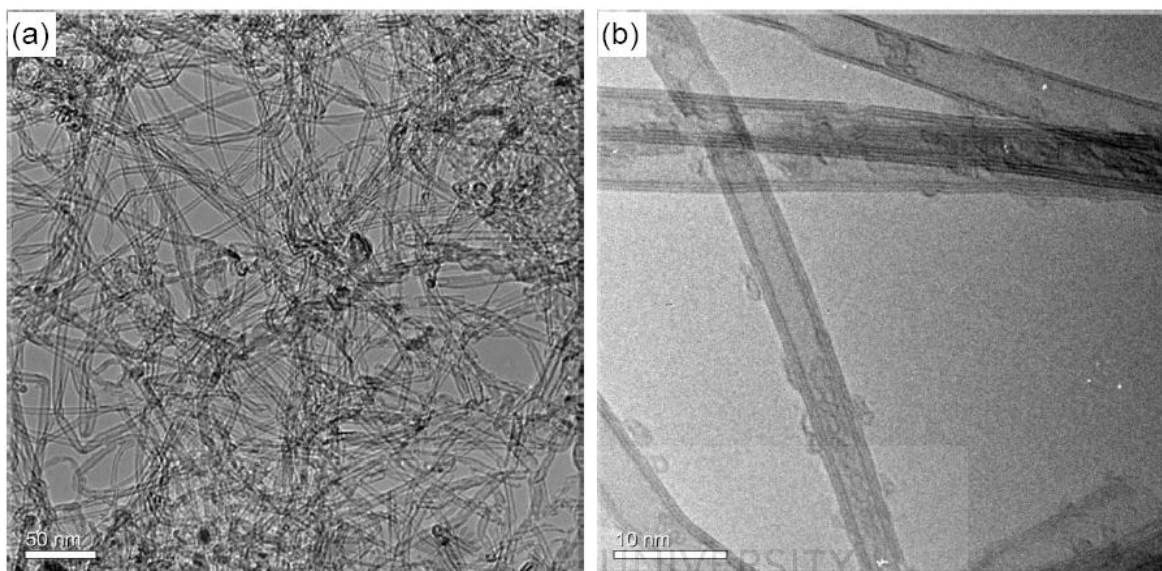


Figure 8.11 TEM images of (a) pristine DWCNTs; and (b) oxidised DWCNTs

SEM images of the DWCNT/N, Pd co-doped TiO₂ nanocomposites show clusters of N, Pd TiO₂ surrounding the DWCNTs to form long „worm-like” structures (**Figure 8.12**). The TiO₂ particles were supported on the walls of the acid-treated DWCNTs to give rough surfaces. The distribution of the TiO₂ particles on the DWCNTs is far from being homogeneous, with some nanocomposites showing much larger diameters. The diameter of the nanocomposites is visibly larger than that of the oxidised DWCNTs due to the TiO₂ coverage. The length of the DWCNTs in the nanocomposites is shorter than that of the oxidised ones. Most of the nanocomposites have an approximate length of about 500 nm. This observation may suggest possible shortening of the DWCNTs during the sol-gel processing. The aggregation of TiO₂ nanoparticles confirms the supporting role of the DWCNTs as centres for the deposition and growth of the sol-gel hydrolysis products, as well as the support for spatial confinement of the N, Pd TiO₂ clusters.

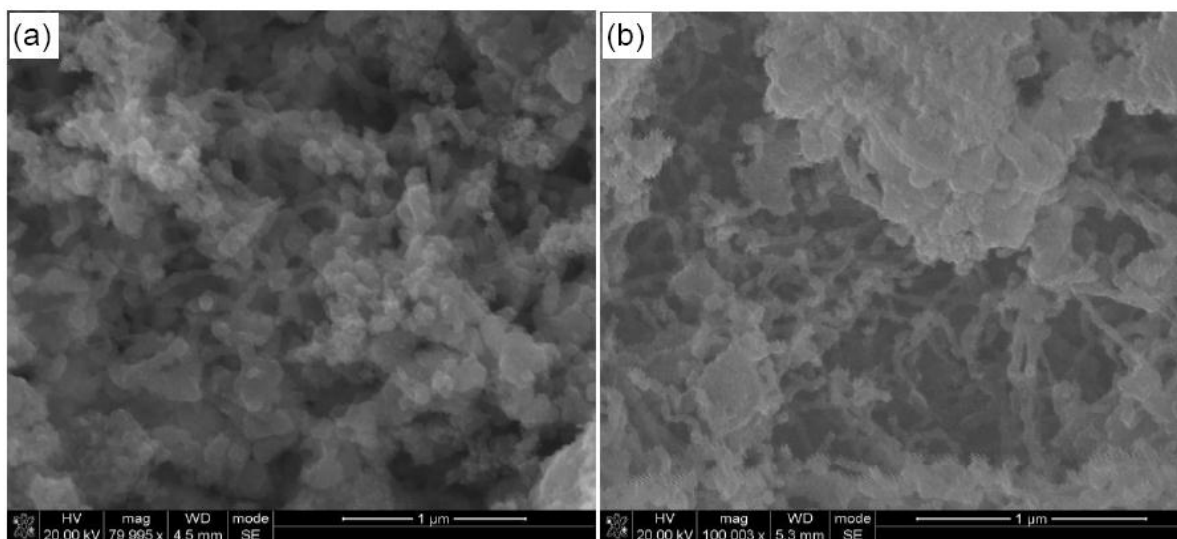


Figure 8.12 SEM images of (a) 10.0% DWCNT/N, Pd TiO₂; and (b) 20.0% DWCNT/N, Pd TiO₂

To explore further the surface structure and morphology of DWCNT/N, Pd TiO₂ nanocomposites, their TEM images were acquired (**Figure 8.13**). The images show TiO₂ particles anchored onto the small-diameter DWCNTs to form long pearl-bead-necklace-like structures. The bead-like TiO₂ particle coverage shows strong contact with the entire DWCNTs. The average size of the TiO₂ nanoparticles is about 10 nm, in agreement with the XRD results.

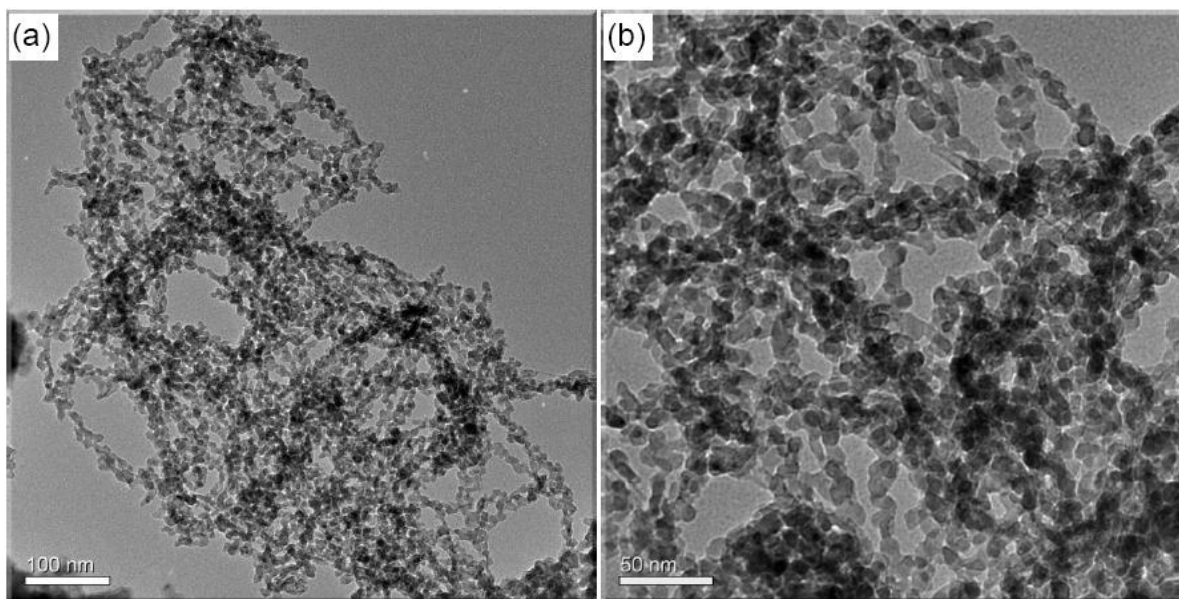


Figure 8.13 TEM images of pearl-bead-necklace-structured 20.0% DWCNT/N, Pd TiO₂ nanocomposite (a) lower magnification; and (b) higher magnification

EDS was carried out on a selected area of one of the DWCNT/N, Pd TiO₂ nanocomposites to probe the elemental composition of the material (**Figure 8.14**). The presence of Ti, O, Pd and C confirmed the existence of Pd doped TiO₂ on the DWCNTs. The intensity of the C peak was much lower compared to the Ti and O peak intensities, suggesting near complete coverage of the DWCNTs by the TiO₂ as observed in the SEM and TEM images. Pd showed the lowest peak intensity as expected because of the low levels (0.5%) used in preparing the materials. The Si could have originated as a contaminant from the glassware whilst the Cu signal came from the copper grid used as the sample support during TEM analysis.

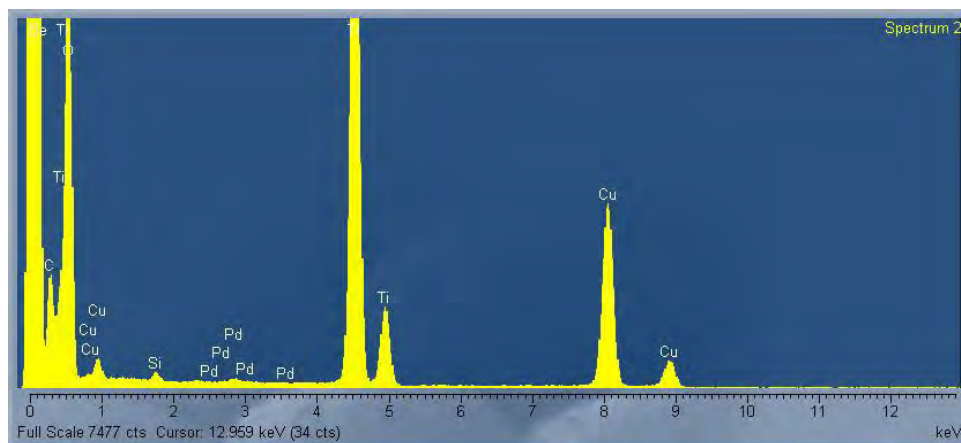


Figure 8.14 EDS of 20.0% DWCNT/N, Pd TiO₂ nanocomposite

Based on the SEM and TEM images of the nanocomposites, it can be proposed that the TiO₂ precursor molecule, titanium isopropoxide, was quickly adsorbed on the nanotubes and reacted with the carboxyl functional groups on the DWCNT surface to generate water molecules in a condensation reaction.²² This reaction was further promoted by the addition of aqueous ammonia solution containing Pd ions. This led to the tight attachment of the molecules on the host surface, forming a uniform guest coating. Upon calcination, the water molecules generated from the condensation reaction evaporated, giving rise to the N, Pd co-doped TiO₂ attached onto the DWCNT surface. Pd²⁺ ions can form coordination bonds with the oxygen on the surface OH groups on the DWCNTs or Ti(OH)_x resulting in the formation of bridged bonds with the DWCNTs or Ti (**Figure 8.15**). Calcination results in the formation of PdO on the N TiO₂ or DWCNT surfaces.²⁵

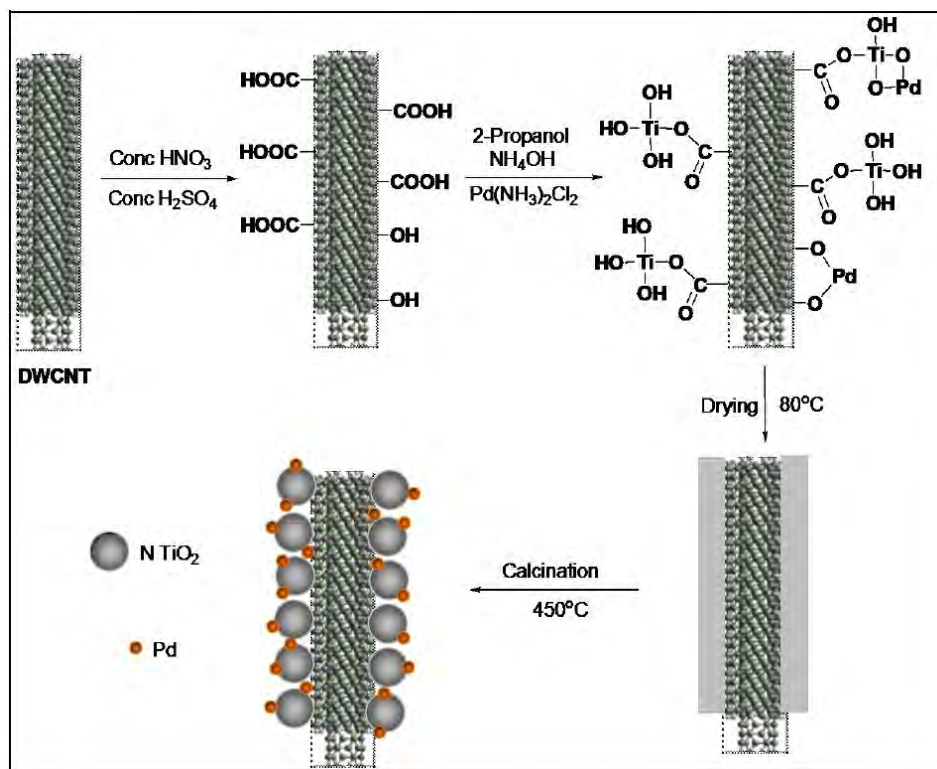


Figure 8.15 Reaction scheme for the formation of DWCNT/N, Pd TiO₂ nanocomposites

8.3.7 Thermal properties

Thermogravimetric analysis results of the pristine and oxidised DWCNTs together with their derivatives (inset) are shown in **Figure 8.16**. TG analysis was performed to provide an estimate of the purity of the DWCNTs and the degree of functionalisation. The thermogram of pristine DWCNTs showed that decomposition occurred between 570°C and 750°C with a weight loss of nearly 87%. The residual materials were the metal catalysts and the amount was approximately 9.3 wt%. A decomposition temperature of 684°C was confirmed by the derivative plot. A small weight loss at 100°C was attributed to the adsorbed water molecules due to moisture on the DWCNTs. The derivative plot also revealed that the tubes were relatively pure since there is only one decomposition peak observed.

Oxidized DWCNTs showed a weight loss at temperatures slightly lower than 100°C, attributed to adsorbed water molecules. A steady weight loss was observed at temperatures above 100°C. This was attributed to the loss of carboxyl

groups. A decomposition centred at 630°C corresponding to a weight loss of 84.5% was assigned to loss of graphitic skeleton of DWCNTs. Oxidation lowered the thermal stability of the DWCNTs. This can be ascribed to some damage to the DWCNTs caused by the creation of defect sites that contain sp³ carbon on the walls of the DWCNTs. Acid treatment removed most of metal catalyst, with a residual weight of 2.9%, noted for the oxidised DWCNTs.

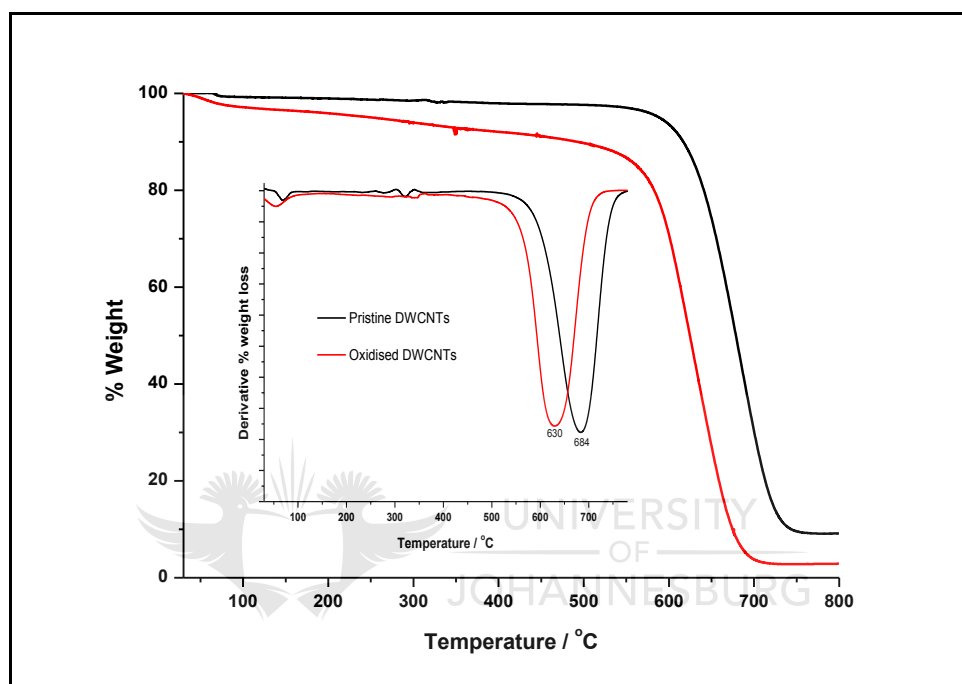


Figure 8.16 Thermograms of pristine and oxidised DWCNTs and their derivatives (inset)

8.4 PHOTOCATALYTIC DEGRADATION STUDIES

The photocatalytic activity of the DWCNT/N, Pd TiO₂ nanocomposites was evaluated by assessing the degradation of Eosin Yellow, a xanthene dye, under simulated solar radiation (**Figure 8.17**). The highest degradation efficiency was observed for the 2.0% DWCNT/N, Pd co-doped TiO₂ composite, with complete dye degradation being realised in 2 h. There was an increase in degradation efficiency with increasing amounts of DWCNTs up to 2.0% DWCNT/N, Pd TiO₂ followed by a decrease with increasingly higher amounts of DWCNTs. The decrease in photoactivity at higher DWCNT percentages correlated very well with

the increase in band gaps observed in the Tauc plots (**Table 8.2**). From the observed trend, it was postulated that there is an optimum DWCNT/N, Pd co-doped TiO₂ ratio that offered favourable conditions for the synergistic effects by incorporating DWCNTs in the nanocomposites. The highest degradation of 99.87% was observed for the 2.0% DWCNT/N, Pd TiO₂ whilst the lowest degradation efficiency (89.72%) occurred with the 40.0% DWCNT/N, Pd TiO₂ (**Table 8.3**). Photocatalytic enhancement can be attributed to the formation of DWCNT/N, Pd TiO₂ heterojunctions which can reduce the rate of the recombination of photo induced electrons and holes. There is also a possibility of shifting the apparent Fermi level to more positive values of the DWCNT/N, Pd TiO₂ nanocomposites compared to pure N, Pd TiO₂ therefore allowing the utilisation of longer wavelength photons for photo activation of the material. DWCNTs themselves can absorb photons, injecting electrons into the TiO₂ conduction band, triggering the formation of highly reactive superoxide and hydroxyl radicals.¹⁶

Gao and co-workers used a conventional sol-gel method to prepare CNT/TiO₂ nanocomposites with different carbon loading in the range up to 20% CNT/TiO₂ by weight. The optimum CNT/TiO₂ ratio for the degradation of methylene blue was found to be in the range of 1.5% to 5% by weight under UV irradiation.¹⁶ A study on the degradation of acetone using TiO₂/CNT nanocomposites gave an optimal amount of TiO₂ and CNTs in the range of 1:0.1 and 1:0.2.²⁸ In another study, a low MWCNT percentage of 0.5% was found to be effective in enhancing the degradation of Eosin Yellow in water using MWCNT/N, Pd TiO₂ nanocomposites.²⁵ MWNT/TiO₂ composite catalysts were prepared by a modified sol-gel method and applied in the photocatalytic degradation of phenol under visible-light irradiation. An optimum synergetic effect was observed for a MWCNT/TiO₂ weight ratio of 20% with an increase in the apparent first-order rate constant by a factor of 4.1.²⁶ The decrease in activity at higher DWCNT loadings (5.0% or higher in this work) can be attributed to photon scattering by the bare carbon phase, as a result of insufficient coverage of the DWCNTs by the N, Pd TiO₂.

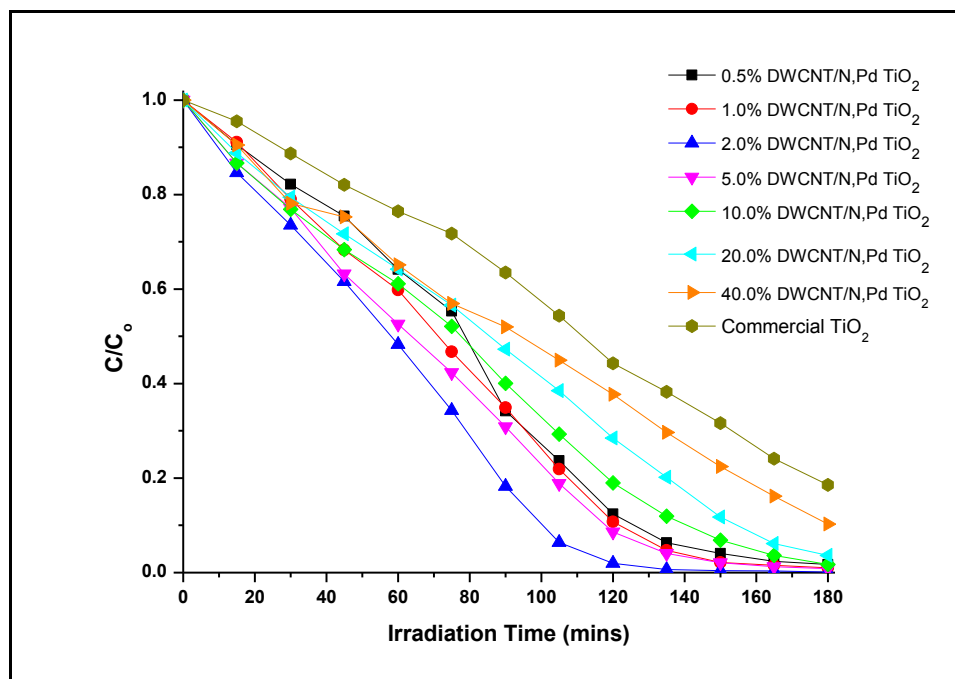


Figure 8.17 Eosin Yellow photodegradation under simulated solar irradiation

UV-Vis scans of the Eosin Yellow photodegradation absorbancies were plotted as a function of irradiation time for the 20.0% DWCNT/N, Pd TiO₂ (**Figure 8.18**) There was a gradual continuous decrease in the absorbancies with increasing irradiation time, confirming the disappearance of the compound. The disappearance of the 515.5 nm absorption band suggests the chromophore responsible for the characteristic colour of the dye was being broken down and no new absorption peaks were formed.

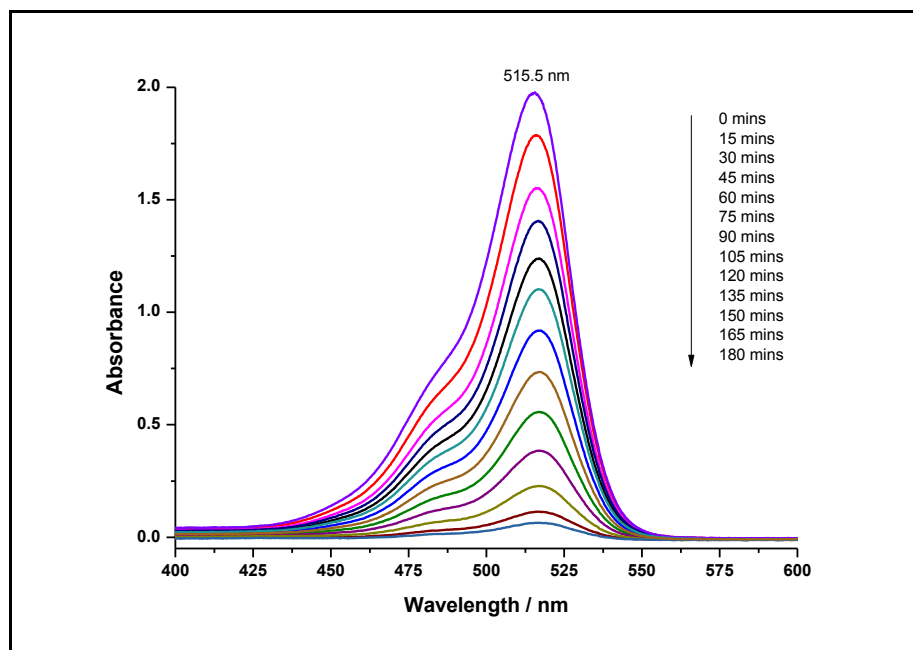


Figure 8.18 Eosin Yellow photodegradation profiles using 20.0% DWCNT/N, Pd TiO₂

The photodegradation of Eosin Yellow in an aqueous suspension of DWCNT/N, Pd TiO₂ nanocomposite catalysts under visible light followed pseudo-first-order kinetics (**Figure 8.19**). The kinetic plots can be fitted into the Langmuir-Hinshelwood model.^{5,15} Incorporation of N and Pd had a profound effect on the degradation efficiency of the nanocomposites. N reduces the TiO₂ band gap by forming states in the inter-gap region whilst Pd can trap photogenerated electrons, thereby enhancing electron-hole separation on the surface of the photocatalyst and increasing photocatalytic activity. DWCNTs have a large electron-storage capacity and may therefore accept photon-excited electrons in the nanocomposites thus reducing or hindering electron-hole recombination.

A rate constant of $3.220 \times 10^{-2} \text{ min}^{-1}$ observed for the 2.0% DWCNT/N, Pd TiO₂ is much higher compared to similar work performed using MWCNT/N, Pd TiO₂ nanocomposites. Similar studies with MWCNTs gave a lower rate constant of $1.34 \times 10^{-2} \text{ min}^{-1}$ for 2.0% MWCNT/N, Pd co-doped TiO₂.²⁵ Thus use of DWCNTs in the nanocomposites led to higher dye-degradation rates compared to MWCNTs. This is probably due to the superior electron storage capability of DWCNTs which led to

reduction in the electron-hole recombination, consequently promoting longer lifetimes for holes that attack the adsorbed dye molecules.

In a study on the photocatalytic activity of MWCNT/TiO₂ nanocomposites, 20% MWCNT/TiO₂ composite catalyst prepared by a sol-gel process gave an apparent rate constant of $7.4 \times 10^{-3} \text{ min}^{-1}$ for 96% degradation of 50 mg/l phenol using visible-light irradiation in 5 h.²⁶ In a different study, 20% MWCNT/TiO₂ nanocomposites were prepared by the sol-gel method and shown to exhibit enhanced methylene blue photodegradation under visible-light irradiation; 0.2 g/l of the photocatalyst applied on 10 mg/l of methylene blue gave a rate constant of $1.0 \times 10^{-3} \text{ min}^{-1}$. The enhancement was attributed to the MWCNTs having excellent charge-transfer ability, the high surface area of the MWCNT/TiO₂ nanocomposites for increased dye adsorption and the formation of Ti–C bonds between CNTs and TiO₂ promoting the visible-light absorption.²⁴ Degradation of methylene blue in an aqueous solution under irradiation of visible light was performed using Cr³⁺, Mg²⁺ and V³⁺ doped CNT/TiO₂ composites prepared by a sol-gel method. Rate constants of $3.92 \times 10^{-3} \text{ min}^{-1}$, $3.22 \times 10^{-3} \text{ min}^{-1}$ and $3.73 \times 10^{-3} \text{ min}^{-1}$, respectively, for each dopant metal ion were observed. A catalyst loading of 1 g/l was used with an initial dye concentration of $1.0 \times 10^{-5} \text{ mol/l}$ and an irradiation period of 2 h.²⁹ In a study on TiO₂ supported on MWCNTs, photocatalytic activity of the materials was elucidated using the photo oxidation of methyl orange under UV (250 W) illumination. In a typical setup, 20 mg of 10% MWCNT/TiO₂ was added to 100 ml of 15 mg/l methyl orange solution and a rate constant value of 0.1299 min^{-1} was observed. The high photocatalytic activity can be ascribed to the high-energy UV radiation used to activate the material as well as possible synergistic effects due to the presence of MWCNTs.³⁰ Anatase TiO₂ nanoparticles were covalently anchored onto acid-treated MWCNTs through a nanocoating-hydrothermal process to obtain TiO₂-MWCNT nanocomposites. The enhanced photocatalytic activity of TiO₂-MWCNT nanocomposites was probed by a photodegradation reaction of methylene blue under visible-light irradiation. A total of 80 mg TiO₂-MWCNTs powder was dispersed in 80 ml of 30 mg/l methylene blue aqueous solution. The suspension was irradiated with a 150 W high-pressure xenon lamp ($\lambda > 420 \text{ nm}$) with continuous stirring and a rate

constant of $2.83 \times 10^{-3} \text{ min}^{-1}$ was observed.¹⁷ Anatase TiO₂ nanoparticles were successfully deposited onto MWCNTs via hydrolysis of titanium isopropoxide in supercritical ethanol. The TiO₂/MWCNT composites were used as photocatalyst for phenol degradation under irradiation of visible light. A 500 W high-pressure Hg lamp with a UV-filter was employed as a light source. In a typical experiment, 40 ml of phenol aqueous solution with a concentration of 50 mg/l was mixed with TiO₂/MWCNT composites (1 g/l) and a doubling of the rate compared to a physical mixture of MWCNTs and TiO₂ was observed.³¹ A photocatalyst based on silver nanoparticles on MWCNT/TiO₂ was successfully prepared by the photo-reduction method. The photocatalytic activity was evaluated by the photocatalytic degradation of reactive brilliant red X-3B dye. The results indicated that the photocatalytic efficiency of MWCNT/TiO₂ increased in the presence of Ag nanoparticles and the photocatalysis reaction followed first-order kinetics. Rate constants of $3.052 \times 10^{-2} \text{ min}^{-1}$ and $2.580 \times 10^{-2} \text{ min}^{-1}$ were reported for the Ag-MWCNT/TiO₂ and MWCNT/TiO₂ nanocomposites, respectively.³² In all these studies, enhancement was mainly attributed to the efficient electron-channelling properties of CNTs and therefore their ability to reduce electron-hole recombination in the nanocomposites. However, the high degradation rates observed in this study are mainly attributed to the use of DWCNTs as supports for the N, Pd TiO₂ resulting in unique pearl-bead-necklace structures.

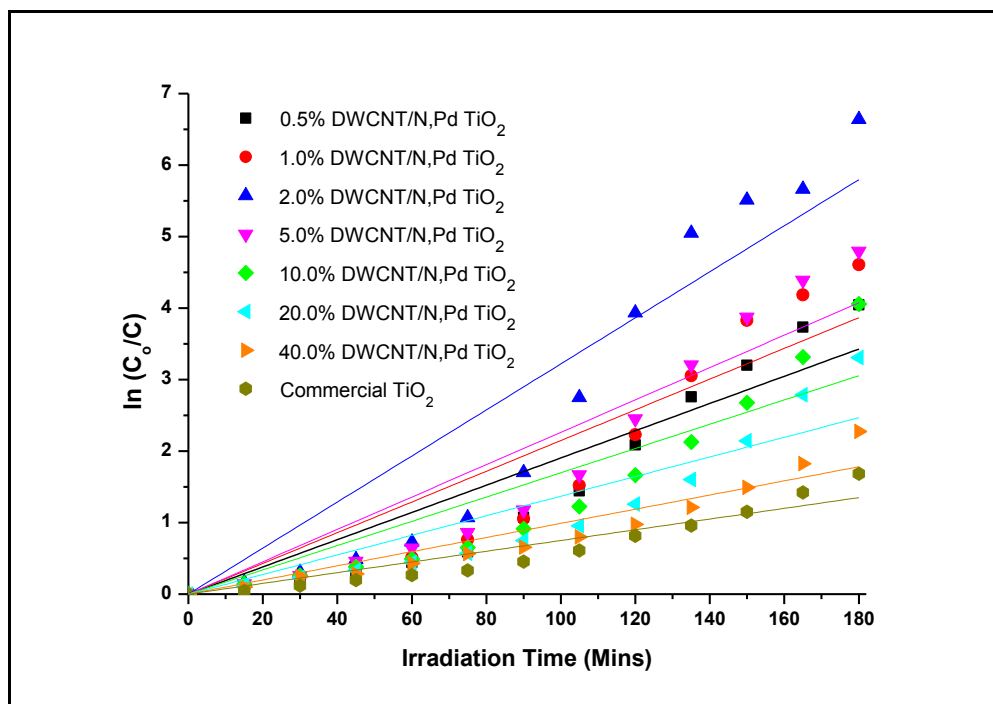


Figure 8.19 Eosin Yellow photodegradation kinetics

There was generally an increase in dye adsorption with increasing amounts of DWCNTs in the nanocomposites (**Table 8.3**). This can be ascribed to their large specific surface area, hollow and double-walled structures. However, there was no correlation between dye adsorption and photodegradation. DWCNTs act as supports for N, Pd TiO₂, promoting even distribution of TiO₂ nanoparticles on the DWCNT surfaces. This reduces particle agglomeration but may also lead to reduced surface area of the nanocomposites if layers of TiO₂ form on the DWCNT surfaces. Uniform coverage of DWCNTs by TiO₂, though difficult to achieve using sol-gel methods, is desirable for increased surface area as well as dye adsorption.

Table 8.3 Dye adsorption, degradation and rate constants

Sample	Dye adsorption (%)	Degradation after 180 min (%)	Rate constant, <i>k</i> (min ⁻¹)
0.5% DWCNT/N, Pd TiO ₂	6.03	98.25	1.904 × 10 ⁻²
1.0% DWCNT/N, Pd TiO ₂	8.10	99.00	2.148 × 10 ⁻²
2.0% DWCNT/N, Pd TiO ₂	9.93	99.87	3.220 × 10 ⁻²
5.0 % DWCNT/N, Pd TiO ₂	6.38	99.17	2.263 × 10 ⁻²
10.0 % DWCNT/N, Pd	11.18	98.27	1.697 × 10 ⁻²
20.0 % DWCNT/N, Pd	8.56	96.34	1.370 × 10 ⁻²
40.0 % DWCNT/N, Pd	19.42	89.72	9.990 × 10 ⁻³
Commercial TiO ₂	5.27	82.85	7.500 × 10 ⁻³

Introduction of N and Pd on TiO₂ and supporting it on DWCNTs led to enhanced visible-light photocatalytic activity for dye degradation, suggesting probable synergistic effects between N, Pd co-doped TiO₂ and DWCNTs. Substitution of O by N in the TiO₂ lattice results in formation of inter-band gap states close to the TiO₂ valence band due to overlap of the O 2p with the N 2p orbitals. This reduces the band gap, favouring the use of less energetic visible light to activate the TiO₂, promoting electrons to the conduction band and creating holes in the valence band.¹¹

Pd metal particles are very effective traps for the electrons due to the formation of a Schottky barrier at the semiconductor-metal interface. At this interface, electrons flow from one material at a higher Fermi level to the other at a lower Fermi level in order to align the Fermi energy levels. In the case of a metal with a higher work function than the n-type semiconductor, such as TiO₂, electrons will flow from the semiconductor into the metal to adjust the Fermi energy levels. This method of reducing electron-hole recombination was found to be effective using platinum-group metals and other noble metal interfaces.³³ DWCNTs act as effective electron-transfer channels since they exhibit high electrical conductivity, high

electron capture ability and high electron storage capacity and are often referred to as super capacitors.³⁴ Formation of bonds between DWCNTs and TiO₂ result in a Schottky barrier being formed at the interface between the DWCNTs and TiO₂, prompting electron transfer from the conduction band of TiO₂ towards the DWCNT surface due to their lower Fermi level. Besides, bonding between DWCNTs and TiO₂ extends the absorption of the nanocomposites into the visible region of the spectrum.²⁴ DWCNTs can also act as photosensitisers, because of their semi-conductive properties, absorbing visible-light radiation and transferring the photogenerated electrons into the conduction band of the N, Pd co-doped TiO₂ particles.³⁵ The generated positively charged DWCNTs can capture electrons from the valence band of N, Pd co-doped TiO₂, leading to the formation of holes.

A mechanism for the enhancement was proposed based on characterisation results and observed photoactivity (**Figure 8.20**). Under UV light illumination, electrons (e⁻) are excited from the valence band (VB) to the conduction band (CB) of TiO₂, creating holes (h⁺) in the VB. In the absence of the DWCNTs or Pd most of these charge carriers would quickly recombine, with only a fraction of the electrons and holes participating in the photocatalytic reaction, resulting in low photoactivity.^{5,36} Introduction of substitutional or interstitial nitrogen in the TiO₂ should result in electrons being excited from the nitrogen 2p orbitals to the TiO₂ conduction band. The generated electrons can be trapped by the doped Pd sitting on the TiO₂ surface, leading to enhanced electron-hole separation.¹¹ In the presence of DWCNTs, electrons can also be shuttled freely along their conducting network resulting in a long-lived charge-separated state between electrons and holes. DWCNTs being sensitiser, can also inject electrons into the TiO₂ conduction band under visible-light irradiation.^{24,26} These electrons can be trapped by the Pd triggering the formation of very reactive superoxide radicals. The holes scavenge surface-adsorbed water or hydroxyl molecules generating highly reactive hydroxyl radicals. On the other hand, the electrons scavenge the oxygen molecules to form very reactive superoxide radicals, which in the presence of water molecules result in the formation of more hydroxyl radicals. The highly oxidising radicals can degrade organic compounds including dyes such as EY used in the present study.

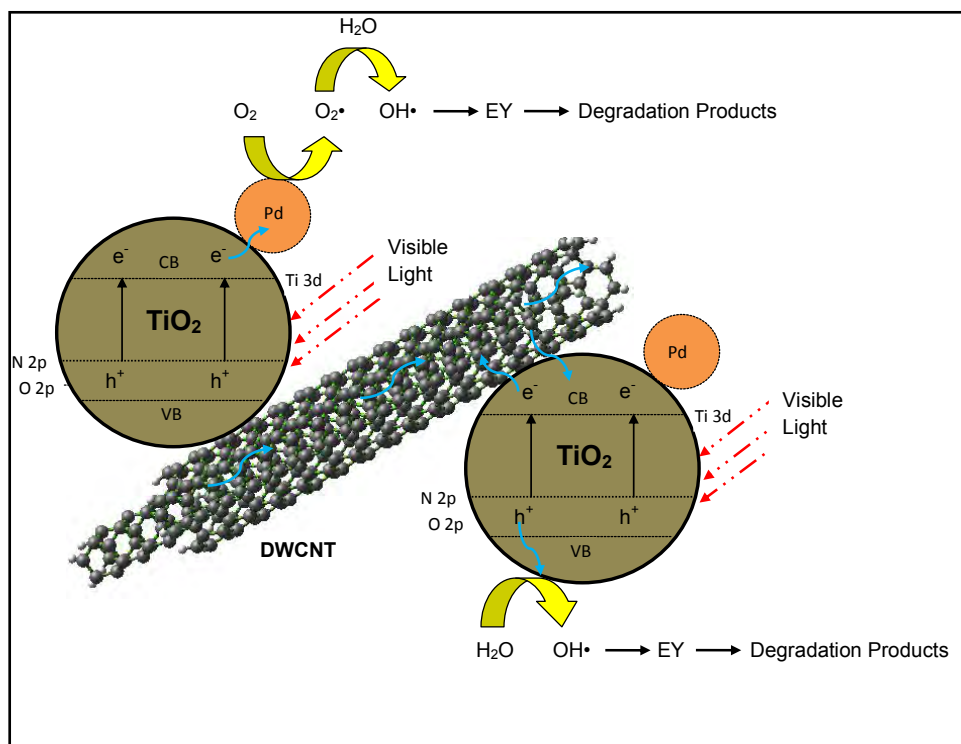


Figure 8.20 Proposed mechanisms for the photocatalytic enhancement

8.5 CONCLUSION

Pearl-bead-necklace-structured DWCNT/N, Pd co-doped TiO₂ nanocomposites were synthesised by a modified sol-gel method and characterised by SEM, EDS, TEM, XRD, UV-Vis, Raman, FT-IR and TGA measurements. Addition of DWCNTs to N, Pd co-doped TiO₂ resulted in modification of the morphology and optical properties of the materials as well as enhancement of the photocatalytic activity towards dye degradation. N doping reduces the TiO₂ band gap whilst Pd is an effective electron trap. Formation of linkages between DWCNTs and N, Pd TiO₂ is a critical factor for enhancing the photocatalysis. The ability of DWCNTs and Pd to accept electrons and transfer them to suitable electron acceptors highlights their mediating roles in the charge-transfer process. The high electron-storage ability of DWCNTs plays an important role in reducing electron-hole recombination and improving the light-energy-harvesting performance of the nanocomposites for solar light photodegradation applications. DWCNTs act as dispersing agents in the nanocomposite systems, reducing N, Pd co-doped TiO₂ agglomeration and

inducing synergistic effects on the photocatalytic properties. The photocatalytic enhancement was found to be limited and only effective at low DWCNT:Ti ratio of 2.0% by weight. DWCNT loadings of greater than 2.0% resulted in lower efficiency. DWCNT/N, Pd co-doped TiO₂ nanocomposites are relevant promising candidates for addressing some of the fundamental issues in many practical applications including the removal of organic pollutants from water.

8.6 REFERENCES

1. Kant R. (2012). Adsorption of dye eosin from an aqueous solution on two different samples of activated carbon by static batch method. *J. Water Resour. Prot.* 4, 93 – 98.
2. Chiang H.M., Chen T.C., Pan S.D. and Chiang H.L. (2009). Adsorption characteristics of Orange II and Chrysophenine on sludge adsorbent and activated carbon fibers. *J. Hazard. Mater.* 161, 1384 – 1390.
3. Pandit P. and Basu S. (2004). Removal of ionic dyes from water by solvent extraction using reverse micelles. *Environ. Sci. Technol.* 38, 2435 – 2442.
4. Ge M., Li J. W., Liu L. and Zhou Z. (2011). Template-free synthesis and photocatalytic application of rutile TiO₂ hierarchical nanostructures. *Ind. Eng. Chem. Res.* 50, 6681 – 6687.
5. Chong M.N., Jin B., Chow C.W.K. and Saint C. (2010). Recent developments in photocatalytic water treatment technology: A review. *Water Res.* 44, 2997 – 3027.
6. Zhang J., Wang Y., Jin Z., Wu Z. and Zhang Z. (2008). Visible-light photocatalytic behavior of two different N-doped TiO₂. *Appl. Surf. Sci.* 254, 4462 – 4466.
7. Asahi R., Morikawa T., Ohwaki T., Aoki K. and Taga Y. (2001). Visible-light photocatalysis in nitrogen-doped titanium oxides. *Sci.* 293, 269 – 271.

8. Qin H.L., Gu G.B. and Liu S. (2008). Preparation of nitrogen-doped titania using sol-gel technique and its photocatalytic activity. *Mater. Chem. Phys.* 112, 346 – 352.
9. Joung S.K., Amemiya T., Murabayashi M. and Itoh K. (2006). Relation between photocatalytic activity and preparation conditions for nitrogen-doped visible light-driven TiO₂ photocatalysts. *Appl. Catal. A: Gen.* 312, 20 – 26.
10. Cong Y., Zhang J., Chen F., Anpo M. and He D. (2007). Preparation, photocatalytic activity, and mechanism of nano-TiO₂ co-doped with nitrogen and iron (III). *J. Phys. Chem. C* 111, 10618 – 10623.
11. Kuvarega A.T., Krause R.W.M and Mamba B.B. (2011). Nitrogen/Palladium-Codoped TiO₂ for Efficient Visible Light Photocatalytic Dye Degradation. *J. Phys. Chem. C* 115, 22110 – 22120.
12. Wang W., Serp P., Kalck P., Silva C.G. and Faria J.L. (2008). Preparation and characterization of nanostructured MWCNT-TiO₂ composite materials for photocatalytic water treatment applications. *Mater. Res. Bull.* 43, 958 – 967.
13. Feng J.M., Wang R., Li Y.L., Zhong X.H., Cui L., Guo Q.J. and Hou F. (2010). One-step fabrication of high quality double-walled carbon nanotube thin films by a chemical vapour deposition process. *Carbon* 48, 3817 – 3824.
14. Matsumoto K., Murakami T., Isshiki T., Kisoda K. and Harima H. (2007). Synthesis and Raman study of double-walled carbon nanotubes. *Diamond Relat. Mater.* 16, 1188 – 1191.
15. Peining Z., Sreekumaran A.N., Shengyuan Y. and Ramakrishna S. (2011). TiO₂-MWCNT rice grain-shaped nanocomposites: Synthesis, characterization and photocatalysis. *Mater. Res. Bull.* 46, 588 – 595.

16. Gao B., Chen G.Z. and Puma G.L. (2009). Carbon nanotubes/titanium dioxide (CNTs/TiO₂) nanocomposites prepared by conventional and novel surfactant wrapping sol-gel methods exhibiting enhanced photocatalytic activity. *Appl. Catal. B: Environ.* 89, 503 – 509.
17. Wang Q., Yang D., Chen D., Wang Y. and Jiang Z. (2007). Synthesis of anatase titania-carbon nanotubes nanocomposites with enhanced photocatalytic activity through a nanocoating-hydrothermal process. *J. Nanopart. Res.* 9, 1087 – 1096.
18. Luca L.D., Donato A., Santangelo S., Faggio G., Messina G., Donato N.G. and Neri G. (2012). Hydrogen sensing characteristics of Pt/TiO₂/MWCNTs composites. *Int. J. Hydrogen Energ.* 37, 1842 – 1851.
19. Lee Y.D., Lee H.J., Han J.H., Yoo J.E., Lee Y.H., Jai Kyeong Kim J.K., Nahm S. and Ju B.K. (2006). Synthesis of double-walled carbon nanotubes by catalytic chemical vapour deposition and their field emission properties. *J. Phys. Chem. B* 110, 5310 – 5314.
20. Flahaut E., Laurent Ch. and Peigney A. (2005). Catalytic CVD synthesis of double and triple-walled carbon nanotubes by the control of the catalyst preparation. *Carbon* 43, 375 – 383.
21. Panagiotopoulou P. and Kondarides D.I. (2004). Effect of morphological characteristics of TiO₂-supported noble metal catalysts on their activity for the water–gas shift reaction. *J. Catal.* 225, 327 – 336.
22. Jiang G, Zheng X., Wang, Y. Li T. and Sun X. (2011). Photo-degradation of methylene blue by multi-walled carbon nanotubes/TiO₂ composites. *Powder Technol.* 207, 465 – 469.
23. Zhang K. and Oh W.C. (2010). Kinetic study of the visible light-induced sonophotocatalytic degradation of MB solution in the presence of Fe/TiO₂-MWCNT catalyst. *Bull. Korean Chem. Soc.* 31, 1589 – 1595.

24. Tian L., Ye L., Deng K. and Zan L. (2011). TiO₂/carbon nanotube hybrid nanostructures: Solvothermal synthesis and their visible light photocatalytic activity. *J. Solid State Chem.* 184, 1465 – 1471.
25. Kuvarega A.T., Krause R.W.M. and Mamba B.B. (2012). Multiwalled carbon nanotubes decorated with nitrogen, palladium co-doped TiO₂ (MWCNT/N, Pd co-doped TiO₂) for visible light photocatalytic degradation of Eosin Yellow in water. *J. Nanopart. Res.* 14, 776. DOI 10.1007/s11051-012-0776-x.
26. Wang W., Serp P., Kalck P. and Faria J.L. (2005). Visible light photodegradation of phenol on MWNT-TiO₂ composite catalysts prepared by a modified sol-gel method. *J. Mol. Catal. A: Chem.* 235, 194 – 199.
27. Akhavan O., Azimirad R., Safad S. and Larijani M.M. (2010). Visible light photo-induced antibacterial activity of CNT–doped TiO₂ thin films with various CNT contents. *J. Mater. Chem.* 20, 7386 – 7392.
28. Yu Y, Yu J.C., Yu J.G, Kwok Y.C., Che Y.K., Zhao J.C., Ding L., Geg W.K. and Wong P.K. (2005). Enhancement of photocatalytic activity of mesoporous TiO₂ by using carbon nanotubes. *Appl. Catal. A: Gen.* 289, 186 – 196.
29. Chen M.L., Bae J.S., Yoon H.S., Lim C.S. and Oh W.C. (2011). The photodegradation effect of organic dye for metal oxide (Cr₂O₃, MgO and V₂O₃) treated CNT/TiO₂ composites. *Bull. Korean Chem. Soc.* 32, 815 – 820.
30. Hu C., Zhang R., Xiang J., Liu T., Li W., Li M., Duo S. and Wei F. (2011). Synthesis of carbon nanotube/anatase titania composites by a combination of sol-gel and self-assembly at low temperature. *J. Solid State Chem.* 184, 1286 – 1292.
31. An G., Ma W., Sun Z., Liu Z., Han B., Miao S., Miao Z. and Ding K. (2007). Preparation of titania/carbon nanotube composites using supercritical

- ethanol and their photocatalytic activity for phenol degradation under visible light irradiation. *Carbon* 45, 1795 – 1801.
32. Wang S., Gong Q., Zhu Y. and Liang J. (2009). Preparation and photocatalytic properties of silver nanoparticles loaded on CNT/TiO₂ composite. *Appl. Surf. Sci.* 255, 8063 – 8066.
 33. Woan K., Pyrgiotakis G. and Sigmund W. (2009). Photocatalytic carbon-nanotube–TiO₂ composites. *Adv. Mater.* 21, 2233 – 2239.
 34. Kongkanand A. and Kamat P.V. (2007). Electron storage in single wall carbon nanotubes. Fermi level equilibration in semiconductor–SWCNT suspensions. *ACS Nano* 1, 13 – 21.
 35. Chen M.L, Zhang F.J., Oh W.C. (2009). Synthesis, characterization, and photocatalytic analysis of CNT/TiO₂ composites derived from MWCNTs and titanium sources. *New Carbon Mater.* 24, 159 – 166.
 36. Yuan Y. Gonghu L., Shannon C., Richard M.L., and Kimberly A.G. (2008). Photoreactive TiO₂/carbon nanotube composites: Synthesis and reactivity. *Environ. Sci. Technol.* 42, 4952 – 4957.

CHAPTER 9

EXFOLIATED GRAPHITE/TiO₂ (EG-TiO₂) NANOCOMPOSITES FOR THE PHOTOCATALYTIC DEGRADATION OF EOSIN YELLOW[†]

Despite the enhanced photoactivity observed with CNT/TiO₂ nanocomposite materials for dye degradation, CNTs are expensive and difficult to synthesise. Exfoliated graphite nanosheets are increasingly attracting scientific and technological interest by virtue of their significant advantages over other carbon materials. Experimental results have revealed that exfoliated graphite is a good absorbent, especially for materials with large molecular size and weak polarity. This chapter highlights the synthesis of exfoliated graphite/TiO₂ nanocomposites for application in dye photodegradation.

9.1 INTRODUCTION



Due to the limited amount of potable water, polluted water must be remediated for re-use or before being re-introduced into the environment. The main aim of treating drinking water is to produce water that is safe (without pathogenic microbes and toxins), attractive (free from colour, taste and odour) and to avoid accumulation of solids, corrosion and after-growth of bacteria in the distribution and transport pipeline.¹ Industrial or agricultural wastewaters, rich in organic chemicals, are potential sources of pollution of natural water bodies. They contain a wide range of toxic compounds, hazardous to the environment as well as to human health, which need special treatment procedures for their removal.² Due to the rising demand for synthetic organic substances, their massive production brought about an inevitable increase in the occurrence and concentration of

[†] Contents of this chapter were based on:

Ndlovu T., Kuvarega A. T., Arotiba A.O., Sampath S., Krause R.W.M. and Mamba B.B. Exfoliated graphite/titanium dioxide nanocomposites for the photodegradation of eosin yellow. *Ind. Eng. Chem. Res.* (under review)

organic contaminants in effluents, sewage and sewage sludge,³ which has led to the drastic deterioration of the water quality in the world, South Africa included.⁴ Azo dyes are common in the textile and paper manufacturing industrial effluent but they are difficult to degrade biologically. If these are not removed from the treated wastewater, they cause formidable contamination of the water, as colour tends to persist even after conventional treatment.⁵ In order to protect the environment from pollution by various chemical materials, adsorption/absorption and decomposition are pointed out to be important in the remediation of water. For the former function, activated carbons have played a great role and for the latter titanium dioxide (TiO₂) with anatase-type structure which has marked photocatalytic activity has widely been studied.⁶

Carbon-carbon composite materials are considered indispensable for use in advanced technologies due to the combination of their low density with the unique thermal, mechanical and biomedical properties.⁷ Exfoliated graphite (EG) is a low-density material which has excellent properties such as compressibility, resilience, thermal stability and corrosion resistance.⁸ It is obtained by subjecting the bisulphate ion intercalated graphite to thermal shock.⁹ The process results in a rapid phase transition of the material resulting in puffed up, very low density graphite.⁹⁻¹²

Exfoliated graphite has been mainly used as a raw material for making flexible graphite sheets. Recently, EG has attracted research attention because of its high sorption capacity¹³ and Kang *et al.*, reported that EG is a good absorbent especially for materials with large molecular size and weak polarity.⁸ Several studies have suggested that the space among the worm-like particles of EG plays the most important role in the sorption of heavy oil.¹⁴⁻¹⁷

The development of carbon nanostructure composites is another emerging area that has led to the design of photocatalysts with tailored properties.¹⁸ The superior physical, mechanical and multifunctional properties of EG including its ability to capture and shuttle electrons, provides a unique opportunity to develop catalyst with multifunctional characteristics. This has prompted an investigation into its

application in photocatalytic pollutant removal from water. Currently, there are no reports on the synthesis of EG/TiO₂ nanocomposites and their applications in visible light driven photodegradation of pollutants. Optimisation of EG usage in various applications including water purification requires assembling of nanostructures such as semiconductor photocatalysts onto their surfaces. A combination of EG and TiO₂ is expected to deliver exceptional performances in removal of organic pollutants from water. In this study EG/TiO₂ nanocomposites were prepared aiming to utilize the excellent electron conductivity of EG to lengthen the lifetime of photogenerated charge carriers in the semiconductor and hence improve the photoactivity.

9.2 EXPERIMENTAL DETAILS

9.2.1 Preparation of Exfoliated Graphite

Natural graphite (Sigma Aldrich) was soaked in H₂SO₄:HNO₃ (3:1) (Merck, SA) acid mixture and left overnight. This was washed several times with deionised water until the water had no sulphate ions and the pH was neutral. The product, graphite intercalated compound (GIC), was dried in an oven (100°C). The GIC was subjected to thermal shock at 800 °C for about 30 seconds forcing the intercalated material out of the graphite lattice, thereby rupturing the layers. This procedure resulted in the puffed material called exfoliated graphite (EG) that is characterised by a very low density of 0.0068 g/ml.

9.2.2 Preparation of Exfoliated Graphite/ TiO₂ nanocomposite

The Exfoliated Graphite/ TiO₂ nanocomposite was prepared as follows; EG (1g) was sonicated in 2-isopropanol (50 ml) for 15 minutes. Titanium (IV) isopropoxide (10 ml) (Merck, SA) was then added and the mixture was left to stir for 30 minutes. Formic acid (13 ml) was gradually added while stirring and this mixture was left to stir for two and a half hours. The mixture was then allowed to age for two hours after which it was repeatedly washed with 2-propanol (Merck, SA) and then distilled water. After filtration, the residue was dried at 100°C overnight. This

product was named EG/TiO₂. This material was used for the photodegradation of eosin yellow under visible light after calcining at 400°C.

9.2.3 Material characterisation

The synthesised materials were characterised using various techniques as described in **Section 3.6**. In addition Brauner Emmett Teller (BET) surface area measurements were performed on a Micromeritics TriStar II. Prior to the analysis the samples were degassed in a vacuum at 150°C for an hour reaching a final pressure of 1 mm Hg.

9.2.4 Evaluation of Photocatalytic Activity

The photocatalytic performances of the materials were evaluated for the degradation of Eosin Yellow (EY) under simulated solar irradiation. Experimental details are given in **Section 3.7**.

9.3 RESULTS AND DISCUSSION



9.3.1 Characterisation of EG and EG-TiO₂

The preparation of EG and EG-TiO₂ was followed by characterisation using SEM, TEM, XRD and Raman spectroscopy. SEM micrographs show that the TiO₂ particles had a spherical morphology and they were evenly distributed on the EG layers as shown in **Figure 9.1**.

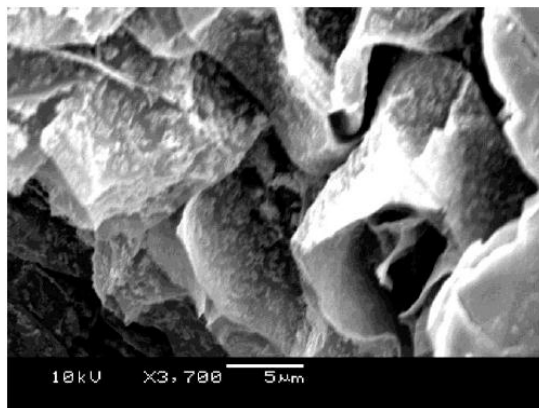


Figure 9.1 SEM image of EG-TiO₂

Figure 9.2(a) presents a typical TEM image of EG/TiO₂ sample clearly indicating many small TiO₂ clusters uniformly deposited on the surface of EG with little agglomeration. The TiO₂ nanoparticles attached onto the surface of EG were less than 10 nm as shown in **Figure 9.2(b)**.

The SEM and TEM observations suggest that a complete conduction network could exist throughout the EG-TiO₂ composite, connecting the TiO₂ particles to the conducting EG. This would allow the illuminated TiO₂ particles to inject their photogenerated electrons into the EG sheets, reducing the charge recombination thereby enhancing dye photodegradation.

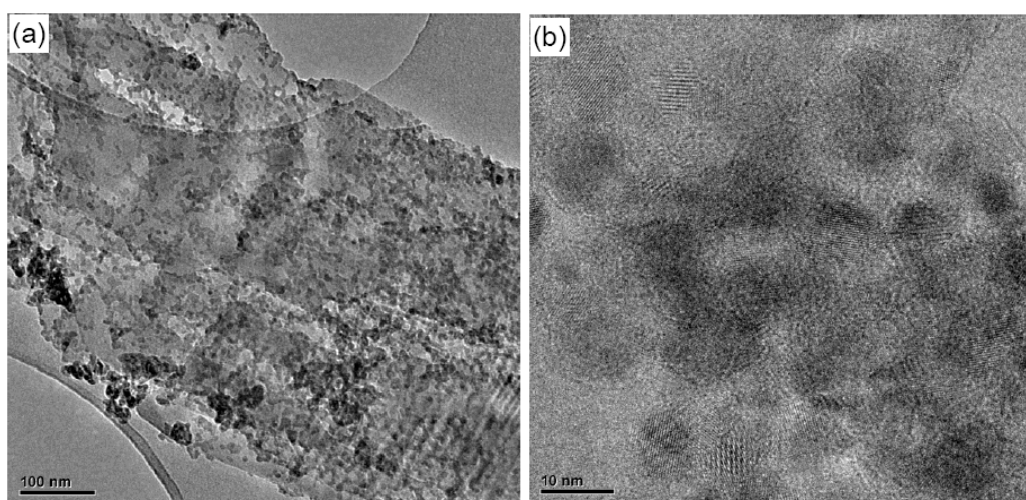


Figure 9.2 TEM images of EG-TiO₂ at different magnifications

XRD analysis was performed to investigate the presence of EG and TiO₂ in the composites. XRD pattern of the EG-TiO₂ photocatalyst prepared revealed the co-existence of anatase-type TiO₂ with graphite as shown in **Figure 9.3(a)**. Peaks at 2θ values of 25.3, 37.6, 48.2, 53.9, 54.8, 62.7 and 75.2 corresponding to the (101), (004), (200), (105), (211), (204) and (215) planes, respectively, can be indexed to the anatase phase of TiO₂. There is a possibility of overlap of the intense peak of the EG peak with the anatase (101) reflection at about $2\theta = 25.6^\circ$.¹⁹ This overlap can result in shielding of either the EG or TiO₂ peak.

Raman spectra of EG/TiO₂ are presented in **Figure 9.3(b)**. The Raman response of graphite typically feature two distinct peaks: the D (disorder) band centred roughly at 1350 cm⁻¹ and the G (graphitic) peak at 1580 cm⁻¹ corresponding to the first-order scattering of the E_{2g} mode.²⁰ The D peak arises from the disruption of the symmetrical hexagonal graphitic lattice as a result of internal structural defects, edge defects, and dangling bonds. The peak can shift depending on the adsorbed species that cause these defects. The G peak is the response to the in-plane stretching motion of symmetric sp₂ C-C bonds.²¹ The high intensity G band observed for the EG/TiO₂ composite confirmed the presence of sp₂ C-C bonds whilst the low intensity D band revealed very little disruption of the graphitic lattice through incorporation of TiO₂.²² Exfoliation led to very little disruption of the hexagonal lattice and this correlates well with the XRD observations.

The presence of TiO₂ on the EG/TiO₂ composite was also confirmed by Raman analysis. Raman active fundamental modes at 144 cm⁻¹ (E_g), 197 cm⁻¹ (E_g), 397 cm⁻¹ (B_{1g}), 518 cm⁻¹ (A_{1g}+B_{1g}) and 640 cm⁻¹ (E_g) confirm the presence of anatase TiO₂. Well-resolved Raman bands observed at 142, 395, 515, and 636 cm⁻¹ are diagnostic of the anatase phase of TiO₂.^{23,24}

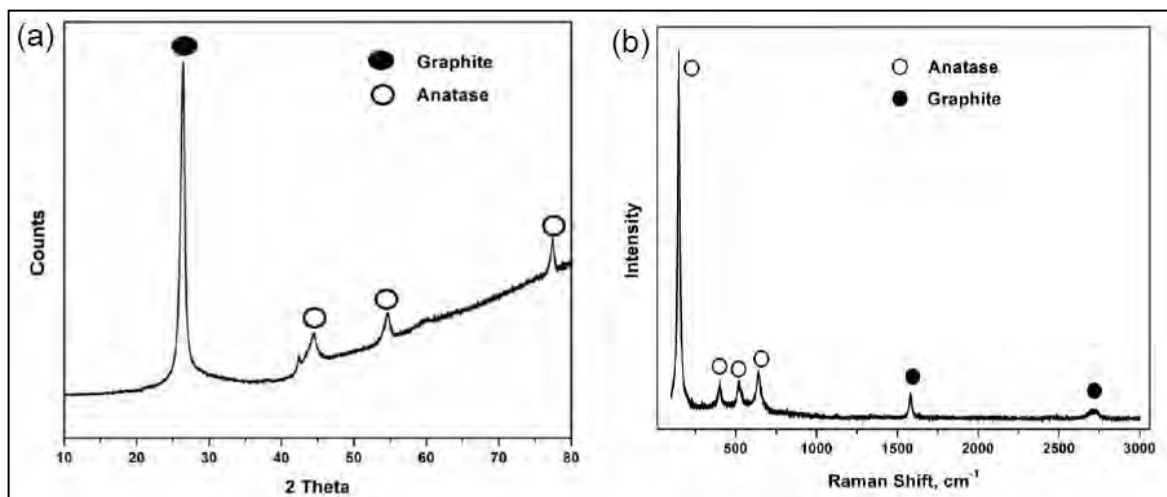


Figure 9.3 (a) XRD and (b) Raman spectra of EG-TiO₂

Generally, a catalyst with high specific surface area and big pore volume for pollutant adsorption is attractive to the enhancement of catalytic performance. The effect of TiO₂ incorporation on the pore volume, pore size and BET surface areas of the samples was investigated by the adsorption-desorption measurement (Table 9.1).

Table 9.1 BET surface area, Pore volume and Pore size

	EG	EG/TiO ₂
BET Surface Area	24.3018 m ² /g	35.2600 m ² /g
Pore Volume	0.070338 cm ³ /g	0.097027 cm ³ /g
Pore Size	11.57742 nm	11.00705 nm

The EG/TiO₂ samples showed increased pore volumes, pore sizes and BET surface areas compared to the EG sample. This can be ascribed to the formation of TiO₂ nano crystallites on the high surface area EG. Such aggregated porous structures with increased surface area might be extremely useful in the photocatalytic process since they might provide efficient transport pathways to reactant and product molecules.^{20,25} They also favourably adsorb pollutant

molecules which may lead to enhanced photoactivity. Surface area of EG was relatively small (20-50 m²/g, usually near 30 m²/g), but due to very large specific pore volume, EG is an oleophilic adsorbent with extremely high capacity.⁷

9.3.2 Photodegradation studies

The EG, EG-TiO₂ and commercial TiO₂ were evaluated for the photodegradation of a model dye, eosin yellow (EY). EG-TiO₂ showed superior photodegradation performance compared to EG and the commercial TiO₂ sample (Degussa P25) (**Figure 9.4(b)**). Increased efficiency in the EG-TiO₂ nanocomposite could be explained by uniform attachment of TiO₂ on the EG as shown in the SEM and TEM images (**Figure 9.1 and 9.2**). Although the precise nature of the EG-TiO₂ interaction is not fully understood, it is believed that the affinity of residual carboxylic acid groups of EG toward the surface hydroxyl groups of TiO₂ strengthens their interaction.²¹ This results in reduced TiO₂ particle agglomeration, increased surface area and thus greater pollutant adsorption capability on the EG-TiO₂ nanocomposites (**Figure 9.4(a)**).

EG has an exceptionally good electron channelling property because of its extensive π electron system. Formation of bonds between the TiO₂ and the EG promotes electron transfer from the TiO₂ to the EG, with the EG acting as electron trapping sites. This enhances the lifetime of holes which participates in pollutant oxidative degradation. EG may also function as a support as well as a centre for the deposition and growth of hydrolysis products of the TiO₂. Dark adsorption studies on EG-TiO₂ showed very minimal changes in the dye concentration over a period of 3 hours. This confirmed that decrease in dye concentration upon visible light irradiation was triggered by the presence of TiO₂ on the EG.

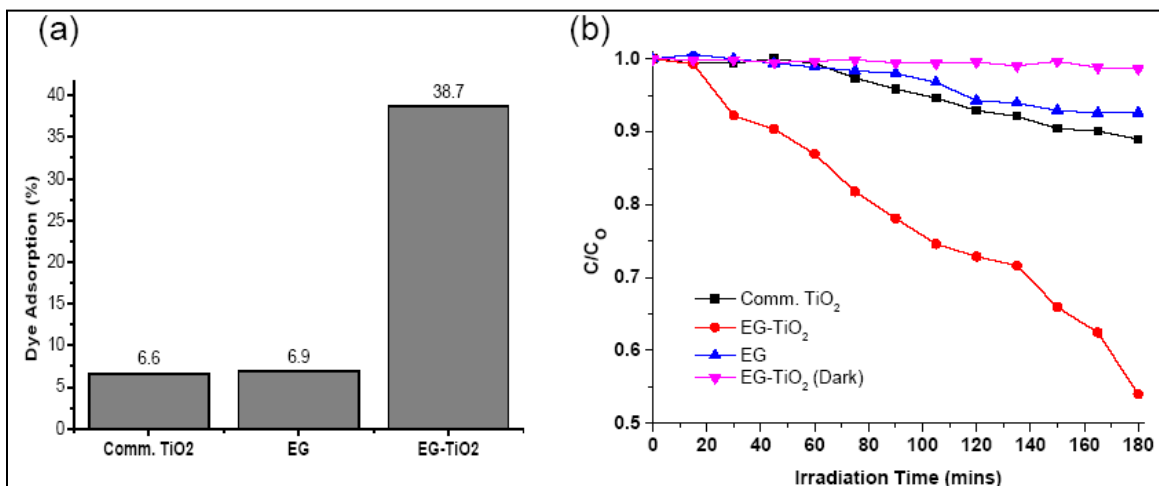


Figure 9.4 (a) Percentage dye adsorption (b) normalised photocatalytic degradation trend

A dye removal efficiency of 46.01% under simulated solar irradiation was observed for the EG-TiO₂ nanocomposite compared to 11.01% and 7.42% for the commercial Degussa P25 and EG respectively. For EG-TiO₂ and TiO₂, the reduction in the dye concentration was attributed to photocatalytic degradation due to the presence of TiO₂ which is a known photocatalyst.²⁶ The degradation efficiency for TiO₂ was lower compared to EG-TiO₂ and this is not surprising since TiO₂ has been shown to suffer from recombination of the electrons and holes which are essential for photodegradation.²⁶ The four fold increase in photoactivity for the EG-TiO₂ compared to the EG and P25 was ascribed to the use of TiO₂ supported on EG. This is because EG is highly conductive which improves charge collection facilitated by the intimate contact between EG and TiO₂, a phenomenon observed for graphene oxide and TiO₂ nanocomposite.²¹ TiO₂ also has polar OH groups which may enhance the interaction on the dye molecules with the EG-TiO₂. This could have led to the high removal/degradation capacity observed for the EG-TiO₂ which was probably due to the electron trapping and channelling effects of EG on the photodegradation process. The use of EG-TiO₂ in the presence of eosin yellow for three hours in the dark resulted in dye removal efficiency of 1.4%, which is much lower than when the solution was irradiated. This suggests that the reduction in the dye concentration on illumination was due to photodegradation and not adsorption. Reduction in the absorbance of the EY peak at 515.5 nm

confirmed the degradation of the dye as the chromophore responsible for that peak gradually disappeared.

Composites of carbon nanotubes and TiO₂ have been shown to increase the photo conversion efficiency of TiO₂ by a factor of 2. Graphitic carbons of various structures have also been found to enhance electron transport in their composites with TiO₂,²¹ hence the investigation of EG-TiO₂ in this study. The three-dimensional structure of EG absorbs strongly in the visible region, thus promoting the use of visible light, and not UV light, for photodegradation of pollutants in water. The use of visible light is a great advantage as it is highly abundant from the sun. Zhang *et al.*, found out that a composite of Degussa P25 TiO₂ and graphene is a good candidate for dye degradation.²⁷ It has also been demonstrated that introducing reduced graphene oxide into a semiconductor nanoparticle matrix boosts its photo electrochemical and photocatalytic performance. Since the EG is composed of a larger number of graphene sheets, the same behaviour may be expected, as supported by results from the current studies. However, the mechanism behind such enhanced performance has not been fully explored.²¹

The photodegradation of EY obeyed the Langmuir – Hinshelwood first order kinetics, with fairly good linear relationships for all the samples (**Figure 9.5**).^{23,28} The rate constant for EG-TiO₂ was much higher than that for EG and commercial Degussa P25. The presence of EG had a profound effect on the degradation efficiency of the nanocomposites. Electron transfer might play an important role in EY photodegradation reaction, based on the structure of EG. EG is a multifunctional inorganic material with many functional groups and loose carbon sheets, which may facilitate the anchoring and dispersion of TiO₂ particles. The graphite sheets have extraordinary electron transporting properties and high electron conductivity.

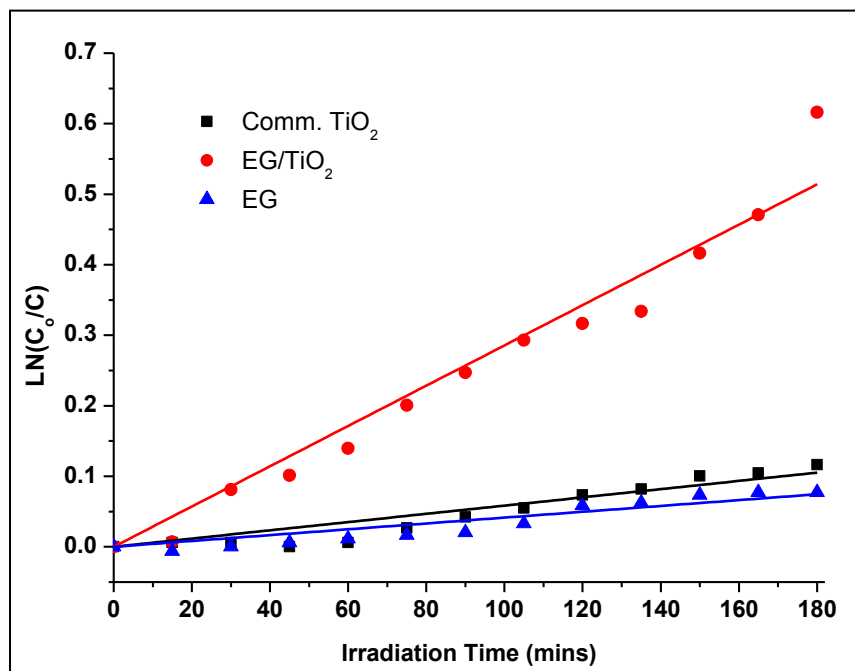


Figure 9.5 Kinetics of EY degradation

There was strong correlation between dye adsorption and photodegradation as observed for the EG-TiO₂ which adsorbed 38.68% of the dye and showed a degradation efficiency of 46.01%, a value higher than that for Degussa P25 TiO₂ which showed the lowest adsorption of only 6.55 % and a dye removal of 11.01% (**Table 9.2**). EG showed a dye adsorption of 6.92%, with the lowest dye removal percentage of 7.42%. This can be explained by the high sorption capacity and good adsorption properties of the EG-TiO₂. The space among worm-like particles of EG has been reported to play an important role in the sorption of heavy oil.¹⁴⁻¹⁷ Supporting TiO₂ on EG resulted in about 4.9 times increase in the photodegradation rate compared to the commercial TiO₂.

Table 9.2 Dye adsorption, dye degradation and rate constants for EG-TiO₂ and Degussa P25

Sample	Dye Adsorption (%)	Dye degradation (%)	Rate constant, k (min ⁻¹)
Comm. TiO ₂	6.55	11.01	5.84 x 10 ⁻⁴
EG-TiO ₂	38.67	46.01	2.86 x 10 ⁻³
EG	6.92	7.42	4.14 x 10 ⁻⁴

Under visible light illumination EG can act as photosensitisers or electron channelling materials. As photosensitisers, photo excited electrons from the EG are injected to the conduction band of TiO₂ through the Ti–C bonds. The generated positively charged EG will in turn capture electrons from the valence band of TiO₂ resulting in the formation of holes on the TiO₂. Holes can react with surface hydroxyl ions or water to produce hydroxyl radicals (OH[•]), while electrons can react with adsorbed molecular oxygen yielding superoxide radicals (O₂^{•-}), which in the presence of water molecules, form highly reactive OH[•] radicals. The highly oxidising OH[•] radicals are capable of degrading the EY to carbon dioxide and water.¹⁹ Alternatively irradiation of TiO₂ with sufficient photons will excite electrons from the valence band to the conduction band, creating holes in the conduction band. The photo generated electrons may then be channelled towards the EG, forming an interior electric field of charge space within the nanocomposite. This can separate the photogenerated charge pairs resulting in reduction in recombination rate and enhanced photo activity (**Figure 9.6**).

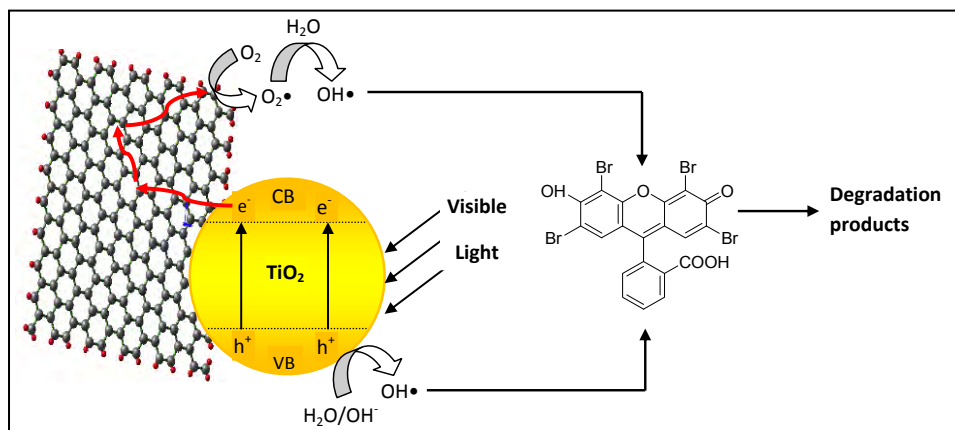


Figure 9.6 Illustration of the photocatalytic activity of the EG-TiO₂ nanocomposite for the degradation of eosin yellow under visible light irradiation.

This improvement in the photo activity suggests the possible application of EG-TiO₂ for the degradation of dyes as well as other organic compounds such as persistent organic compounds (POPs). Due to the low density of EG, this material floats on the surface of water. When stirred it is evenly distributed but immediately floats when stirring stops. This implies that the recovery of this material from water can be an easy process, unlike the powder TiO₂, which needs to be filtered.

9.4 CONCLUSION

TiO₂ nanoparticles were deposited onto the layers of EG using a sol-gel method to obtain a floating nanocomposite referred to as EG-TiO₂. The TiO₂ nanoparticles were evenly distributed on the EG surface with a particle size of less than 10 nm. Illuminating a solution containing eosin yellow dye, with simulated solar light, in the presence of the nanocomposite resulted in enhanced dye removal efficiency compared to using EG and TiO₂ individually. TiO₂ is a known photocatalyst while the role of EG could be electron trapping and channelling which helps reduce electron-hole recombination making the composite a better photocatalyst.

9.5 REFERENCES

1. Mamba B.B., Rietveld L.C. and Verberk J.Q.J.C. (2008). SA Drinking Water Standards under the microscope. *The Water Wheel*, 24 – 27.
2. Santi C.A., Cortes S., D'Acqui L.P., Sparvoli E. and Pushparaj B. (2008). Reduction of organic pollutants in Olive Mill Wastewater by using different mineral substrates as adsorbents. *Bioresour. Technol.* 99, 1945 – 1951.
3. Rogers H.R. (1996.) Sources, behaviour and fate of organic contaminants during sewage treatment and sewage sludges. *Sci. Total Environ.* 185, 3 – 26.
4. Mhlanga S.D., Mamba B.B., Krause R.W.M. and Malefetse T.J. (2007). Removal of organic contaminants from water using nanosponge cyclodextrin polyurethanes. *J. Chem. Technol. Biot.* 388, 382 – 388.
5. Li M., Li J.T. and Sun H.W. (2008). Decolorizing of azo dye Reactive red 24 aqueous solution using exfoliated graphite and H₂O₂ under ultrasound irradiation. *Ultrason. Sonochem.* 15, 717 – 723.
6. Tsumura T. (2002). Composites between photoactive anatase-type TiO₂ and adsorptive carbon. *Appl. Surf. Sci.* 196, 429 – 436.
7. Sementsov Y.I., Prikhodko G.P., Revo S.L., Melezhyk A.V., Pyatkovskiy M.L. and Yanchenko V.V. (2004). Synthesis and structural peculiarities of the exfoliated graphite modified by carbon nanostructures. *Hydrogen Materials Science and Chemistry of Carbon Nanomaterials* 405 – 414.
8. Kang .F, Zheng Y.P., Wang H.N., Nishi Y. and Michio I. (2002). Effect of preparation conditions on the characteristics of exfoliated graphite. *Carbon* 40, 1575 – 1581.

9. Ramesha G.K. and Sampath S. (2007). Exfoliated graphite oxide modified electrode for the selective determination of picomolar concentration of lead. *Electroanalysis* 19, 2472 – 2478.
10. Xiao P., Xiao M. and Gong K. (2001). Preparation of exfoliated graphite/polystyrene composite by polymerization-filling technique. *Polymer* 42, 4813 – 4816.
11. Bonnissel M., Luo L. and Tondeur D. (2001). Compacted exfoliated natural graphite as heat conduction medium. *Carbon* 39, 2151 – 2161.
12. Cao X., Yang G., Wei S. and Li C. (2008). The electrochemical behaviour of an exfoliated graphite electrode in simulated seawater containing oil. *J. appl. electrochem.* 38, 1571 – 1575.
13. Inagaki M. and Suwa T. (2001). Pore structure analysis of exfoliated graphite using image processing of scanning electron micrographs. *Carbon* 39, 915 – 920.
14. Zheng Y.P. Wang H.N. Kang F.Y. Wang L.N. and Inagaki M. (2004). Sorption capacity of exfoliated graphite for oils-sorption in and among worm-like particles. *Carbon* 42, 2603 – 2607.
15. Tryba B. (2003). Exfoliated Graphite as a New Sorbent for Removal of Engine Oils from Wastewater. *Spill Sci. Technol. Bull.* 8, 569 – 571.
16. Toyoda M., Moriya K., Aizawa J., Konno H. and Inagaki M. (2000). Sorption and recovery of heavy oils by using exfoliated graphite Part I: Maximum sorption capacity. *Desalination* 128, 205 – 211.
17. Toyoda M. and Inagaki M. (2003). Sorption and Recovery of Heavy Oils by Using Exfoliated Graphite. *Spill Sci. Technol. Bull.* 8, 467 – 474.
18. Kamat P.V. (2012). TiO₂ Nanostructures: Recent physical chemistry advances. *J. Phys. Chem. C* 116, 11849 – 11851.

19. Kuvarega A.T., Krause R.W.M. and Mamba B.B. (2012). Multiwalled carbon nanotubes decorated with nitrogen, palladium co-doped TiO₂ (MWCNT/N, Pd co-doped TiO₂) for visible light photocatalytic degradation of Eosin Yellow in water. *J. Nanopart. Res.* 14, 776 – 792.
20. Stankovich S., Dikin D., Piner R., Kohlhaas K., Kleinhammes A., Jia Y., Wu Y., Nguyen S. and Ruoff R. (2007). Synthesis of graphene-based nanosheets via chemical reduction of exfoliated graphite oxide. *Carbon* 45, 1558 – 1565.
21. Bell N.J., Ng Y.H., Du A., Coster H., Smith S.C. and Amal R. (2011). Understanding the enhancement in photoelectrochemical properties of photocatalytically prepared TiO₂-reduced graphene oxide composite. *J. Phys. Chem. C* 115, 6004 – 6009.
22. Ramesh P. and Sampath S. (2003). Electrochemical characterisation of binderless, recompressed exfoliated graphite electrodes: Electron-transfer kinetics and diffusion characteristics. *Anal. Chem* 75, 6949 – 6957.
23. Kuvarega A.T., Krause R.W.M. and Mamba B.B. (2011). Nitrogen/Palladium-Codoped TiO₂ for Efficient Visible Light Photocatalytic Dye Degradation. *J. Phys. Chem. C* 115, 22110 – 22120.
24. Sasaki T., Nakano S., Yamauchi S. and Watanabe M. (1997). Fabrication of titanium dioxide thin flakes and their porous aggregate. *Chem. Mater.* 9, 602 – 608.
25. Yu J., Hai Y. and Cheng B. (2011). Enhanced photocatalytic H₂-production activity of TiO₂ by Ni(OH)₂ cluster modification. *J. Phys. Chem. C* 115, 4953 – 4958.
26. Rodriguez P., Reinert L., Comet M., Kighelman J. and Fuzellier H. (2007). Synthesis of structured titanium dioxide from carbonaceous templates: Preparation of supported nanoscaled titania particles. *Mater. Chem. Phys.* 106, 102 – 108.

27. Zhang H., Lv X., Li Y., Wang Y. and Li J. (2010). P25-Graphene composite as a high performance photocatalyst. *ACS nano* 4, 380 – 386.
28. Savoskin M., Yaroshenko A., Lazareva N., Mochalin V. and Mysyk R. (2006). Using graphite intercalation compounds for producing exfoliated graphite–amorphous carbon–TiO₂ composites. *J. Phys. Chem. Solids* 67, 1205 – 1207.



CHAPTER 10

CONCLUSIONS AND FUTURE PERSPECTIVES

10.1 CONCLUSIONS

The main thrust of the present work was to synthesise nanomaterials with tailored properties and to show the intrinsic correlation between the physicochemical properties of those nanomaterials and their activity in the photodegradation of organic pollutants in water. This study has shown that nitrogen and PGMs can simultaneously be introduced on the TiO_2 in a modified sol-gel method by taking advantage of the solubility of PGM precursors in aqueous ammonia or 2-propanol. This sol-gel modification resulted in N, PGM co-doped TiO_2 nanoparticles with enhanced photocatalytic activity for dye degradation and NOM removal compared to commercial Degussa P25 under visible-light irradiation. The enhancement correlated well with the amount of the PGM dopant. A maximum photodegradation efficiency of 100% in 3 hrs was realised with the N, Pd co-doped TiO_2 (0.6% Pd). These findings suggest that, in general, higher photo efficiencies can only be observed at optimal metal-dopant levels since higher metal dopant percentages caused a decrease. Results from this study showed that N, PGM co-doped TiO_2 are promising photocatalytic materials for organic pollutant removal in water-treatment systems and can be considered good candidates for future photocatalytic applications.

The second major finding was that introduction of N and PGMs resulted in modification of the optical and electronic properties of the co-doped TiO_2 . There was an overall band-gap reduction which can be attributed to the synergistic formation of inter-band gap states between the valence band and the conduction band of the TiO_2 . This was supported by XPS results which showed no evidence for orbital hybridisation. Band-gap reduction shifted the absorption edge of the material to the visible region, allowing use of solar radiation to activate the photocatalyst.

The most obvious finding to emerge from this study was that the calcination temperature has an effect on the size and crystallinity of the N, PGM co-doped TiO₂. At low temperatures the particles were small and less crystalline. An increase in calcination temperature resulted in particle agglomeration and increased crystallinity. This had a bearing on pollutant adsorption and consequently, photodegradation.

One of the more significant findings to emerge from this study was that PGMs appear to effectively trap photogenerated electrons, reducing the rate of electron/hole recombination, hence enhancing the activity of reactive holes and superoxide radicals for organic pollutant degradation. This was clearly observed by the changes in the photoactivity with varying amounts of the PGM dopant.

The source of radiation was shown to have an effect on the rate of photodegradation. The tungsten filament lamp gave lower degradation rates compared to the xenon mercury lamp. This was attributed to the differences in the power output of the lamps as well as their distance from the reaction vessel. The full UV-Vis spectrum resulted in higher photo efficiency compared to the low-energy ($\lambda > 450$ nm) visible radiation.

Functionalisation of CNTs improved their dispersion in aqueous media and promoted the uniform attachment of the inorganic components onto their walls. This study determined that supporting co-doped TiO₂ onto CNTs will result in further photocatalytic enhancement, which is a function of the amount of CNTs incorporated into the nanocomposite. Low CNT loadings gave higher photocatalytic activity compared to composites with higher percentages of CNTs. This is attributed to the aggregation of the CNTs at higher percentages, leading to uneven coating of the co-doped TiO₂ on their surfaces. There was an improvement in visible-light harvesting capabilities of CNT/N, Pd co-doped TiO₂ nanocomposites, which decreased with increasing amount of CNTs. DWCNTs were more effective in reducing the band gap of TiO₂ compared to MWCNTs. The relevance of CNTs in modification of the morphology and optical properties of the CNT/N, Pd co-doped TiO₂ as well as enhancement of the photocatalytic activity

towards dye degradation was clearly supported by the current findings. Formation of bonds between CNTs and the N, Pd TiO₂ is a crucial factor for photocatalytic enhancement. The high electron storage and channelling ability of CNTs plays an important role in reducing electron-hole recombination and improving the solar-light-energy-harvesting performance of the nanocomposites for solar-light photodegradation applications.

The results of this investigation showed that the presence of CNTs in CNT/N, Pd co-doped TiO₂ leads to increased pollutant adsorption. However, there was no correlation between pollutant adsorption and photocatalytic activity as highly adsorbing nanocomposites showed lower photoactivity.

Photocatalysis based on N, PGM co-doped TiO₂ nanocatalysts and CNT/N, Pd co-doped TiO₂ nanocomposites using solar radiation is a promising method for the treatment of contaminated water (**Figure 10.1**). The systems, applied at ambient temperature, promise to be inexpensive and viable alternatives or complementary methods for the removal of organic pollutants from water and wastewater.

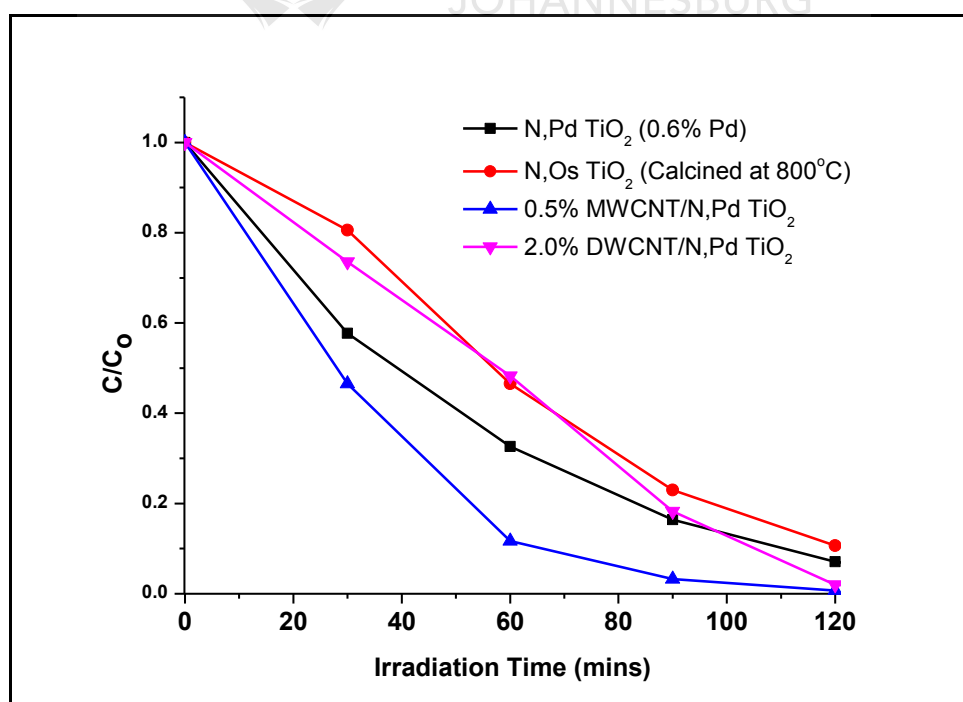


Figure 10.1 Comparison of the dye degradation efficiency of the highest performing photocatalysts

10.2 FUTURE PERSPECTIVES

This research has thrown up many questions in need of further investigation. The findings provide the following insights for future research:

- Various spectroscopy studies need to be conducted to probe the ultrafast excitation and charge recombination processes to identify the factors that limit the energy-conversion efficiency. More research is needed to better understand these processes and come up with strategies aimed at enhancing the photo efficiency.
- To date, only limited spectroscopic studies have been conducted to establish the electron-hole transfer processes on the semiconductor. A better understanding of interfacial charge transfer kinetics is important in designing more efficient photocatalysts for water decontamination.
- The photocatalytic enhancement in co-doped TiO_2 or CNT/co-doped TiO_2 which results from electron trapping by PGM species or CNTs, dictates the overall photocatalytic properties of the material. Theoretical studies using density functional theory (DFT) need to be performed to probe interactions of surface-to-adsorbed species and obtain a better understanding of the surface-binding aspects and reactivity.
- There are still major technical challenges such as the optimum system setup and catalyst recovery, therefore predictions for the long-term success of photocatalytic systems for water purification is still in the infancy.
- A number of possible future studies using the same experimental setup but many different pollutants are apparent. This would give an insight into the possible application of the materials in water containing a complex mixture of pollutants. Future trials should assess the effectiveness of the materials on a full selective decontamination regimen. The work presented herein

dealt with a small volume of the solution, where the effects of diffusion and other transport phenomena are minimal.

- Further work needs to be done to establish the effects of parameters such as pH, catalyst concentration, initial pollutant concentration, radiation source (UV or visible) and type of pollutants.
- Opportunities for TiO₂ now lie in more challenging areas such as energy conversion and storage. TiO₂ nanostructures have recently shown promise in designing Li-ion and Na-ion storage batteries. While the synthesised materials have been applied in water pollution control, evaluation of their performance in energy generation may be a step in the right direction in solving the world's mounting energy and water pollution problems.
- Another potential application of the CNT/N, Pd co-doped TiO₂ nanocomposites is CO₂ reduction in which light energy is used to activate TiO₂ to reduce CO₂ with the potential to produce fuels such as methane. It is recommended that further research be undertaken in these areas.